Università degli Studi di Palermo

AREA QUALITÀ, PROGRAMMAZIONE E SUPPORTO STRATEGICO
SETTORE STRATEGIA PER LA RICERCA
U. O. DOTTORATI

Dottorato di Ricerca in Scienze Fisiche e Chimiche
Dipartimento di Fisica e Chimica - Emilio Segrè
Settore Scientifico Disciplinare (corrisponde a quello del Tutor) – PHYS-05/A

INVESTIGATING EXOPLANETARY ATMOSPHERES THROUGH TRANSMISSION SPECTROSCOPY

IL DOTTORE
MATTIA CLAUDIO D'ARPA

IL COORDINATORE
MARCO CANNAS

IL TUTOR
GIUSEPPINA MICELA

CICLO XXXVII
ANNO CONSEGUIMENTO TITOLO 2025

Non est ad astra mollis e terris via

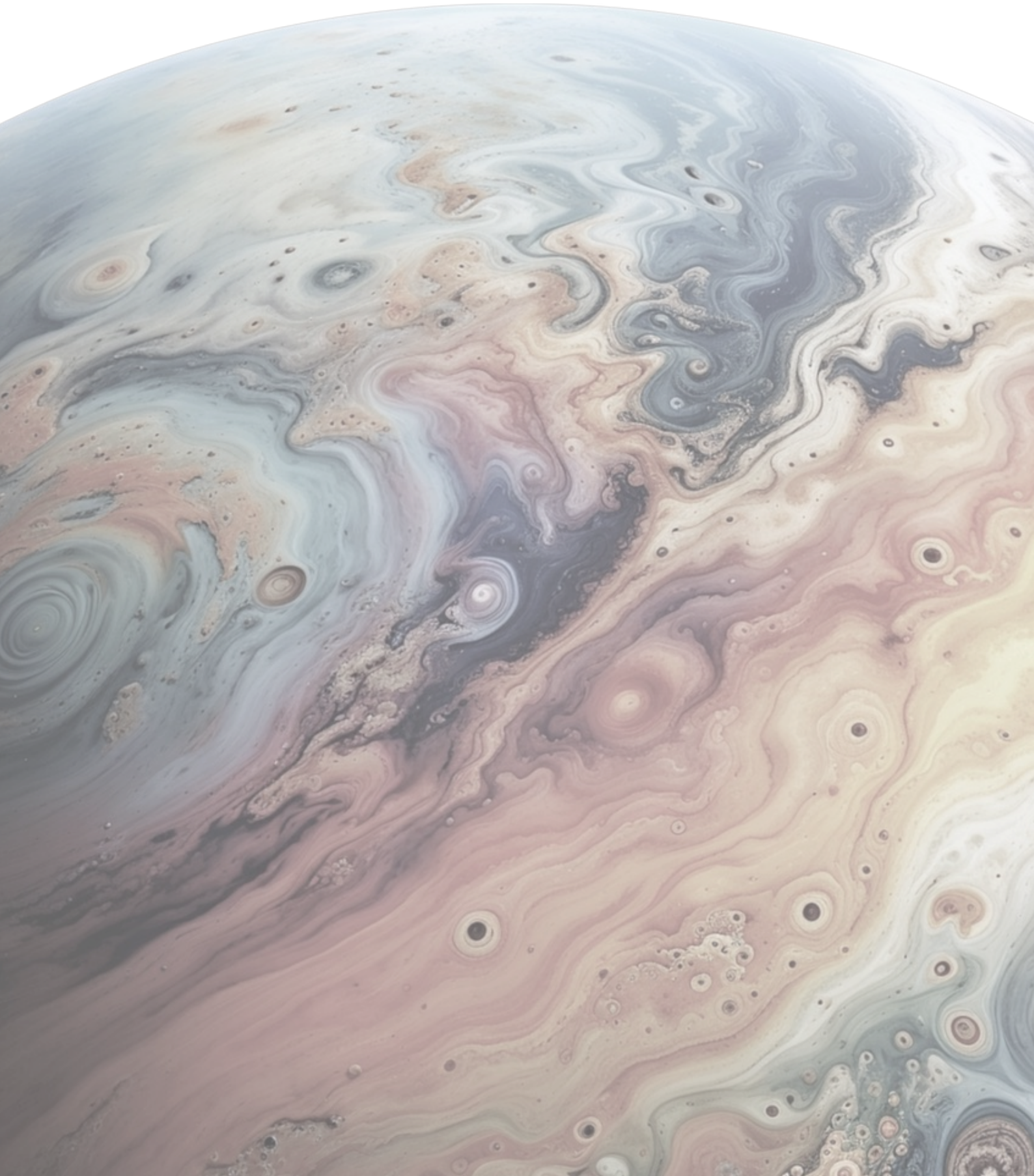

Contents

ABSTRACT

Over thirty years since the first exoplanet was identified, the tally of recognized exoplanets has surged dramatically to exceed 6000. This swift increase in discoveries has largely resulted from the deployment of the highly productive Kepler and **Transiting Exoplanet Survey Satellite (TESS)** missions, dedicated to extensively surveying exoplanets from space. The identification of initial exoplanets spurred interest in exploring their atmospheric properties. The primary challenge in directly observing exoplanet atmospheres stems from the significant contrast ratio between the planet and its host star. Fortunately, not long after, scientists identified a highly beneficial group of exoplanets, known as transiting planets, which enabled the initial detection of an exoplanetary atmosphere. This group primarily consists of planets orbiting closely with short periods, which increases the likelihood of transit events occurring within their orbits. An exoplanet transit occurs when the planet moves across the face of its star from the observer's viewpoint. When an exoplanet is in transit, some stellar light travels through its atmosphere, and based on the atmospheric composition, subtle spectral features are imprinted on the observed stellar spectrum. This technique is known as transmission spectroscopy.

This thesis is focused on the search and characterisation of atmospheric signals from the exoplanet atmosphere, the transmission spectrum, using both high- and low-resolution transmission spectroscopy observations of several exoplanets.

The majority of the research presented in this thesis pertains to applying the method I developed for deriving the transmission spectrum of individual lines while thoroughly removing Earth and stellar contaminants. I will discuss various studies focusing on KELT-9 b, the most scorching exoplanet discovered. Among these, I will detail the planet's atmospheric analysis through single line examination as outlined in D'Arpa et al. (2024b), introducing my method for extracting and fitting transmission spectra of individual lines. I will also compare the findings from D'Arpa et al. (2024b) with other research conducted by the **Global Architecture of Planetary System (GAPS)** collaboration concerning the single line analysis of KELT-9 b. Furthermore, I will demonstrate how this method, initially devised for KELT-9 b, can be applied to other subjects, including several hot Jupiters. This includes work in progress utilizing **Echelle SPectrograph for Rocky Exoplanets and Stable Spectroscopic Observations (ESPRESSO)** and other studies. A notable application of the framework developed for single line analysis is using both the Hα line and the He I triplet as markers of two distinct star-planet interactions: stellar activity and photo-evaporation as discussed in Guilluy et al. (2024) and D'Arpa et al. (2024a).

Regarding the low-resolution spectroscopy I will introduce the preliminary results of one ongoing project regarding the comparison between different pipelines used to extract the transmission spectra from **Hubble Space Telescope (HST) Wield Field Camera 3 (WFC3)** data. I will show how slightly different results obtained by these pipelines would lead to differences in the chemical composition retrieved.

List of Figures

List of Tables

List of Acronyms

Ariel Atmospheric Remote sensing Infrared Exoplanet Large Survey

BIC Bayesian Information Criterion

CARMENES Calar Alto high-Resolution search for M dwarfs with Exoearths with Near-infrared and optical Échelle Spectrographs

CCF Cross Correlation Function

CLV Centre to Limb Variation

CoRoT COnvection ROtation and planetary Transits

DE-MCMC Differential Evolution Markov chain Monte Carlo

DRS Data Reduction Software

ESA European Space Agency

ESO European Southern Observatory

ESPRESSO Echelle SPectrograph for Rocky Exoplanets and Stable Spectroscopic Observations

FWHM Full Width at Half Maximum

GAPS Global Architecture of Planetary System

GP Gaussian Processes

GTO Granted Time Observation

HARPS High Accuracy Radial velocity Planet Searcher

HARPS-N High Accuracy Radial velocity Planet Searcher for the Northern emisphere

HJ Hot Jupiter

HST Hubble Space Telescope

JWST James Webb Space Telescope

KELT Kilodegree Extremely Little Telescope

LTE	Local Thermal Equilibrium
MCMC	The Markov Chain Monte Carlo
NASA	National Aeronautics and Space Administration
NIST	National Institute of Standards and Technology
NLTE	Non Local Thermal Equilibrium
RM	Rossiter-McLaughlin
RME	Rossiter-McLaughlin Effect
RV	Radial Velocity
STIS	Space Telescope Imaging Spectrograph
TauREx	Tau Retrieval for Exoplanets
TESS	Transiting Exoplanet Survey Satellite
TNG	Telescopio Nazionale Galileo
TSM	Transmission Spectroscopy Metric
UHJ	Ultra Hot Jupiter
VALD3	Vienna Atomic Line Database
VLT	Very Large Telescope
WASP	Wide Angle Search for Planets
WFC3	Wield Field Camera 3

Chapter 1

General overview

This thesis concentrates on the atmospheric characterization of extrasolar planets through transmission spectroscopy observations. This chapter provides an overview of the exoplanet field, beginning with a discussion of the key elements involved in the search for new worlds. It then offers a general review of our current understanding of exoplanet atmospheres based on both theoretical and observational studies, concluding with a section specifically focused on studying these atmospheres using transmission spectroscopy.

1.1 Detection of exoplanets: a life-long resume

While the human desire to explore their loneliness in the universe is hard to date, our discovery of new exotic worlds where to find cosmic neighbours has only started very recently. The first exoplanet was discovered in 1992, only few years before my birth, by Wolszczan & Frail (1992) who detected periodic variations in the arrival time of emitted beams from pulsar PSR B1257+12. Three years later, our solar system got its first grade cousin as Mayor & Queloz (1995) made the first **Radial Velocity (RV)** planetary detection (see **RV** technique in Section 1.1.1) discovering a Jupiter sized object around the main sequence star 51 Peg with a much closer orbit to its host star than previously thought possible. This discovery was followed by many similar detections, resulting from a re-analysis of previous datasets (Marcy & Butler 1996; Butler & Marcy 1996). I was born approximately two years later than Mayor & Queloz (1995) revolutionary discovery (as stated by the 2019 Nobel prize). At that point, according to the **National Aeronautics and Space Administration (NASA)** Exoplanet Archive[1], only 11 planets were discovered employing the **RV** technique and consisting of a single hot Jupiter and its host star, as they were easier to detect. In 2000, the millennium and the transit revelations kicked off. The first planetary transit was observed simultaneously by Charbonneau et al. (2000) and Henry et al. (2000), who witnessed a period decrease in the star brightness during the planet inferior conjunction in its radial velocity orbit.

[1] https://exoplanetarchive.ipac.caltech.edu/index.html

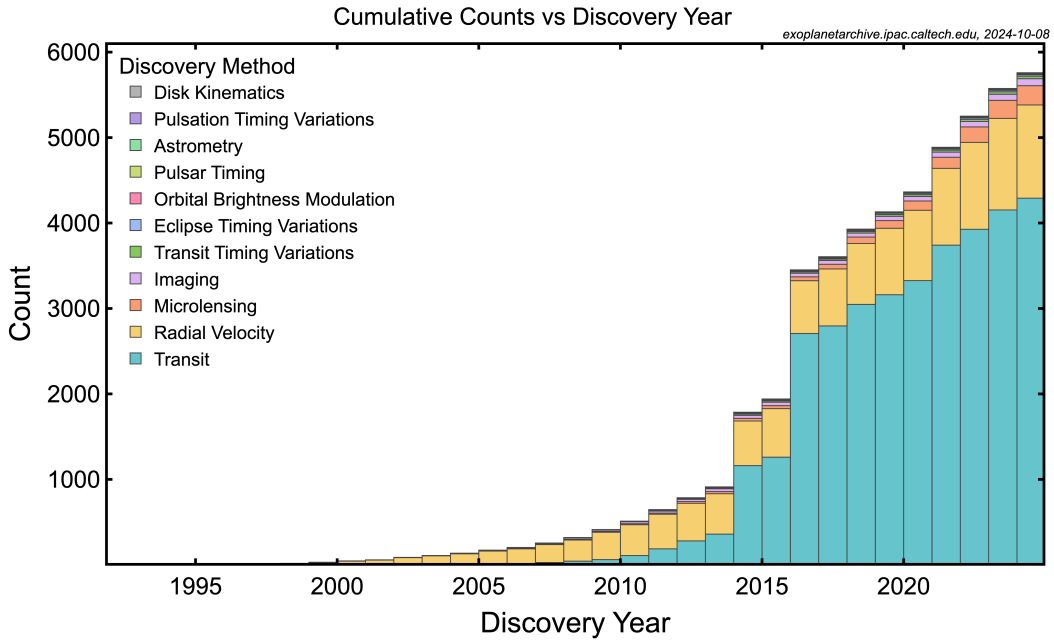

Figure 1.1: Cumulative counts of exoplanets as a function of the year taken from **NASA** Exoplanet Archive.

In particular, Henry et al. (2000) only showed half of a transit and they could not have claimed the discovery unless Charbonneau et al. (2000) showing two complete transits. In 2007, when I was ten, the number of planets discovered reached 255 planets, before exponentially increasing in the following years thanks to the survey devoted to detect transiting planets: **COnvection ROtation and planetary Transits (CoRoT)** satellite (Baglin et al. 2007), and the **NASA**'s Kepler satellite (Koch et al. 2007), which discovered hundreds of confirmed planets and potentially thousands more yet to be confirmed from 2009 to 2013, during its main mission and many more during the K2 phase. The outburst of transit method starting from 2009 can be clearly seen in Fig. 1.1 where is shown the cumulative counts of exoplanets discovered per year grouped by discovery method with the peaks in the histogram in 2014 and 2016 corresponding to the release of new confirmed planets by Kepler. At the end of my bachelor thesis on exoplanets in 2019 the number of confirmed planets just overcame 4000 detections in 27 years. At that point, **Transiting Exoplanet Survey Satellite (TESS)** (Ricker et al. 2015) step over and the number of planets kept growing. In 2021 at the beginning of my PhD adventure the discovered planets were almost 4800, 1000 less than the current number at the date[2]. Will they reach 6000 before my PhD defence?

In Section 1.1.1 and Section 1.1.2 I will deepen the two main methods used to discover exoplanets, already introduced above, the radial velocity and the transit method.

[2] 5832 at the 29/01/2025, according to the **NASA** Exoplanet Archive

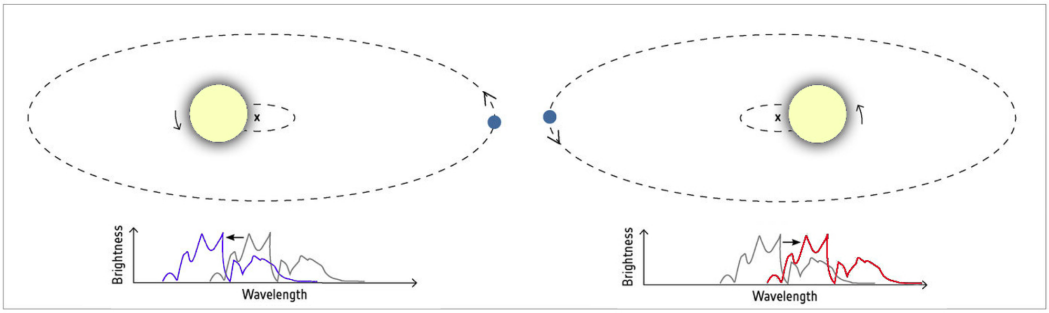

Figure 1.2: Illustration of the radial velocity method. The stellar spectrum seen by an observer is blueshifted (left) and redshifted (right) as the star orbits the system barycentre. Credit: eso.org

1.1.1 A spectroscopic method: the radial velocities to constrain the mass

Since the pioneering detection of an exoplanet orbiting a Sun-like star by Mayor & Queloz (1995), the **RV** method has been heavily utilized. This approach is not designed to directly observe an exoplanet, but rather to measure the changes in velocity it causes in the star's spectrum for binary systems. It involves a spectroscopic method that estimates the periodic Doppler shifts in the star's spectral lines, resulting from the gravitational influence the unseen planet exerts on its host star. This is clear in Fig. 1.2, where the effect of the planet orbiting around the star can be seen in the stellar spectrum. The radial velocity semi-amplitude (K) of the star's Doppler shift, induced by the planet's orbit, can be expressed as:

$$K_* = \frac{M_p \sin i}{(M_* + M_p)^{2/3}} \left(\frac{2\pi G}{P}\right)^{1/3} \frac{1}{\sqrt{1-e^2}} \tag{1.1}$$

where P represents the planet's orbital period, $M_\star$ and M_P denote the stellar and planetary masses (considering the assumption that $M_\star \gg M_P$), e is the orbit's eccentricity, and i is the inclination relative to the line of sight. For a circular orbit, the radial velocity fluctuations are sinusoidal, reaching their peak at K. Stellar mass is often estimated via a mass-spectral-type relationship or other observable data. With knowledge of $M_\star$ and P, and by measuring K, Eq. 1.1 allows us to compute $M_P \sin i$. Nevertheless, without the system's inclination, and given that $\sin i \leq 1$, this method typically offers an upper limit for the planetary mass. Eq. 1.1 further reveals that for a given star, radial velocity semi-amplitudes are maximized for planets with greater mass and shorter orbital periods.

It is useful to take our Solar System's planets as an example to understand the quantities we are talking about: Earth, with its orbit at 1 astronomical unit (AU), causes the Sun to move by $\sim$ 10 cm/s. For Earth-like planets orbiting closer to their star, this effect increases to about 1 m/s. This value is still below what substantial planets like Jupiter can exert on their star, with speeds surpassing 10 m/s, particularly at closer proximities, reaching hundreds of meters per second (Bozza et al. 2016). Currently, the most

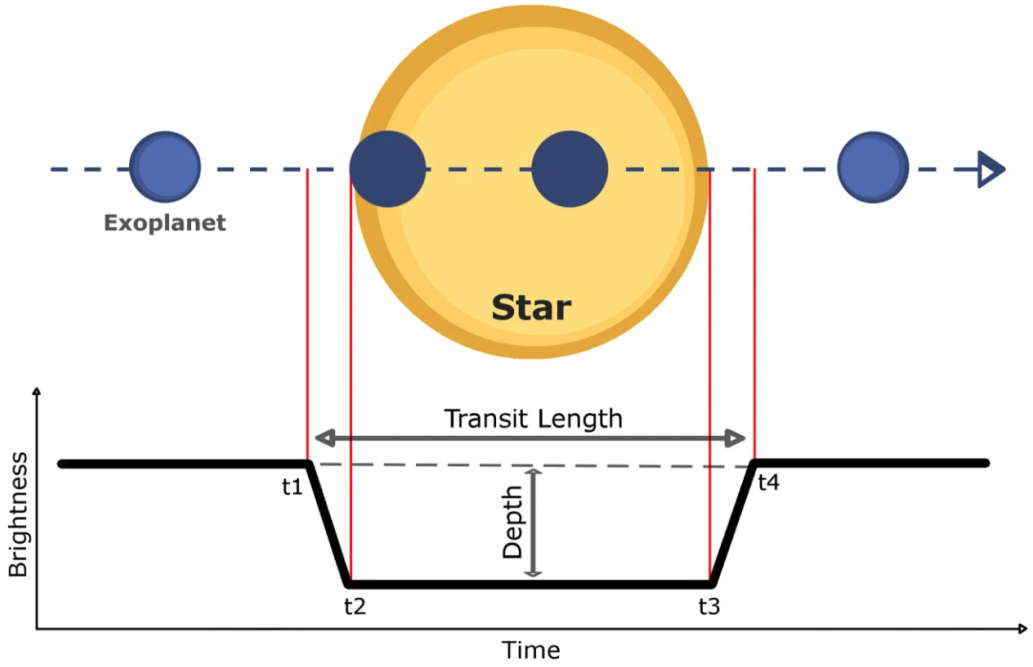

Figure 1.3: Illustration of the transit method for detection of exoplanets. If the orbital plane of a system appears nearly edge-on, the planet will cross the disk of the star. As the exoplanet orbits the star, different brightness values are obtained. Some parameters that can be extracted from a light curve are: Beginning of ingress (t1); end of ingress (t2); beginning of egress (t3); end of egress (t4); transit length; and transit depth. From Jara-Maldonado et al. (2020)

advanced spectrographs for detecting exoplanets include the **High Accuracy Radial velocity Planet Searcher (HARPS)** Pepe et al. (2000) at the 3.6-meter telescope at the La Silla Observatory in Chile, its counterpart in the northern hemisphere, **High Accuracy Radial velocity Planet Searcher for the Northern emisphere (HARPS-N)** (Cosentino et al. 2012), at the **Telescopio Nazionale Galileo (TNG)** in La Palma, Spain, and the newly introduced **Echelle SPectrograph for Rocky Exoplanets and Stable Spectroscopic Observations (ESPRESSO)** spectrograph Pepe et al. (2010) at the **Very Large Telescope (VLT)** in Paranal, Chile. The two **HARPS** instruments are both able to reach a **RV** precision of 1 m/s while **ESPRESSO** can push to 0.1 m/s meaning that nowadays we are able to detect planets with masses similar to the Earth (see Section 1.3 for an insight on the exoplanet demography).

1.1.2 A photometric method: the transit to constrain the radius

As the **RV** method has been the pathfinder of exoplanet detections, nowadays the transit method is unequivocally the most prolific. As extrasolar systems are randomly oriented in space, an ensemble of them can have orbital planes close enough to the observer's line of sight, that one or more planets in the system can transit the visible disk of the host star. This requires the planetary system to be almost edge on (i $\sim$ 90 degrees, having

defined the inclination i as the angle formed by the line of sight and the perpendicular to the orbital plane). With this constraint, the probability for a transit to occur is given by the following formula:

$$P_{\text{tra}} = 0.0045 \left(\frac{R_\star + R_\text{p}}{R_\odot} \right) \left(\frac{1\,\text{au}}{a} \right) \left(\frac{1 + e\cos\omega}{1 - e^2} \right), \tag{1.2}$$

where $R_\star$ and R_p are the stellar and planetary radius, a is the semi-major axis and ω represents the argument of the periastron (e.g., Charbonneau et al. 2007). The geometry of a transit is shown in Fig. 1.3 where can be seen that, if a planet transits, the occultation of the parent star disc will lead to a periodic drop in the stellar flux called transit depth, δ:

$$\delta = \frac{\Delta f}{f} \sim \left(\frac{R_\text{p}}{R_*} \right)^2 \tag{1.3}$$

The drop in stellar flux is observed trough a photometer that can be mounted on a spacecraft such as in the cases of Kepler and **TESS**, or in ground-based telescopes such as the **Kilodegree Extremely Little Telescope (KELT)** (Siverd et al. 2009) and the **Wide Angle Search for Planets (WASP)** (Pollacco et al. 2006). From Eq. 1.3, we can estimate the radius of the planet, R_p, by measuring the flux change during a transit and knowing the stellar radius, R_*. In this context, using the solar system as a reference is advantageous. Specifically, an Earth-sized planet transiting a Sun-like star causes a transit depth of $8.3 \times 10^{-5}\%$, while a Jupiter-sized planet results in a 1% decrease (expressed in units of stellar flux). Consequently, the transit method is particularly effective for detecting large planets, such as the one first discovered by Charbonneau et al. (2000), or systems where the planet-to-star radius ratio is significant. The impact of this detection bias on the currently known planetary population will be further examined in Section 1.3. The key parameter obtained through the transit technique is the planetary radius. However, by observing multiple transits, one can also determine the orbital period, which leads to the calculation of the orbit using the host star's mass and Kepler's Third Law:

$$\frac{a_p^3}{P_p^2} = \frac{GM*}{4\pi^2} \tag{1.4}$$

where a_p is semi-major axis, P_p is period of the planet, G is the gravitational constant, and M_* is the mass of the host star (where we assume $M_p << M_*$).

There are several other detection methods that I did not introduce in the previous Sections such as the direct imaging (Traub & Oppenheimer 2010), the microlensing (Mao & Paczynski 1991; Gould & Loeb 1992), and the astrometry (Perryman et al. 2014). Each detection method has sensitivity to specific ranges or type of planets and plays an important role in discovering exoplanets, but since this thesis is focused on exoplanetary atmospheres which are strictly connected to the transit method, I will not discuss them.

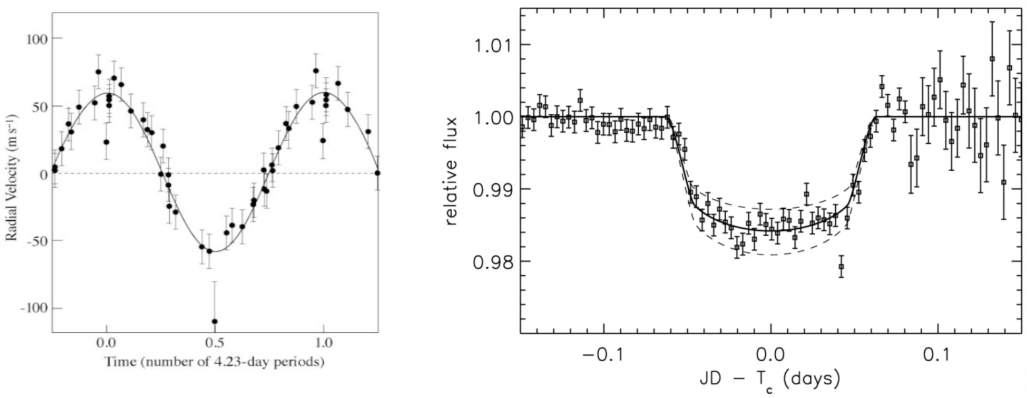

Figure 1.4: First planets detected with the two main methods. Left panel: first **RV** detection, 51 Pegasi b by Mayor & Queloz (1995). Right panel: first transit light curve, HD-209458 b by Charbonneau et al. (2000).

1.2 Combining the two methods: the physical properties

1.2.1 The mass-radius diagram

The two techniques outlined before enable us to determine the mass and radius of the studied planets with the first detections for each technique shown in Fig. 1.4. With these parameters, the average density of exoplanets can be calculated. This, in turn, places particular constraints on their internal structure. Yet, for smaller planets, density alone cannot uniquely identify their interior composition. Figure 1.5 displays confirmed exoplanets to date (depicted as black dots) as a function of planetary mass and radius, alongside mass-radius curves (solid lines) for planets made of pure substances like water, rock, iron, hydrogen, and water. This diagram demonstrates that, for smaller planets, various compositions can result in the same density. A planet with specific mass and radius values might possess a significant amount of water ice (termed an ocean planet) or have a substantial rocky iron core with some H_2 and/or He, as discussed by Zeng et al. (2019).

1.2.2 The Rossiter-McLaughlin Effect

During transit, **RV** measurements can help determine a planet's projected obliquity. A prevalent method for assessing system obliquity involves detecting the Rossiter-McLaughlin (**Rossiter-McLaughlin (RM)**) radial-velocity anomaly, initially observed by Rossiter (1924) and McLaughlin (1924), in the context of binary eclipses. We often refer to this method as the classical **RM**. Over time, other methods have been developed, including Doppler tomography (Collier Cameron et al. 2010) and reloaded-**RM** (Cegla et al. 2016). All three techniques utilize high-resolution observations as the exoplanet transits across the star's disc. The underlying principle is the rotation of the stellar disc from the observer's perspective, leading to one hemisphere being red-shifted and

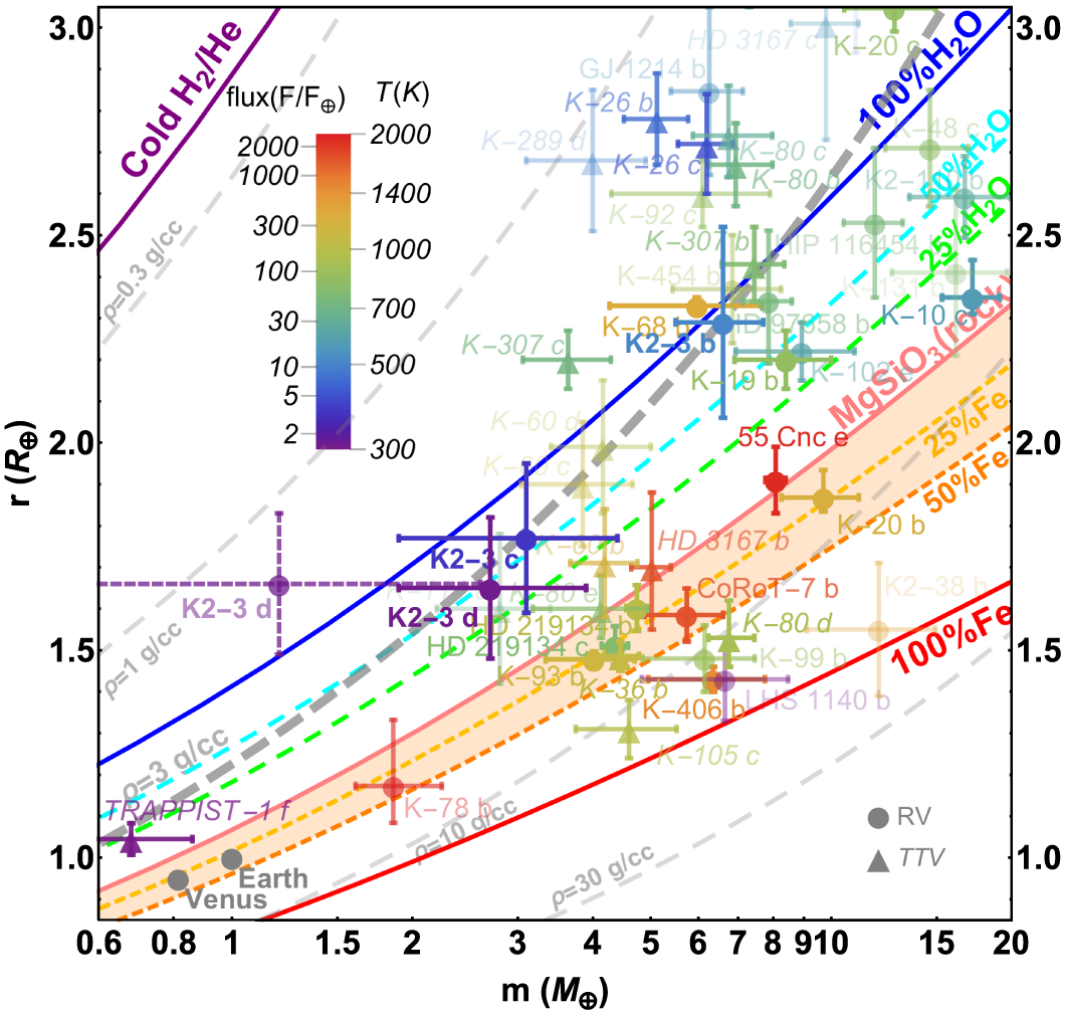

Figure 1.5: Mass-radius diagram for exoplanets for which the mass and radius have been both measured with a relative error better than 30%. The solid lines represent the different compositions. The planetary data are taken from the NASA exoplanet archive and updated to August 30, 2017. From Damasso et al. (2018).

the other blue-shifted. As the planet transits its host star's disc, it obscures areas with different projected velocities. These obscured sections will be absent in the observed stellar spectrum, causing spectral line deformation. The **RM** is highly influenced by the system's geometry and the star's projected rotation speed (vsini). In the classical **RM**, the alteration in radial velocity of the stellar lines due to decreased flux from the blue or red-shifted hemispheres during transit is quantified. For example, if the planet conceals blue-shifted regions of the stellar disc during transit, the observed spectral lines will shift to red and vice versa (see Fig. 1.6). To a first approximation, assuming a spin-orbit alignment angle (also referred to as projected obliquity) $\lambda \sim 0°$, the semi-amplitude of the **Rossiter-McLaughlin Effect (RME)** can be approximated as follows (Triaud et al. 2017):

$$A_{\rm RM} \simeq \frac{2}{3}\left(\frac{R_{\rm p}}{R_\star}\right)^2 v \sin i_\star \sqrt{1-b^2}, \tag{1.5}$$

where b represents the impact parameter, $R_{\rm p}$ is the planet's radius, and $R_\star$ is the star's radius. For stars that rotate rapidly and in systems where large planets orbit small stars, the anomalous radial momentum increases since the planet obscures a larger section of the star's disc with a larger radial velocity. The Doppler tomography technique analyses the variations in line shape during an exoplanet's transit. By subtracting the average line shape measured when the planet is not transiting, the dark areas (caused by the exoplanet) on the star's surface emerge as positive radial-velocity bumps that move in accordance with the exoplanet's position on the stellar disc. This bumps progression produces a phenomenon known as the Doppler shadow, which can be modelled using parameters similar to those used for the classical Rossiter-McLaughlin effect. The reloaded-**RM** method involves reconstructing the velocity field obscured by the planet during transit by examining line profiles. This approach is sensitive to differential rotation, can determine the star's true inclination $i_\star$, and considers additional stellar influences such as convective blueshift and limb-darkening changes. Bourrier et al. (2017) have indicated that conventional **RM** measurements of λ may contain significant biases resulting from alterations in line profiles.
The **RM** effect can be seen for different scenarios in Fig. 1.6. The **RV** collected during a transit clearly show a behaviour depending on the geometry of the transit as in the three cases illustrated. This can help us understand the geometry of the orbit of the planet and retrieve key parameters such as the projected obliquity λ. The impact of **RME** in the analysis of high resolution data for the characterisation of planetary atmospheres will be seen in Chapters 2, 3 and 4.

1.3 A brief insight on the exoplanets demography

The accumulation of various observational methods has led to the discovery of over 5800[3] exoplanets around different star types. Statistical estimates using different detection techniques, as Howard et al. (2010) and Batalha (2014) suggest, indicate that on average, every star in the galaxy hosts at least one planetary companion, implying the

[3] 29/01/2025, according to the **NASA** Exoplanet Archive

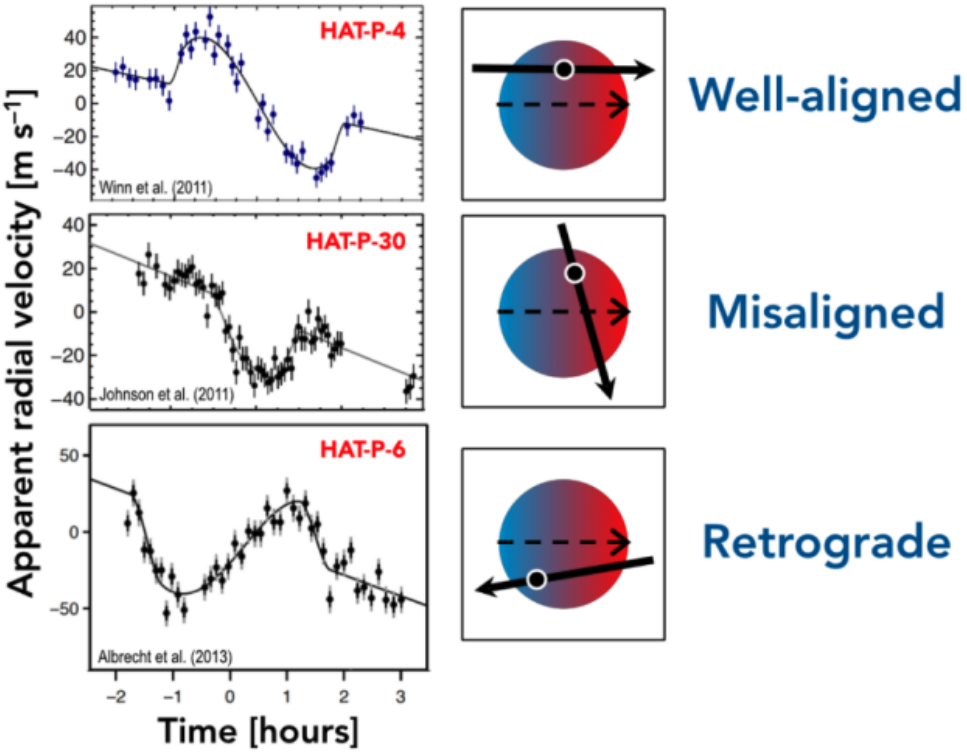

Figure 1.6: The **RM** effect of different exoplanets. Left panels: corresponding **RV** signals. Right panels: three transit geometries that produce identical photometric light curves, but differ in spin-orbit alignment. From Mar Rivera Colomer thesis.

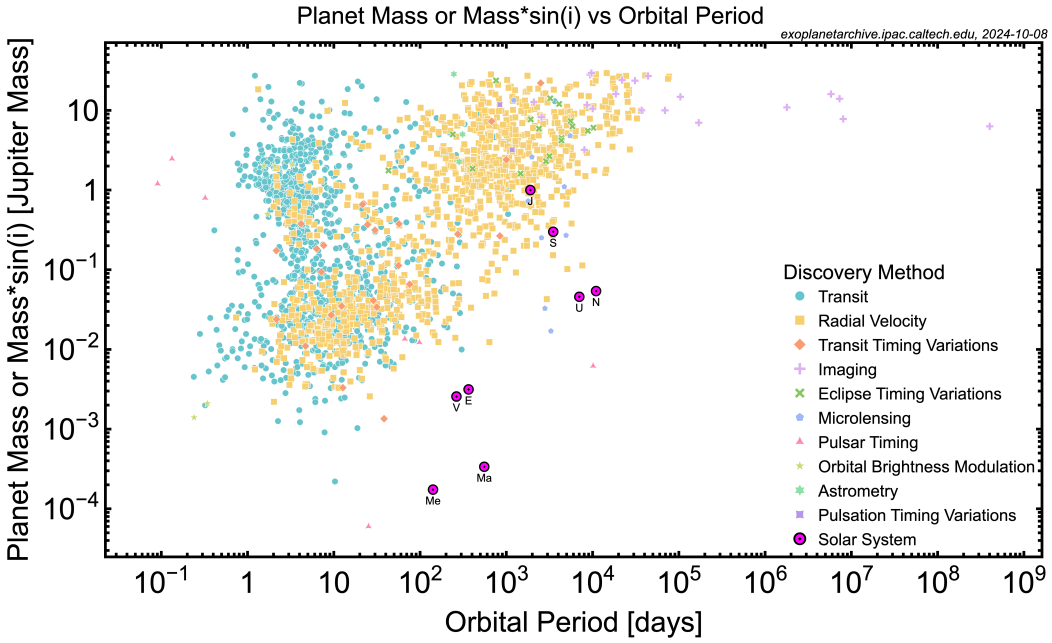

Figure 1.7: Mass of detected planets vs their orbital period. The different markers and colours indicate the several different technique used for the detection. Taken from **NASA** Exoplanet Archive.

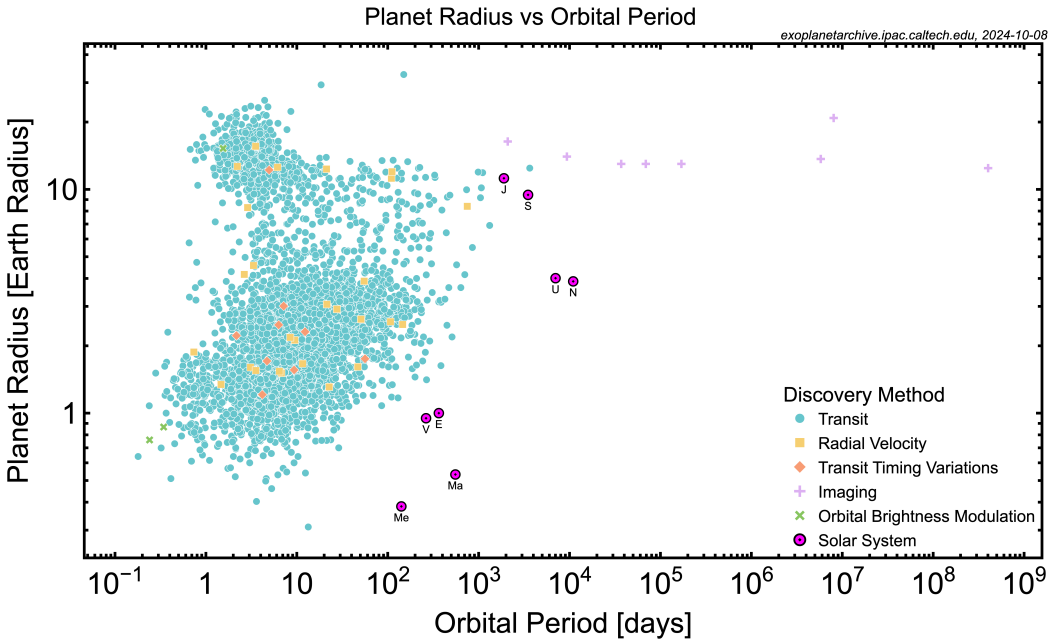

Figure 1.8: Radius of detected planets vs their orbital period. The different markers and colours indicate the several different technique used for the detection. Taken from **NASA** Exoplanet Archive.

existence of billions of planets just within the Milky Way. Fig. 1.7 and Fig. 1.8 provide a comparative analysis of known exoplanets and solar system planets, showcasing plots of mass and radius versus orbital period. We do not know both radii and masses for all the planets discovered nowadays, therefore the samples in the two figures do not fully overlap. However, these comparisons reveal a vast diversity in exoplanet characteristics, emphasizing the distinct nature of planetary systems compared to our solar system.

Exoplanet detection is biased towards large, closely orbiting planets, which are easier to observe, resulting in their over-representation in exoplanet databases. Additionally, many planets fall outside or below the detection capabilities of current surveys, rendering them virtually unseen. Fig. 1.8 shows that transit surveys are sensitive to the smallest exoplanets, from smaller solar system-sized planets at 0.01 AU to slightly larger than Jupiter at 1 AU. Fig. 1.7 shows that radial velocity surveys find Earth-mass planets at 1 AU and much larger ones, up to two orders of magnitude greater than Jupiter, at 10 AU, while microlensing surveys can spot Jupiter-mass planets at 5 AU. Direct imaging surveys, beyond 10 AU, mainly identify super-Jupiters. By integrating multiple detection approaches, a comprehensive picture of planetary populations emerges, though observational biases must be acknowledged. Radial velocity and transit surveys reveal that super-Earths ($R_{\rm p} < 4 R_\oplus$) and sub-Neptunes ($R_{\rm p} > 4 R_\oplus$) are the most prevalent exoplanets and are commonly found within 1 AU, while giant planets, located between 1 and 10 AU, orbit a smaller portion of stars. We will delve into these planet types in detail in the next Section, following an introduction to exoplanetary atmospheres.

Certain anticipated samples have been observed to be absent from the radius-period diagram in Fig. 1.8, among which the radius valley, or Fulton gap, and the Neptunian desert. According to Fulton et al. (2017), there is a scarcity of close-in planets—those with orbital periods under 100 days—in the radius range between 1.5 and 2 $R_\oplus$. This area is termed the radius valley, located around 1.8 $R_\oplus$ and is not visible in Fig. 1.8 because of the scale. With the Neptunian desert we denote the region that would contain hot sub-Saturns, given their smaller masses compared to hot Jupiters and Saturns. However, very few planets have been found in what is also referred to as the evaporation desert (middle-left region of Fig. 1.8). While the causes of the radius valley remains uncertain, various plausible explanations exist for the Neptunian desert. A prominent mechanism is photo-evaporation, which can significantly impact low-mass planets with hydrogen envelopes positioned within $\sim$0.1 AU. Owen & Wu (2017) found that evaporation can inherently explain why exoplanets are sparse around the evaporation desert, contingent on the atmospheric masses they possessed before beginning atmospheric mass loss. Specifically, planets prone to atmospheric mass loss will either shed mass until entirely stripped or achieve a stable atmospheric mass. The evaporation or radius valley occurs between planets with stripped cores and those capable of sustaining their atmospheres. The absence of planets in this region is due to the complete removal of their envelopes if their atmospheric mass fraction (M_{atm}/M_{core}) was originally below 0.01. Conversely, the evaporation desert arises from planets with atmospheric mass fractions around 1 that evolved to lower mass (Owen 2019). I will discuss the effect of photo-evaporation in the work introduced in Section 4.2 regarding the photo-evaporation of TOI-5398 b.

1.4 Exoplanetary atmospheres

Exploring the atmospheres of exoplanets offers a promising approach to resolving the degeneracies in potential internal compositions for planets with specific masses and radii. Furthermore, investigating these atmospheres is crucial for bridging the gap between a planet's interior and its atmosphere while addressing various scientific inquiries. For instance, atmospheric study enables detailed descriptions of known exoplanets, including molecular makeup, haze or cloud presence, and temperature-pressure inversion profiles (e.g., Madhusudhan et al. 2016). It links atmospheric composition to planetary formation and migration, with accurate assessments of elemental abundances, like C, H, and O, providing insight into the formation locations within the protoplanetary disk (e.g., Madhusudhan et al. 2014). Moreover, by analysing atmospheric circulation, temperature-pressure profiles, chemical compositions, and biomarkers, one can evaluate an exoplanet's surface conditions and potential habitability (e.g., Seager 2013). As the diversity of discovered exoplanets grows and the first transiting planets are detected, significant efforts have focused on detecting and comprehending their atmospheres. HD209458 b was notably the first transiting planet with an atmospheric detection, made by Charbonneau et al. (2002) using the **Space Telescope Imaging Spectrograph (STIS)** on the **Hubble Space Telescope (HST)**, where sodium (Na I) line absorption was prominently observed. This discovery sparked a rapidly expanding area of study, driven by advancements in astronomical technology and extensive atmospheric modelling efforts. Theoretical research plays a crucial role in predicting the atmospheric species of specific exoplanets.

In the next subsections, I will introduce the different types of exoplanets, especially focusing on their expected atmospheric properties.

1.4.1 Hot Jupiters

Hot Jupiters are massive gas giants with masses and sizes comparable to that of Jupiter (Mp $\sim$ 0.3 - 3 M_J, $R_p \sim$ 0.2 - 2 R_J, Stevens & Gaudi 2013) orbiting their stars in less than 10 days. They reside in close proximity to their stars (a $<$ 0.1 AU), receiving intense stellar radiation, which results in equilibrium temperatures ranging from 800 to 2200 K. For over ten years, they were the predominant type of exoplanets discovered, largely because they are the simplest to spot via transit and radial velocity methods.

Since massive planets are unlikely to originate in the hot inner areas of a protoplanetary disk, various early evolution scenarios have been suggested to explain their brief orbital periods. Hot Jupiters might migrate through gas disc migration, where a giant planet shifts before the protoplanetary gas disc disperses by transferring angular momentum with the disc or by high-eccentricity migration, a process allowing planets with high eccentric orbits to alter their trajectories over time due to interactions with other celestial bodies, such as other planets or the disc's gas and dust (see Baruteau et al. 2014; Rasio & Ford 1996, and references).

Despite their detection is biased by instrumental limitations, Hot Jupiters are inherently

uncommon, with an occurrence rate around main sequence stars of merely about 0.5 - 1% (Fressin et al. 2013). Their prevalence is significantly influenced by the metallicity of the host star, as metal-rich stars tend to host gas giant planets more frequently (Fischer & Valenti 2005). The metallicity of the host star can indicate the quantity of material available on the protoplanetary disc for forming giant planets through core accretion (Johnson et al. 2010).

In the field of exoplanet atmospheric science, Hot Jupiters are extensively studied due to their considerable expected spectral features. This is attributed to their high temperatures and substantial circumference, which result from their size and extended scale heights (see Section 1.5 for the definition). For example, the scale height of hot Jupiter HD-209458 b is approximately 550 km (Lecavelier Des Etangs et al. 2008), compared to Earth's 11 km. HD-209458 b also has an orbital period of about 3.5 days. Situated close to their host stars, hot Jupiters endure intense irradiation, reaching equilibrium temperatures over 1000 K. These elevated temperatures were first theoretically predicted by Seager & Sasselov (2000) and have been empirically validated through secondary eclipse observations conducted with Spitzer, revealing strong infrared emissions from several exoplanets. At these temperatures, a planetary atmosphere is expected to be mainly composed by H_2O (water vapour) and H_2, being the H_2O the most significant spectral feature expected in their atmosphere (Seager & Sasselov 2000), particularly in the infrared. Water vapour absorption has been identified in the atmosphere of several hot Jupiters (Deming et al. 2013). Depending on the metallicity and temperature of these planets, other atoms and molecules can also be found in their atmosphere, such as carbon monoxide (CO), carbon dioxide (CO_2), and methane (CH_4) as several studies found (e.g., Snellen et al. 2010; Brogi et al. 2012). At the higher temperatures of very hot Jupiters, titanium oxide (TiO) and vanadium oxide (VO) could also cause strong features in the transmission spectra. The detection of atomic and molecular species may be difficult due to the presence of hazes, small particles suspended in the atmosphere of exoplanets that can be probed by the detection of a Rayleigh scattering slope in the transmission spectrum (Lecavelier Des Etangs et al. 2008), which results from the dispersion of starlight at bluer wavelengths by small particles. This feature has already been observed in several hot Jupiters and Neptune-sized planets (Murgas et al. 2020). However, star spots in the stellar surface could mimic the Rayleigh scattering feature (Oshagh et al. 2014). On the other hand, the presence of clouds in an atmosphere, masses of solid and/or liquid particles produced by the condensation of atmospheric gases, can naturally explain featureless transmission spectra.

1.4.2 Ultra Hot Jupiters

In recent years, a distinctive category of exoplanets known as ultra-hot Jupiters has been identified. These are tidally locked gas giants that orbit very close to early-type stars (A-F), completing their orbits in mere hours or days. The intense irradiation these planets receive results in extreme temperature gradients between their day and night sides (Komacek & Showman 2016). This strong stellar radiation heats the gas, potentially causing the planets' atmospheres to expand beyond their Roche lobes (e.g., Yan &

Henning 2018), which may induce atmospheric evaporation processes. The equilibrium temperatures of these planets exceed 2000 K (usually 2200 K is the threshold adopted to distinguish between a **Hot Jupiter (HJ)** and an **Ultra Hot Jupiter (UHJ)**) and can peak above $\sim$ 10,000 K in the exospheres of their day sides (Wyttenbach et al. 2020). The night side is thought to be cloudy and element-poor, whereas the day side, free of clouds, consists of a thermal ionosphere due to ionization of neutral elements by stellar radiation (Helling et al. 2019). Unlike cooler Jupiters, ultra-hot Jupiters lack water vapor in their day-side atmospheres because the high temperatures dissociate such molecules. Observations have consistently evidenced this, revealing a plethora of metals like Na I, Ca II, Ca II, Fe I, Fe II, and Mg I in their atmospheres (e.g., Hoeijmakers et al. 2019).

A notable feature of these planets is their atmospheric structure, with various studies showing thermal inversions, where temperature increases with altitude. The identified emissions of species like Fe I, TiO, and H_2O (e.g., Pino et al. 2020) serve as direct proof of these temperature inversions. Theoretically, stronger temperature inversions are expected in ultra-hot Jupiters orbiting early-type stars, as predicted by Lothringer & Barman (2019). Furthermore, the stark day-night temperature contrasts are likely to drive significant atmospheric circulation, with horizontal winds potentially reaching speeds comparable to the speed of sound (Showman et al. 2020). Despite the relatively limited number of known ultra-hot Jupiters, they have become focal points of study due to the brightness of their host stars, their high temperatures, and favourable planet-to-star radius ratios, making them ideal for atmospheric investigations as shown by the atmospheric characterisation of KELT-9 b, the hottest exoplanet known, in Section 2.1.

1.4.3 Super-Earths and Sub-Neptune

Kepler's findings notably revealed a significant number of planets sized between 1-4 $R_\oplus$ absent in our solar system, sparking interest in their formation and evolutionary processes. This group includes both gaseous, Neptune-like planets and smaller, rocky super-Earths. Approximately half of solar-type stars possess at least one planet smaller than Neptune, according to Fressin et al. (2013). Unlike giant planets, which show a marked correlation between abundance and stellar metallicity, planets with $R_p \sim R_\oplus$ exhibit only a weak, if any, dependence based on metallicity, although there is a noticeable increase for short-period (10-100 days) planets (1.7 - 4.0 $R_\oplus$) around metal-rich stars, as noted by Petigura et al. (2018). The bulk density distributions of these planets vary more than those of hot Jupiters, as reported by Lopez & Fortney (2013) for example. The prevailing theory for their formation involves the accretion of solids beyond several AU, followed by migration through the gas disc. Post gas-disc dissipation, these planets evolve through mechanisms shaping their final masses and compositions. They may have solid surfaces with minimal atmospheres mainly composed of Si, Mg, Fe, C, and O, or they may act as transitional planets with rocky cores enveloped in H-rich atmospheres or significant H_2O ices/fluids. In contrast to the primitive atmospheres of giant planets, these bodies may exhibit evolved atmospheres potentially containing diverse species, offering insight into their formative and evolutionary histories. Due to the relative small size of their atmospheres and their smaller surface gravity, Hot super-

Earths and sub-Neptune planets are likely the most prone to evaporation and potential atmospheric loss which can be detected by analysing their hydrogen and/or helium envelopes as already done for Saturn-mass planets (e.g., Nortmann et al. 2018, and Section 4.2), and warm Neptunes (e.g., Palle et al. 2020a). In this context, Seager & Sasselov (2000) proposed that substantial EUV (10-92nm) and X-ray (0.5-10nm) radiation could lead to strong He I absorption features at 1083 nm in their transmission spectra. The EUV flux first ionizes He I into He II, that then recombines back to He I populating the triplet 2^3S metastable state, which subsequently scatter in the 2^3S-2^3P transition. Exploration of He I as a proxy for atmospheric evaporation, as suggested by Oklopčić & Hirata (2018), highlights its potential for assessing mass loss from stellar irradiation (see also Sanz-Forcada et al. 2022). Interstellar absorption significantly impacts studies of hydrogen Lyman α (Ly-α) lines, traditionally used to monitor atmospheric escape.

1.5 Transmission Spectroscopy

One of the primary goals when investigating exoplanet atmospheres is to characterize Earth-like planets to determine their potential habitability. However, the quest to explore planets similar to Earth must remain on hold—despite the relative abundance of Earth-like planets in the cosmos (Bryson et al. 2020), our current telescopes and instruments are not yet capable of studying the atmospheres of Earth analogs. The discovery of a notably large number of exoplanets orbiting very close to their stars, at distances less than about 0.05 AU and with short orbital periods, has made it possible to start examining the atmospheres of some of these planets. Due to their proximity to their stars, these planets exhibit high temperatures, leading to greater planet-to-star contrast. Moreover, hot planets are particularly interesting because the elements that compose them remain in a gaseous state in their atmospheres. For this reason, atmospheric observations are a probe of the planet's composition, unlike colder planets, where various elements are in a condensed state. Despite the numerous exoplanets identified to date, atmospheric characterization studies have been conducted on only a small fraction of 247 planets[4].

1.5.1 A quick look at the physics of transmission spectroscopy

In this section I summarise this technique which is used and deepen trough all the Chapters of this thesis.
A detailed insight on the physics of transmission spectroscopy can be found in Tinetti et al. (2012) and can be seen in Fig. 1.9, where the path of the starlight crossing the planetary atmosphere is shown.

Planets with short orbital periods situated very near to their host stars have a higher chance of experiencing transit events, with an occurrence rate of about 10% for hot Jupiters. During a transit, the exoplanet crosses in front of its host star relative to our

[4]According to the *IAC community database for exoplanet atmospheric observations*https://research.iac.es/proyecto/exoatmospheres/index.php

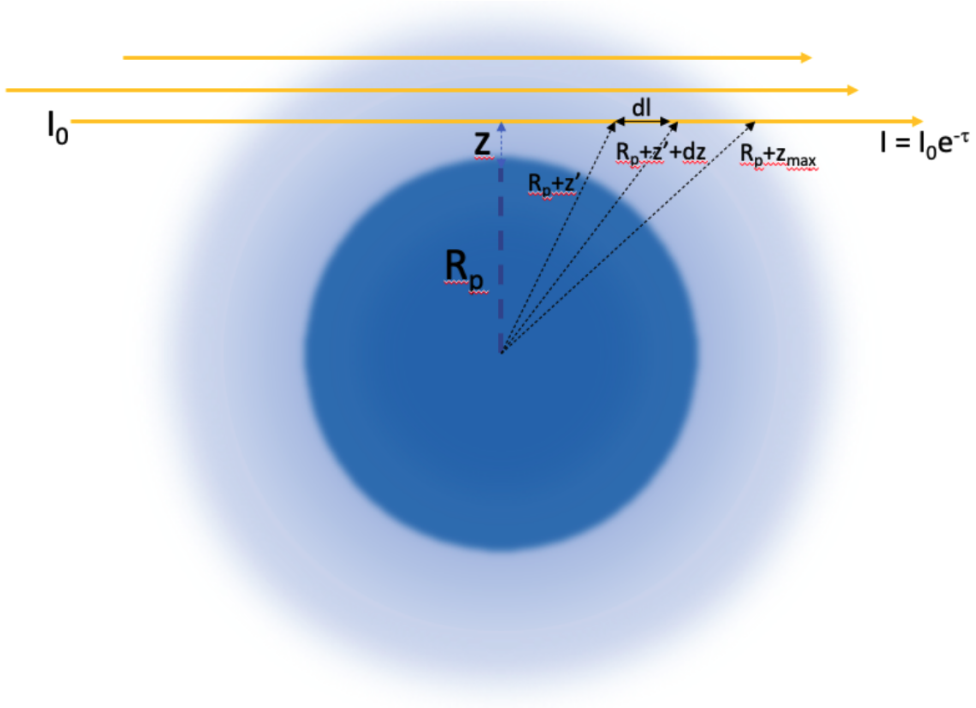

Figure 1.9: Illustration of the paths of the stellar photons filtered through the planetary atmosphere during a primary transit observation with the observer being placed on the right of the image. Adapted from Tinetti et al. (2012).

viewpoint, obstructing a portion of the star's light (see Fig. 1.3). The reduction in stellar flux received, denoted δ, can be measured with great precision and is proportional to the projected area of the planet relative to the star, as described approximately by Eq. 1.3, where $R_{\rm p}$ is the planet's radius and R_* is the well-determined star's radius, while minor effects from stellar limb-darkening are disregarded in Eq. 1.3. The primary transit enables us to acquire transmission spectra probing the exoplanet's terminator region, the area between the illuminated and dark sides of the planet, leading to signatures embedded in the stellar flux. When stellar light traverses the exoplanet's atmosphere, it is absorbed and scattered at frequencies characteristic of the constituent atoms and molecules. Consequently, the atmosphere becomes opaque at these specific wavelengths, and the exoplanet appears to have a slightly larger radius, measurable from the transit depth. Thus, assessing transit depth across different wavelengths yields the transmission spectrum of the exoplanet.

A transmission spectrum is thus an absorption spectrum, due to the atoms and molecules present in the atmosphere of the terminator region. As short-period planets are usually tidally locked, with extreme day-night temperature gradients, probing the planetary terminator can provide information on the presence of atmospheric circulation (e.g., winds) that redistribute the energy between the two planetary faces (Showman et al. 2020).

1.5.2 The Transmission Spectroscopy Metric

There are several ways to establish whether a transiting planet is a good candidate for transmission spectroscopy, with the **Transmission Spectroscopy Metric (TSM)** developed by Kempton et al. (2018) being the most used. This metric is based on the calculation of the exoplanet atmosphere annulus area (TA) with respect to the stellar disc area, which can be defined as follows:

$$TA = \frac{\pi(R_{\rm p} + nH)^2 - \pi R_{\rm p}^2}{\pi R_\star^2}, \tag{1.6}$$

where $R_{\rm p}$ represents the planet's radius, H denotes the atmospheric scale height, n indicates the count of H needed to determine the entire thickness of the atmosphere (nH), and $R_\star$ refers to the stellar radius. On expanding this equation and disregarding the second-order term similar to H^2, we derive an approximate measure of the spectral features' strength:

$$TA \simeq \frac{2R_p nH}{R_*^2}. \tag{1.7}$$

In the previous Equations, we introduced the atmospheric scale height, H, defined as

$$H = \frac{k_B T_{eq}}{\mu m_H g} \tag{1.8}$$

with k_B the Boltzmann's constant, T_{eq} the equilibrium temperature of the planet,m_H the mass of the hydrogen atom, μ the mean molecular weight, and g the gravity. Note that g = $GM_p/R_{\rm p}^2$ with G the gravitational constant and M_p the mass of the exoplanet. The

scale height is a good estimate of the atmospheric extension, retrieved by combining the hydrostatic equilibrium equation:

$$\frac{dP}{dZ} = -g\rho, \tag{1.9}$$

where ρ is the density, with the equation of state of an ideal gas:

$$\rho = \frac{M_p P}{R T_{eq}}, \tag{1.10}$$

giving therefore, the height where the pressure exponentially decreases. Considering the definitions above and including the brightness of the star (mag) as an estimation of the signal-to-noise ratio (S/N), from Eq. 1.7 we obtain the transmission spectroscopy metric (**TSM**) as defined in Kempton et al. (2018):

$$TSM = (Scale factor) \times \frac{R_{\rm p}^3 T_{\rm eq}}{M_p R_{\star}^2} \times 10^{-\frac{\rm mag}{5}} \tag{1.11}$$

The scale factor integrates various constants along with μ and n, which are challenging to ascertain. For an atmosphere primarily composed of H_2 and He I (10%), $\mu \sim 2.3$ serves as a suitable approximation; an atomic hydrogen atmosphere corresponds to μ = 1.3, whereas a completely dissociated hydrogen atmosphere uses $\mu \sim 1$. Meanwhile, n not only depends on the specific atmosphere but is also influenced by the spectral resolution of the observations. By calculating the **TSM** parameter, one can evaluate the anticipated transmission spectroscopic signal across various known planets. In Section 4.2 we discuss the importance of the **TSM** in the case of warm saturn TOI-5398 b.

The initial observation of an atmosphere around an exoplanet was conducted by Charbonneau et al. (2002). By utilizing the approach suggested in Seager & Sasselov (2000), which involves dividing the transit observations—comprising both planetary and stellar signals—by those taken outside transit (displaying only the stellar spectrum), they acquired an optical transmission spectrum of HD209458 b. This spectrum revealed a sodium absorption feature at $0.023 \pm 0.006\%$. Notably, HD209458 b is the planet with the highest **TSM** when considering the scale factor (see Hord et al. 2024, for a recent list of the **TSM** values). This pioneering detection was succeeded by numerous others. For example, Vidal-Madjar et al. (2003) discovered hydrogen in HD209458 b's atmosphere, and Tinetti et al. (2007) achieved the first molecular detection of water vapour in the atmosphere of the hot Jupiter HD189733 b.

Recent studies of atmospheres around exoplanets closely orbiting their stars primarily utilize two methodologies: (a) Low-resolution spectroscopy (LRS) conducted with telescopes situated in space, and (b) High-resolution spectroscopy (HRS) performed using ground-based facilities. An essential characteristic of a spectrograph is its 'resolving power' ($R = \lambda/\Delta\lambda$), which defines the tiniest wavelength distinction that can be discerned at that particular wavelength. This is also expressed relative to the Doppler effect, as the ratio of the speed of light to the smallest detectable Doppler velocity:

$$R = \lambda/\Delta\lambda = c/\Delta v \tag{1.12}$$

It is important not to conflate the resolving power with the spectral binning, which refers to the wavelength interval ($\Delta\lambda$) separating two successive points in the transmission spectrum. Spectral resolution is related to a spectrograph's capacity to differentiate between very nearby spectral lines and analyse their profiles. We will refer to spectrographs with R $>$ 20000 as 'high-resolution,' and those with R $>$ 100 and R $<$ 2000 as 'low-resolution.'

In the next Sections I will discuss these two techniques that will be used in the works deepen in this thesis.

1.5.3 High-Resolution Spectroscopy

Over the past ten years, high-resolution spectroscopy (R $>$ 20000) has emerged as a prevalent approach for exploring exoplanetary atmospheres. Unlike low-resolution methods, high-resolution techniques do not focus on variations in the planet-to-star radius ratio across different wavelengths but instead aim to detect the direct influence of the exoplanet's atmosphere on the host star's spectrum. This is achieved by identifying additional spectral features, facilitated by the varying velocities of the star, Earth, and exoplanet. The inaugural high-resolution study of an exoplanet's atmosphere used the Hobby-Eberly Telescope (R $\sim$ 60000) and successfully resolved Na I doublet lines in HD189733 b's atmosphere (Redfield et al. 2008). A few years later, Snellen et al. (2010) employed the cross-correlation method to identify CO molecules in an exoplanet atmosphere for the first time, using the CRyogenic high-resolution InfraRed Echelle Spectrograph (CRIRES; R $\sim$ 50 000 - 100 000) at the **VLT**. The first paper to describe the modern technique for deriving transmission spectra from high-resolution data was by Wyttenbach et al. (2015), utilizing the High Accuracy Radial velocity Planet Searcher (**HARPS**; R $\sim$ 115 000) at **European Southern Observatory (ESO)**'s La Silla 3.6m telescope, where Na I was detected once more in HD189733 b's atmosphere. Since then, the use of high-resolution spectroscopy for atmospheric studies has escalated dramatically.

Working with high resolving power instruments has two big advantages:

- First of all, at high spectral resolution each molecule is resolved into a dense forest of individual lines. These lines are unique for every molecule, are like fingerprints. Therefore it is easy, at least in principle, to understand, through line-matching with model templates, which atmospheric constituent we are dealing with (see Fig. 1.10);
- Secondly, at high spectral resolution we can distinguish the planetary motion from the stellar, and telluric contamination. Since the planet moves around its host star, its spectrum is Doppler shifted in the order of tens km s^{-1}which is 1000 greater than the changing component of the star radial velocity.

There are two primary methods that have emerged for investigating an exoplanet's atmosphere using high-resolution spectroscopy. The first method involves deriving the transmission spectrum of an exoplanet around distinct spectral lines, like the Na I dou-

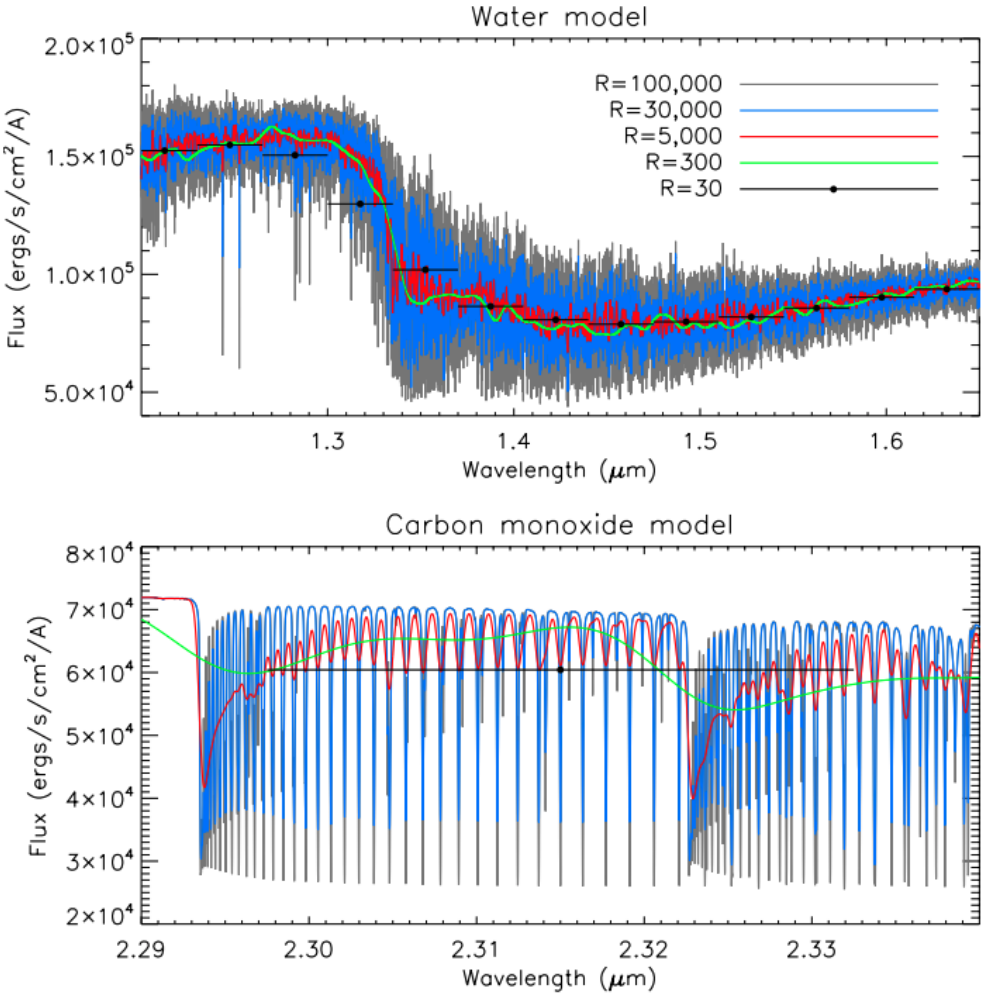

Figure 1.10: The effect of decreasing spectral resolution. The two panels show different wavelength regions of a model hot Jupiter atmosphere containing water and carbon monoxide. The model has been convolved to different spectral resolutions. The overplotted points represent the typical resolution resulting from current space-based observations and trace out only broad molecular features. Note how many individual CO lines are lost between a resolution of R=100000 and R=300. From Birkby (2018).

blet or the He I triplet, as well as other elements that generate a few detectable lines in the transmission spectrum. The second method, primarily employed to identify species that produce thousands of weak individual spectral lines in the transmission spectrum, is the cross-correlation technique. These methods are complementary and can be simultaneously applied through a consistent observation strategy of the host star, conducted continuously before, during, and after the exoplanet transits.

Single Line Analysis

Wyttenbach et al. (2015) has established itself as a key reference for extracting the transmission spectrum at specific lines of an exoplanet, utilizing high-resolution spectroscopy. This approach relies on differential spectroscopy, which involves comparing stellar spectra captured during the planet's transit across the stellar disc with those obtained when the planet is not transiting. Despite the seemingly straightforward nature of this technique, the high resolution of the spectra introduces some critical challenges that must be addressed, including correcting for Earth's atmospheric interference and managing the radial velocities of the three bodies involved in the observations. In fact, when the starlight reaches the telescope on Earth, the spectrum observed contains the stellar signal, the possible planetary atmosphere and the Earth atmospheric contaminations. The several steps involved in the analysis are listed in the next paragraphs.

The Earth contribution: the telluric lines The first step in the analysis involves preprocessing the spectra to remove contamination from Earth's atmosphere, known as telluric absorption, which is caused by molecules such as water vapour, oxygen, and carbon dioxide. These telluric features can overlap with the planetary signals and must be carefully removed to ensure accurate measurements.

For a period, the primary approach was the one introduced by Vidal-Madjar et al. (2010) and Astudillo-Defru & Rojo (2013), which has been employed in numerous atmospheric research studies (e.g., Wyttenbach et al. 2015). This technique is based on the assumption that the telluric lines across the night vary in a manner proportional to the airmass changes. Based on this assumption, it's possible to scale all spectra's telluric lines to the same airmass. Nevertheless, as mentioned in Casasayas-Barris et al. (2017), considering the Earth's orbital movement during the night, dividing spectra that are not in the Earth's rest frame leads to residuals in the positions of telluric lines due to slight misalignments. Additionally, rapidly rotating standard stars have been employed to adjust telluric lines (e.g., Casasayas-Barris et al. 2018).

Currently, one of the most used tools, and the primary used in this thesis, is Molecfit (Smette et al. 2015; Kausch et al. 2015), as the telluric lines are totally corrected, achieving a noise level precision. This advanced software developed by **ESO** (European Southern Observatory) models the telluric absorption based on real-time atmospheric conditions. Molecfit generates synthetic transmission spectra of Earth's atmosphere (see Fig. 1.11), which are fitted to the observed data to identify and correct for telluric features. Molecfit is the tool used in all the works described in Chapter 2, 3 and 4.

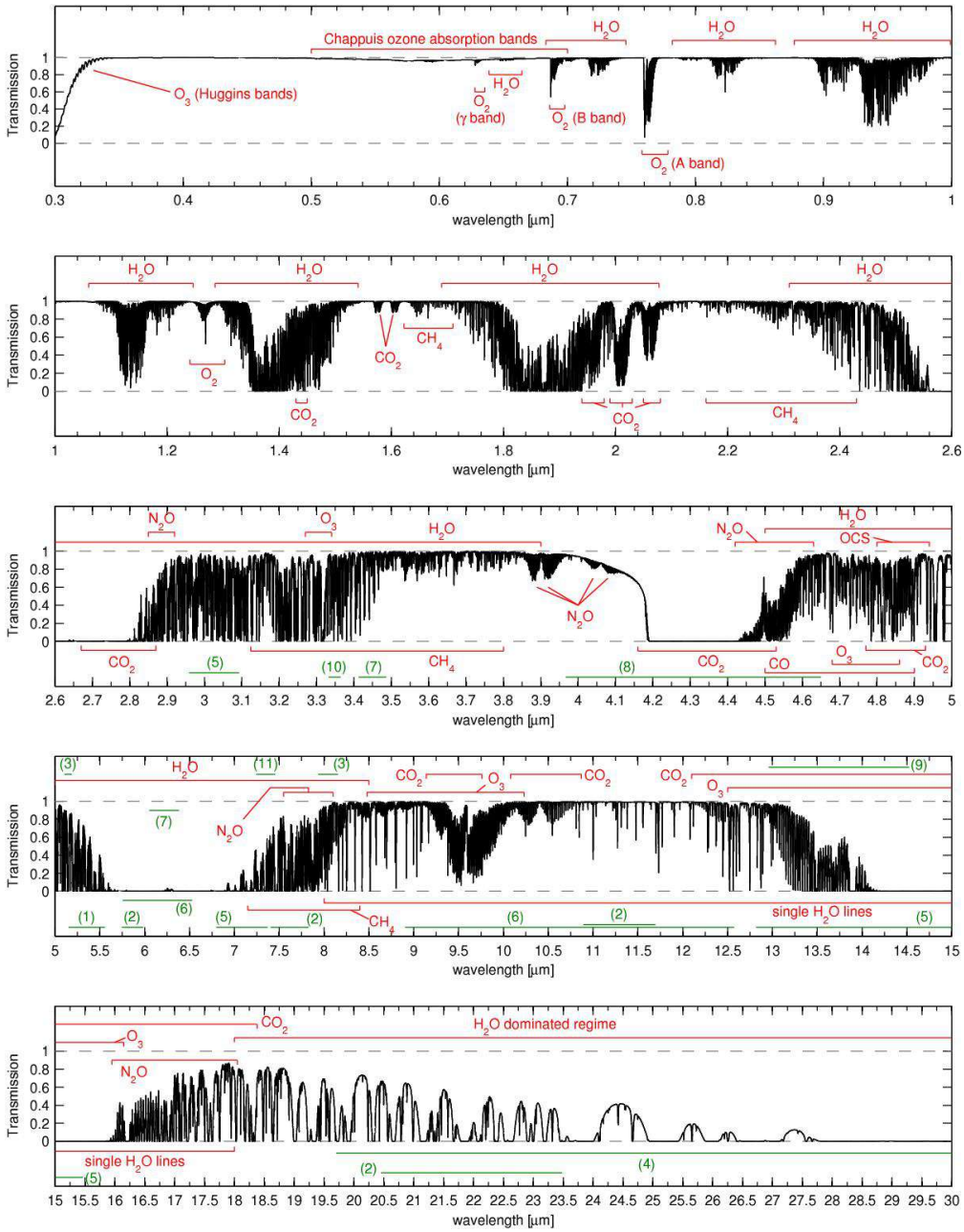

Figure 1.11: Synthetic absorption spectrum of the sky between 0.3 and 30 μm calculated with LBLRTM module from Molecfit with a resolution R $\sim$ 10000 using the annual mean profile for Cerro Paranal. The eight main molecules O_2, O_3, H_2O, CO, CO_2, CH_4, OCS, and N_2O contribute more than 5% to the absorption in some wavelength regimes. The red regions mark the ranges where they mainly affect the transmission, minor contributions of these molecules are not shown. The green regions denote minor contributions from the other molecules. From Smette et al. (2015).

Other employed techniques to remove the telluric lines involve the use of the Principal Component Analysis (PCA) algorithm. The flux in each pixel as a function of time can be described through a set of auto-vectors (air mass, throughput, water vapour content, etc.) and their corresponding eigenvalues. The PCA aim is to find a set of auto-vectors whose linear combination represents every possible temporal trend present in between the various spectral channels. The PCA technique has been used in several studies regarding near Infra-Red spectroscopy such as Damiano et al. (2019) for the detection of H_2O and CO in the atmosphere of HD209458 b and HD189733 b with CRIRES, or Giacobbe et al. (2021), where it helped detecting five molecules in the atmosphere of HD209458 b with GIANO-B.

Once the telluric lines are eliminated, we remain with the residuals which contain the planetary signal buried in the stellar one.

The stellar contribution: the graveyard of planetary lines When using high resolution observations, the radial velocities of the observer and the target are noticeable as shifts in the stellar spectra. First, as we are observing from Earth, we need to consider its radial-velocity variation during the observations. Although this change is small during the night ($\sim$ 1 km s^{-1}) its absolute radial velocity can be of the order of tens of km s^{-1}depending on the position in the orbit around the Sun, the target we are observing, and the position of the observatory on the Earth surface. Second, the star we are observing (and the planets that are part of the extrasolar system) is approaching or moving away from the Solar system. This is the so-called systemic velocity, and it is due to the movement of the stars inside the Galaxy. Third, the target of our observations is a star hosting at least one planet. If we imagine a two-body system (one planet and one star) for simplicity, due to the gravitational field, the planet pulls the star around the centre of the system while moving along its orbit, and vice-versa. This movement is translated to a radial-velocity change of the star that can be well defined by a Keplerian orbit around the system barycentre as described by Eq. 1.1. Finally, during the transit, the exoplanet changes its position along the orbit with respect to the observer's line-of-sight. Similarly to Eq. 1.1, assuming a circular orbit (e = 0) and $M_p << M_*$, the planet radial-velocity semi-amplitude is given by:

$$Kp = \frac{K_* M_*}{M_p}, \tag{1.13}$$

where K_* has been defined in Eq. 1.1. Once the spectra have been corrected of telluric contamination and are shifted to the stellar rest frame where all stellar lines are exactly at the same position, we can proceed with the extraction of the transmission spectrum hidden among the stellar lines.

The standard procedure to remove the stellar contribution from our spectra consists in computing a high S/N stellar spectrum that results from the combination of all spectra taken when the planet is not transiting. Then, all spectra are divided by this stellar spectrum, called master-out-of-transit. Following this division, under ideal circumstances, we anticipate observing inclined absorption features during transit, corresponding to

the planet's anticipated radial velocity shift, as depicted in Fig. 2.2. The planet's radial velocity at each exposure can be determined by:

$$RV = K_p \sin(2\pi\phi), \tag{1.14}$$

where ϕ signifies the planet's orbital phase at that specific exposure. These velocities allow us to adjust the absorption features to the planet's rest frame using the Doppler shift described by Eq. 1.12, ensuring alignment. Ultimately, all the in-transit residuals are aggregated to construct the transmission spectrum. The procedure listed in this Section will be seen again in detail among the several works in this Thesis.

The role of the stellar activity With stellar activity we include all stellar processes that may change the stellar spectrum in the time scales of the observations, such as stellar activity or pulsations. In the visible, stellar activity can become very important for particular stars (Cauley et al. 2018), making the atmospheric study of the exoplanets in these systems extremely challenging. This is the case, for example, of exoplanet AU Mic b, a Neptune-sized planet orbiting a very young ($\sim$ 20 Myr) pre-main sequence M dwarf. Palle et al. (2020b) attempted to study the atmosphere of AU Mic b, concluding that the strong emission observed in the stellar lines produced by stellar activity and its variation during the observations do not permit the study of the exoplanet atmosphere. One the other hand, pulsating stars introduce time-variations in the stellar continuum and lines. When searching for absorption excess from the exoplanet atmosphere in the stellar spectrum, the identification of the exoplanet signals can be hampered by pulsation features. One example is WASP-33 b, an ultra hot Jupiter orbiting a δ Scuti star that pulsates every $\sim$ 1 hour (von Essen et al. 2019). Although the detection of WASP-33 b's atmosphere has been possible (Yan et al. 2019), several pulsation features are observable in the transmission spectrum.

The RME + Centre to Limb Variation (CLV) Recently, two effects have started to gain importance as additional challenges when attempting to detect exoplanetary atmospheres: the **RM** effect (**RME**) and the **CLV**.
The importance of the **RM** effect in atmospheric studies was first pointed out by Louden & Wheatley (2015). This effect is produced due to the different projected velocities of the stellar surface that are blocked by the planet (see Fig. 1.6). Due to the symmetry of the **RME**, this effect is expected to be small in the stellar rest frame. However, in the planet rest frame (where the absorption of the exoplanet is expected) the symmetries are broken and spurious signals appear in the transmission spectrum. It is very important to note that, in addition to the intrinsic strength of the **RME**, which depends on the geometry of the planet-star system (see Eq. 1.5), the planet radial-velocity change during the observation is crucial in order to disentangle the atmospheric absorption from the **RM** effect. The **CLV** may also potentially affect the line profiles during transits. The stellar continuum in the photosphere has lower intensity near the stellar limb with respect to the centre of the disc. This effect is related to the optical depth of the photosphere. The balance between the lines formed at different heights depends on the limb angle and the stellar latitude. Although the impact of this effect in the final transmission spectrum is

usually fainter than the **RM** effect, it has been observed that, in some cases, the strength of the **CLV** effect can be of the same order as some of the atmospheric signals detected on hot Jupiters (e.g., Yan et al. 2017; Czesla et al. 2015; Khalafinejad et al. 2017). For terrestrial planets, for which the atmospheric features in the transmission spectra will be fainter, the **CLV** and **RM** effects are expected to be critical.

In Section 2.1.2 and 4.2.2 I will discuss how I modelled and removed the Rossiter-Mclaughlin Effect and the Center to Limb Variation, before computing the transmission spectrum. An example of **RME+CLV** effect can be seen in the 2d maps in the top panels of Fig. 2.2 as the brighter region in contrast with the atmospheric signal represented by a darker region. While in the mid panel I show the modelling of both effects.

The cross-correlation technique

The single line analysis is a powerful tool to retrieve important information on the atmosphere of an exoplanet as discussed in Section 2.1. However, it requires a high S/N and deep lines such as the Balmer ones as the sodium doublet. To still be able to detect thin spectral lines in a planet's atmosphere is possible to make use of the cross-correlation (CC) with model templates. This technique exploits the fact that is known precisely at what wavelengths certain lines are formed, and by selecting a sufficient number of spectral lines we average out the photon noise to obtain the measurement of some average spectral line. The cross-correlation technique is based on the comparison of a synthetic atmospheric spectrum with the reduced data, after removing the stellar contribution from the observed spectra.

The CC takes the following mathematical form:

$$CC(v) = \sum_{i}^{N} x_i T_i(v). \tag{1.15}$$

Here x_i are each of the N spectral points in the planet's spectrum, T_i are the correspondent values of the template Doppler shifted to radial velocity v. This template takes non-zero values inside a spectral line, but it is zero in between the lines. This operation is identical to a weighted average of x for all values i that are inside the spectral lines of interest. There are similar mathematical implementations in the literature, but they all rely on averaging many spectral lines to effectively reduce the noise in the measurement. Although we know the relative positions of all the planet's spectral lines given by quantum mechanics, we may not know the instantaneous Doppler shift of the entire spectrum. So we compute this average over a range of Doppler shifts applied to the template, making the template-dependent on the radial velocity v. In this way, we combine all the molecular lines of the planetary spectrum in one single function (the cross-correlation function, **Cross Correlation Function (CCF)**). In other words, through the CC technique, we scan the model through the residuals and evaluate how much the template is a good fit for our observations. At the correct radial velocity, when the template is exactly aligned with the planetary spectrum, meaning that they have the same Doppler shift, the **CCF** reaches the maximum . Typically this **CCF** will be computed for every

spectrum obtained during the time series. Since the radial velocity of the planet changes throughout the transit, the peak location of the **CCF** has shifted accordingly. We can therefore construct the **CCF** along two dimensions where the horizontal direction is the radial velocity and the vertical direction is the time series. Different planetary radial velocity semi-amplitude are then tested to shift the CCFs in the planetary rest frame. In this way, we construct a velocity-velocity diagram composed of different realizations of the one-dimensional time-averaged **CCF**. At the correct orbital velocity, the signal of the planet adds constructively and the time-averaged **CCF** are maximized. The maximum of this velocity-velocity matrix gives us the best-fitting planet's radial velocity semi-amplitude, which can be used to derive the planetary mass and orbital inclination respectively if we are dealing with a non-transiting planet. An example of CC applied to HD209458 b can be found in Fig. 1.12 from Giacobbe et al. (2021), where in the different panels is shown the velocity-velocity diagram introduced above for different atomic species. We introduce other application of the CC technique to detect both atomic and molecular species in the next section.

A resume of high resolution spectroscopy findings

As already discussed, one of the major advantages of using high resolution spectroscopy is that we are not only able to detect chemical species, but also to resolve single spectral lines from an exoplanet atmosphere, opening a window to study the dynamics and properties of the layers where the spectral lines are formed (Lecavelier Des Etangs et al. 2008).

The examination of individual spectral lines began in the visible spectrum when Redfield et al. (2008) successfully resolved the Na I D lines in the atmosphere of exoplanet HD 189733 b, utilizing high-resolution observations with the Hobby-Eberly Telescope. Some years later, Wyttenbach et al. (2015) again observed Na I in this planet's atmosphere, this time employing **HARPS** observations. Subsequent analyses using **HARPS** and **HARPS-N** transit observations on other hot Jupiters yielded similar findings (e.g., Casasayas-Barris et al. 2017; Chen et al. 2020). The presence of this element has also been confirmed in the atmosphere of WASP-52 b utilizing the **ESPRESSO** (R $\sim$ 140000, Pepe et al. 2014; Chen et al. 2020).

Conversely, leveraging the near-infrared component of the **Calar Alto high-Resolution search for M dwarfs with Exoearths with Near-infrared and optical Échelle Spectrographs (CARMENES)** spectrograph (Quirrenbach et al. 2014), researchers made the initial observation of metastable He I at 1038nm in the atmospheres of the sub-Saturn mass planet WASP-69 b (Nortmann et al. 2018) and the Neptune-mass planet HAT-P-11 b (Allart et al. 2018). Following these findings, other studies identified He I in the atmospheres of model hot Jupiters such as HD209458 b (Alonso-Floriano et al. 2019) and HD 189733 b (Salz et al. 2018), as well as in smaller bodies like the warm Neptune GJ-3470 b (Palle et al. 2020a). In recent years, Guilluy et al. (2020) reported the observation of He I in HD189733 b using the GIANO-B spectrograph at the Telescopio Nazionale Galileo (**TNG**), prompting a more in-depth examination of the He I triplet by the Italian **Global Architecture of Planetary System (GAPS)** consortium (Guil-

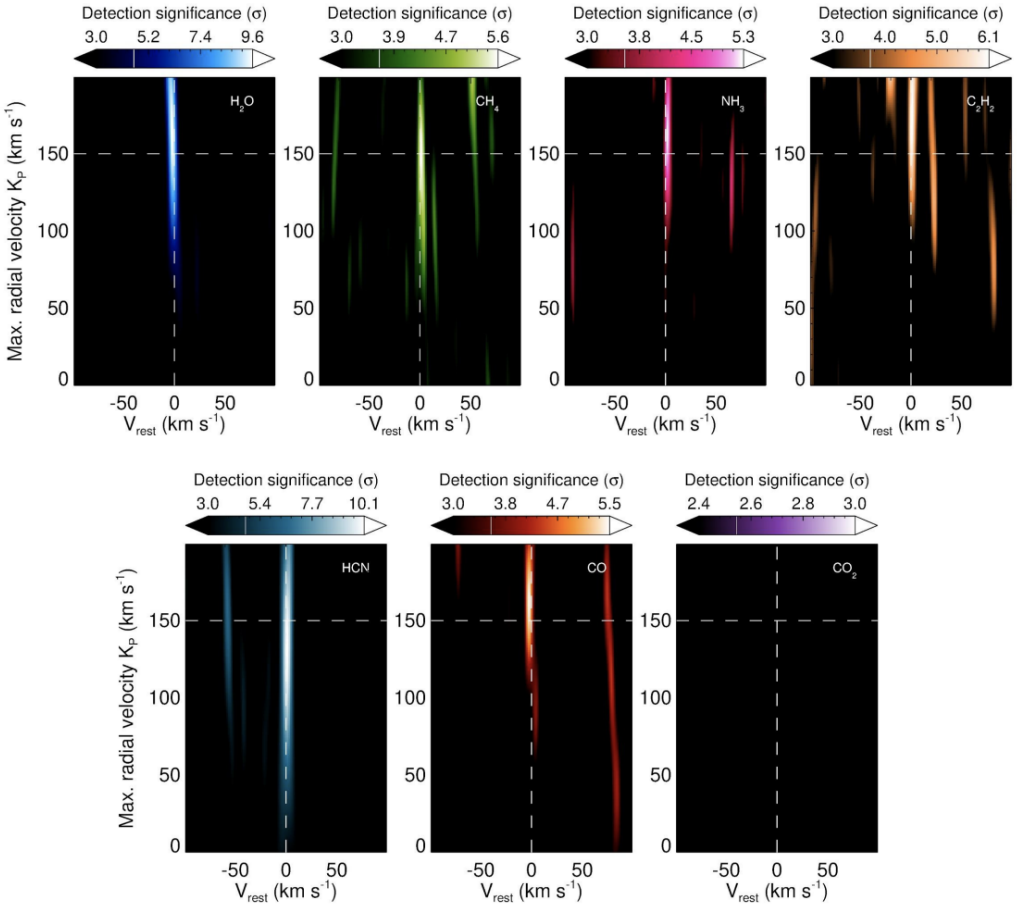

Figure 1.12: Detection significance for H_2O, CH_4, NH_3, C_2H_2, HCN, CO, and CO_2. Each panel shows the CC, as a function of the planet maximum radial velocity (KP) and the planet rest-frame velocity (Vrest). White dashed lines denote the known velocity of HD 209458 b, that is (KP, Vrest) = (145, 0) km s^{-1}. From Giacobbe et al. (2021).

luy et al. 2022a, 2023). In Guilluy et al. (2024), discussed in Chapter 4, we continued this line of inquiry by analysing the He I triplet in a selected group of targets, including GJ-3470 b and HAT-P-11 b mentioned earlier. Detecting molecules and atomic species with weaker features requires the use of the cross-correlation technique. Due to their extremely high temperatures, several ions have been detected in the atmospheres of ultra hot Jupiters, with most of the studies performed using high resolution spectroscopy observations and the cross-correlation technique. Absorption of single lines such as the Na I doublet, magnesium (Mg I), ionised calcium (Ca II), and the hydrogen Balmer lines have been detected in several of them with different facilities as deeply discussed in Chapter 2 when introducing my work on KELT-9 b, the hottest planet known to date, with an equilibrium temperature around 4000 K. In this target, in addition to the well known neutral and ionised iron (Fe I, Fe II; e.g., Hoeijmakers et al. 2018), the observations show an extremely rich atmosphere of rare neutral and ionised metals such as Sc II, Ti II, CrII, and Y II as recently discovered by Borsato et al. (2023).

Several works presented in this thesis follow the path set by the works introduced above employing mostly the single line analysis but also the cross-correlation with templates. In Chapter 2, 3 and 4, I focused on the importance of single line analysis to characterise the exoplanetary atmospheres via retrieving information, e.g., on the height of the species in the atmosphere, on the presence of winds and on the indication of star-planet interaction.

1.5.4 Low-Resolution Spectroscopy

Although using very high resolution we are able to resolve the spectral lines taking advantage of the Doppler velocities, one of the disadvantages is that this technique suffers from the contamination of the Earth's atmosphere when the observations are performed from ground. The Earth's atmosphere modifies the stellar continuum spectrum which is not calibrated. Thus, the absolute flux information is lost, and we are only able to measure relative differences of the local continuum (excess of absorption or emission). This situation is different when using space-based spectrographs operating at low-resolution. The first exo-atmospheric studies have been carried out by employing space-borne facilities, that are more stable and do not have the problem of our atmosphere's contamination. Eighteen years of space-borne LRS observations have advanced our understanding of exo-atmospheres. In the nIR, the **HST/Wield Field Camera 3 (WFC3)** provided transmission spectra for tens of HJs and some Sub-Neptunes (e.g., Sing et al. 2016; Tsiaras et al. 2019), thus allowing the retrieval of important atmospheric information, such as the atmospheric composition, or the presence of hazes and clouds as discussed in Section 5.2. However, the narrow spectral coverage (1.1-1.7 μm) of the **HST/WFC3/**G141 grism, mainly allowed for H_2O detection, while the abundances of other molecules (like CH_4, NH_3, HCN, CO, and CO_2) often remained unconstrained. In the VIS, the Space Telescope Imaging Spectrograph (**HST/STIS**) and the Advanced Camera for Surveys (**HST**/ACS) are sensitive to optical slopes of transmission spectra which in turn constrain sources of scattering (e.g. aerosols or molecular Rayleigh scattering) in the atmospheres. Several tools are now employed to extract a planetary

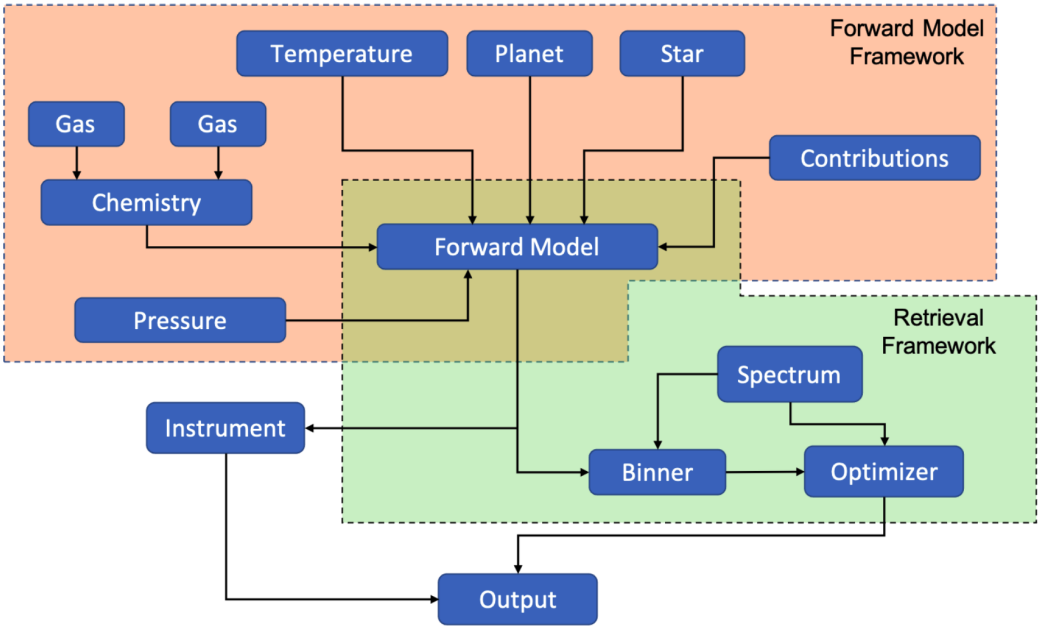

Figure 1.13: The comprehensive layout of atmospheric retrieval for low resolution spectroscopy observations is depicted, emphasizing the dual-framework structure: the forward model framework, which is tasked with building the forward model, and the retrieval framework, which focuses on matching the forward model to an observed spectrum. Adapted from Al-Refaie et al. (2021).

spectrum from the spatially scanned low-resolution raw images (e.g., Tsiaras et al. 2018; Kreidberg et al. 2018a, and more in Section 5.2). The main idea is extracting two types of light curves: a broad wavelength band white light curve (WLC), covering the whole range of the spectrograph, and several spectroscopic light curves (SLC) created in different wavelength bins usually uniformly spaced. The WLC is commonly employed to correct the SLCs from the systematic noise introduced by the instrument. The transmission/emission spectrum is then constructed from the SLCs by determining the planet-star radii ratio as a function of wavelength. Robust retrieval algorithms are successively employed to interpret low-resolution spectra and derive atmospheric properties. The first attempt at employing a retrieval tool to analyse the transmission spectra of exoplanets dates back to Madhusudhan & Seager (2009), who ran millions of 1D atmospheric models to explain the empirical spectra of both HD 189733 b and HD 209458 b. The term 'retrieval' means fitting an atmospheric model to an observed spectrum and estimating the model parameters with their uncertainties. Atmospheric retrieval technique for exoplanets have been developed to address the "degeneracy problem". Fig. 1.13 shows a schematic representation of atmospheric retrieval for exoplanets, where we can see that performing atmospheric retrieval requires three main ingredients: (i) an observed atmospheric spectrum, (ii) an atmospheric model, and (iii) an estimator to select the best fitting model. These ingredients belong to two separate frameworks: the forward model framework responsible for constructing the forward model, and the retrieval framework responsible for fitting the forward model to observations. The forward model

acts as a bridge between these two frameworks. The atmospheric spectrum is mainly determined by the pressure-temperature (P-T) profile and the chemical composition of the atmosphere. These are calculated under equilibrium conditions in such models, with the possibility of including clouds. The parameters for forward models used in retrievals correspond to three broad properties: chemical composition, P-T profile and clouds/hazes. The chemical composition of the atmosphere is represented by the volume mixing ratio of the species, such as the number density of each species relative to the total number density. Typically, for H_2-rich species, the prominent absorbers such as H_2O, CH_4, NH_3, CO CO_2, Na, K, etc. are included. The mixing ratios are usually assumed to be uniform in the region of the atmosphere probed by the observations. The model may also account for opacity due to the presence of clouds or hazes in the atmosphere. To date, there are different robust frameworks widely used to interpret LRS data and derive strong atmospheric properties, e.g. the Non-linear Optimal Estimator for MultivariatE Spectral analySIS (NEMESIS, Irwin et al. 2008), the CaltecH Inverse ModEling and Retrieval Algorithms (CHIMERA Line et al. 2013) and the **Tau Retrieval for Exoplanets (TauREx)** (Waldmann et al. 2015). In Chapter 5, I will show an application of **TauREx** in the comparison of the pipelines used to extract transmission spectra from Hubble Space Telescope (**HST**) Wield Field Camera 3 (**WFC3**) described in Section 5.2

1.6 Instruments

In this Section I will introduce the instruments concerning the works in this thesis including **HARPS-N**, GIANO-B, **ESPRESSO**, **Atmospheric Remote sensing Infrared Exoplanet Large Survey (Ariel)** space mission and the **HST** Wield Field Camera 3.

1.6.1 HARPS-N

High Accuracy Radial velocity Planet Searcher for the Northern hemisphere (HARPS-N) is an echelle spectrograph located at the 3.6m Telescopio Nazionale Galileo (**TNG**), La Palma. It covers a wavelength range of 383 to 693 nm, and has a spectral resolution R = 115,000 (Cosentino et al. 2012). It is designed to obtain high-precision radial velocity measurements while avoiding spectral drifts due to temperature and air pressure variations, thanks to very accurate control of pressure and temperature. **HARPS-N** is fiber-fed by the Nasmyth B Focus of the 3.6 INAF - **TNG** telescope through a Front End Unit (FEU). The two fibers (A and B, used for the target and to obtain the sky spectrum or a simultaneous calibration lamp, respectively) have an aperture on the sky of 1”; this produces a resolving power of 115,000 in the spectrograph. The spectrum is projected onto an e2V CCD 231 detector, which allows 69 spectral orders. I used **HARPS-N** data in several works introduced in this thesis thanks to the Italian collaboration **GAPS** (Covino et al. 2013). I will discuss the analysis of the data collected with **HARPS-N** in Chapter 2, 3 and 5.

1.6.2 GIANO-B and the GIARPS configuration

GIANO-B spectrograph mounted on the 3.6-meter **TNG** telescope acts as the nIR counterpart of **HARPS-N**. GIANO-B achieves nearly contiguous coverage of the entire Y, J, H, and K bands in the nIR (0.92-2.45 μm), split into fifty orders (from 32 to 81), at a mean spectral resolving power of R = 50,000 (Oliva et al. 2006). It has been the first spectrograph mounted on a 4-m class telescope to combine such broad spectral coverage with such high resolving power. The minimum integration time is 10 seconds, the possible integration times on target are 10, 30, 60, 100, 200, 300, and 600 seconds. GIANO-B can acquire spectra either of astrophysical objects and sky simultaneously, or of calibration lamps (halogen for flat-field and U-Ne for wavelength calibration) and dark frames. In its initial configuration (March 2015 - August 2016) the spectrograph was located in the **TNG** Nasmyth-A focus and it was fed with two fibers of 1" angular diameter at a fixed angular distance of 3" on the sky. In September 2016 the spectrograph has been moved to the Nasmyth-B focus (hence the name GIANO-B) and now the light reaches directly the telescope through a slit. The observations are performed with the nodding acquisition mode following an ABAB pattern. Originally, at each nodding position, a fiber (on-sky) fed the spectrograph, while a second fiber, located at the other nodding position pointed to the sky, providing an accurate reference for subtracting the thermal background and telluric emission lines. Each time the telescope noded, the fibers swapped, i.e. the object fiber became the sky fiber and vice versa. In the current configuration with the direct light feed from the telescope, the target and sky spectra are always taken in pairs but using the two nodding positions along the slit (A and B) separated by 5". With the focus change in 2016, the observing mode called GIARPS (Claudi et al. 2017) started. In the GIARPS observing mode GIANO-B can operate simultaneously with **HARPS-N** (resolving power of R = 115,000) to achieve high-resolution spectroscopy over the full visual and near-infrared range (0.383-2.45 μm with a small gap between 0.7-0.92 μm) in a single exposure. The two spectrographs are still able to work separately, so it is possible to have three different configuration: HARPS–N only; GIANO–B only; and GIARPS by splitting the light with a dichroic. The data analysed in the works in Chapter 4 have been acquired employing the GIARPS configuration.

1.6.3 ESPRESSO

The **ESPRESSO** (Echelle SPectrograph for Rocky Exoplanet and Stable Spectroscopic Observations) instrument (Pepe et al. 2010, 2014), mounted on the Very Large Telescope (**VLT**) at the European Southern Observatory (**ESO**), is a state-of-the-art high-resolution spectrograph. Designed for ultra-precise radial velocity measurements, **ESPRESSO** enables the detection and characterization of Earth-like exoplanets around nearby stars, as well as conducting cutting-edge astrophysical research.

Among the key Features of **ESPRESSO** we can find:

- Unmatched Radial Velocity Precision: **ESPRESSO** achieves a precision down to 10 cm/s, making it one of the most accurate spectrographs in the world;

- Multi-UT Capability: It can combine light from all four Unit Telescopes of the **VLT**, allowing for unprecedented sensitivity;
- Broad Spectral Range: It covers wavelengths from 380 to 780 nm, optimizing its ability to observe a wide variety of astronomical phenomena;
- Stability: Its advanced design minimizes environmental effects, ensuring ultra-stable spectroscopic observations over time.

These characteristics make **ESPRESSO** one of the most advanced spectrograph in the world resulting in several scientific contributions in various areas of modern astronomy, including exoplanet discovery and characterization. For example, **ESPRESSO** confirmed the existence of the Earth-like exoplanet Proxima Centauri b, refining its mass to 1.17 Earth masses (Suárez Mascareño et al. 2020). In Section 3.3 we introduce its role in the atmospheric characterisation with the preliminary analysis of WASP-94A b.

1.6.4 Ariel

The **European Space Agency (ESA)** Atmospheric Remote sensing Infrared Exoplanet Large Survey (**Ariel**) space telescope is a 0.64 m^2 telescope, planned to be launched in 2029. It will be the first telescope dedicated to study the atmosphere of a large population of exoplanets, characterising their thermal structures, chemical compositions, cloud properties and dynamical processes as a function of longitude, latitude and altitude for about 1000 exoplanets ranging from Jupiters and Neptunes down to super-Earth size orbiting different types of stars. The mission will use transit, eclipse and phase curve techniques and revisit some planets with multiple techniques at different times. It will use simultaneously observations obtained in three photometric bands in the visible/near infrared and three spectroscopic channels in the infrared (1.10-7.80 μm). A detailed description of the **Ariel** Mission is provided in the **Ariel** Red Book (**ESA**/SCI(2020)1). The observations are separated into "Tiers" (Tinetti et al. 2016; Edwards & Tinetti 2022), each with different goals:

- Tier 1 Reconnaissance survey: These observations will use a low spectral resolution (4 spectral resolution elements covering the 1.10 - 7.80 μm range, with an average SNR $\geq$ 7) to characterise about 1000 transiting planets. They aim to answer basic questions through the large statistical sample of observed planets, such as determining the fraction of planets that have cloudy atmospheres, the fraction of small planets that have retained their primary envelope, removing mass-radius degeneracies to constrain planet interiors, obtaining rough estimates of planet properties like temperature, albedo or the presence of main molecules, and classifying the planets through colour-colour diagrams. The **Ariel** Tier 1 survey mode will also allow for rapid and broad classification of planets, so that decisions can be made about priorities for future observation with Tier 2 and Tier 3. The necessary performance can be reached in less than 10 transits/eclipses for the majority of targets.

- Tier 2 Deep survey: This tier uses a higher spectral resolution (R $\sim$ 10 for 1.10 $< \lambda <$ 1.95 μm; R $\sim$ 50 for 1.95 $< \lambda <$ 3.90 μm; R $\sim$ 15 for 3.90 $< \lambda <$ 7.80 μm; with an average SNR $\geq$ 7) on a sub-sample of about 500 planets, which constitutes the core of the mission. Tier 2 spectroscopic observations will be essential for quantitively uncovering atmospheric structure and composition (main components and trace gases), as well as searching for potential correlations between atmospheric chemistry and basic parameters like planetary radius, density, temperature, stellar type and metallicity.

- Tier 3 Benchmark planets: This tier is aimed at examining the temporal and spatial variability in exoplanet atmospheres using observations. It focuses on planets where **Ariel** can achieve its highest spectral resolving power and a signal-to-noise ratio (SNR) of $\geq$ 7 within one or two observations (representing about a 10% sample). Tier 3 observations by **Ariel** will track changes in the thermal profile both vertically and horizontally over time. These findings will, for the first time, assess the uncertainty from only having disc-averaged and time-integrated spectra. By aggregating observations over time for a Tier 3 planet, an unparalleled SNR will be obtained, allowing for an in-depth examination of atmospheric chemistry and dynamics.

- Tier 4 Phase-curves and bespoke observations: This tier caters to specific targets of interest, including non-transiting ones. Tier 4 allows for custom observations with tailored requirements, such as phase curves.

1.6.5 HST WFC3

The **WFC3** is one of the most advanced and versatile instruments aboard the **HST**. Installed during the final servicing mission (SM4) in May 2009, **WFC3** has been pivotal in advancing our understanding of a wide range of astrophysical phenomena, including galaxies, stars, and exoplanets. It operates in two primary channels: ultraviolet/visible (UVIS) and near-infrared (NIR), making it an indispensable tool for both imaging and spectroscopy across a broad spectral range. Its key features include:

- Broad Wavelength Coverage: **WFC3** observes in ultraviolet (200–400 nm), visible (400–700 nm), and near-infrared (700–1700 nm) wavelengths. This broad range allows for diverse applications, from studying distant galaxies to characterizing exoplanet atmospheres;
- Wide Field of View: The UVIS channel provides a large 162" $\times$ 162" field of view with a spatial resolution of 0.04"/pixel, while the NIR channel covers a 123" $\times$ 136" field of view at 0.13"/pixel, supporting both large-scale surveys and detailed studies;
- Grism Spectroscopy: The NIR channel is equipped with grisms that facilitate slitless spectroscopy, enabling the characterization of the atmospheres of exoplanets

by analysing their transmission and emission spectra.

WFC3 has revolutionized the study of exoplanets, particularly in the characterization of their atmospheres in the low-resolution context. Its grism mode and high sensitivity make it an ideal tool for detecting molecular features and thermal profiles. It proved to be extremely important for the detection of Water vapour in exoplanet atmospheres, including HD 209458 b, where **WFC3** confirmed the presence of water vapour and refined its atmospheric properties (Line et al. 2016), WASP-121 b with the revealing of water vapour and evidence of atmospheric escape at extreme temperatures (Lothringer et al. 2022). Moreover **HST WFC3** proved its ability also with smaller planets with the detection of water vapour and of the presence of a largely cloud-free sky in the atmosphere of the Neptune-sized HAT-P-11 b (Fraine et al. 2014), and with the observations of water vapour in the habitable-zone exoplanet K2-18 b, sparking discussions about its potential habitability (Benneke et al. 2019).

The **WFC3** has provided unprecedented insights into the atmospheres of exoplanets, laying the foundation for the next generation of space telescopes like the **James Webb Space Telescope (JWST)**. Its ability to characterize atmospheric features such as water vapour, cloud structures, and thermal profiles has significantly expanded our understanding of planetary diversity and habitability.

1.7 Overview of the work presented in this thesis

During my PhD thesis I focused on the atmospheric characterization of extrasolar planets. Most of the targets I analysed during the PhD are short-period gas giant planets such as Hot-, Ultra-Hot-Jupiters and warm-saturns. As introduced in the previous sections of this thesis, this subsample of planets are the perfect candidates to perform transmission spectroscopy due to their large scale height because of their large equilibrium temperature.

In the following chapters of this thesis, I will review the results of my research work during the three years of my PhD showing already published works and highlighting the next works in preparation.

For the main part of my research, I have used the single line analysis technique to analyse the spectra acquired with the high-resolution spectrograph **HARPS-N** mounted on the **TNG** mainly within the Italian collaboration **GAPS**.

In Chapter 2 I will introduce several works concerning the analysis of the hottest exoplanet known, KELT-9 b. Among these I will present the atmospheric characterisation of the planet via single line analysis in D'Arpa et al. (2024b) where I will introduce the method I developed to extract and fit the transmission spectrum of individual lines. Then, I will discuss about the constraining of the Oxygen abundance, before comparing the results obtained in D'Arpa et al. (2024b) with other works within the **GAPS** collaboration devoted to the single line analysis of KELT-9 b.

In Chapter 3 I will show the validation of the method described in Chapter 2 that I

performed with Valerio Fardella as part of his master thesis. I will then discuss the extension of the method to several different targets, including TOI-1518 b, an **UHJ** with properties similar to KELT-9 b. I will then extend the method developed for **HARPS-N** data to **ESPRESSO** data for the analysis of WASP-94A b.

In Chapter 4 I will introduce one of the possible applications of the framework I developed for the single line analysis, focusing on the joint use of the Hα line and the He I triplet as indicators of two different mechanisms: the stellar activity (Guilluy et al. 2024) and the photo-evapouration (D'Arpa et al. 2024a).

In Chapter 5 I will introduce the work regarding the comparison of the pipelines used to extract the transmission spectra with the **HST WFC3**

Finally in Chapter 6 I will discuss and summarise the results obtained during the thesis.

Chapter 2

The record holder of single lines detected: KELT-9 b

In the context of exoplanet characterisation, high-resolution spectroscopy is one of the most powerful methods to investigate the atomic and molecular atmospheric makeup. Compared to their space-based counterparts, ground-based spectrographs are able to achieve a higher resolving power, such as the R$\sim$115,000 of **High Accuracy Radial velocity Planet Searcher for the Northern emisphere (HARPS-N)** (Cosentino et al. 2012) or the 140,000 of **Echelle SPectrograph for Rocky Exoplanets and Stable Spectroscopic Observations (ESPRESSO)** (Pepe et al. 2010, 2014). At such resolutions, individual lines can be resolved, breaking the degeneracy induced by broad spectral features in low resolution spectra (Birkby 2018). On the other hand, ground-based observations are affected by telluric contaminations, making more complex the extraction of the planetary spectrum.

During my PhD research I worked on the realisation of a complete framework devoted to the extraction and fitting of exoplanetary transmission spectrum within the context of high resolution spectroscopy. The framework follows the steps highlighted and explained in Section 1.5 and has been originally developed to extract all the possible single lines in the peculiar atmosphere of the Ultra-Hot Jupiters (**Ultra Hot Jupiter (UHJ)**) KELT-9 b, the hottest planet discovered to date (Gaudi et al. 2017) . The exoplanet is in a nearly-polar (λ = 85.78 deg), short-period (1.48 days) orbit at a separation of about 0.03 AU from its host star. Also known as HD195689, the B9.5–A0 host star features an effective temperature in the range of 10,000 K, a radius (R_*=2.36 $R_\odot$) and a mass (M_*=2.52 $M_\odot$) (Gaudi et al. 2017, and Table 2.2) resulting in a density of 0.53 g cm^{-3}. The tremendous stellar irradiation experienced by KELT-9 b, leads its day-side equilibrium temperature to reach about 4600 K (Gaudi et al. 2017), making this planet hotter than most stars. Hence, its scorching temperature induces the atmosphere to inflate substantially, making this planet an ideal target for transmission spectroscopy.

A wide variety of metallic species, both ionised and neutral, have been identified in the atmosphere of KELT-9 b. The cross-correlation technique led to the detection of Fe I,

Fe II, Ti II (Hoeijmakers et al. 2018), Na I, Cr II, Sc II and Y II signatures (Hoeijmakers et al. 2019), Ca I, Cr I, Ni I, Sr II, and Tb II at the 5σ level, and Ti I, V I, and Ba II above the 3σ level (Borsato et al. 2023). Furthermore, line studies of its primary transit unveiled the presence of O I (Borsa et al. 2021b), Mg I and Fe II (Cauley et al. 2019), Hα (Yan & Henning 2018), ionized calcium (i.e. H&K doublet and near-infrared triplet) (Yan et al. 2019; Turner et al. 2020), the Hydrogen Balmer series up to Hδ (Yan & Henning 2018; Cauley et al. 2019; Turner et al. 2020; Wyttenbach et al. 2020) and the Paschen β line (Sánchez-López et al. 2022).

In this chapter I will focus on several works I carried on regarding this peculiar alien world. In Section 2.1 I will introduce my work on the atmospheric characterisation of KELT-9 b via single-line analysis published on A&A as D'Arpa et al. (2024b) and carried within the **Global Architecture of Planetary System (GAPS)** collaboration. In Section 2.2 I will discuss a future application of the observative results presented in Section 2.1, aimed to the constrain the C/O ratio in the atmosphere of KELT-9 b using the **Non Local Thermal Equilibrium (NLTE)** models. Finally, in Section 2.3 I will deepen the comparison with other studies on the same target conducted within the **GAPS** collaboration.

2.1 Atmospheric characterisation of KELT-9 b via single-line analysis

In this work, I analysed six primary transits of the ultra-hot Jupiter KELT-9 b obtained with the **HARPS-N** high-resolution spectrograph in the context of the Global Architecture of Planetary Systems (GAPS2) project, to characterise the atmosphere via single-line analysis. The possibility of using six transits is one of the major advantages of this work respect to the others on the same target, due to the large S/N ratio obtained combining the single nights. We extracted the transmission spectrum of each individual line by comparing the master out-of-transit spectrum with the in-transit spectra and computing the weighted average of the tomography in the planet reference frame. We corrected for the centre-to-limb variation and the Rossiter-McLaughlin effect by modelling the region of the star disc obscured by the planet during the transit and subtracting it from the master-out spectrum. We detected all six observable lines of the Balmer series within the **HARPS-N** wavelength range, from Hα to Hζ , with a significance exceeding 5σ. We also focussed on metal species, detecting Na I, Ca I, Ca II, Fe I, Fe II, Mg I, Ti II, Sc II, and Cr II lines. This is the first detection in the atmosphere of an exoplanet of Hϵ and Hζ lines, as well as of individual lines of Sc II and Cr II. Our detections are supported by a comparison with published synthetic transmission spectra of KELT-9 b obtained accounting for non-local thermodynamic equilibrium effects. The results underline the presence of a systematic blueshift due to night-side to day-side winds. The single-line analysis allowed us not only to assess the presence of atomic species in the atmosphere of KELT-9 b, but also to further characterise the local stratification of the atmosphere. Coupling the height distribution of the detected species with the velocity shift retrieved, we acknowledged the height distribution of night-side to day-side winds. Moreover, the

Table 2.1: **HARPS-N** observing log.

Night	Date	Program	P.I.	Spectra (In/Out of transit)	Mean S/N[a]	Exposure time [s]	Airmass
1	2017-07-31	A35DDT4	Ehrenreich	49 (24/25)	137	600	1.019 - 1.730
2	2018-06-10	**GAPS**	Micela	36 (23/13)	123	600	1.019 - 2.164
3	2018-07-20	OPT18A_38	Ehrenreich	46 (23/23)	120	600	1.019 - 1.675
4	2018-07-23	**GAPS**	Micela	68 (44/24)	79	300	1.019 - 1.535
5	2018-09-01	**GAPS**	Micela	57 (44/13)	99	300	1.019 - 1.800
6	2018-09-04	**GAPS**	Micela	64 (44/20)	87	300	1.019 - 1.426

[a] The mean Signal to Noise ratio (S/N) has been computed as the average of all the orders of all the spectra for each night. We show the S/N as a function of wavelength in Fig. 2.11.

study of the rotational broadening of the different species supports the prediction of a tidally locked planet rotating as a rigid body. In the following subsection I will describe the various steps of the analysis.

2.1.1 Observations

We analysed a total of six KELT-9 b primary transits, observed from July 2017 to September 2018 with **HARPS-N** at the **Telescopio Nazionale Galileo (TNG)** (see Table 2.1). Four of these transits were acquired in the context of the long-term observing programme at the Telescopio Nazionale Galileo (**TNG**) telescope 'GAPS2: the origin of planetary systems' – awarded to the Italian Global Architecture of Planetary System (**GAPS**) Collaboration (P.I Micela; see Guilluy et al. 2022b), while the two remaining have been collected by other programs (P.I. Ehrenreich). **HARPS-N**, being the northern-hemisphere's twin of **European Southern Observatory (ESO)**'s **High Accuracy Radial velocity Planet Searcher (HARPS)**/3.6 m telescope, is a fiber-fed cross-dispersed echelle spectrograph which covers the 3830–6900 Å spectral range at an average resolution of $\mathcal{R} \sim 115{,}000$ (Cosentino et al. 2012). For each night of observation, the exposure time per spectrum was set to either 600 s or 300 s, leading to an average Signal to Noise ratio (S/N), averaged over all the spectral orders, of 126 and 88, respectively. In addition to the spectra taken in transit, a number of out-of-transit observations were also acquired. These act as baseline for the stellar flux and allow one to derive the master-out spectrum, which includes only the stellar contribution (see Section 2.1.2). A complete overview of the observations, including the date, program number, PI, number of in- and out-of-transit spectra, average S/N and airmass range is given in Table 2.1. We also show the S/N as a function of wavelength in Fig. 2.11. The night reports for the different nights do not give any critical observing conditions to remark . For the analysis of Hζ we had to discard 8 spectra (out of 202 in-transit spectra used) where the S/N was too low in the bluest part of the spectrum.

Borsa et al. (2021b) discussed the negligibility of line broadening due to the exposure time (i.e. 4.7, 3.5, and 1.3 km s^{-1}on average for exposure times of 400, 300, and 111 s, respectively) for **Calar Alto high-Resolution search for M dwarfs with Exoearths with Near-infrared and optical Échelle Spectrographs (CARMENES)** data. In our case, combining all the 6 nights, we obtain a mean exposure time of 433s weighting the in-transit exposure times for the mean S/N of each of our 202 in-transit spectra.

Table 2.2: Stellar and planetary parameters of the KELT-9 system adopted in this work.

Parameter	Value	Reference
$T_{\rm eff}$ [K]	9600 ± 400	Borsa et al. (2019)
M_* [$M_\odot$]	2.32 ± 0.16	Borsa et al. (2019)
R_* [$R_\odot$]	2.418 ± 0.058	Borsa et al. (2019)
$\log_{10}(g)$	4.1 ± 0.3	Borsa et al. (2019)
$M_{\rm p}$ [$M_{\rm J}$]	2.88 ± 0.35	Borsa et al. (2019)
$R_{\rm p}$ [$R_{\rm J}$]	1.936 ± 0.047	Borsa et al. (2019)
a [AU]	0.03368 ± 0.00078	Borsa et al. (2019)
P [days]	1.48111871(16)	Ivshina & Winn (2022)
$T_{\rm c}$ [days]	2458415.362562(81)	Ivshina & Winn (2022)
i [deg]	86.79 ± 0.3	Gaudi et al. (2017)
λ [deg]	85.78 ± 0.46	Borsa et al. (2019)
$K_{\rm p}$ [km s^{-1}]	246	This work
$v_{\rm sys}$ [km s^{-1}]	-17.74 ± 0.11	Hoeijmakers et al. (2019)
e	0 (fixed)	Gaudi et al. (2017)
$v \sin i_*$ [km s^{-1}]	111.4 ± 1.2	Gaudi et al. (2017)

We therefore included the line broadening in our analysis with the **NLTE** models as discussed in Section 2.1.4.

2.1.2 Transmission spectra extraction

We employed the 3.7 version of the **HARPS-N Data Reduction Software (DRS)** (Pepe et al. 2002) to do an initial reduction of the **HARPS-N** raw data, which includes a correction for the blaze function that takes care of both the instrumental blaze and the Earth atmospheric change thanks to the Atmospheric Dispersion Corrector. We operate with S1D spectra that have been created by the **DRS** starting from the S2D images. During the merging procedures, the **DRS** takes care of the overlaps between the 69 **HARPS-N** orders. At this stage, the data contain the stellar signal, the planetary signal, and the telluric contamination, all given in the solar system barycentric reference frame. The wavelength information is given in air. For each transit, we calculated the transmission spectra of the single lines following the procedure described in Wyttenbach et al. (2015), hence comparing out-of-transit and in-transit spectra.

The first step of the analysis consists in correcting the observed spectra for telluric contamination. To do so, we employ `Molecfit` [1] (Smette et al. 2015; Kausch et al. 2015), a specialised **ESO** tool designed to handle the correction of telluric atmospheric lines in astronomical spectra through the use of a line-by-line radiative transfer model. Although the software was specifically developed to correct data obtained with **ESO** instruments, in principle it is able to correct spectra from non-**ESO** ground-based spec-

[1] http://www.eso.org/sci/software/pipelines/skytools/molecfit

trographs as well, and recently, **ESO** released an additional experimental support for **HARPS-N**. Telluric correction is particularly important in the red part of the **HARPS-N** spectra, where the Earth atmosphere's H_2O and O_2 absorption features become relevant. In Fig. 2.1, we show an example of telluric removal in the vicinity of the Hα region. `Molecfit` returns telluric corrected spectra in the solar barycentric reference frame. Therefore, we shifted the spectra in the stellar reference frame by correcting for the star's systemic radial velocity, $v_{\rm sys}$. The telluric corrected spectra are then normalised to a common continuum level in a narrow wavelength range around each absorption line of interest. The normalisation around a small region should also remove all the possible wavelength gradients arising from changes in the overall transmission of the atmosphere and other slow changes in the spectrograph.

For each night, we computed the transmission spectra in the stellar reference frame as the ratio between each spectrum and the weighted average out-of-transit spectrum (master-out). By stacking all spectra sorted by phase, we obtain a 2D map (also referred as tomography) such as the one shown in Fig. 2.2. From this map, we can clearly see how the joint contribution of the Rossiter-McLaughlin Effect (**Rossiter-McLaughlin Effect (RME)**) (Rossiter 1924; McLaughlin 1924) and the Center-to-Limb Variations (**Centre to Limb Variation (CLV)**), which arise respectively from the stellar rotation and the limb darkening, is a major contribution that needs to be modeled and removed. The **RME** and **CLV** compete with the planetary atmospheric signal to shape what we observe in the 2D map such as Fig. 2.2 according to the geometry of the transit.

We corrected for the **RME+CLV** effects by adopting an analogous method to that described by Yan et al. (2017) and Casasayas-Barris et al. (2017), and already applied in Guilluy et al. (2024), which involves the use of stellar models. We used ATLAS9 stellar models (Kurucz 1992, 2005, 2014, 2017) to compute the disk-integrated stellar model considering the system parameters listed in Table 2.2. We computed the spectra for the case of a non-rotating star as well as a rotating star. We used `PyLightCurve` (Tsiaras et al. 2016) to calculate the planet's path during the transit to evaluate the part of the stellar disc obscured by the planet at each phase (hereafter, obscured region). We then built a 0.01 R_* $\times$ 0.01 R_* pixel size grid to approximate the stellar disc and for each phase we performed the following operations:

- for each pixel belonging to the obscured region, we computed the intensity according to the limb darkening angle and the radial velocity shift with respect to stellar rotation axis;

- we computed the spectrum of the obscured region using the ATLAS9 models, summing the spectrum of each pixel properly shifted by its own radial velocity.

Instead of using different model spectra at different limb darkening angles, μ, and interpolating to compute the right intensity for each pixel, we used an analytical approach. We computed the limb darkening coefficients for our stellar model using the `ExoTethys` (Morello et al. 2020) function `Sail` adopting a quadratic limb darkening

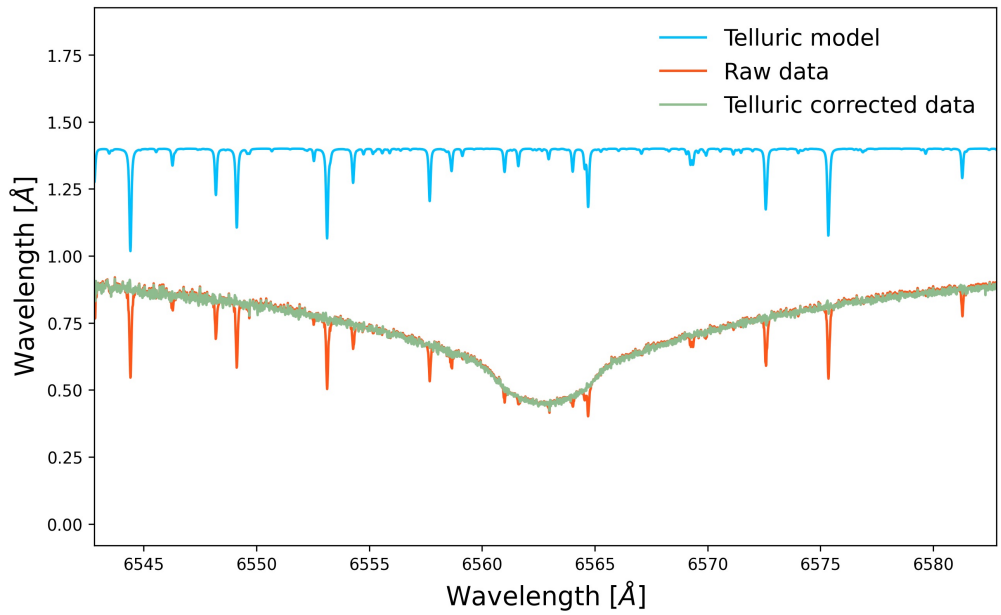

Figure 2.1: An example of telluric correction on a KELT-9 spectrum observed by **HARPS-N** on 2017-07-31. After normalisation, the **DRS** processed data (in red) was telluric corrected with `Molecfit` (green line) using the telluric model (in blue), here shifted upwards for clarity.

law:

$$\frac{I_\lambda(\mu)}{I_\lambda(1)} = 1 - c_{1,\lambda}(1-\mu) - c_{2,\lambda}(1-\mu)^2, \tag{2.1}$$

where:

- λ indicates a specific spectral bin/passband;
- $\mu = \cos\theta$, θ being the angle between the line of sight and the normal to the stellar surface;
- $I_\lambda(\mu)$ is the stellar intensity profile and $I_\lambda(1)$ is the intensity at the center of the disk;
- $c_{1,\lambda}$ and $c_{2,\lambda}$ are the limb darkening coefficients.

We note that the different choice of the limb darkening law can be a possible cause of discrepancy with other analysis since the **RME+CLV** modelling strongly relies on the part of the stellar disk occulted. However, since we do not have any spatially resolved spectrum of the star, it is not possible stating exactly which limb darkening law would better mimic the real observations.

The integrated flux, F_λ, as a function of the limb darkening angle, μ, can be expressed

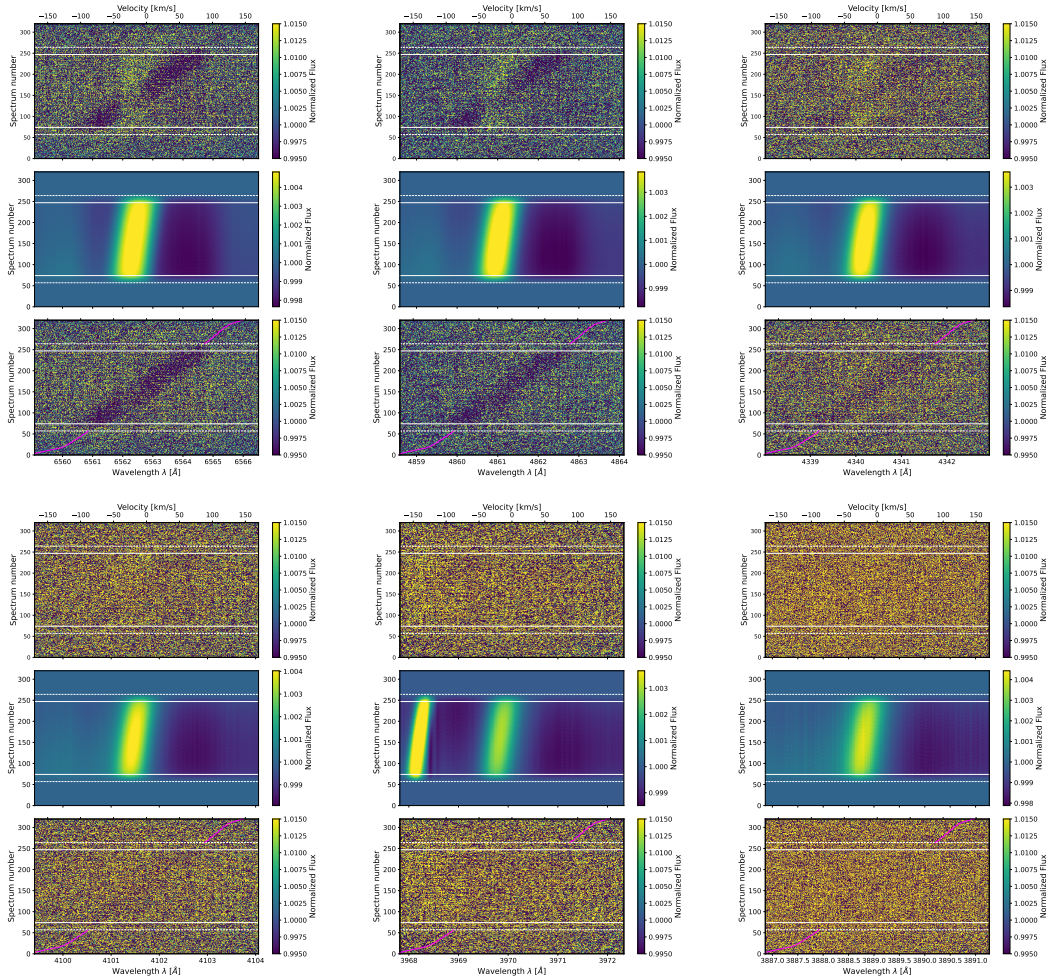

Figure 2.2: *Top panels*: Raw tomography in the stellar reference frame for the hydrogen Balmer lines (Top row, left to right: Hα , Hβ and Hγ ; Bottom row, left to right: Hδ , Hϵ and Hζ). The planetary atmospheric absorption can be distinguished as a darker region following the expected planetary **Radial Velocity (RV)** profile, and the **RME** as a brighter feature. We also show the planetary radial velocity profile during out-of-transit with a magenta line. The contact points are represented with white dashed and continuous lines. *Middle panels*: Model tomography in the stellar reference frame computed as explained in Section 2.1.2. *Bottom panels*: Corrected tomography obtained by dividing the raw one by the model one.

as

$$F_\lambda = 2\pi \int_0^1 I_\lambda(\mu)\ \mu\ d\mu. \tag{2.2}$$

By combining Equations 2.1 and 2.2 and solving the integral analytically, we obtain $I_\lambda(1)$. At this point, knowing $I_\lambda(1)$ and the limb darkening coefficients, we are able to compute the flux for each μ (and hence for each pixel) using Eq. 2.1. The integrated flux F_λ corresponds to the non-rotating model spectrum. The rotational broadening is given by the sum of the different contributions of each pixel properly shifted by their own radial velocity. The observed master-out is broadened by the stellar rotation and hence we used the rotationally broadened model as a comparison to the master-out to normalise the non-rotating model continuum. We then subtracted the modelled obscured region from the master-out spectra and divided all spectra by this quantity. The average continuum for the **RME+CLV** models is set to one before applying the correction. An example of the planet absorption for the Balmer series spectra in the stellar reference frame before and after the correction for **RME** and **CLV** is shown in Fig. 2.2. From the comparison between top and bottom panels of Fig. 2.2, we can see that following this framework, we are able to remove the **RME+CLV** contaminations while not changing the planetary signal. This is particular easy to observe in target such as KELT-9 b with their peculiar transit, but may be more challenging when the two effects overlap such as in the case of HAT-P-67 b (Sicilia et al. 2024). We have not considered the potential distortion of line profiles caused by gravity darkening. However, it is noteworthy that such distortions are rarely considered in the literature (Guilluy et al. 2022a), and are anticipated to be negligible for this target, as indicated by Cauley & Ahlers (2022), who state that the gravity darkening is expected to be less relevant respect the other effects considered (such as **RME** and **CLV**) with the present level of achievable precision. Furthermore, we did not include in our models broadening due to the exposure time since the polar orbit of KELT-9 b causes the planet to obscure approximatly the same portion of the star in terms of velocity. In fact, during the 600s exposure the difference in the velocity occulted is below 1 km s^{-1}.
Once the spectra in the stellar reference frame had been corrected, we shifted all the in-transit spectra to the planet reference frame by correcting for its radial velocity profile in a circular orbit scenario

$$RV(\Phi) = K_\mathrm{p}\ \sin 2\pi\Phi, \tag{2.3}$$

where Φ is the orbital phase and K_p is the radial velocity of the planet, computed using the parameters listed in Table 2.2. The final transmission spectrum of each line is calculated as the error-weighted average of all the full in-transit spectra (T_2-T_3) in the planet reference frame. The uncertainties have been originally computed as the square root of the **DRS** corrected flux and then propagated during the entire process.

2.1.3 Single Line Analysis Results

For each analysed line, we extracted the transmission spectrum as described in Section 2.1.2 and then performed a Gaussian fit returning the absorption depth, the **Full Width**

at Half Maximum (FWHM), and the velocity shift with respect to the line wavelength corresponding to a zero radial velocity. We used the Python package `Scipy CurveFit` [2], which employs non-linear least squares to fit a function, setting 100 km s^{-1}as velocity range. For some lines we adopted a smaller wavelength range (e.g., 80 km s^{-1}) due to the closeness with other strong lines. We left the continuum offset as a free parameter and we used the retrieved values to normalise the spectra to one, and hence we do not report the continuum values in the best-fit tables. Our definition of significance is based on the retrieved value of the Gaussian fit and it is defined as the ratio between the absorption depth value and its error.
The adopted procedure of modelling and removing of **RME + CLV** strongly depends on the size of the obscured region of the stellar disk, which, at first order, we consider equal to the planetary radius. To include the atmospheric extension, we translate the line absorption depths, returned by the Gaussian fit, into planetary radii and use these values to repeat the **RME + CLV** removal with an increased size that accounts for both the planetary radius and the atmospheric extension. We repeat the loop, retrieving a new depth expressed in planetary radii, until the threshold convergence (0.001 $R_{\rm p}$) is reached.

Hydrogen Balmer Series

We focused on the Hydrogen Balmer series by analising all the lines observable in the **HARPS-N** wavelength range, hence spanning from Hα to Hζ . In Fig. 2.3 we show the transmission spectra around each Balmer line. We significantly detect all the lines observable in the available wavelength range with the first significant detection of Hϵ and Hζ . The parameters of the Gaussian best fit are listed in Table 2.3.
- Hα : we detect Hα with a significance of $\sim 60\sigma$. Hα has already been detected in this target by Yan & Henning (2018) and Turner et al. (2020) with **CARMENES**, and by Cauley et al. (2019) using PEPSI. The Balmer series has been analysed by Wyttenbach et al. (2020) using Night 1 and Night 3 data, detecting Hα , Hβ , Hγ and Hδ , but not Hϵ (tentative detection) and Hζ (non detection). As shown in Fig. 2.12, our results are in good agreement ($\leq 3\sigma$) with Turner et al. (2020) and Wyttenbach et al. (2020), but in disagreement ($\geq 5\sigma$) with Cauley et al. (2019) and Yan & Henning (2018).
- Hβ : we detect Hβ with a significance of $\sim 31\sigma$ and, as for Hα , our result agrees (2σ) with Wyttenbach et al. (2020), but it is at odds (7σ) with Cauley et al. (2019).
- Hγ and Hδ : these lines have been detected in the atmosphere of just a few exoplanet (HD189733 b, KELT-9 b, and KELT-20 b/MASCARA-2 b; Cauley et al. 2016; Cauley et al. 2019; Casasayas-Barris et al. 2019), with Wyttenbach et al. (2020) being the only one who detected both lines in the atmosphere of KELT-9 b. We detect Hγ and Hδ with a significance of 25σ and 12.2σ respectively, further supporting Wyttenbach et al. (2020) detection, especially for Hδ .
- Hϵ : we significantly detect Hϵ for the first time in the atmosphere of an exoplanet with a significance of 6.8σ. Hϵ , already marginally detected by Wyttenbach et al. (2020),

[2] https://docs.scipy.org/doc/scipy/reference/generated/scipy.optimize.curve_fit.html

falls in a region in which two other strong lines are present, namely Ca II H at 3968.47 Å and Fe I at 3969.25 Å. The Ca II H line is discussed in Section 2.1.3 and it is more than 100 km s^{-1}away from the core of Hϵ and hence it does not affect our detection. The Fe I line lies between the Ca II H lines and Hϵ , and we find that is shifted by 8.67 km s^{-1}similarly to the other Fe lines (see Section 2.1.3). The region including Ca II H, Fe I, and Hϵ is shown in Fig. 2.13 with the corresponding Gaussian fits.
- Hζ : we detect Hζ for the first time in the atmosphere of an exoplanet, with a significance of 5.7σ. We find that it is deeper than the upper limit measured by Wyttenbach et al. (2020), who expected the absorption to be the smallest among the Balmer lines in the **HARPS-N** range. Instead, we find Hζ to be the second deepest line after Hα , though with a very large uncertainty (almost three to ten times larger than the other lines). The discrepancy is most likely due to the low S/N in the bluest region covered by **HARPS-N** that forced us to discard eight spectra, because of their low S/N. The low signal affects significantly both the uncertainties and the normalisation process, because of the difficulty of finding a pseudo-continuum region around the line core, which may have led to overestimating the line depth. We also investigated the possibility that the larger depth is due to the presence of other lines in the region, namely Fe I at 3888.51 Å and Ca I at 3889.10 Å lines. We analysed these lines adopting the procedure described in Section 2.1.2 and obtained that the depth and **FWHM** are similar to those obtained analising Hζ , while the velocity shifts in both cases correspond to the exact position of Hζ . Furthermore, the analysis of the Ca I and Fe I lines presented in Sections 2.1.3 and 2.1.3 reveals that the detected lines of those species are shallower compared to those obtained for Ca II at 3889.10 Å and Fe I at 3888.51 Å.

A detailed discussion about the differences in the Hα and Hβ transmission spectra observed by Cauley et al. (2019), Yan & Henning (2018), Turner et al. (2020) and Wyttenbach et al. (2020) is given by Fossati et al. (2020). Their conclusions stress that the variations could stem from distinct instruments and resolving powers, but more likely, they arise from the slightly different methodologies employed to extract the planetary signal. The major contributions to the discrepancies seem to be the normalisation, the removal of the **RME+CLV** effects, and the systemic velocity adopted in the different studies, with the latter being responsible for the velocity shifts (see Fossati et al. 2020, for more details). We can extend the conclusions that Fossati et al. (2020) drew for the other works to our results, which fit well in the scenario, considering the slightly different approaches used in the analyses.

Another plausible explanation to the discrepancy may be the intrinsic presence of in-transit variations along a single transit as pointed out by Cauley et al. (2019). Thanks to our sample of 6 nights, we are able to explore the presence of variability using our method by analising Hα , Hβ , and Hγ individually for each night. Fig. 2.14 and Table 2.7 show that the individual nights best-fit results scatter around the value obtained analising all nights together. None of the parameters seem to show a trend that depends on the different exposure time used in the first three nights (600s) and in the last three (300s). Focusing on the Hα absorption depths, we see an apparent intrinsic variability of the order of $\sim$30% in our dataset, with depths spanning over a range (0.78 $\pm$ 0.05 -

Table 2.3: Summary of the results obtained from the Gaussian fits to the detected H I Balmer lines.

	Gaussian fit					**NLTE** model		
Line (Wavelength in Å)	Depth [%]	R_p	**FWHM** [km s^{-1}]	v [km s^{-1}]	χ^2_{red}	ν_{mic} [km s^{-1}]	ν_{mac} [km s^{-1}]	χ^2_{red}
Hα (6563)	0.97 ± 0.02	1.56 ± 0.01	49.25 ± 0.95	-3.34 ± 0.36	1.37	2.0 ± 1.5	21 ± 3	0.66
Hβ (4861)	0.64 ± 0.02	1.39 ± 0.01	45.0 ± 1.58	-5.67 ± 0.61	1.08	1.0 ± 0.8	24 ± 1	0.71
Hγ (4340)	0.51 ± 0.03	1.33 ± 0.01	36.63 ± 2.17	-5.74 ± 0.86	0.66	3.0 ± 0.5	24 ± 2	0.60
Hδ (4102)	0.62 ± 0.05	1.38 ± 0.03	28.97 ± 2.79	-8.24 ± 1.13	1.03	1.0 ± 1.2	10 ± 12	0.90
Hϵ (3970)	0.39 ± 0.06	1.25 ± 0.03	30.65 ± 5.35	-5.36 ± 2.11	0.70	1.0 ± 1.7	19 ± 16	0.83
Hζ (3889)	0.92 ± 0.16	1.53 ± 0.08	26.1 ± 5.4	-7.56 ± 2.16	3.60	14.0 ± 4.8	1 ± 14	3.75

[a] We report the Depth, **FWHM** and v columns representing the Gaussian best fit parameters, while R_p is the transit depth translated into planetary radii. ν_{mic} and ν_{mac} are the micro- and macro-turbulence velocity respectively, for the best fitting **NLTE** model. For both analysis we also report the reduced chi-squared, χ^2_{red}.

1.18 ± 0.03) that includes all the results from other works. Since our datasets have two common transit observations (2017-07-31 and 2018-07-20), we deepened the comparison with Wyttenbach et al. (2020). Fig. 2.15 shows that: i) our results are generally in good agreement ($<3\sigma$) with those of Wyttenbach et al. (2020), except for the velocity shift of Hϵ , which has been previously only tentatively detected; ii) the best fit parameters considering two nights are closer to the ones that we obtain with six nights than the results obtained analysing the single nights separately, hinting that increasing the global S/N plays a major role in the final results.

We conclude that the discrepancies may generally arise from the joint contribution of several factors, such as different instrumentation and datasets, or they origin from the slightly different methods used to extract the planetary signal, as already discussed by Fossati et al. (2020), or from the different K_p used. However, the analysis of six nights using the same instrument and the same framework hinted to an intrinsic variability which covers the range of the different values retrieved in the different works. The possible causes of this variability are still unclear, but one cannot exclude that it originates in the planetary atmosphere. A similar intrinsic variability has already been noted by Fossati et al. (2023a) analysing **HARPS-N** data of **UHJ** KELT-20 b, despite, in their case, the amplitude of the variation was not significative.

Metal lines

We analysed several metal species by employing the same method used for the Balmer series. We used the **National Institute of Standards and Technology (NIST)**[3]to aid identifying the strongest lines in the **HARPS-N** range for each species, focusing on both neutral and ionized species. We do not detect any He (listed here despite not being a metal), Li, Be, K, Sr, Y, Ni, and Ba lines. We stress that these species have not been detected on KELT-9 b in previous studies (Hoeijmakers et al. 2018; Yan & Henning 2018; Cauley et al. 2019; Hoeijmakers et al. 2019; Borsato et al. 2023; Ridden-Harper et al. 2023) neither via single line analysis nor using cross correlation with templates. Instead, we detect Na, Mg, Ca, Sc, Ti, V, Cr, and Fe lines with a significance greater than 3σ. In the following sections, we list our results for each species in order of ascending

[3] https://physics.nist.gov/PhysRefData/ASD/lines_form.html

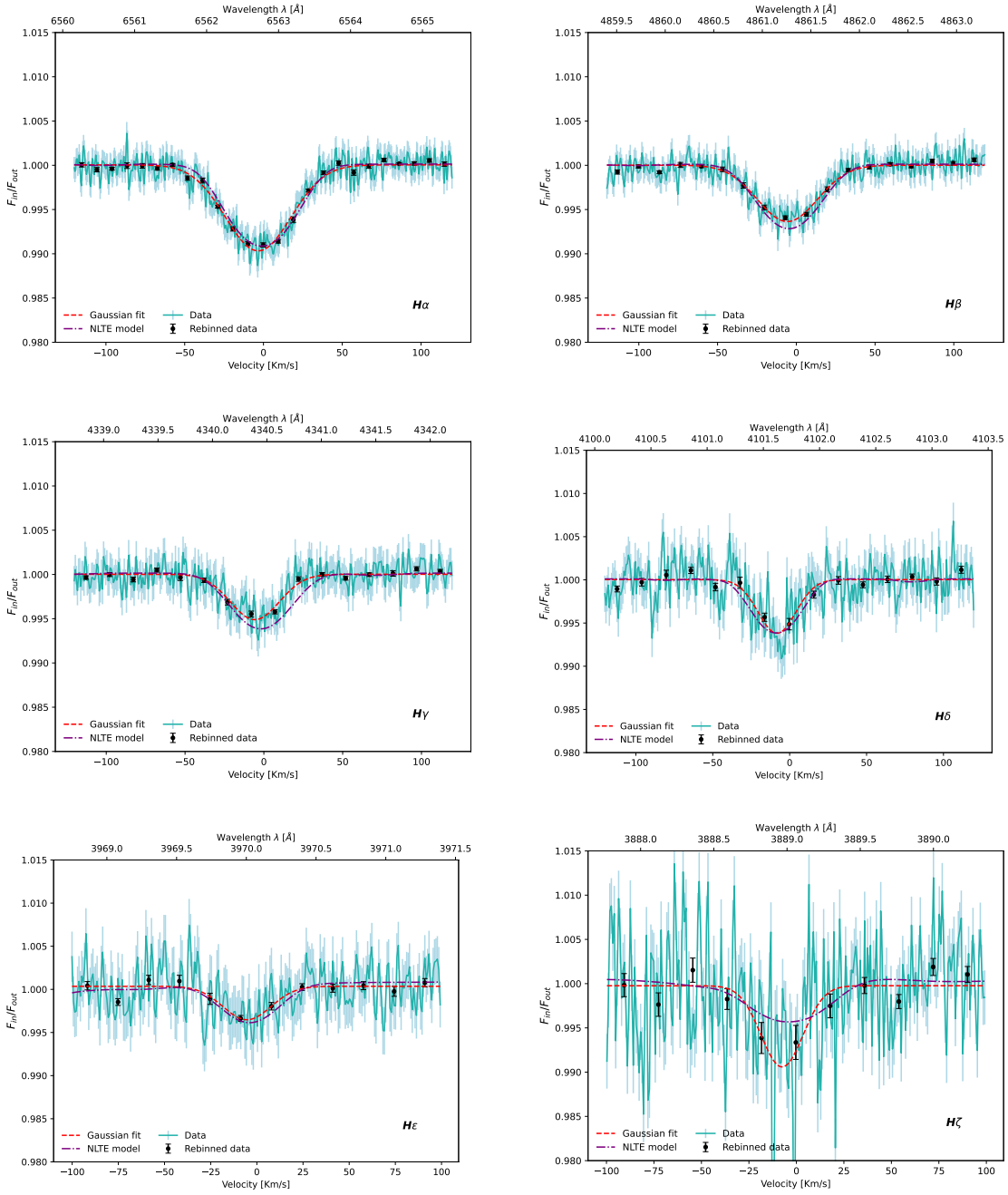

Figure 2.3: Balmer series transmission spectra: all the figures have the same range on the y-axis to underline the differences between the single lines. The red dashed lines represent the Gaussian best fit those results are listed in Table 2.3, while the black dots are for a 20x binning of then observed data. Hζ presents a wider scatter compared to the other lines due to the low S/N in the bluest part of the **HARPS-N** range. The purple lines show the **NLTE** broadened models as discussed in Section 2.1.4. The small gradient of the **NLTE** model for Hϵ is due to the vicinity with the Ca H line at 3968.47 Å.

Table 2.4: Summary of the results obtained from the Gaussian fits to the detected metal lines, except for iron.

	Gaussian fit					**NLTE** model		
Line (Wavelength in Å)	Depth [%]	R_p	**FWHM** [km s^{-1}]	v [km s^{-1}]	χ^2_{red}	ν_{mic} [km s^{-1}]	ν_{mac} [km s^{-1}]	χ^2_{red}
Na D1 (5895.92)	0.15 ± 0.02	1.11 ± 0.01	17.44 ± 2.03	-4.59 ± 0.84	0.62	1.0 ± 0.02	12 ± 4	1.2
Na D2 (5889.95)	0.16 ± 0.01	1.11 ± 0.01	23.68 ± 2.58	-6.68 ± 1.05	0.81	1.0 ± 0.01	14 ± 3	1.01
Mg I (5167.3216)	0.14 ± 0.02	1.10 ± 0.01	24.10 ± 3.97	-4.14 ± 1.56	1.24	4.0 ± 0.3	20 ± 4	1.35
Mg I (5172.7)	0.10 ± 0.02	1.07 ± 0.01	22.88 ± 4.46	-4.39 ± 1.81	1.00	1.0 ± 0.1	24 ± 5	1.09
Mg I (5183.62)	0.10 ± 0.01	1.07 ± 0.01	23.76 ± 3.86	-5.06 ± 1.57	0.70	1.0 ± 0.2	24 ± 7	0.88
Mg I (5528.4)	0.08 ± 0.02	1.06 ± 0.01	9.35 ± 2.76	-7.63 ± 1.15	0.68	1.0 ± 0.3	10 ± 11	0.66
Ca II (5041.62)	0.07 ± 0.01	1.05 ± 0.01	52.01 ± 11.86	-15.78 ± 4.39	1.11	4.0 ± 2.1	24 ± 10	1.09
Ca II (5270.27)	0.07 ± 0.01	1.05 ± 0.01	22.39 ± 5.0	-3.59 ± 2.04	0.66	1.0 ± 0.6	19 ± 8	0.66
Ca II (6122.22)	0.08 ± 0.01	1.06 ± 0.01	16.01 ± 3.25	-8.74 ± 1.34	0.46	8.0 ± 0.8	1 ± 14	0.47
Ca II (6439.07)	0.04 ± 0.01	1.03 ± 0.01	29.0 ± 10.58	-8.55 ± 4.24	0.57	1.0 ± 0.6	24 ± 10	0.58
Ca II (6717.69)	0.07 ± 0.02	1.05 ± 0.01	20.68 ± 5.3	-7.16 ± 2.11	0.54	3.0 ± 1.9	10 ± 13	0.54
CaH (3968.47)	0.67 ± 0.06	1.41 ± 0.03	29.05 ± 3.09	-2.66 ± 1.17	0.73	8.0 ± 3.7	1 ± 9	0.93
CaK (3933.66)	0.54 ± 0.06	1.34 ± 0.03	22.14 ± 2.79	-3.86 ± 1.14	2.17	3.0 ± 1.0	1 ± 7	1.39
Sc II (4320.745)	0.15 ± 0.02	1.11 ± 0.02	24.58 ± 4.51	-4.72 ± 1.83	0.87	4.0 ± 1.5	12 ± 9	0.88
Sc II (5031.01)	0.08 ± 0.02	1.06 ± 0.01	11.4 ± 3.3	-11.22 ± 1.36	0.62	12.0 ± 2.6	24 ± 23	0.70
Sc II (5239.811)	0.06 ± 0.02	1.04 ± 0.01	17.72 ± 5.69	-7.53 ± 2.34	0.75	1.0 ± 2.3	5 ± 15	0.75
Sc II (5526.785)	0.09 ± 0.02	1.06 ± 0.01	15.92 ± 3.21	-9.05 ± 1.30	0.61	1.0 ± 0.9	1 ± 11	0.58
Sc II (5657.907)	0.06 ± 0.01	1.04 ± 0.01	29.44 ± 6.65	-9.37 ± 2.66	0.59	3.0 ± 0.9	21 ± 10	0.60
Ti II (4290.21)	0.13 ± 0.03	1.09 ± 0.02	14.25 ± 4.05	-4.94 ± 1.68	0.90	2.0 ± 0.3	1 ± 7	0.96
Ti II (4300.04)	0.16 ± 0.02	1.11 ± 0.02	22.3 ± 4.06	-4.39 ± 1.65	0.95	1.0 ± 0.0	24 ± 14	1.12
Ti II (4395.03)	0.15 ± 0.03	1.11 ± 0.02	16.06 ± 3.93	-5.74 ± 1.62	1.27	4.0 ± 1.7	1 ± 4	1.34
Ti II (4443.8)	0.14 ± 0.03	1.10 ± 0.02	10.5 ± 2.69	-11.48 ± 1.12	0.84	1.0 ± 0.7	24 ± 7	0.95
Ti II (4468.49)	0.19 ± 0.02	1.13 ± 0.01	13.36 ± 1.91	-8.46 ± 0.79	0.65	14.0 ± 2.2	23 ± 18	0.79
Ti II (4501.26)	0.12 ± 0.02	1.09 ± 0.01	17.85 ± 3.07	-8.2 ± 1.26	0.57	14.0 ± 4.0	24 ± 5	0.66
Ti II (4533.96)	0.19 ± 0.02	1.13 ± 0.01	15.62 ± 2.07	-4.86 ± 0.86	0.76	8.0 ± 3.3	1 ± 3	0.78
Ti II (4571.97)	0.20 ± 0.02	1.14 ± 0.01	15.53 ± 1.9	-6.89 ± 0.78	0.71	1.0 ± 0.9	24 ± 6	0.97
Ti II (4805.0)	0.09 ± 0.02	1.07 ± 0.02	14.35 ± 4.03	-2.09 ± 1.67	0.99	14.0 ± 6.4	7 ± 10	1.01
Ti II (5188.68)	0.11 ± 0.01	1.08 ± 0.01	15.04 ± 2.27	-10.43 ± 0.94	0.53	3.0 ± 2.2	1 ± 6	0.60
Cr II (4558.64)	0.09 ± 0.03	1.06 ± 0.02	14.52 ± 5.55	-9.34 ± 2.3	1.34	1.0 ± 0.3	10 ± 12	1.37
Cr II (4588.19)	0.09 ± 0.02	1.06 ± 0.01	33.89 ± 8.26	4.4 ± 3.26	1.16	4.0 ± 0.3	24 ± 3	1.16
Cr II (4618.8)	0.06 ± 0.02	1.04 ± 0.01	17.01 ± 6.6	-6.17 ± 2.72	0.79	2.0 ± 1.0	7 ± 8	0.76
Cr II (4824.13)	0.06 ± 0.01	1.04 ± 0.01	18.56 ± 5.32	-4.87 ± 2.18	0.51	1.0 ± 0.8	11 ± 13	0.52

Notes: For each line, we show the wavelength in Å.

atomic number. The best-fit parameters are listed in Table 2.4.

Sodium

The neutral sodium doublet lines, named Na D1 and Na D2 in this study, are among the most studied and detected lines in single line analyses due to their capability to probe the upper layers of the atmosphere. The sodium doublet has already been detected in KELT-9 b by Langeveld et al. (2022) using **HARPS-N** data collected during Night 1 and Night 3. Our results are in excellent agreement with their, since they retrieve a mean depth of 0.16 ± 0.03 %, while we retrieve 0.15 ± 0.02 % and 0.16 ± 0.01 % for Na D1 and Na D2 respectively. The mean velocity shift they retrieve is -4.1 ± 2.9 km s^{-1}while ours is -4.59 ± 0.84 km s^{-1}and -6.68 ± 1.05 km s^{-1}for Na D1 and Na D2 respectively. The sodium doublet will also be analysed, using the same dataset employed in this work, in a dedicated study (Sicilia et al. 2025) that aims to perform a population study on several **GAPS** targets.

Magnesium

We identify a significant absorption on each of the neutral Magnesium b triplet lines ($\sim$ 5167-5183 Å), as previously reported by Cauley et al. (2019), plus the Mg I line at 5528.40 Å. Our Mg I triplet line depths are more than 3σ away from the results reported by Cauley et al. (2019), except for the Mg I 5167.23 Å line, which is consistent within 1σ. Instead, our **FWHM** results are more in agreement (1σ difference) with Cauley et al. (2019), the first line at 5167.3216 Å being 2σ away. The line shifts have remarkably large error bars, similarly to Cauley et al. (2019). The discrepancies in the fitted values between our study and Cauley et al. (2019) are probably due to the latter employing lower resolution spectra from PEPSI ($\mathcal{R}\sim$50,000) compared to **HARPS-N**. The Mg I lines at 5167.23 and 5172.70 Å are located in the vicinity of the Fe II 5169.0282 Å line, as highlighted by Hoeijmakers et al. (2019) in their Fig. 8. To avoid any potential contamination from this iron line, we restrict the velocity range around the centre of the reddest line to $\pm$ 80 km s^{-1}. This excludes the Fe II line, which does not appear in neither transmission spectrum (see Fig. 2.17). For the first time, we detect an additional Mg I line at 5528.40 Å with a 4.5σ significance.

Calcium

We extracted transmission spectra for five Ca I and two Ca II lines. The best Gaussian fit parameters are listed in Table 2.4, while the transmission spectra are shown in Fig. 2.18. We detect for the first time five individual lines of neutral calcium with significance larger than 3σ and with absorption depths of 0.04–0.08% that translate into planetary radii of 1.03–1.06 $R_{\rm p}$. The region around these lines is not affected by other species observed in the atmosphere of KELT-9 b, supporting their identification. This is the first detection of individual Ca I lines in the atmosphere of KELT-9 b, though Ca I has been detected in the atmosphere of KELT-9 b by Borsato et al. (2023) through cross-correlation technique on **HARPS-N** Night 1 and Night 3 data along with two nights obtained with **CARMENES**.

We also detect the Ca II H&K doublet, finding an absorption depth of 0.67$\pm$0.05% and 0.54$\pm$0.06% that translate into planetary radii of 1.42 $R_{\rm p}$ and 1.33 $R_{\rm p}$, respectively. Ca II has been detected by Borsato et al. (2023) and Turner et al. (2020) as well. The Ca II H&K lines have been identified by Yan et al. (2019) using both cross-correlation and single line analysis. Yan et al. (2019) reports a combined H&K line depth of 0.78$\pm$0.04 % corresponding to 1.47$\pm$0.02 $R_{\rm p}$, in agreement with our measurement of the Ca II H line. We already discussed the fact that the Ca II H line is blended with the Hϵ and Fe I lines as shown in Fig. 2.13. However, by choosing a narrower range around the line, we are able to avoid the contamination and perform a Gaussian fit.

Scandium

Singly ionised scandium displays a few strong lines in the **HARPS-N** range, among which we could identify five of them (see Fig. 2.19 and Table 2.4) ranging between 1.06 $R_{\rm p}$ and 1.15 $R_{\rm p}$. Despite ionised scandium was also identified through cross-correlation

by both Hoeijmakers et al. (2019) and Borsato et al. (2023) with high significance ($>5\sigma$ and $>10\sigma$, respectively), this is the first time Sc II individual lines are observed. We also searched for neutral scandium signatures, but we failed to identify any of them, which supports the non-detection by Hoeijmakers et al. (2019) obtained via cross-correlation.

Titanium

Starting from the database, we searched for the strongest Ti lines in the wavelength range we have available. We confidently detected ten Ti II lines with a significance greater than 3σ (Table 2.4). We confirm the previous three Ti II detections made by Cauley et al. (2019) and uncover eleven new ones. Overall, we find an average line depth of $0.14\pm0.03\%$ (corresponding to $\sim$ 1.1 $R_{\rm p}$) and an average **FWHM** of 17.34 ± 4.61 km s^{-1}for the identified Ti II lines, which are comparable to previous results. Individual values for the detection significance, absorption depth, $R_{\rm p}$, **FWHM**, and v_{sys} are reported in Table 2.4 and shown in Fig. 2.20 and Fig. 2.4. To mitigate blending effects and avoid false detections, we excluded from the analysis some Ti II lines that were too close to other lines of different atomic species.

We could not identify Ti I, despite it was tentatively detected by Borsato et al. (2023), but with a low significance ($\sim3\sigma$) even with cross-correlation, hinting to the weakness of the signal. Ti II has been previously detected via cross-correlation by Hoeijmakers et al. (2018, 2019) and Borsato et al. (2023) with a significance of $\sim18\sigma$, $\sim25\sigma$, and $\sim17\sigma$ respectively, supporting our single line detections. We notice a discrepancy between our resulting mean line shift from the zero point and those obtained by Hoeijmakers et al. (2019) and Borsato et al. (2023). We recover a mean velocity shift of-5.19 ± 1.45 km s^{-1}, while they reported systemic velocity values in the-18 to-20 km s^{-1}range. By subtracting the stellar systemic velocity we adopted from their result (-17.74 km s^{-1}), we obtain $v_{\rm sys}$ $\sim$ 0-3 km s^{-1}and hence a difference in retrieved values, which may arise from the different methods and data sets used.

Vanadium

Neither V I nor V II were found by Hoeijmakers et al. (2019), but recently V I was tentatively detected by Borsato et al. (2023) at $\sim3.5\sigma$. We do not detect any V II single lines, but report the possible detection of one V I line at 4379.23 Å (4.3σ), as shown in the tomography and in the transmission spectrum in Fig. 2.21. In a 2 Å range around the line of interest, we do not find possible contaminating species, supporting the detection of V I in the atmosphere of KELT-9 b.

Chromium

Ionised chromium was successfully observed in previous studies in the atmosphere of KELT-9 b via cross-correlation (Hoeijmakers et al. 2019; Borsato et al. 2023) with high statistical significance ($>7\sigma$). Neutral chromium was also detected at more than 5σ by Borsato et al. (2023), while Hoeijmakers et al. (2019) only report a tentative detection. Our single line analysis reveals for the first time four Cr II lines with a significance

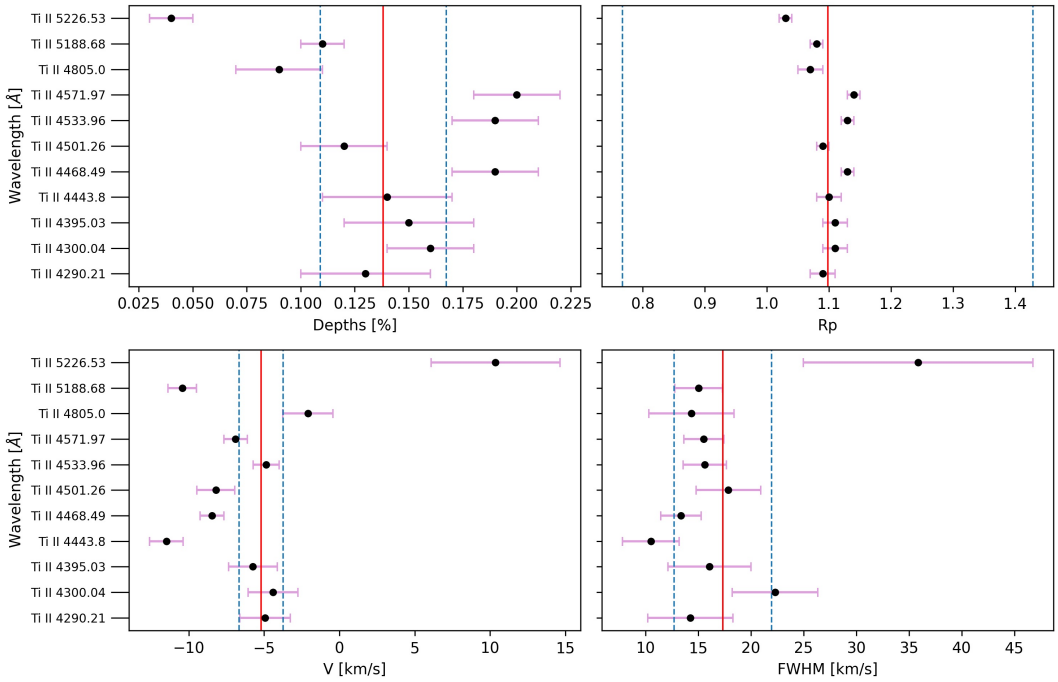

Figure 2.4: Best fit parameters for each TiII lines. The red and dashed blue lines represent respectively the mean and its uncertainty.

larger than 3σ (see Fig. 2.22 and Table 2.4). Despite being detected by Borsato et al. (2023) via cross-correlation, we did not detect any neutral chromium line due to the weakness of the features.

Iron

Iron is the chemical species that displays the most lines in the optical range and thus it has always been an ideal target for cross-correlation analysis. We focused mainly on Fe I and Fe II, which have been detected both via cross-correlation (Hoeijmakers et al. 2018, 2019; Borsato et al. 2023) and single line analysis (Cauley et al. 2019), detecting 10 Fe I and 25 Fe II lines. We also conducted an investigation into the presence of lines corresponding to Fe III, Fe IV and Fe V, however, no detections were made in these cases. From Fig. 2.5 and 2.6, we can see that Fe I lines are on average shallower and more narrow than Fe II lines. The velocity shift values of the Fe I lines are in agreement among them, except for a few isolated points (which are still within 2σ). Instead, Fe II lines present a larger scatter in velocity shifts. The Fe I and Fe II spectra are shown in Fig. 2.23 and Fig. 2.24, while the best fit parameters are shown in Fig. 2.5 and Fig. 2.6.

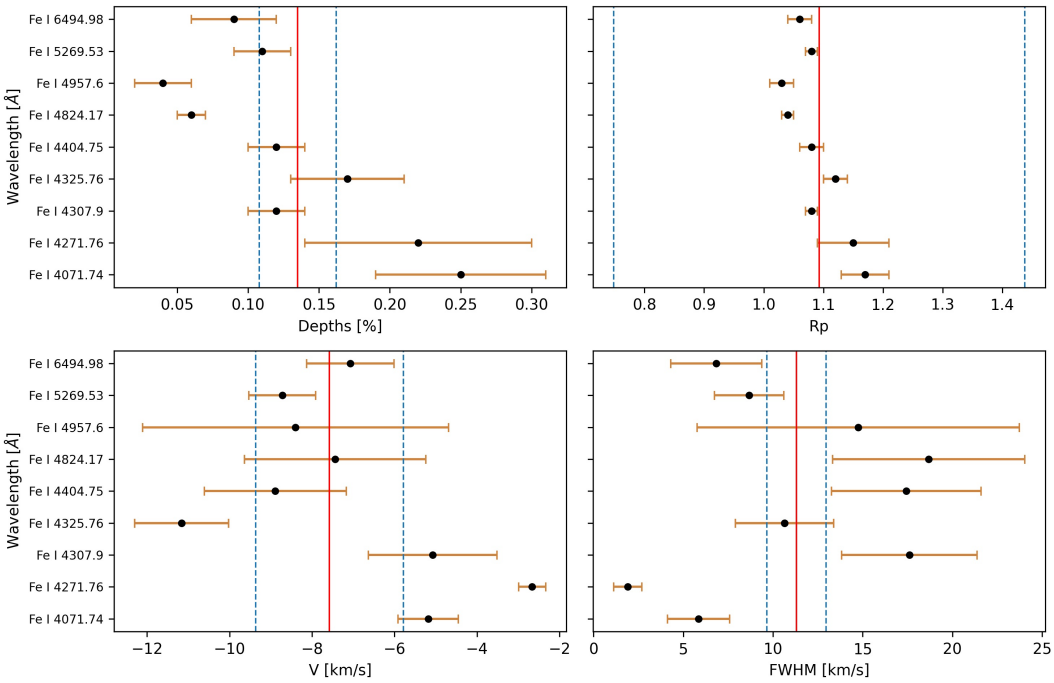

Figure 2.5: Same as Fig. 2.4, but for Fe I.

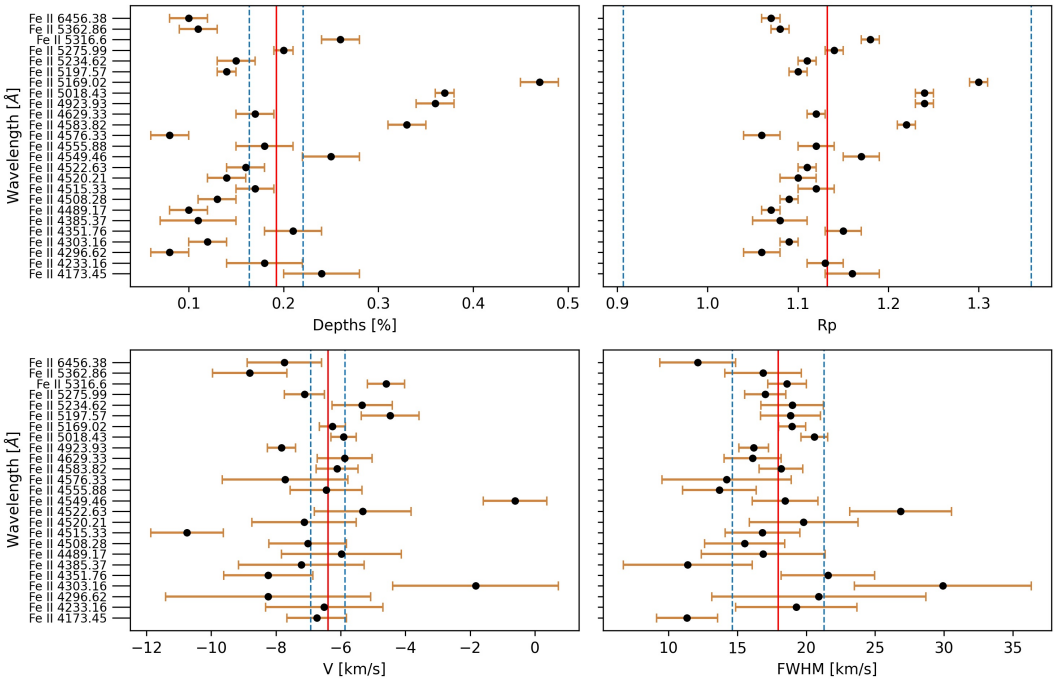

Figure 2.6: Same as Fig. 2.4, but for Fe II.

Table 2.5: Summary of the results obtained from the Gaussian fits to the detected iron lines.

	Gaussian fit					**NLTE** model		
Line [a]	Depth [%]	R_p	**FWHM** [km s^{-1}]	v [km s^{-1}]	χ^2_{red}	ν_{mic} [km s^{-1}]	ν_{mac} [km s^{-1}]	χ^2_{red}
Fe I 4071.74	0.25 ± 0.06	1.17 ± 0.04	5.86 ± 1.73	-5.18 ± 0.73	1.09	4.0 ± 1.9	1 ± 15	1.12
Fe I 4271.76	0.22 ± 0.08	1.15 ± 0.06	1.91 ± 0.79	-2.66 ± 0.33	0.84	1.0 ± 0.8	7 ± 17	0.86
Fe I 4307.9	0.12 ± 0.02	1.08 ± 0.01	17.6 ± 3.79	-5.07 ± 1.56	0.59	1.0 ± 2.4	1 ± 13	0.57
Fe I 4325.76	0.17 ± 0.04	1.12 ± 0.02	-10.65 ± 2.74	-11.16 ± 1.14	0.8	1.0 ± 0.4	2 ± 11	0.92
Fe I 4404.75	0.12 ± 0.02	1.08 ± 0.02	17.43 ± 4.17	-8.89 ± 1.72	0.81	2.0 ± 1.0	1 ± 11	0.83
Fe I 4824.17 [b]	0.06 ± 0.01	1.04 ± 0.01	18.67 ± 5.36	-7.44 ± 2.2	0.52	1.0 ± 0.8	11 ± 13	0.52
Fe I 4957.6	0.04 ± 0.02	1.03 ± 0.02	14.75 ± 8.97	-8.4 ± 3.71	0.95	1.0 ± 0.1	1 ± 21	1.01
Fe I 5269.53	0.11 ± 0.02	1.08 ± 0.01	8.67 ± 1.93	-8.72 ± 0.81	0.7	1.0 ± 0.6	5 ± 7	0.66
Fe I 5328.03 [a]	0.05 ± 0.01	1.03 ± 0.01	31.75 ± 8.72	-9.46 ± 3.46	0.57	14.0 ± 10.1	24 ± 16	0.59
Fe I 6494.98	0.09 ± 0.03	1.06 ± 0.02	6.83 ± 2.52	-7.07 ± 1.06	0.7	1.0 ± 0.2	16 ± 15	0.78
Fe II 4173.45	0.24 ± 0.04	1.16 ± 0.03	11.35 ± 2.21	-6.74 ± 0.92	1.03	2.0 ± 1.2	1 ± 9	1.1
Fe II 4233.16	0.18 ± 0.04	1.13 ± 0.02	19.28 ± 4.41	-6.51 ± 1.81	1.52	1.0 ± 1.1	3 ± 10	1.54
Fe II 4296.62	0.08 ± 0.02	1.06 ± 0.02	20.93 ± 7.75	-8.24 ± 3.16	0.87	3.0 ± 3.5	21 ± 10	0.85
Fe II 4303.16	0.12 ± 0.02	1.09 ± 0.01	29.9 ± 6.41	-1.83 ± 2.56	0.97	3.0 ± 1.9	24 ± 8	1.02
Fe II 4351.76	0.21 ± 0.03	1.15 ± 0.02	21.58 ± 3.4	-8.24 ± 1.39	0.89	2.0 ± 1.0	9 ± 9	0.92
Fe II 4385.37	0.11 ± 0.04	1.08 ± 0.03	11.4 ± 4.67	-7.22 ± 1.94	1.29	3.0 ± 0.4	22 ± 7	1.35
Fe II 4489.17	0.1 ± 0.02	1.07 ± 0.01	16.88 ± 4.49	-5.98 ± 1.85	0.79	1.0 ± 1.1	4 ± 15	0.79
Fe II 4508.28	0.13 ± 0.02	1.09 ± 0.01	15.54 ± 2.91	-7.02 ± 1.2	0.68	1.0 ± 0.9	1 ± 9	0.68
Fe II 4515.33	0.17 ± 0.02	1.12 ± 0.02	16.82 ± 2.71	-10.75 ± 1.12	1.0	3.0 ± 1.3	2 ± 11	1.01
Fe II 4520.21	0.14 ± 0.02	1.1 ± 0.02	19.82 ± 3.94	-7.13 ± 1.61	1.11	1.0 ± 1.6	4 ± 12	1.16
Fe II 4522.63	0.16 ± 0.02	1.11 ± 0.01	26.84 ± 3.69	-5.32 ± 1.49	0.95	4.0 ± 0.8	20 ± 5	0.95
Fe II 4549.46	0.25 ± 0.03	1.17 ± 0.02	18.47 ± 2.38	-0.61 ± 0.98	1.42	4.0 ± 0.4	4 ± 6	1.34
Fe II 4555.88	0.18 ± 0.03	1.12 ± 0.02	13.69 ± 2.67	-6.45 ± 1.11	1.27	2.0 ± 1.3	7 ± 7	1.28
Fe II 4576.33	0.08 ± 0.02	1.06 ± 0.02	14.21 ± 4.68	-7.72 ± 1.94	0.88	1.0 ± 0.7	1 ± 9	0.85
Fe II 4583.82	0.33 ± 0.02	1.22 ± 0.01	18.17 ± 1.58	-6.11 ± 0.65	1.17	4.0 ± 2.9	6 ± 5	1.24
Fe II 4629.33	0.17 ± 0.02	1.12 ± 0.01	16.1 ± 2.07	-5.88 ± 0.85	0.64	3.0 ± 1.0	10 ± 8	0.64
Fe II 4923.93	0.36 ± 0.02	1.24 ± 0.01	16.19 ± 1.07	-7.83 ± 0.44	0.96	3.0 ± 1.0	1 ± 4	1.0
Fe II 5018.43	0.37 ± 0.01	1.24 ± 0.01	20.6 ± 0.96	-5.91 ± 0.39	0.63	4.0 ± 0.5	11 ± 4	0.87
Fe II 5169.02	0.47 ± 0.02	1.3 ± 0.01	19.44 ± 1.11	-24.11 ± 0.45	1.56	4.0 ± 0.4	1 ± 3	1.66
Fe II 5197.57	0.14 ± 0.01	1.1 ± 0.01	18.86 ± 2.17	-4.47 ± 0.89	0.54	1.0 ± 1.2	9 ± 6	0.57
Fe II 5234.62	0.15 ± 0.02	1.11 ± 0.01	18.98 ± 2.26	-5.34 ± 0.93	0.72	2.0 ± 1.2	8 ± 6	0.72
Fe II 5275.99	0.2 ± 0.01	1.14 ± 0.01	17.02 ± 1.5	-7.12 ± 0.62	0.62	3.0 ± 0.4	3 ± 7	0.63
Fe II 5316.6	0.26 ± 0.02	1.18 ± 0.01	18.61 ± 1.39	-4.6 ± 0.57	0.85	4.0 ± 1.7	1 ± 6	0.98
Fe II 5362.86	0.11 ± 0.02	1.08 ± 0.01	16.86 ± 2.78	-8.8 ± 1.15	0.75	14.0 ± 1.4	24 ± 11	0.81
Fe II 6456.38	0.1 ± 0.02	1.07 ± 0.01	-12.13 ± 2.76	-7.74 ± 1.15	0.57	1.0 ± 0.4	1 ± 9	0.6

[a] Fe I line detected by Cauley et al. (2019) that we showed to be Cr II line thanks to the use of the individual **NLTE** models.
[b] Blending between two different lines.

2.1.4 Comparison with NLTE models

The intense ultraviolet (UV) radiation that the planet experiences as a result of the host star's high temperature and close orbital separation leads to significant deviations from **Local Thermal Equilibrium (LTE)** (Fossati et al. 2021). These authors highlighted how the Hα and Hβ transmission spectra are in an excellent match with their models once **NLTE** effects are taken into account in the computation of both the temperature-pressure structure and the transmission spectrum. Hence the observations can be used to further constrain the theoretical models, and thus the physical properties of the exoplanet atmosphere. Furthermore, as Fossati et al. (2021) mentioned, the **NLTE** synthetic transmission spectrum can be used to guide future observations aiming at detecting features in the observed transmission spectrum, as done by Borsa et al. (2021b). **NLTE** synthetic transmission spectra considered in this work and published by Fossati et al. (2021) have been computed using the Cloudy for Exoplanets (CfE) interface, which enables one to use the Cloudy general purpose **NLTE** radiative transfer code for modelling the atmospheric structure of middle and upper planetary atmospheres and generating transmission spectra. All necessary information about CfE, Cloudy, and the **NLTE** models of KELT-9 b can be found in Fossati et al. (2021).

As for the results in Section 2.1.3, we divide our comparison with **NLTE** models in two sections, one for the hydrogen Balmer series and one for the metal lines. Fossati et al. (2021) and Fossati et al. (2020) already compared their **NLTE** models with those obtained by other works detecting Balmer lines mentioned in Section 2.1.3. For the analysis of the detected metal lines, we used the **NLTE** models to support our detections, checking the presence of features in the **NLTE** spectra in the same region where we find an absorption signal in the observed transmission spectrum. To further verify that an observed absorption feature in the **NLTE** spectrum was due to a specific species, we also used **NLTE** models computed accounting only for hydrogen and the specific species considered. Hereafter, we refer to the latter as "individual **NLTE** models", while we call global **NLTE** models, the **NLTE** transmission spectrum computed accounting for all species.

Then, we carried out an analysis similar to Borsa et al. (2021b), where we used different microturbulence (ν_{mic}; velocity of gas on a scale smaller than the pressure scale height, implemented by adding it in quadrature to the thermal velocity) and macroturbulence (ν_{mac}; velocity of gas on a scale larger than the pressure scale height) velocity values to account for any additional line broadening. We created a grid of models with different ν_{mic} values ranging between 1 and 14 km s^{-1}(in steps of 1 km s^{-1}), and for each model, we convolved the transmission spectrum with: i) the rotational profile of the annulus representing the atmosphere (as done by Brogi et al. 2016), ii) a step function to include the broadening due to exposure time (with a size of 4.7 km s^{-1}, retrieved from the in-transit mean exposure time of 404 s) and, iii) a Gaussian kernel with a **FWHM** equal to a ν_{mac} broadening between 1 and 25 km s^{-1}, in steps of 1 km s^{-1}. We then selected the ν_{mic}–ν_{mac} pair that minimises the χ^2. To this end, for each spectral feature, we shifted the **NLTE** synthetic spectrum to match the centers of the observed lines. This is necessary because, when generating spectra, the Cloudy code (used to generate

the **NLTE** spectra; Ferland et al. 2017) does not locate spectral lines at the expected wavelength, but at the center of the spectral bin in which the line falls, which thus depends on the spectral resolution used to compute the synthetic spectra. This is why the **NLTE** synthetic spectrum cannot be used to derive line shifts from the observations. We remark that this coarse placement of the spectral lines impacts exclusively the computation of the output spectra and not the **NLTE** radiative transfer, which is instead computed considering the actual line wavelengths. Before the comparisons all the models are normalised by dividing for a fitted continuum in a small range around the line. The best fitting **NLTE** synthetic spectra for each line are shown along with the observed transmission spectra and Gaussian fits from Fig. 2.3 to 2.24. The best ν_{mic}–ν_{mac} values along with the $\chi^2_{\rm red}$ values are listed in Table 2.3. We stress that the $\chi^2_{\rm red}$ values that we report in Table 2.3, Table 2.4 and Table 2.5 may be underestimated due to the search of the ν_{mic}–ν_{mac} models that minimize the $\chi^2_{\rm red}$.

Hydrogen Balmer Series

Fossati et al. (2021) already presented a comparison between their **NLTE** and **LTE** synthetic spectra for Hα and Hβ and the transmission spectra presented by Yan & Henning (2018), Turner et al. (2020), Cauley et al. (2019) and Wyttenbach et al. (2020), noticing a good χ^2 agreement, and that the **NLTE** synthetic transmission spectrum fits significantly better the observations compared to the **LTE** model. We extended their comparison for Hα and Hβ to our results including the other Balmer lines detected. The $\chi^2_{\rm red}$ reported in Table 2.3 suggests that **NLTE** models are in good agreement with our results: Hα and Hβ $\chi^2_{\rm red}$ values are compatible with the ones listed in Fossati et al. (2021) and all the values are below 1 except for Hζ . This discrepancy may be explained by the large S/N of the observations in that spectral region that gives rise to normalisation problems. However, despite the low $\chi^2_{\rm red}$, the **NLTE** model predicts the existence of the Hζ line supporting our detection.

Metals

For the analysis of the metal lines, it is important to consider that the **NLTE** models have been computed using solar abundances and that the synthetic transmission spectra have been computed using the sub-stellar temperature-pressure profile, which is probably overestimating the temperature at the terminator region probed by the observations (Fossati et al. 2021). These two effects may lead to discrepancies in the comparison with the observations in terms of depth and shape of the lines.
- **Na**: the Na lines are both predicted by the **NLTE** models, which, however seem to expect deeper lines, possibly due to a different abundance.
- **Mg**: the Mg I triplet b lines detected are predicted by the individual Mg I **NLTE** model, which also confirms the presence of a Mg I line at 5528.40 Å, corroborating our detections. We stress also that the best ν_{mic}–ν_{mac} pair for this single line is in agreement with the ones found for the two reddest lines of the triplet.
- **Ca**: the synthetic **NLTE** spectra predict the existence of both the Ca I lines we detected, although these two lines are just above the 3σ threshold for the detection. The

Ca II H line shows a larger broadening than the Ca II K line as already found by the Gaussian fit with a ν_{mic} of 8 km s^{-1}and 4 km s^{-1}, respectively.
- **Sc**: the comparison with **NLTE** models and the use of the individual species is particularly important for species like Scandium that have never been detected via single line analysis and that could be confused for other lines. In our case, the global **NLTE** model predicts the existence of all detected Sc II lines, but individual models show that the 5657 Å and 5684 Å lines might be blended with other weaker lines, respectively a close Sc II and Na I, with the latter line not detected in the atmosphere of KELT-9 b.
- **Ti**: None of the detected lines are predicted by the individual Ti II **NLTE** models, while few of them may originate by the contamination of other species predicted by the global **NLTE** model. For the lines where the global **NLTE** model does not predict the existence of any feature due to other species, we checked the presence of other lines of species detected in the **Vienna Atomic Line Database (VALD3)** database (Piskunov et al. 1995), which is more complete compared to **NIST**. We conclude that the detected features may be due to ionized titanium, which has been detected via single line analysis and cross correlation by Hoeijmakers et al. (2018, 2019) and Borsato et al. (2023).
- **V**: neither the global nor the individual **NLTE** models predict the presence of the V I line at 4379.23 Å that we tentatively detected. The line is present in the **NIST** database and the reason why the **NLTE** model does not predict it may be related to the solar abundance adopted by the model or by the assumption on the temperature profile at the terminator region.
- **Cr**: as for Scandium, the comparison with the **NLTE** model is particularly useful for the identification and detection of Chromium lines; the individual Cr II synthetic spectrum predicts the existence of all detected lines showing also the blending with weaker lines (at 4558.64 Å and 4618.8 Å) that seems not to affect our detections. Also in this case, the individual **NLTE** model does not forecast the presence of any of the Cr I features, supporting our non-detection.
- **Fe**: the synthetic **NLTE** models predict the presence of the detected Fe I lines, except for the line at 4824.17 Å previously detected by Cauley et al. (2019), which is instead due to Cr II. The large **FWHM** obtained for the line at 5328.03 Å is due to blending with two Fe I lines, while the analysis of the 5269.53 Å line shows the presence of a strong nearby Ca I line. Overall, we report a good match between our Fe II detections and the theoretical **NLTE** model. We remark that the Fe II lines at 5316.6 Å and 4351.76 Å might be affected by blending.

2.1.5 Discussion

The large amount of single lines detected allows us to better constrain the behaviour of KELT-9 b atmosphere. In the analyses discussed below, we excluded the lines with large **FWHM** that the comparison with **NLTE** models proved to be blended with other lines. By coupling the depth of the line with the altitude at which it forms, we are able to construct a map of the species detected as a function of altitude. Our observations allow us to probe the atmosphere up to 1.5 $R_{\rm p}$, which is still well below the Roche Lobe (1.95$R_{\rm p}$). In the upper atmospheric layers, $\sim$1.25 $R_{\rm p}$, neutral Hydrogen and Ca II H&K

form, while ionised iron forms below, extending down to 1.1-1.0 R_p, where it mixes with neutral Fe. Just below 1.2 R_p we find Ti II, while between 1.10 and 1.04 we find scandium and Cr II. Neutral calcium is the species that forms deeper in the atmosphere, just above 1.03 R_p. Using the temperature-radius profile from Fossati et al. (2021), we can couple the heights that we retrieved from the Gaussian fits with the modelled atmospheric temperature obtained accounting for **NLTE** effects, as shown in Fig. 2.7. We find that, in the upper atmosphere, H I Balmer lines form at a temperature higher than 7500 K, while Ca II lies above 8200 K. Slightly below 1.3 R_p, we find Fe II ranging from 5000 K to 8000 K. Ti II and Fe I show a common range in height corresponding to a temperature of 4800–6600 K. Sc II and Mg I lie between 5000 K and 6000 K, while Ca I and Cr II, which lie lower in the atmosphere, have temperatures below 5000 K.
The **NLTE** models predicted number densities for each neutral and ionised species support our detections. As a matter of fact, the general trend is that ionised species have higher abundances compared to the neutral ones (see Fig. 2.8), corroborating the detection of Sc II, Ti II and Cr II. We are not able to find ionised magnesium due to the lack of strong lines in the **HARPS-N** wavelength range, while for Ca and Fe we detect both the neutral and the ionised lines, probably because of their higher abundance compared to the elements for which we find only ionised species.

Fig. 2.9 shows the possible relations among our Gaussian best fit parameters. The distribution in height has been already discussed before, but from the histogram we can clearly see how most of the lines detected are below 1.15 planetary radii, while only a few lines of Fe II, Ca II and the Balmer lines lie above. Overall, we find all lines to be blue-shifted, with the distribution peaking around $-6\,\mathrm{km\,s^{-1}}$and ranging from 0 $\mathrm{km\,s^{-1}}$to -11 $\mathrm{km\,s^{-1}}$, except for two points above 0 $\mathrm{km\,s^{-1}}$. We do not find a clear correlation between the velocity shift and the height distribution, suggesting the homogeneous motion of the atmosphere in the probed layers. The systematic blueshift is expected by the presence of night-to-dayside winds to due the fact that we are observing the planet terminator. General circulation models for **Hot Jupiter (HJ)** predicts wind speeds of typically 2–4 $\mathrm{km\,s^{-1}}$, that is slightly smaller than the 6 $\mathrm{km\,s^{-1}}$that we retrieve. The **FWHM** of the lines detected returns a quasi-symmetric distribution peaked at $\sim$20 $\mathrm{km\,s^{-1}}$, with a tail due to the Ca II and H Balmer lines, which have different physical origin since their broadening is mostly due to collisional effects rather than rotational ones.

We focused on the possible correlation between the **FWHM** and the height distribution comparing the line widths and the height distribution in Fig. 2.9 in a similar way as done by Borsa et al. (2021a). We excluded the H I and Ca II lines for the reason explained above. Assuming the planet and its atmosphere rotate as a rigid body with a rotation period equal to 6.6 $\mathrm{km\,s^{-1}}$(tidally locked), we obtain the velocity-radius profile shown by the purple line in the bottom panel of Fig. 2.9. Despite most of our points are at lower radii, our results follow the tidally locked profile, supporting the expectation of tidally locked rotation. In our analysis, we retrieve the **FWHM** from a Gaussian fit. Although this does not take into consideration the fact that during the transit only an annulus is visible, and that another profile would be required (Brogi et al. 2016), we decided to fit

Table 2.6: Mean values of ν_{mic} and ν_{mac} for each species detected.

Species	ν_{mic} [km s^{-1}]	ν_{mac} [km s^{-1}]
H I	3.67 ± 0.93	16.50 ± 4.12
Na I	1.0 ± 0.02	13.0 ± 3.5
Mg I	1.75 ± 0.12	19.50 ± 3.63
Ca I	3.40 ± 0.61	15.6 ± 5.02
Sc II	4.50 ± 0.97	13.0 ± 7.73
Cr II	2.00 ± 0.34	13.0 ± 4.91
Fe I	2.70 ± 1.07	6.90 ± 4.54
Fe II	2.96 ± 0.28	7.92 ± 1.66
All the species [a]	3.03 ± 0.25	10.03 ± 1.43
O I [b]	3.0 ± 0.7	13 ± 5

We excluded from the analysis, the Ti II lines since the **NLTE** models do not predict their presence.

[a] We did not include the H I and Ca II lines since their broadening is mostly due to collisional effects.

[b] Results from Borsa et al. (2021b) with **CARMENES** data.

a Gaussian profile as we aim for a qualitative comparison between the statistics inferred from our results and the expected rotational profile shown in purple in Fig. 2.9.

The impact of **NLTE** effects in the atmosphere of KELT-9 b has already been discussed by various studies (Fossati et al. 2020, 2021), and the inclusion of **NLTE** effects in the modelling scheme has been found to be necessary to reproduce the observations. The key impact of **NLTE** effects in the planetary atmosphere is in the significant increase of the temperature in the middle and upper atmosphere. The overpopulation of Fe II which drives heating, significantly increases the absorption of stellar near-UV radiation, where the host star's spectral energy distribution peaks, further increasing the heating rate. This process leads to the strong temperature inversion that we see in Fig. 2.7.

In summary, we compared our line fitting results to **NLTE** models, finding that the line profiles, including the line depths, are well described by the **NLTE** synthetic spectra. Furthermore, **NLTE** models have played a key role to identify and confirm the single line detections presented here, hinting at the blending of different lines, which allowed us to explain why few lines showed large **FWHM** values. We computed the mean ν_{mic} and ν_{mac} for each species obtaining the results listed in Table 2.6.

Borsa et al. (2021b) found ν_{mic} = 3.0 $\pm$ 0.7 km s^{-1}and ν_{mac} = 13 $\pm$ 5 km s^{-1}analysing the oxygen triplet at about 7770 Å with **CARMENES** data. The mean values of ν_{mic} and ν_{mac} that we retrieve including all the species except for H I, Ca II and Ti II agree with their results. We investigated the possible correlation between ν_{mic} and ν_{mac} and the height distribution, shown in Fig. 2.10, and we did not find any significant correlation.

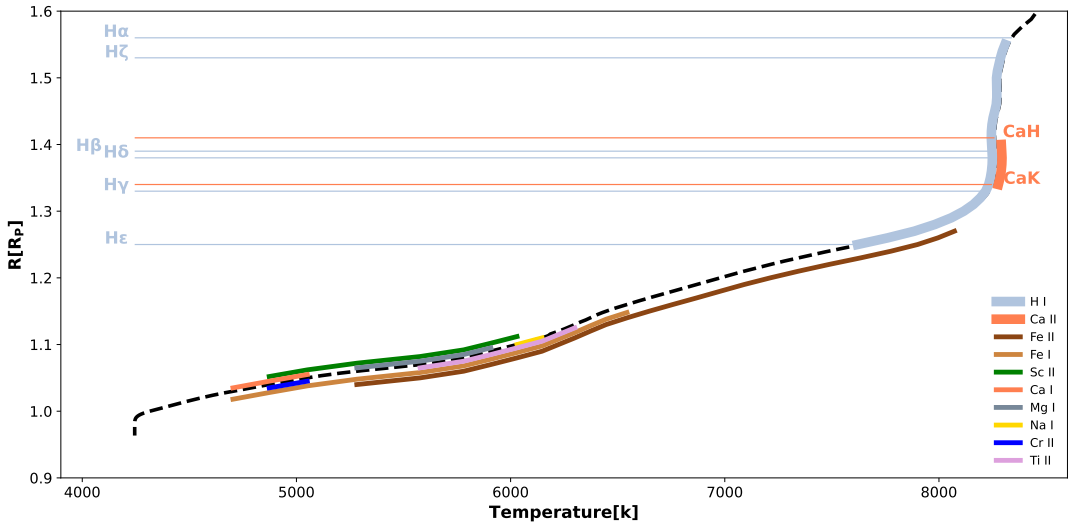

Figure 2.7: Height distribution of chemical species detected expressed in planetary radii as a function of atmospheric temperature. H I and Ca II lie on top, but still well below the Roche (1.95 $R_{\rm p}$). The other metals are distributed at lower altitudes. The black dashed line represents the temperature profile presented by Fossati et al. (2021) accounting for **NLTE** effects. The full lines representing each species height distribution are shifted with respect to the black dashed line for clarity.

We stress that we consider ν_{mic} and ν_{mac} as fudge parameters needed to explain the observed extra-broadening, but they still do not have a well defined physical meaning. The ν_{mic} values, considering their uncertainties, are compatible with zero.

2.1.6 Conclusions

In summary, we analysed six transit observations of the ultra-hot Jupiter KELT-9 b taken with the **HARPS-N** spectrograph mounted at the **TNG**. The elevated temperature of the planet results in the significant extension of the atmosphere and leads to an increase in the signal-to-noise ratio of the data, making it the perfect target for transmission spectroscopy. We employed the single line analysis technique to search for a variety of metal lines across different species, ranging from the lightest elements like hydrogen to the heaviest like iron. Thanks to the strong atmospheric signal due to the combination of six observational nights, we were able to identify 70 individual lines belonging to seven different species, Na I, Ca I, Ca II, Fe I, Fe II, Mg I, Ti II, Sc II and Cr II. This is more than any other study utilising this technique has ever found. Our approach allowed us to confirm previous detections and make new ones, such as the discovery of Hϵ and Hζ that had been deemed only tentative up to now. Hζ displayed a larger depth than expected and we stress that it might be influenced by normalisation problems arising from the low S/N in the bluest part of the wavelength range covered by **HARPS-N**. We also detected Cr II and Sc II single lines for the first time in the atmosphere of

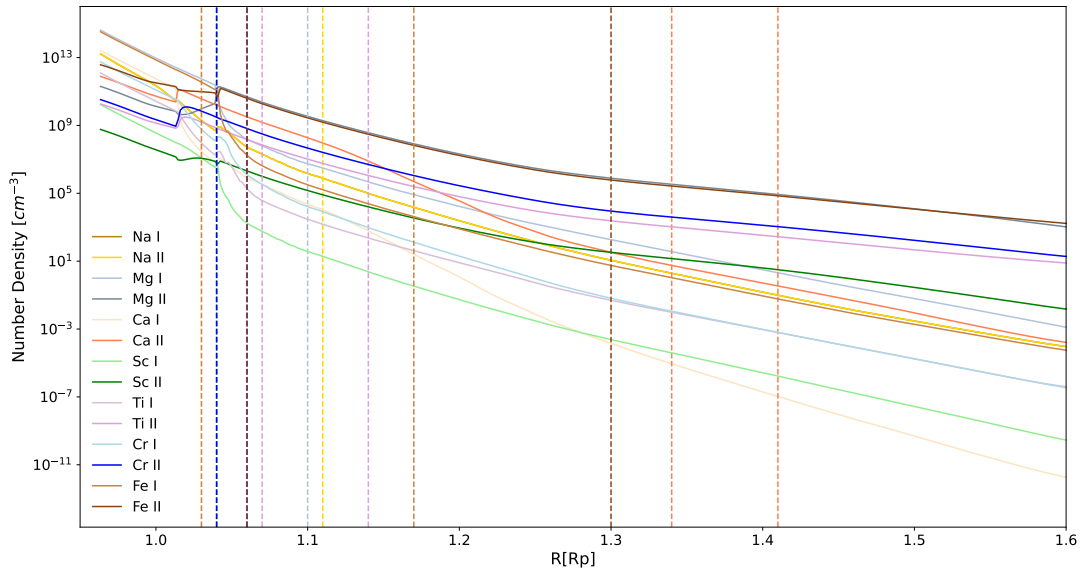

Figure 2.8: Number densities predicted by the **NLTE** model of Fossati et al. (2021) for the detected atoms in neutral and singly ionised form. The dashed lines indicate the height probed by the observations. Generally, the ionised species have higher number densities compared to the neutral ones.

an exoplanet, along with many new lines from already detected species. Among the chemical species that we looked for, we could not find He, Li, Be, K, Sr, Y, Ni, Ba, and Mn single lines. Even though the atmospheric signal is strong, with an average S/N of $\sim$100, one possible reason for these non-detections is the intrinsic weakness of those lines, which might not be sufficient for a single line analysis study.

Single line analysis in transmission proved to be a powerful tool to support and confirm detections made with cross-correlation studies, while delivering important physical information about the width and depth of the lines, which in turn provides clues about the turbulence and the stratification of the atmosphere, in addition to information on the physical and chemical structure of the atmosphere. By juxtaposing our absorption lines with **NLTE** models, we could verify the presence of detected features and distinguish regions where line blending may be occurring. Most of the lines analysed experience a velocity blueshift corroborating the existence of night-to-dayside winds in the atmosphere, especially for the lines forming between 1.07 and 1.20 planetary radii. The rotational velocity and the height distribution generally agree with the hypothesis of a tidally locked rigid rotating body. In conclusion, our study marks a significant contribution to the application of the single line analysis technique: we yielded an unprecedented number of individual lines, detecting many of them for the very first time in an exoplanetary atmosphere. The large number of lines detected allowed us to further corroborate the presence of winds and to clarify the atmospheric stratification of KELT-9 b.

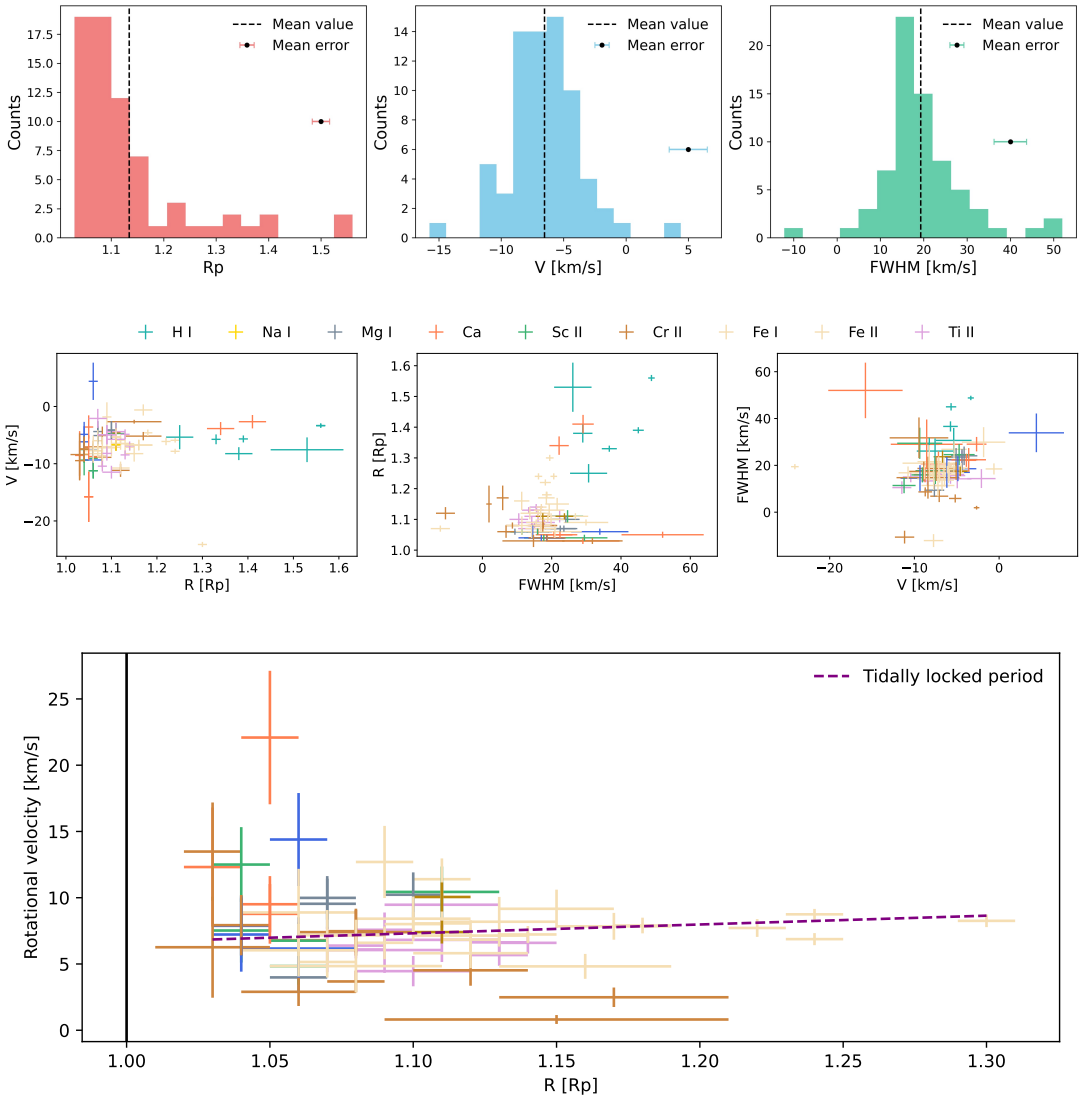

Figure 2.9: Analysis of Gaussian best fit parameters of all detected lines. *Top panel*: histograms of height, velocity, and **FWHM**. *Middle panel*: Relations between velocity, height, and **FWHM**. *Bottom panel*: Rotational velocity against the height in the atmosphere (in planetary radii); the purple dashed line represents the profile expected for the tidally locked scenario, while the black line represents the planetary radius.

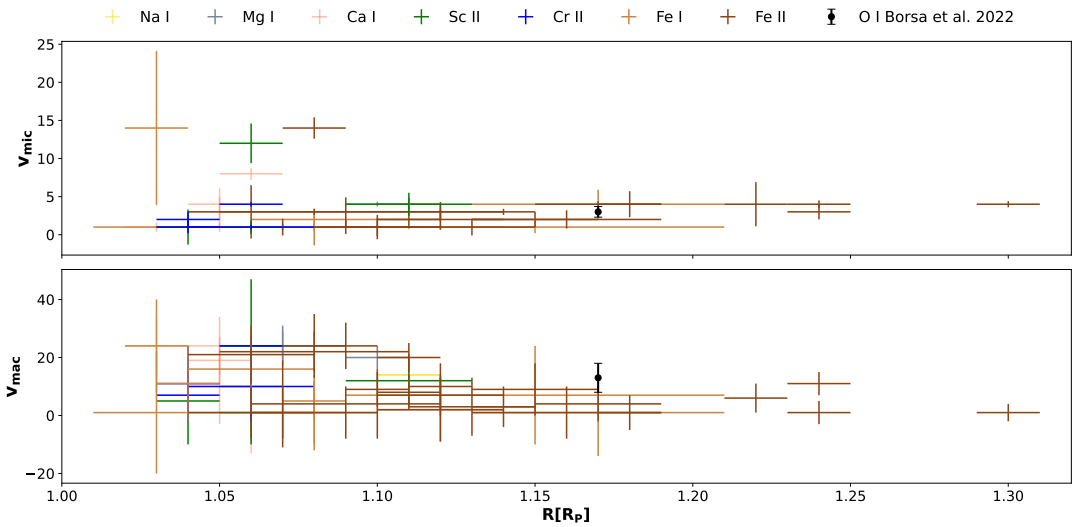

Figure 2.10: Distribution of ν_{mic} and ν_{mac} as a function of the height, for the different species detected. We also report, as comparison, the values retrieved by Borsa et al. (2021b) with **CARMENES** data.

2.1.7 Additional Figures and Tables

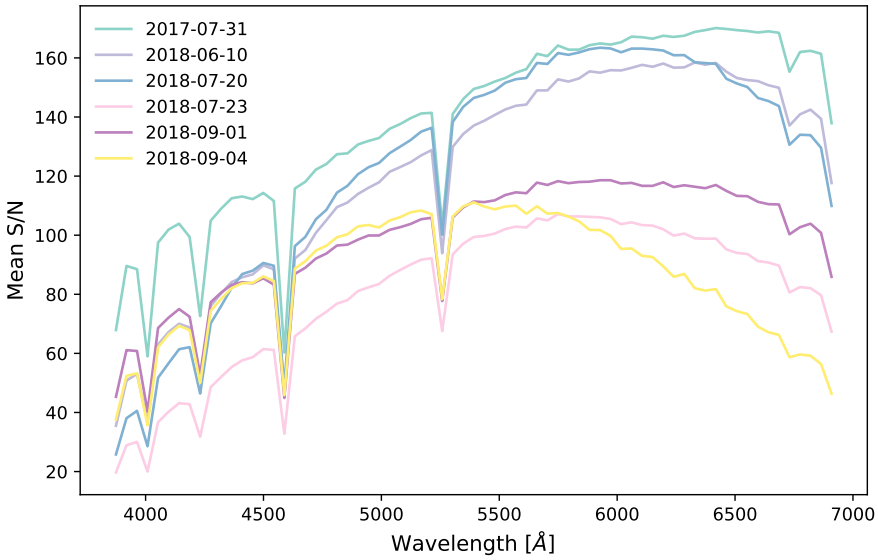

Figure 2.11: Mean S/N as a function of wavelength for each night analysed. Each point in the wavelength axis is referred to the S/N value for each of the 69 **HARPS-N** orders.

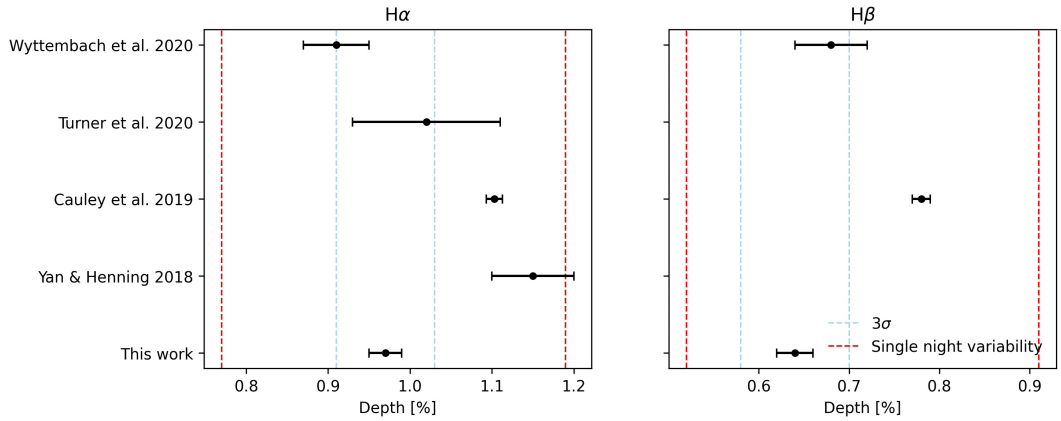

Figure 2.12: Absorption depth comparison with previous detections for Hα and Hβ . The cyan dashed lines represent the 3σ confidence for our results. Hα results are in good agreement with Turner et al. (2020) and Wyttenbach et al. (2020), but at odds with Cauley et al. (2019) and Yan & Henning (2018), while Hβ is in good agreement with Wyttenbach et al. (2020), but not with Cauley et al. (2019). We stress that, apart from Wyttenbach et al. (2020), the other data have been collected with different instruments. The red dashed lines represent the minimum and maximum values retrieved from analysing each night individually (see also Fig. 2.14).

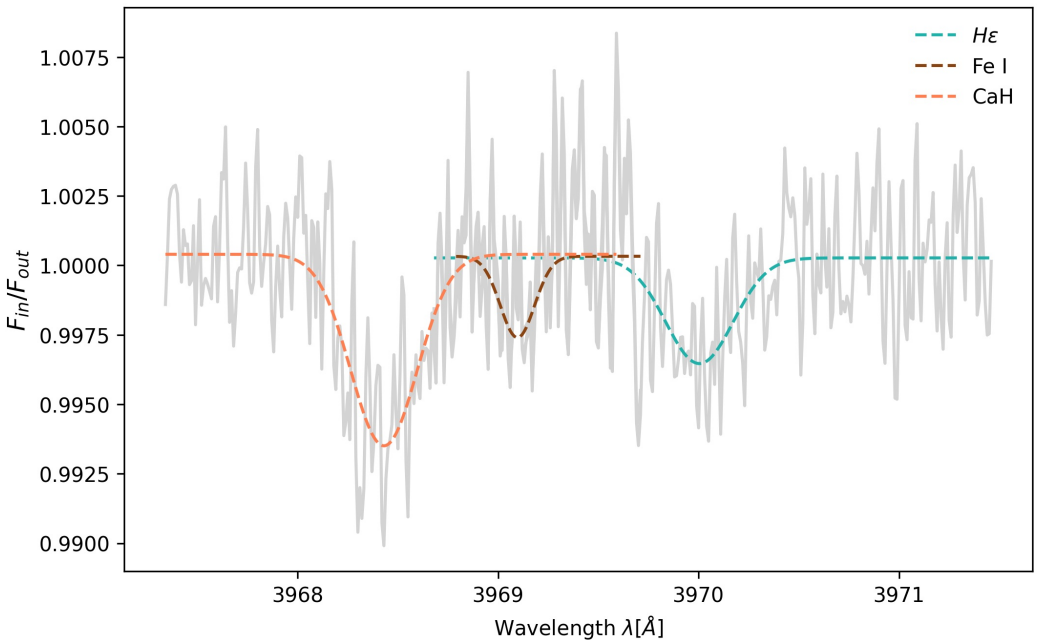

Figure 2.13: Region including Ca II H, Fe I and Hϵ with the corresponding Gaussian fits.

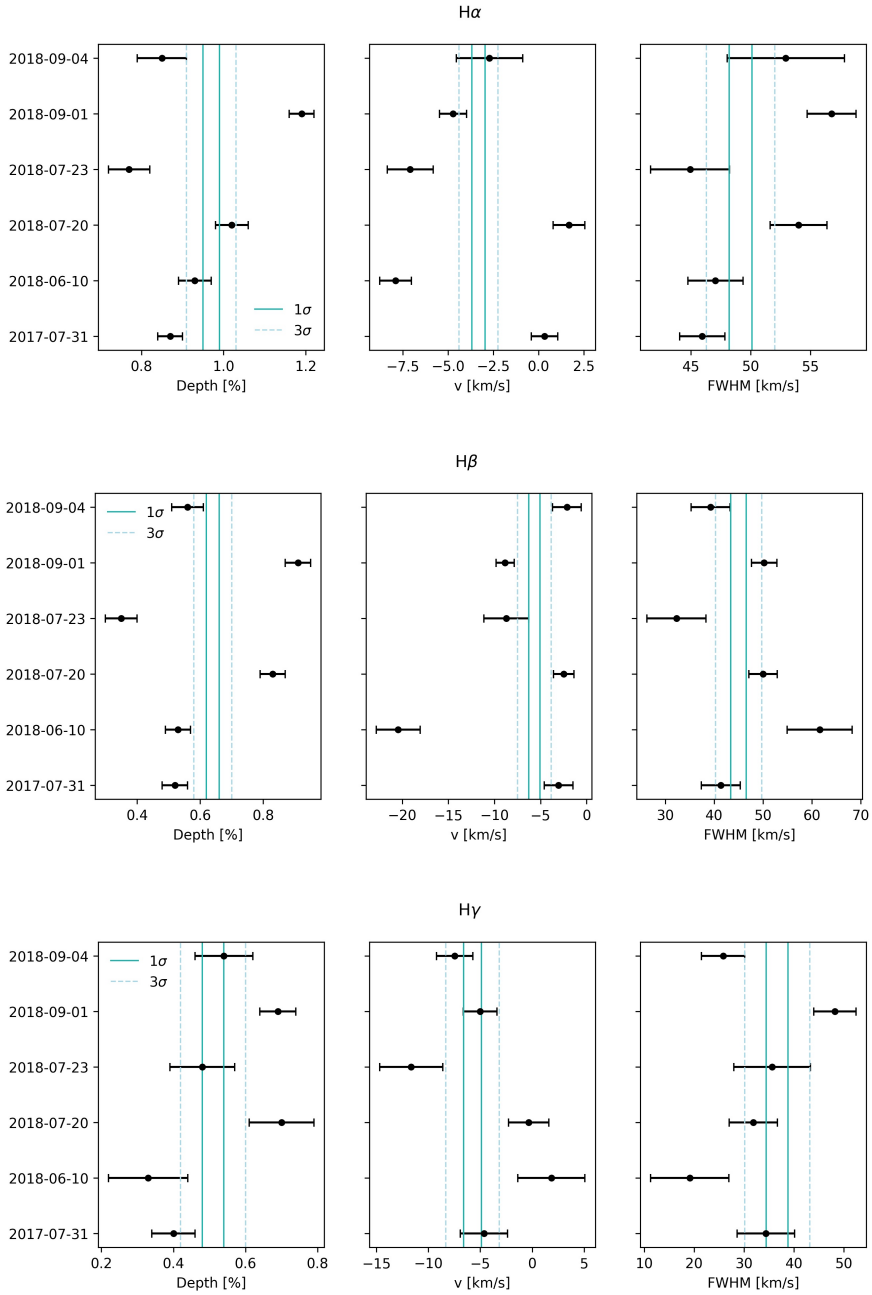

Figure 2.14: Best fit parameters obtained analising each night individually for Hα , Hβ and Hγ . Cyan full and dashed lines represent respectively 1σ and 3σ confidence for the values obtained including all nights. Although single nights results may differ in some cases from those obtained from all nights combined, they are scattered around the expected values. The discrepancy possibly arises from the low signal of the individual nights. We stress that the scale of the nightly variability is larger than the comparison with the other results shown in Fig. 2.12.

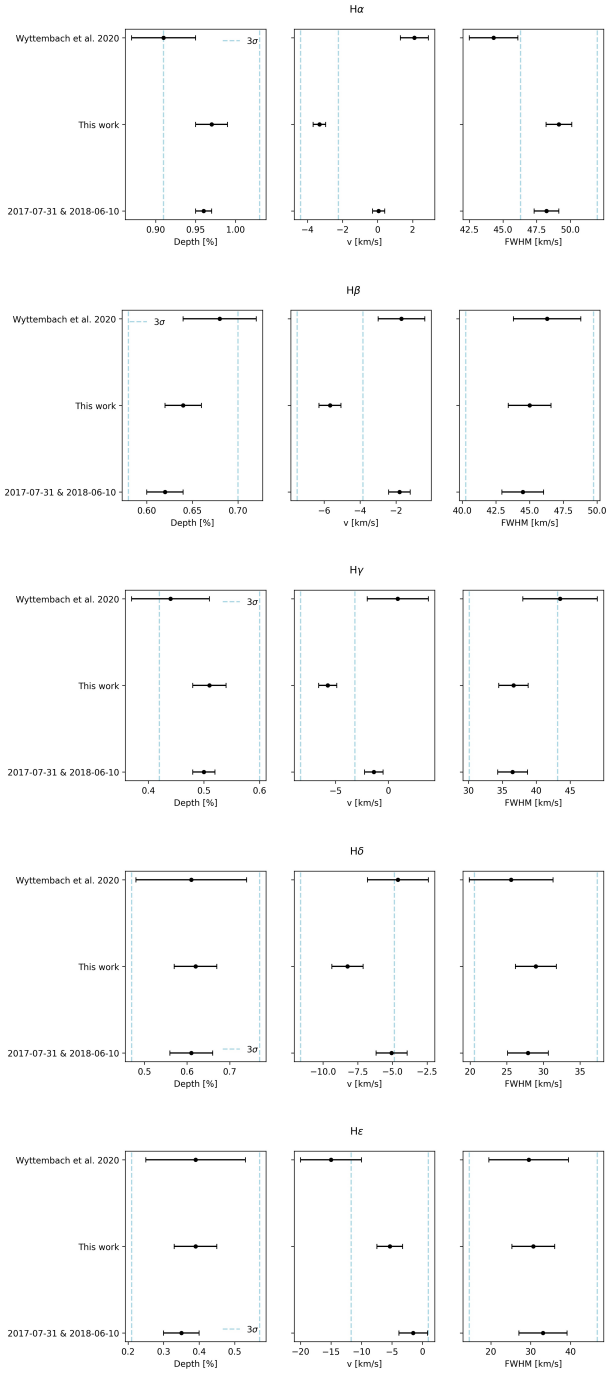

Figure 2.15: Best fit parameters comparison with Wyttenbach et al. (2020). We also show the results obtained with the method used in this work only for the same 2 transit observations used by Wyttenbach et al. (2020). The cyan dashed lines represent the 3σ confidence interval for our results using all the available nights. For all lines, our results are in good agreement with Wyttenbach et al. (2020) except for the velocity shift of Hϵ , which has been only tentatively detected by Wyttenbach et al. (2020).

Table 2.7: Best Gaussian fit parameters for individual analysis of Hα , Hβ and Hγ .

Night	Depth [%]	R_p	**FWHM** [km s^{-1}]	v [km s^{-1}]
Hα				
2017-07-31	0.87 ± 0.03	1.51 ± 0.01	45.94 ± 1.89	0.33 ± 0.73
2018-06-10	0.93 ± 0.04	1.54 ± 0.02	47.04 ± 2.31	-7.9 ± 0.88
2018-07-20	1.02 ± 0.04	1.58 ± 0.02	53.99 ± 2.38	1.69 ± 0.88
2018-07-23	0.77 ± 0.05	1.46 ± 0.02	44.93 ± 3.3	-7.09 ± 1.27
2018-09-01	1.19 ± 0.03	1.66 ± 0.02	56.76 ± 2.05	-4.72 ± 0.75
2018-09-04	0.85 ± 0.06	1.5 ± 0.03	52.93 ± 4.9	-2.71 ± 1.83
Combined	0.97 ± 0.02	1.56 ± 0.01	49.15 ± 0.95	-3.32 ± 0.36
Hβ				
2017-07-31	0.52 ± 0.04	1.33 ± 0.02	41.36 ± 3.99	-3.05 ± 1.55
2018-06-10	0.53 ± 0.04	1.34 ± 0.03	61.62 ± 6.65	-20.44 ± 2.38
2018-07-20	0.83 ± 0.04	1.49 ± 0.02	50.0 ± 2.91	-2.48 ± 1.1
2018-07-23	0.35 ± 0.05	1.23 ± 0.03	32.3 ± 6.05	-8.71 ± 2.42
2018-09-01	0.91 ± 0.04	1.53 ± 0.02	50.24 ± 2.58	-8.85 ± 0.98
2018-09-04	0.56 ± 0.05	1.35 ± 0.03	39.28 ± 3.99	-2.14 ± 1.57
Combined	0.64 ± 0.02	1.39 ± 0.01	45.0 ± 1.58	-5.67 ± 0.61
Hγ				
2017-07-31	0.4 ± 0.06	1.26 ± 0.03	34.38 ± 5.74	-4.64 ± 2.28
2018-06-10	0.33 ± 0.11	1.22 ± 0.07	19.15 ± 7.84	1.86 ± 3.23
2018-07-20	0.7 ± 0.09	1.43 ± 0.05	31.87 ± 4.84	-0.32 ± 1.94
2018-07-23	0.48 ± 0.09	1.31 ± 0.05	35.61 ± 7.68	-11.65 ± 3.04
2018-09-01	0.69 ± 0.05	1.42 ± 0.03	48.19 ± 4.24	-5.0 ± 1.62
2018-09-04	0.54 ± 0.08	1.34 ± 0.04	25.82 ± 4.32	-7.45 ± 1.75
Combined	0.51 ± 0.03	1.33 ± 0.01	36.63 ± 2.17	-5.74 ± 0.86

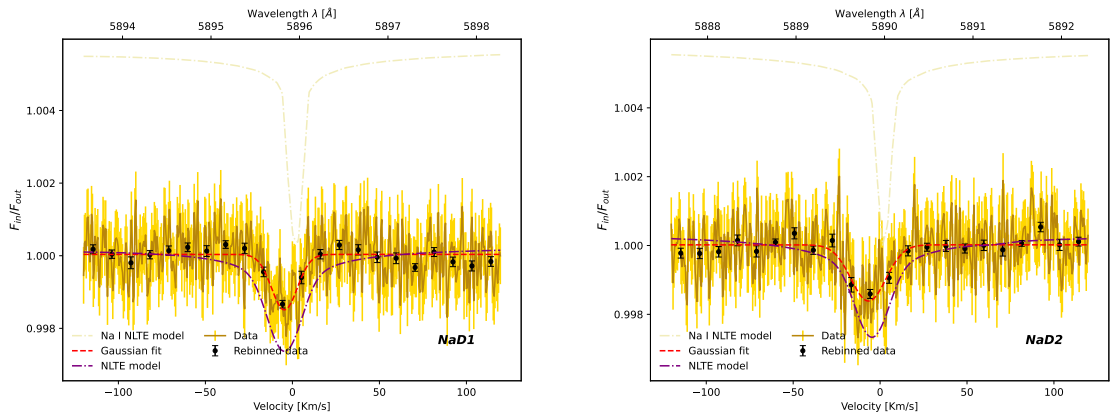

Figure 2.16: Same as Fig. 2.3, but for the neutral sodium doublet. We also show the individual Na I **NLTE** spectrum (computed considering only the H and the Na I species) shifted upwards for clarity and not broadened.

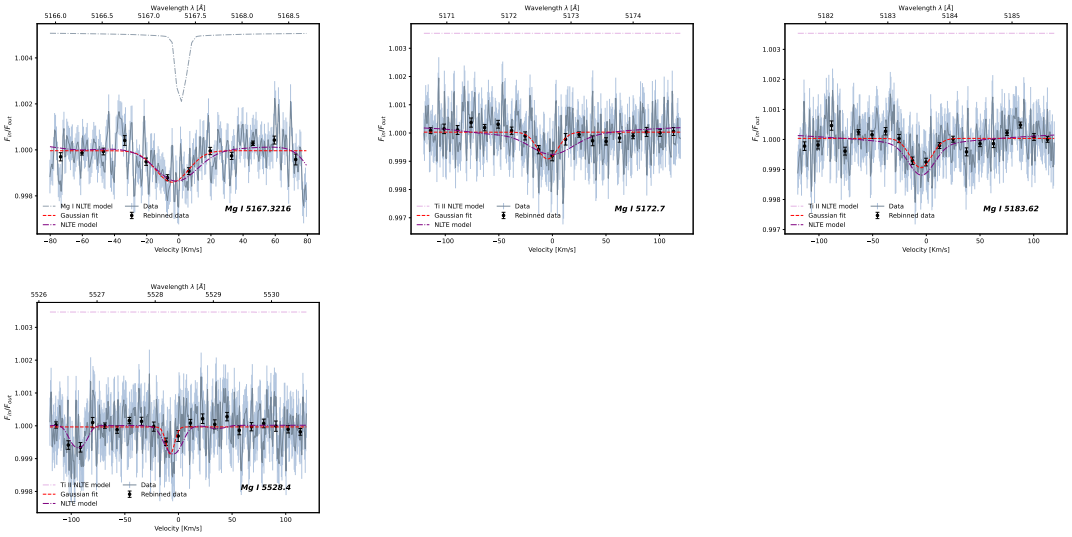

Figure 2.17: Same as Fig. 2.16, but for the Magnesium lines. The top row panels and the bottom left one show the Magnesium triplet lines around 5167-5183 Å, while the bottom right panel shows the Magnesium line detected at 5528.40 Å.

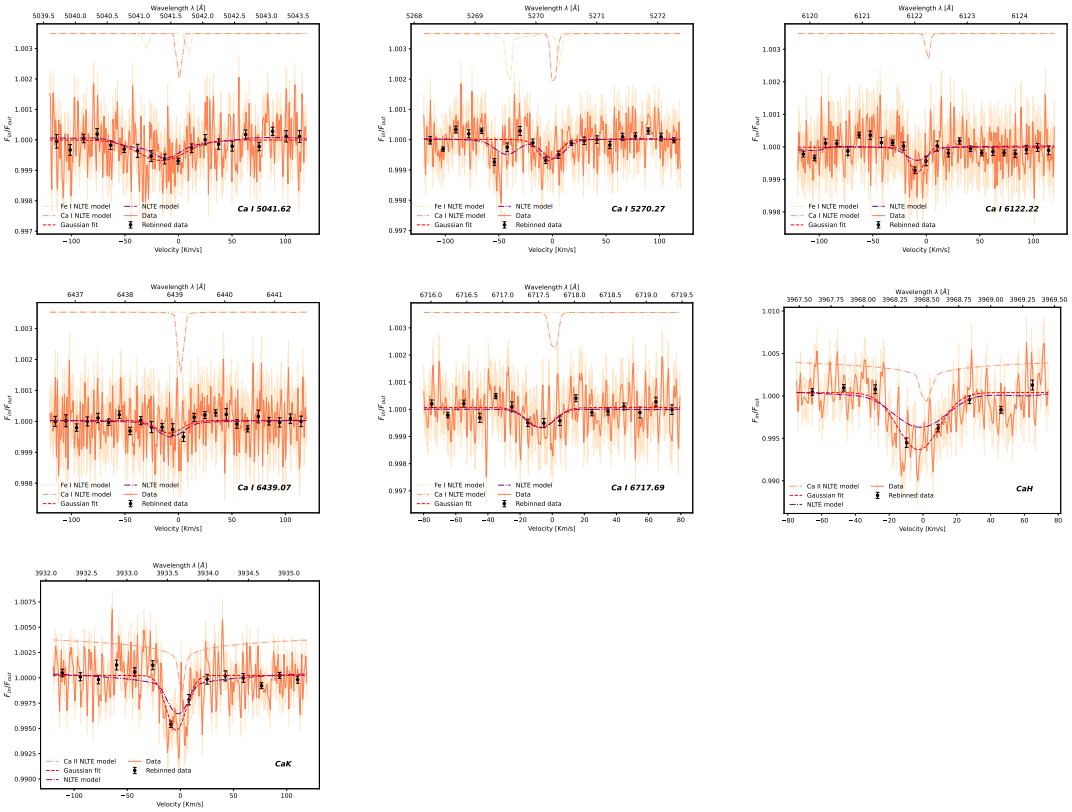

Figure 2.18: Same as Fig. 2.17, but for neutral and ionised calcium lines.

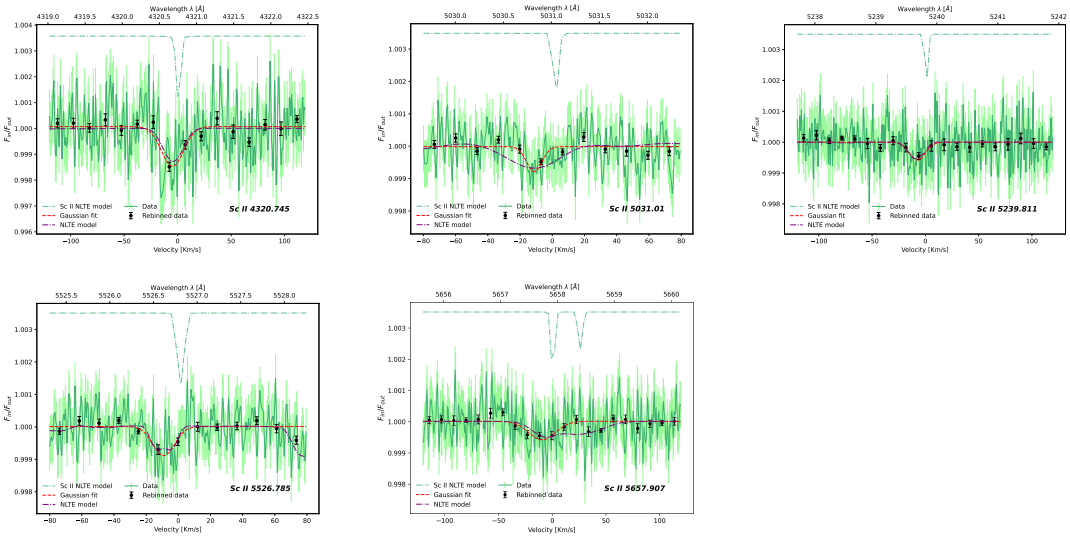

Figure 2.19: Same as Fig. 2.17, but for ionised scandium lines.

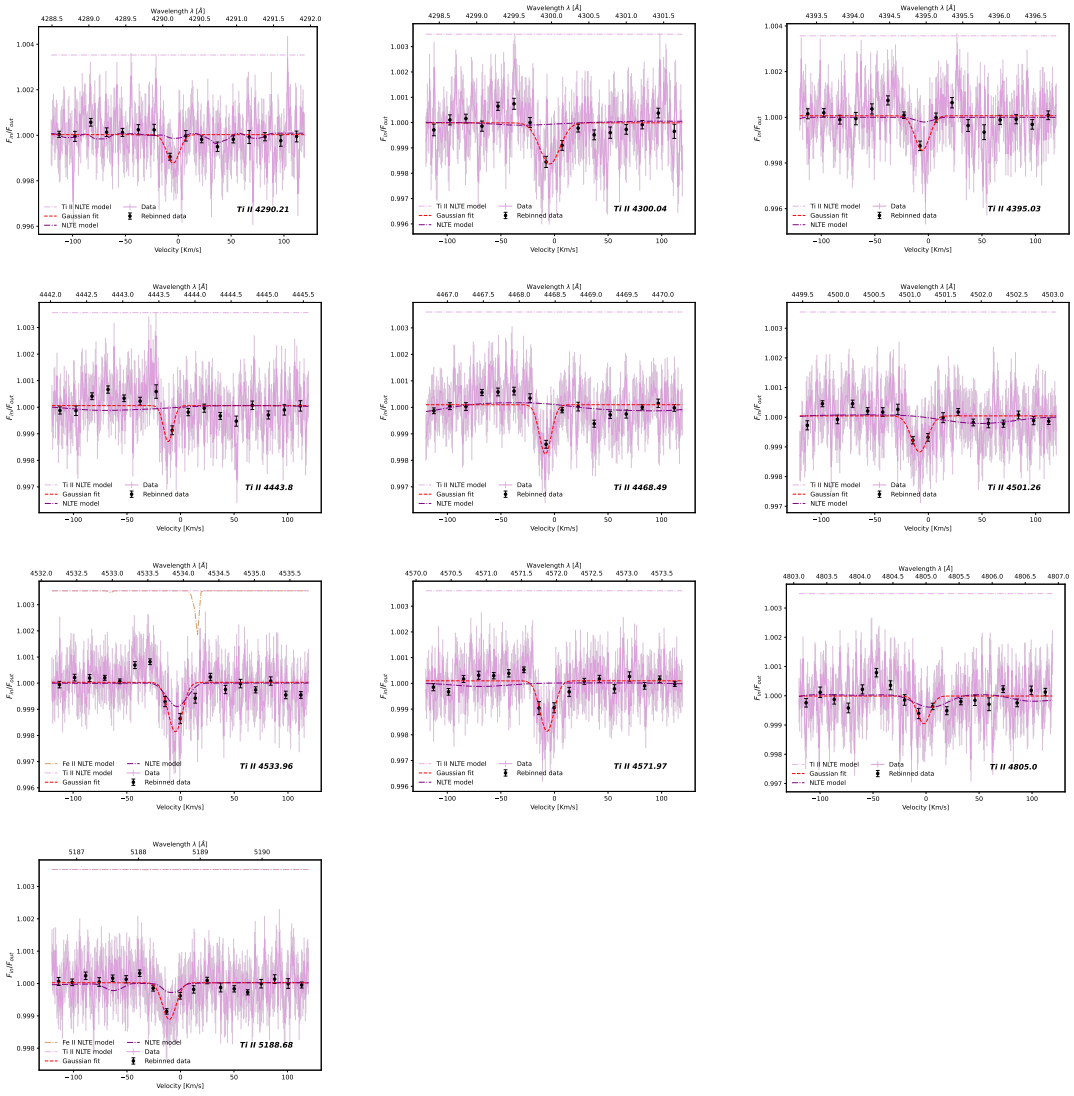

Figure 2.20: Same as Fig. 2.17, but for the Titanium lines detected with significance greater than 3σ.

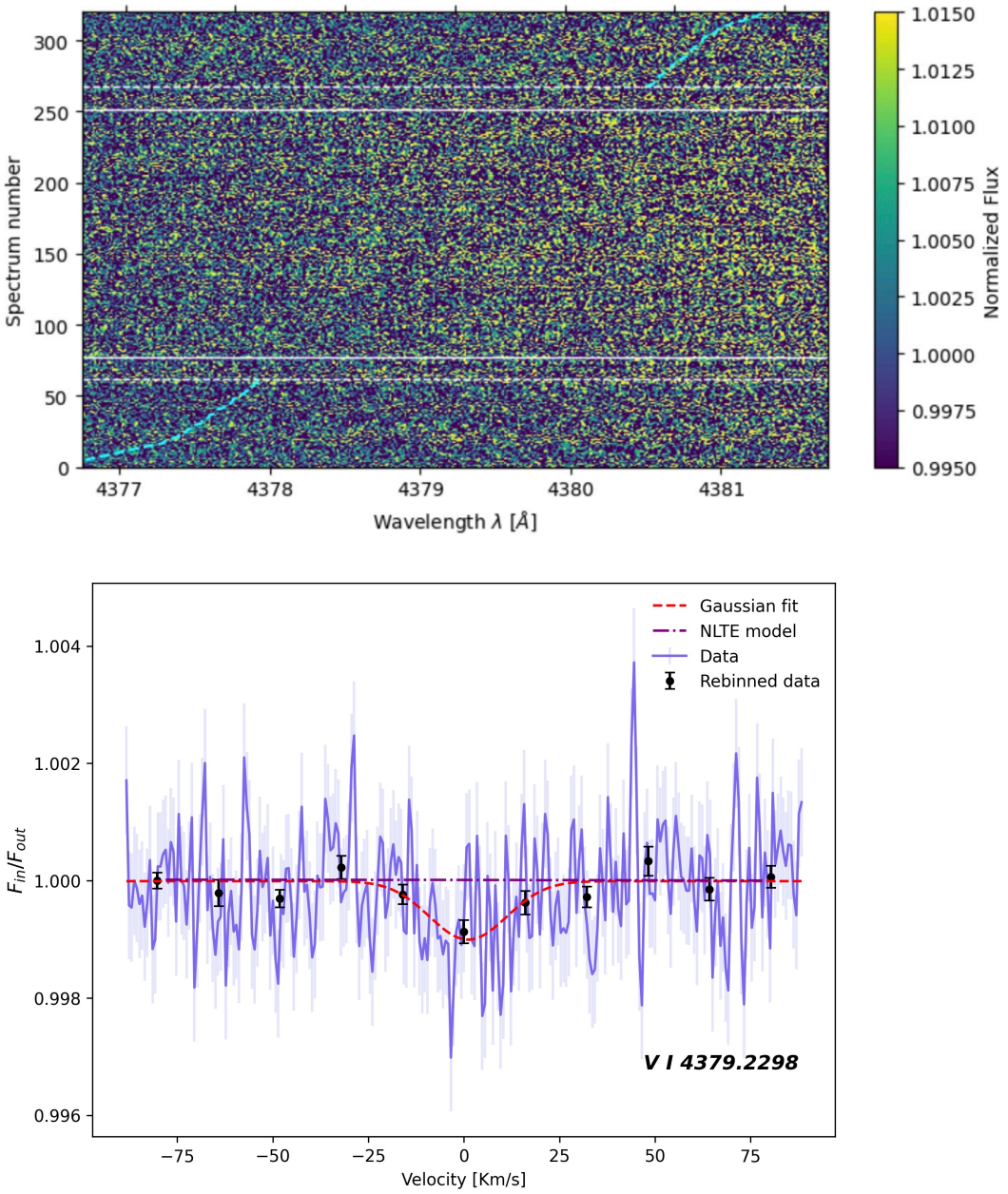

Figure 2.21: Vanadium I tentative detection: star reference frame tomography (left) and transmission spectrum (right).

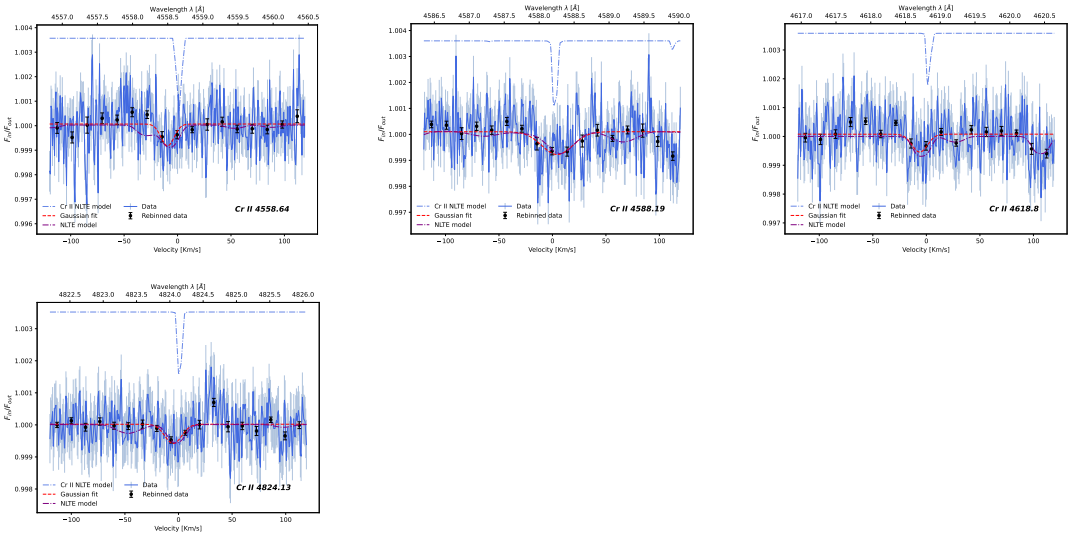

Figure 2.22: Same as Fig. 2.17, but for Chromium.

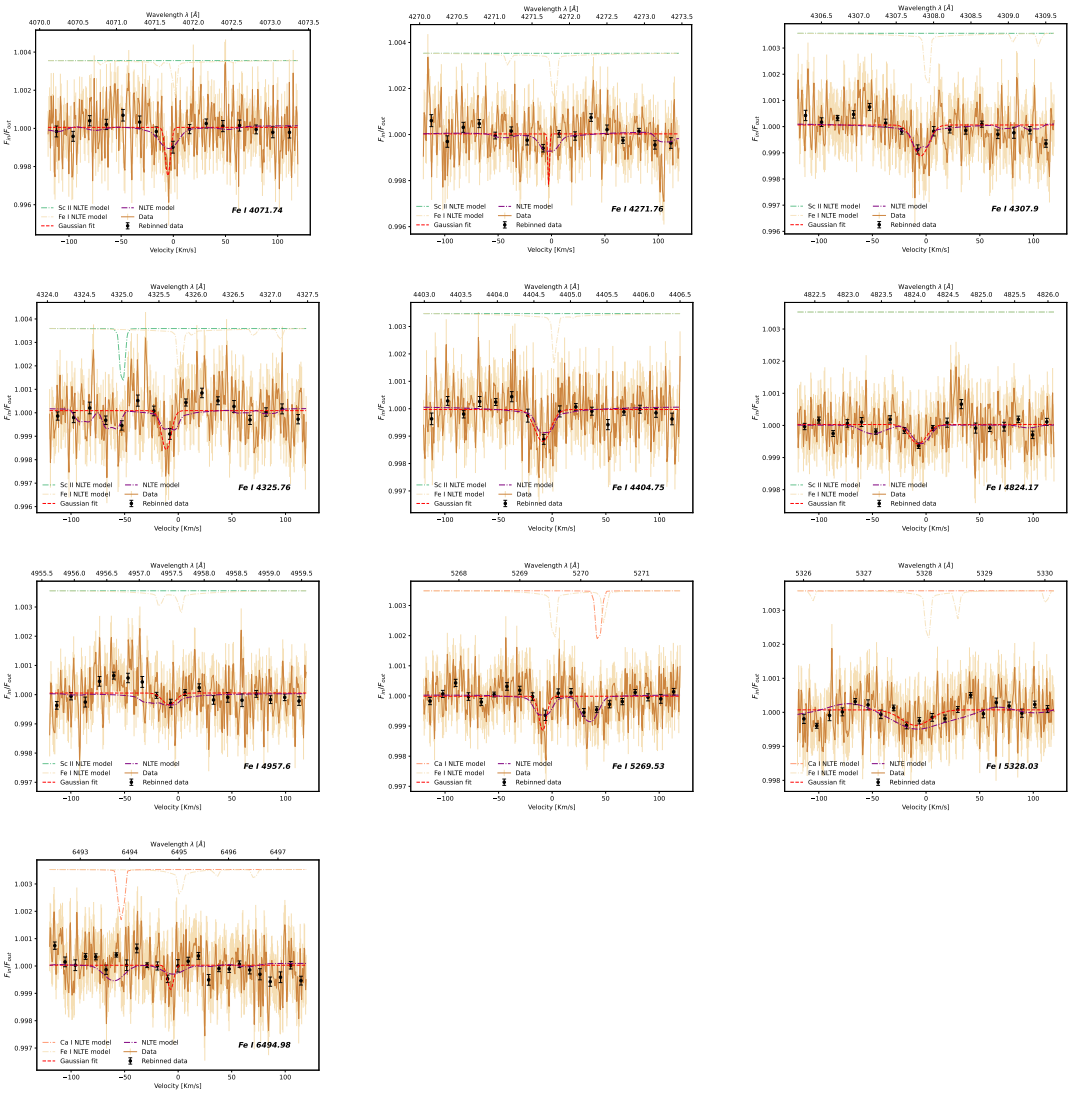

Figure 2.23: Same as Fig. 2.17, but for Fe I.

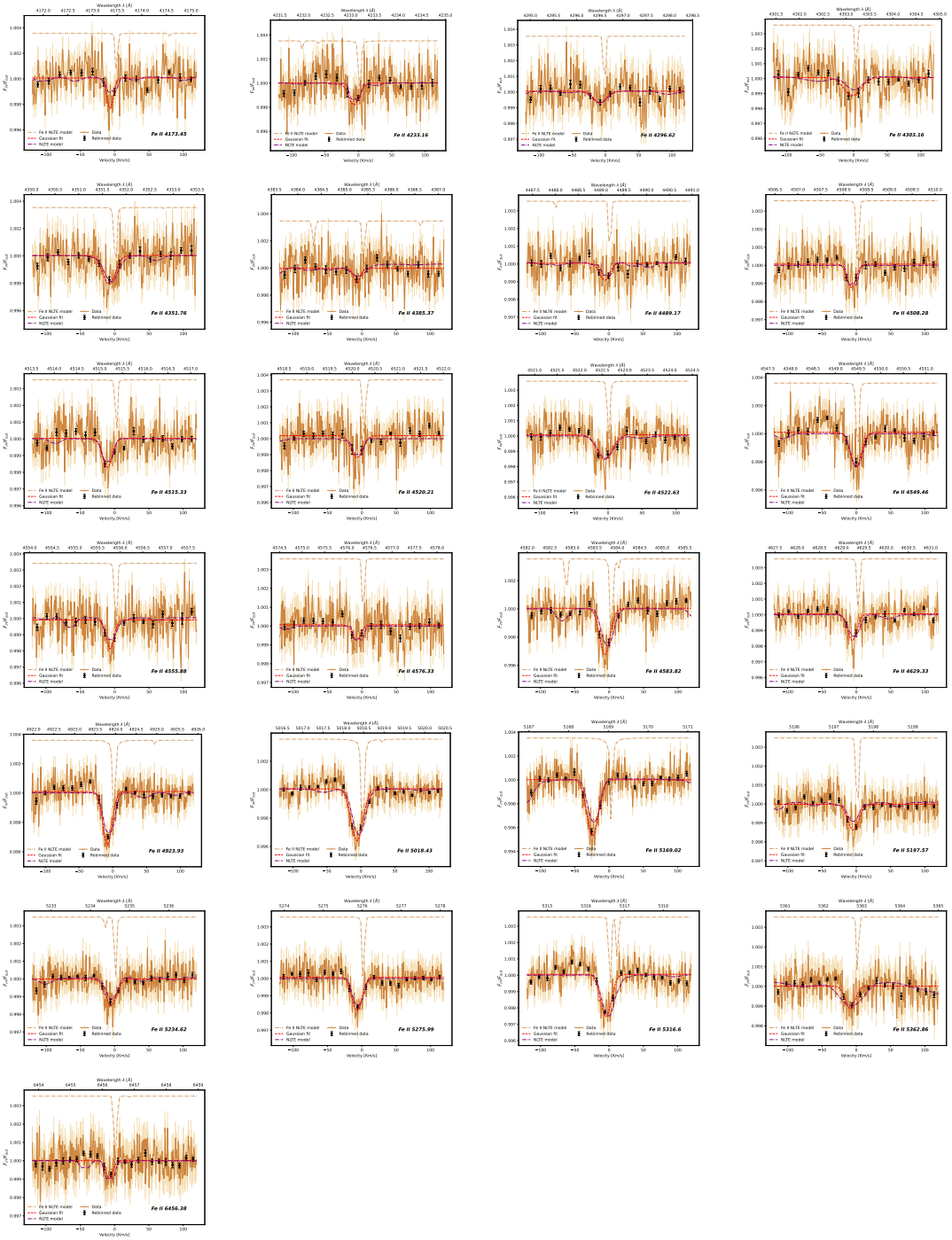

Figure 2.24: Same as Fig. 2.17, but for Fe II.

2.2 The use of NLTE models to constrain C/O ratio in the atmosphere of KELT-9 b

In the previous Section, I introduced my work (D'Arpa et al. 2024b) where is discussed the comparison of the observed lines of several elements in the atmosphere of KELT-9 b with the **NLTE** models generated by Luca Fossati and already presented in several of his works (Fossati et al. 2021, 2020). The models used in D'Arpa et al. (2024b) have been generated at different ν_{mic} but fixing the metallicity at the solar one.

In this section, I will first introduce more in detail the **NLTE** effects already discussed in Section 2.1.4 and then, I will discuss the strategy used to constrain the C/O ratio using the information extracted from the comparison between the **NLTE** models and the observed data.

2.2.1 The importance of NLTE effects on exoplanetary atmospheres

The concept of Non-Local Thermodynamic Equilibrium (**NLTE**) refers to situations where the population of energy states of atoms, molecules, or ions does not follow the distributions predicted by the Boltzmann and Saha equations, which describe local thermodynamic equilibrium (**LTE**). In **NLTE** conditions, the rate of population of energy states is influenced not only by the local temperature but also by external radiation processes and unbalanced collisions, making atmospheres more complex to model and interpret.
In planetary atmospheres, particularly in ultra-hot Jupiters such as KELT-9 b, **NLTE** conditions arise due to high temperatures and intense radiation from the host star, leading to significant deviations from local equilibrium. These **NLTE** effects primarily impact metals present in the atmospheres, such as magnesium (Mg) and iron (Fe), whose energy levels can be overpopulated or underpopulated compared to **LTE** predictions.
In the context of high-temperature planetary atmospheres, iron and magnesium play crucial roles in regulating thermal balance. For example, Fe II is a dominant heater due to its abundance and its ability to absorb radiation in the ultraviolet bands, which are particularly intense in hot stars like KELT-9 b's host star. In **NLTE** conditions, some Fe II levels are overpopulated, leading to increased radiative absorption and consequent heating of the upper atmosphere. In contrast, magnesium, especially in the forms of Mg I and Mg II, tends to be underpopulated, reducing the effectiveness of cooling through radiative transitions involving these energy levels.
Fossati et al. (2021) used the Cloudy radiative transfer code, which includes **NLTE** effects, to model the temperature-pressure (TP) profile of KELT-9 b. The **NLTE** model from Cloudy was combined with the HELIOS code for the lower part of the atmosphere, which operates under **LTE** conditions. This combination was necessary because Cloudy is optimized for simulating **NLTE** conditions in the upper atmosphere, where gas density is low and non-equilibrium effects are more pronounced, while HELIOS is more accurate for denser, hotter regions where **LTE** is a good approximation.
In the case of KELT-9 b, Fossati et al. (2021) found that the TP profile obtained in **NLTE**

was significantly hotter than previous **LTE** models, with temperature differences up to 2000 K in the line formation region. Specifically, the temperature increased from about 4000 K to 8500 K in the pressure range of 1 to 10^{-7} bar, remaining roughly constant at lower pressures. This temperature increase is mainly due to the overpopulation of energy levels of ionized iron (Fe II), which enhances radiative heating, while ionized magnesium (Mg II) contributes marginally to cooling due to its underpopulation (Fossati et al. 2020; Turner et al. 2020).
The results obtained by Fossati et al. (2021) clearly demonstrate that **NLTE** effects significantly impact the thermal structure of KELT-9 b's atmosphere. Models that do not consider **NLTE** effects tend to underestimate the upper atmospheric temperature and, consequently, misinterpret the formation of spectral lines, especially in the ultraviolet bands. The **NLTE** simulations produce stronger absorption lines, particularly in the ultraviolet, where differences can reach up to 30% compared to **LTE** models. This leads to a better match between models and observations of transmission lines, such as those of hydrogen Hα and Hβ , providing strong support for the findings (Yan & Henning 2018; Hoeijmakers et al. 2018; Turner et al. 2020).
These studies suggest that interpreting observations of ultra-hot Jupiter atmospheres must consider **NLTE** effects, especially for metals like Fe and Mg, which play a crucial role in determining temperature and pressure structure in the upper regions. The approach adopted by Fossati et al. (2020) represents an important step forward in understanding the dynamics of these extreme exoplanetary atmospheres and highlights the importance of detailed models that include non-equilibrium effects.

2.2.2 Constraining of the Oxygen abundance

The results I obtained in D'Arpa et al. (2024b) described in Section 2.1.3 allowed us to retrieve key information about the **NLTE** effects on KELT-9 b. Our comparison between the observed transmission spectra of several metals and the expected **NLTE** models developed by Fossati, managed to discriminate the best ν_{mic}–ν_{mac} couple to minimise the $\chi^2_{\rm red}$. The mean results for the different species agree with previous results from Borsa et al. (2021b) hinting that the best ν_{mic}-ν_{mac} is 3.03 $\pm$ 0.25 km s^{-1}& 10.03 $\pm$ 1.43 km s^{-1}, while Borsa et al. (2021b) ones lie in the 3.0 $\pm$ 0.7 km s^{-1}& 13 $\pm$ 5 km s^{-1}, respectively for ν_{mic} and ν_{mac}. The similar results, obtained with different instrumentation allow us to further try to determine the best metallicity of the **NLTE** models. We generated a grid of several models with the Magnesium, Iron and Oxygen abundances ranging from 0.2 times the solar one to 5 times, while the ν_{mic} spanning from 1 km s^{-1}to 8 km s^{-1}. We investigated the Magnesium and Iron because, as explained before, they are the elements most sensitive to the **NLTE** effects.

At further step, I adopted a framework similar to the one introduced in D'Arpa et al. (2024b). I took each **NLTE** model in the grid (i.e., models with different abundances) and I applied a broadening to include the planetary rotation and the smearing effect as discussed in Section 2.1.4. Then, I varied both ν_{mac} and ν_{mac} and fitted the models to the data computing the χ^2. We repeated the procedure described above for several lines detected in D'Arpa et al. (2024b). We compared the different models for the deepest of

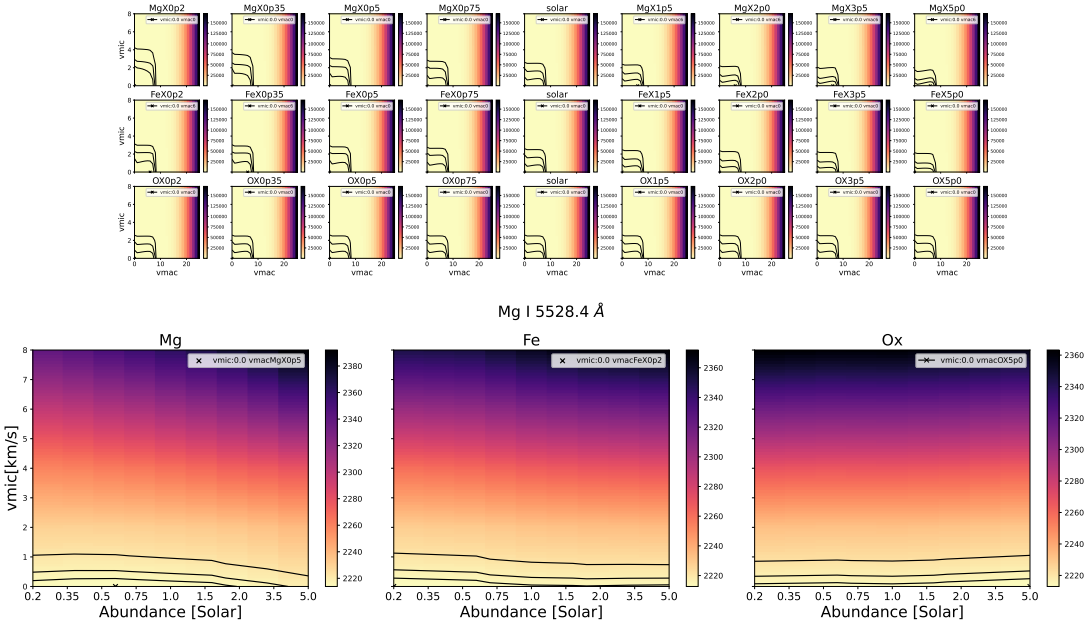

Figure 2.25: Chi square distributions obtained with the grid of models for the Mg I at 5528 Å. Top panels: $\chi^2_{\rm red}$ distribution for different $\nu_{\rm mic}$-$\nu_{\rm mac}$ pairs as a function of the different abundances of magnesium, iron and oxygen. Bottom panels: $\chi^2_{\rm red}$ distribution for different $\nu_{\rm mic}$ as a function of the abundance for models with $\nu_{\rm mac}$ fixed to 13 km s^{-1}. The black lines represent the contour plots.

the neutral magnesium lines detected, while for the iron lines, we selected only 1 neutral line and 3 for the ionised ones, focusing on the lines with a depth retrieved between 1.16 and 1.18 $R_{\rm p}$. We selected these lines to perform a better comparison with the Oxygen triplet detected by Borsa et al. (2021b) with a depth of 1.17 $R_{\rm p}$.

2.2.3 Magnesium and iron results

For each line investigated we repeated the procedure described above obtaining the plots observable in Fig. 2.25, 2.26, 2.27 and 2.28. In the top panels of each Figure we can see the $\nu_{\rm mic}$-$\nu_{\rm mac}$ maps for the different abundances, with the contour plots hinting at the best distributions of the two parameters. In the bottom panels, we show the $\nu_{\rm mic}$ as a function of the different abundances fixing $\nu_{\rm mac}$ at 13km s^{-1}since this is the value obtained by Borsa et al. (2021b) for the oxygen.

From the $\nu_{\rm mic}$-$\nu_{\rm mac}$ maps we can see that:

- for the Mg I line, the best $\nu_{\rm mic}$-$\nu_{\rm mac}$ values do not depend on the Magnesium, Iron and Oxygen abundances, although, the contour plots suggest a slight dependence on the magnesium abundance, with larger $\nu_{\rm mic}$ preferred for lower abundances and smaller $\nu_{\rm mic}$ preferred for larger abundances. This is clear also from the bottom panels of Fig. 2.25 where the best $\nu_{\rm mic}$ is always close to 0km s^{-1}and no clear

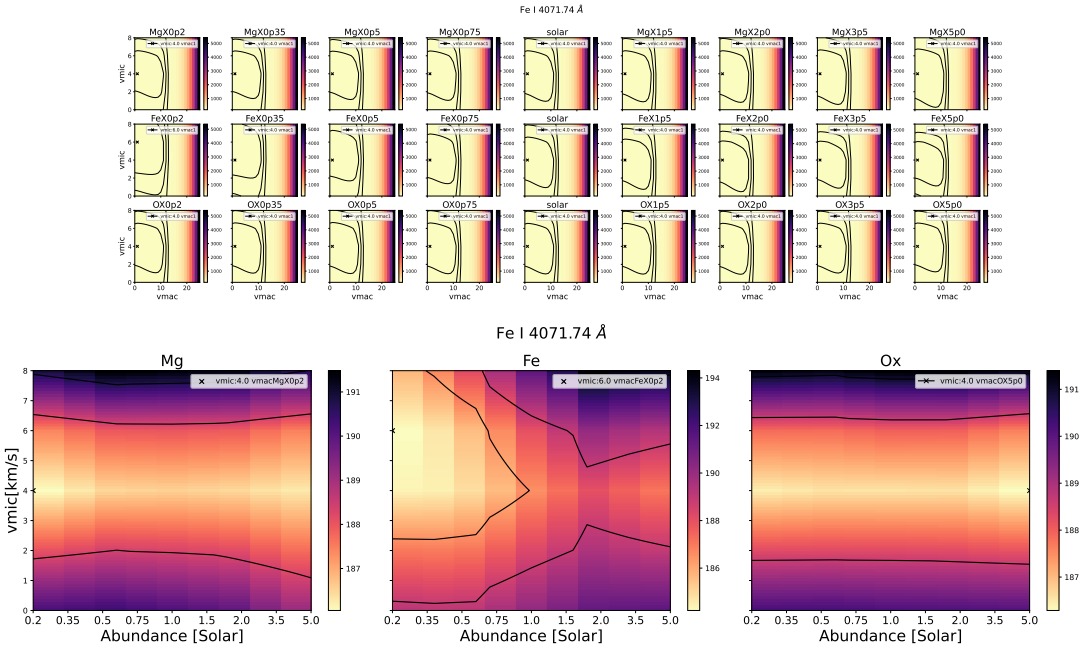

Figure 2.26: Same as Fig. 2.25 for the neutral iron line at 4071 Å.

convergences can be seen;

- The neutral iron line investigated does not show a particular pattern for any of the investigated abundances with the best ν_{mic}-ν_{mac} pair being 4 km s^{-1}and 1 km s^{-1}. Fixing the ν_{mac} to 13 km s^{-1}leads to a best ν_{mic} around 4-6 km s^{-1}. It is clear from the left and right bottom panels in Fig. 2.26, that this result does not depends on the magnesium and oxygen abundances while for the iron abundances, the minimum χ^2_{red} is reached at lower iron abundances;
- From the ν_{mic}-ν_{mac} maps as a function of the abundance, we can see that the ionised iron lines show well-constrained ν_{mic}-ν_{mac} values and a clear dependence on the iron abundance. This is even more clear in the ν_{mic} vs abundances plots where the correlation between the two parameters is clear. From these three lines, it seems that adopting a ν_{mac} of 13 km s^{-1}leads to a best iron abundances models that spans between 0.75x and 1.5x solar iron abundance, with the best ν_{mic} around 4-6 km s^{-1}.

Oxygen results

We then moved to the Oxygen triplet investigated by Borsa et al. (2021b) who provided its transmission spectrum extracted from the **CARMENES** data. We modelled the three lines altogether fitting them simultaneously, repeating the same procedure described above for the other lines, obtaining the maps shown in Fig. 2.28 which show interesting behaviours. From the top panels of Fig. 2.28 we can see that the ν_{mic}-ν_{mac} pair is not dependent on the Magnesium abundance, while from the contours we can see that they

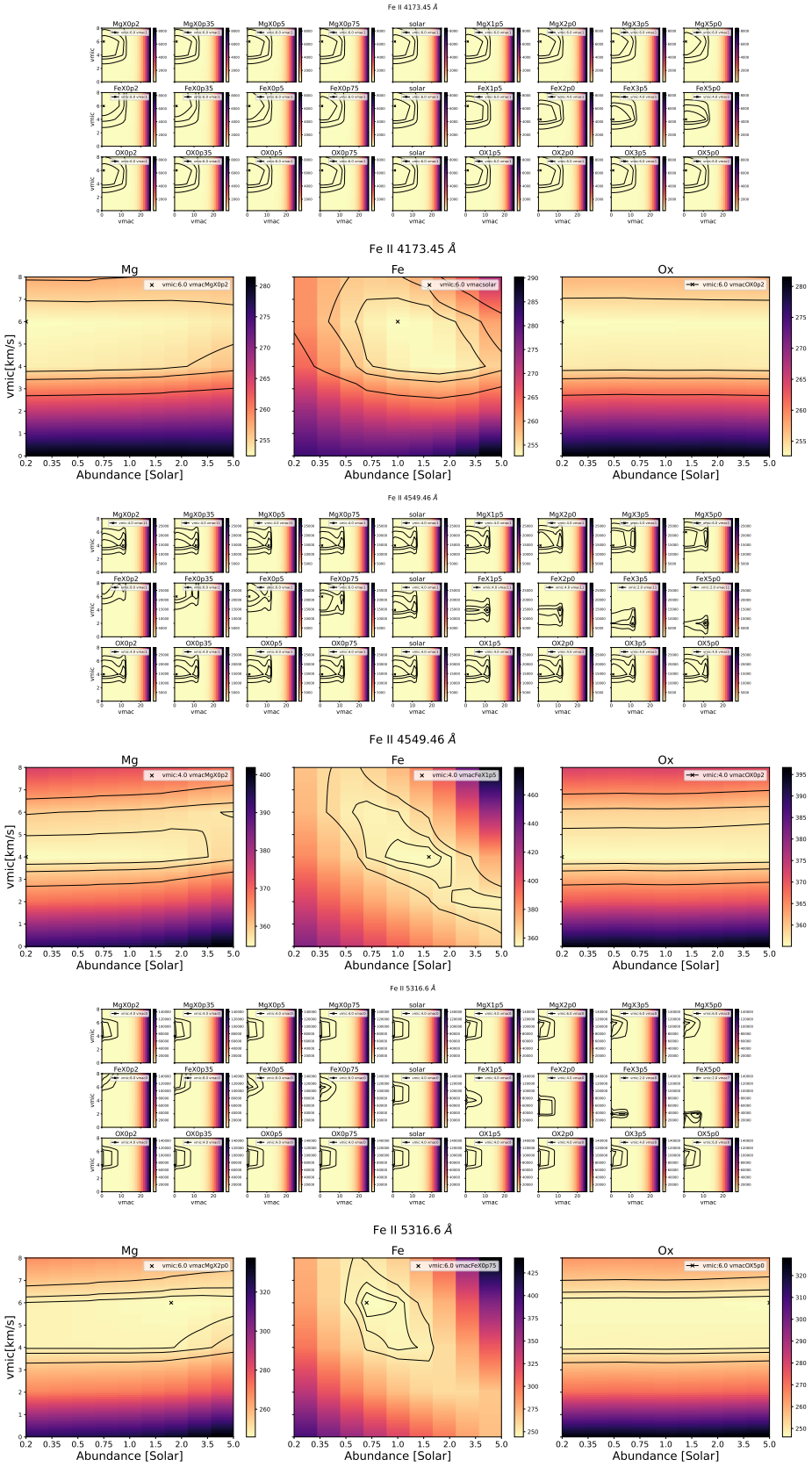

Figure 2.27: Same as Fig. 2.25 for the ionised iron lines at 4173.45 Å, 4549.46 Å and 5316.60 Å.

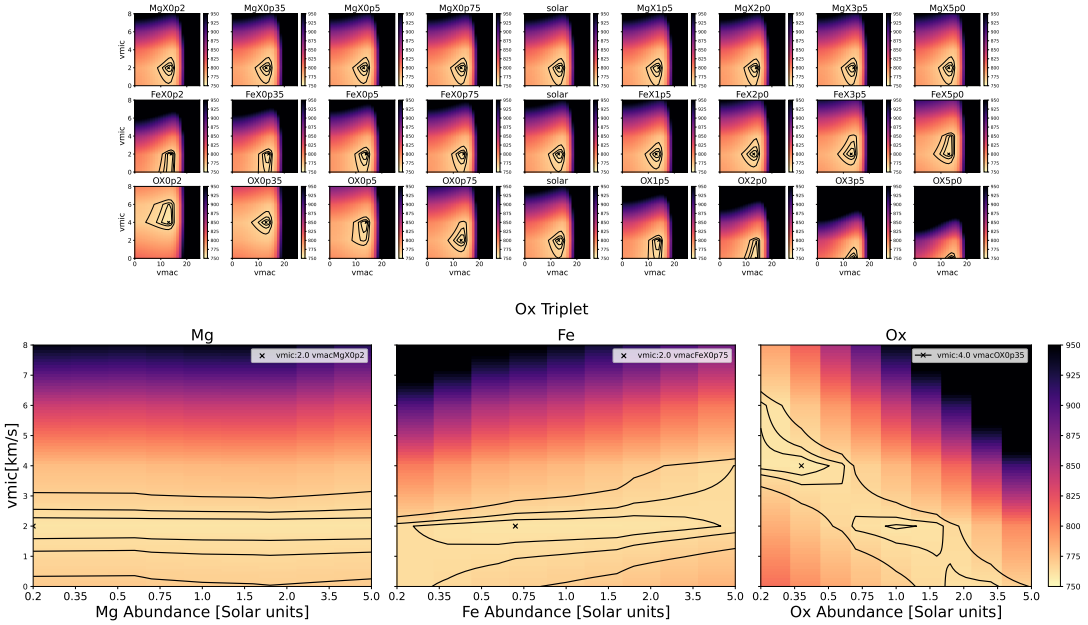

Figure 2.28: Same as Fig. 2.25 for the oxygen triplet lines from Borsa et al. (2021b).

slightly depend on the Iron abundance, and clearly on the oxygen one as expected. In all the cases, from the contours it is clear that the best pair is well constrained. Fixing the ν_{mac} to 13 km s^{-1}we see that the minimum $\chi^2_{\rm red}$ is reached for ν_{mic} = 4 km s^{-1}for the oxygen models, favouring the model with 0.35x the solar abundance.

2.2.4 Results and future developments

The next step in our work will be further investigating and corroborating the abundances of Magnesium, Iron and Oxygen employing more **NLTE** models, including models with mixed abundances. When the final abundances will be known, we will move our attention to constraining an upper limit to the Carbon which is undetected on the atmosphere of KELT-9 b. After the upper limit on the C/O ratio will be fixed along with the abundances of Iron and Magnesium, it will be possible to investigate the formation history of this enigmatic planet.

2.3 Exploring KELT-9 b atmosphere within the GAPS programme at TNG

Due to its very peculiar nature, KELT-9 b is one of the most studied exoplanets. Its high equilibrium temperature makes it hotter than most of the stars in the universe, leading to extreme conditions. Moreover, its A0 type star, should be free of any stellar activity phenomena, such as spots and faculae, that may lead to fake detections or other effects discussed in Chapter 4. Therefore, it is not a surprise that it is the best target to be

studied in single line analysis. Within the **GAPS** collaboration we carried several works regarding its single lines, especially focusing on the Iron and Sodium lines. In the next sections, I will introduce and summarise two of the latest work where I was involved, focusing, in particular, on the comparison of the results with the one by D'Arpa et al. (2024b) I introduced in Section 2.1 and on the differences between the method adopted.

2.3.1 Studies of atmospheric Fe II winds in ultra-hot Jupiters KELT-9 b and KELT-20 b.

Within the **GAPS** collaboration I participated in the work led by Monika Stangret (Stangret et al. 2024) on the study of atmospheric Fe II winds in ultra-hot Jupiters KELT-9 b and KELT-20 b, in parallel to my work on KELT-9 b.

The main goal of the study was to investigate the atmospheric properties of two well-known UHJs, KELT-9 b and KELT-20b, focusing on the detection of iron (Fe II) lines in their atmospheres. The presence of Fe II in the atmospheres of UHJs is particularly intriguing due to its implications for understanding high-temperature chemistry and wind dynamics within these exoplanets. Other studies, including D'Arpa et al. (2024b), have suggested that strong winds transport material from the day side, which is intensely heated by the star, to the cooler night side, creating detectable blue-shifted absorption lines.

The study aimed to:

- Detect and analyse individual Fe II lines in the atmospheres of these UHJs using transmission spectroscopy. This helps to identify the presence of the atomic species and assess their distribution across the planetary atmosphere;
- Examine atmospheric wind patterns by measuring the velocity shifts of the detected lines. Blue-shifted lines can indicate strong winds moving from the day side to the night side of the planet, providing insights into atmospheric circulation;
- Compare results with theoretical models that account for NLTE effects, enhancing the understanding of high-temperature atmospheric processes.

Extraction of the transmission spectra

The main differences with respect to D'Arpa et al. (2024b) can be found in some steps of the framework to extract the transmission spectra and to fit them.

The first step in the analysis involves preprocessing the spectra to remove contamination from Earth's atmosphere, known as telluric absorption. The primary tool used for telluric correction in this study is Molecfit as already presented in D'Arpa et al. (2024b). After pre-processing, the spectra are shifted to the stellar rest frame. This involves correcting for the barycentric motion of the Earth (i.e., the Earth's movement around the centre of mass of the solar system) and the radial velocity of the star due to its orbital

motion caused by the planet. This step is essential to align the spectra in a way that isolates the planetary signal. An additional challenge arises from the systemic velocity of the planet-star system, which can vary across different studies. The systemic velocity affects the position of the absorption lines and must be accurately determined to properly isolate the planetary atmospheric signal. The study considered various systemic velocity values reported in the literature and refined them through their analysis, highlighting the importance of this parameter in accurately modelling the Rossiter-McLaughlin effect and atmospheric winds.

RME+CLV removal Two significant stellar effects must be corrected to accurately interpret the transmission spectra: the Rossiter-McLaughlin (**Rossiter-McLaughlin (RM)**) effect and the center-to-limb variation (**CLV**). We already discussed in the previous chapter as in D'Arpa et al. (2024b) I modelled and removed the **RME+CLV**, which is slightly different respect, as in this case.

Stangret's study modelled these effects using synthetic spectra computed with Spectroscopy Made Easy (SME) software, which uses Kurucz stellar atmospheres and the **VALD3** line list. The models were generated for various limb-darkening angles and at different phases of the planetary orbit, taking into account the planet's varying coverage of the stellar disk. These models were then used to correct the observed spectra, removing the **RME** and **CLV** influences to isolate the planetary signal accurately.

This represents the first difference with respect to D'Arpa et al. (2024b) as in my work, I used one unique stellar model generated with ATLAS9 and, then, I used Exothetys to retrieve the limb darkening dependent models as explained in Section 2.1.2.

Gaussian Fit To quantify the atmospheric signal, a Gaussian profile is fitted to the transmission spectra of each detected Fe II line. This fitting process involves a **The Markov Chain Monte Carlo (MCMC)** approach to simultaneously estimate the parameters of the Gaussian, as well as the contributions from the **RME** and **CLV** models. The **MCMC** algorithm is employed to determine the best-fit parameters for the planetary signal, which include the amplitude (strength) of the absorption line, the full width at half maximum (**FWHM**), and the velocity of the planetary signal (combining the systemic velocity and wind velocity). The velocity of the planetary signal, v_{pl}, is modeled using the equation:

$$v_{pl} = K_p \sin(2\pi\phi(t)) + v_{sys} + v_{wind} \tag{2.4}$$

where:

- K_p is the semi-amplitude of the planet's radial velocity,
- $\phi(t)$ is the orbital phase,
- v_{sys} is the systemic velocity,
- v_{wind} represents the velocity of the atmospheric winds.

The Gaussian model, **RM**, and **CLV** corrections are fitted simultaneously using the **MCMC** analysis, ensuring that the final extracted planetary signal is free from stellar influences. Only lines for which all parameters converge are considered as reliable detections. This is different compared to the way we modelled the **RME+CLV** and fitted the transmission spectra in D'Arpa et al. (2024b).

An example of modelling and removal of **RME+CLV** and the extraction of the transmission spectrum can be seen in the top panels of Fig. 2.29 where is shown: in the first the residual map obtained for the Fe II line at 5018.4 Å for KELT-9 b in the stellar rest frame. The light-tilted signal is the atmospheric signal of Fe II, while the dark almost vertical signal is the **RM** effect. The white horizontal lines indicate the start and end of the transit, while the tilted white line indicates the expected trace of the Fe II line considering velocities coming from the planet's atmosphere, assuming v_{sys} = -21.61 km s^{-1}as the average v_{sys} from our analysis. In the second panel, the best fit model of the planetary signal and of the **RM** and **CLV** effects. Third panel: Same as the top panel, but with the **RM** and **CLV** effects corrected. In the fourth panel, the transmission spectrum of the detected line (gray dots). The black dots indicate the binned transmission spectrum with a step of 0.1 Å. The red line is the best Gaussian fit of the planetary signal derived from the **MCMC** analysis, the blue line shows the **LTE** model, and the green line indicates the **NLTE** model. Finally in the bottom panel, the residuals after removing Gaussian fit from the TS.

Results

For KELT-9 b, 21 single lines of Fe II were detected, all showing a blue shift that indicates strong day-to-night side atmospheric winds. The cross-correlation method also detected blue-shifted signals with a high signal-to-noise ratio. The study found that the detected lines are consistent with models that assume non-local thermodynamical equilibrium effects. The measured blue-shifted lines indicate strong atmospheric winds moving from the day side to the night side of the planet. The systemic velocity measured was slightly larger compared to values reported in the literature, supporting the detection of significant winds.

The study notes that the detection of Fe II lines in KELT-9 b is consistent with D'Arpa et al. (2024b), who detected 25 lines using the same dataset but a different methodology. D'Arpa et al. (2024b) approach reported some overlapping results, but there were differences in the lines excluded due to blending with other species or insufficient convergence in the **MCMC** analysis used in this work. Specifically, four lines detected by D'Arpa et al. (2024b) were excluded in this study due to issues with convergence or potential blending with other atmospheric lines. All the lines detected in Stangret et al. (2024) have been detected in D'Arpa et al. (2024b).

As stated previously, despite sharing the same dataset, there are some major differences in the **RME+CLV** modelling and removal and in the fitting of the best parameters. As can be seen in top panel of Fig. 2.30 and in bottom panel of Fig. 2.31, most of the lines detected in both studies are overlapping, with some small differences in the velocities of

the winds and depths retrieved. Generally, this discrepancies are within 1σ uncertainty, confirming the robustness of the results.

2.3.2 A homogeneous search for Na I and its possible variability in ten gas giant exoplanets

Sodium (Na I) is one of the most extensively studied elements in exoplanetary atmospheres because of its strong absorption features in the visible spectrum, particularly the Na I D doublet lines at 5889.95 Å (D2) and 5895.92 Å (D1). Detecting and characterizing sodium in exoplanet atmospheres can provide insights into atmospheric dynamics, temperature profiles, and the presence of high-altitude winds.

A specific study, conducted as part of the **GAPS** (Global Architecture of Planetary Systems) program, was focused on the detection and analysis of sodium in the atmospheres of ten gas giants, including KELT-9 b, using high-resolution transmission spectroscopy data from the **HARPS-N** spectrograph mounted on the Telescopio Nazionale Galileo (**TNG**). The data analysis was performed using the public tool `SLOPpy` (Spectral Lines Of Planets with python Sicilia et al. 2022), which efficiently corrects for telluric contamination, stellar effects, and extracts the transmission spectra to identify the absorption features of atmospheric species. The method is similar to the ones described in the previous sections for D'Arpa et al. (2024b) and Stangret et al. (2024). An example of the extracted sodium doublet can be seen in Fig. 2.32.

Results

A key aim of this work was to verify the presence and variability of sodium absorption signals in the selected targets, compare the results with theoretical models, and assess the influence of data quality and analysis methods.

In this study, KELT-9 b was observed over six nights, yielding high-confidence detections of the Na I D lines. The main results for KELT-9 b's sodium absorption are as follows: Both Na I D1 and D2 lines were detected with absorption depths of approximately $-0.13 \pm 0.02\%$, indicating the presence of sodium in the upper atmosphere of KELT-9 b. The observed blue shift of approximately -7 km s^{-1}suggests strong day-to-night atmospheric winds, consistent with the high-speed dynamics expected in ultra-hot Jupiters. The line profiles were fitted using a double Gaussian model within an **MCMC** framework. The resulting full width at half maximum (**FWHM**) of 18.3 km s^{-1}reflects broadening effects likely caused by thermal motion and high-altitude winds. Despite variability in line depths across individual nights, the overall signal remained consistent across all observations, supporting the robustness of the sodium detection.

In D'Arpa et al. (2024b) I analysed the same **HARPS-N** dataset for KELT-9 b, focusing on a single-line analysis approach that carefully modeled stellar contamination, such as the center-to-limb variation (**CLV**) and Rossiter-McLaughlin effect (**RME**). Here is a comparison of the results: D'Arpa et al. (2024b) reported slightly shallower absorption depths for the Na I D lines, around -0.11% for both D1 and D2. These differences could

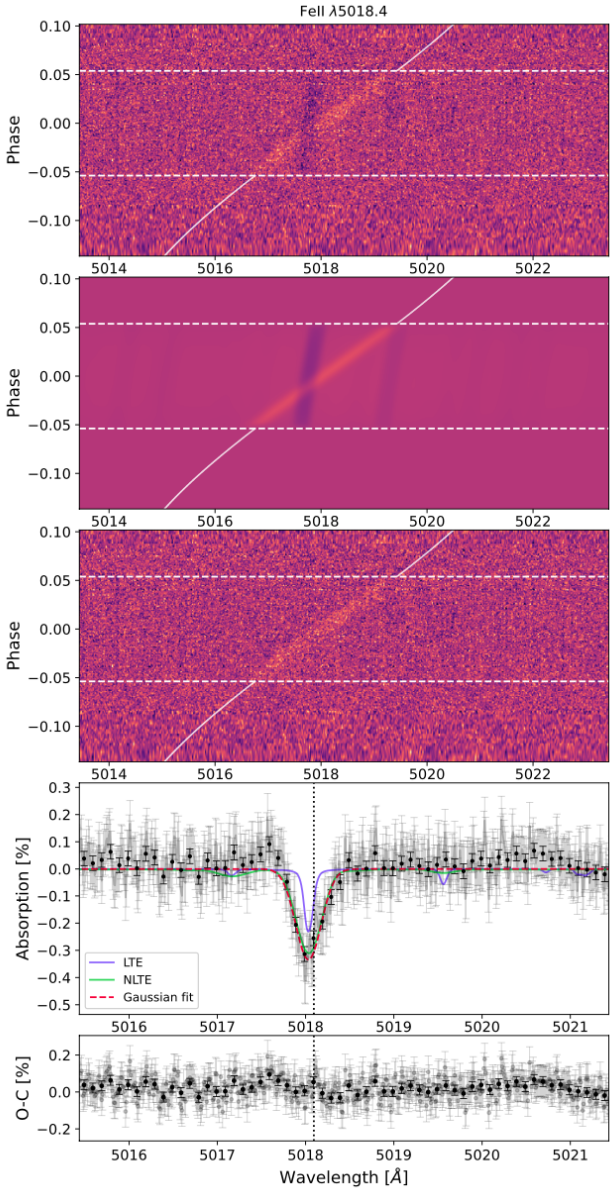

Figure 2.29: Top panel: Residual map obtained for the Fe II line at 5018.4 Å for KELT-9 b in the stellar rest frame. The light-tilted signal is the atmospheric signal of Fe II, while the dark almost vertical signal is the **RM** effect. The white horizontal lines indicate the start and end of the transit, while the tilted white line indicates the expected trace of the Fe II line assuming v_{sys} = -21.61 km s^{-1}as the average v_{sys} from our analysis. Second panel: Best fit model of the planetary signal and of the **RM** and **CLV** effects. Third panel: Same as the top panel, but with the **RM** and **CLV** effects corrected. Fourth panel: Transmission spectrum of the detected line (gray dots). The black dots indicate the binned transmission spectrum with a step of 0.1 Å. The red line is the best Gaussian fit of the planetary signal derived from the **MCMC** analysis, the blue line shows the **LTE** model, and the green line indicates the **NLTE** model. Bottom panel: Residuals after removing Gaussian fit from the TS. From Stangret et al. (2024).

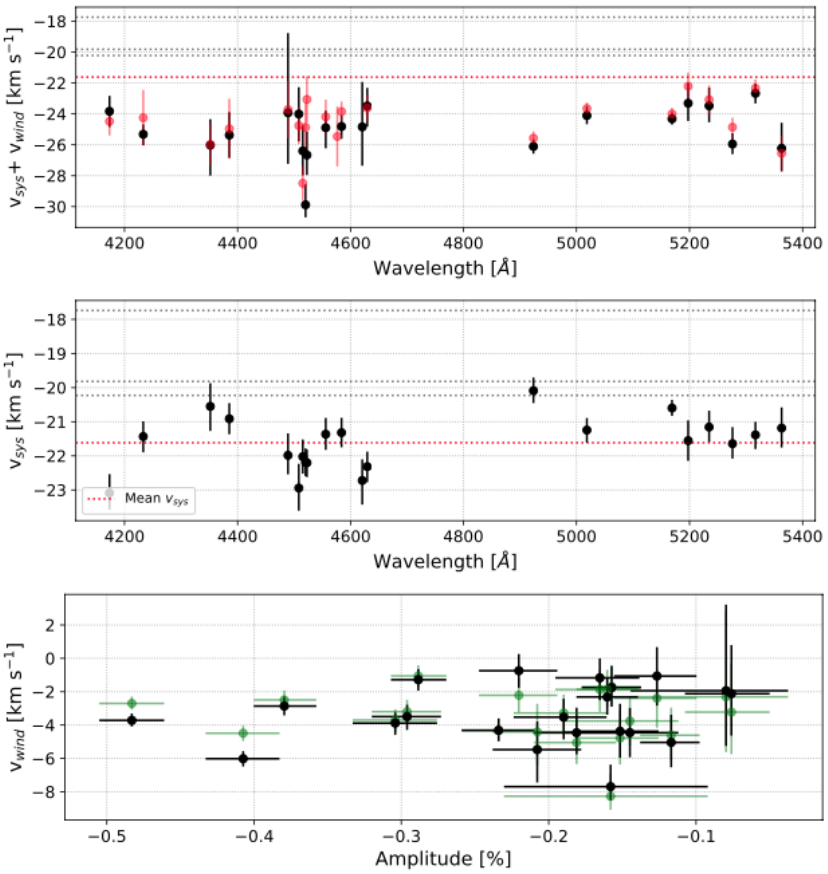

Figure 2.30: Top panel: fitted v_{sys}+wind for each of the detected lines. The red dots represent the results of D'Arpa et al. (2024b). Middle panel: fitted v_{sys} for each of the detected lines in Stangret et al. (2024). The red dashed horizontal lines indicate the mean value of the v_{sys} = -21.61 $\pm$ 0.77 km s^{-1}, while the grey horizontal dashed lines indicate literature v_{sys} values: -17.74 $\pm$ 0.11 km s^{-1}(Hoeijmakers et al. 2019), -19.819 $\pm$ 0.024 km s^{-1}(Borsa et al. 2019), and -20.22 $\pm$ 0.49 km s^{-1}(GAIA). Bottom panel: v_{wind} versus amplitude (corresponding to the depth in D'Arpa et al. (2024b)) plot, where green points represent the values calculated by correcting the fitted v_{sys}+wind by the mean v_{sys} and the black points represent the values corrected by v_{sys} fitted for each of the lines separately.

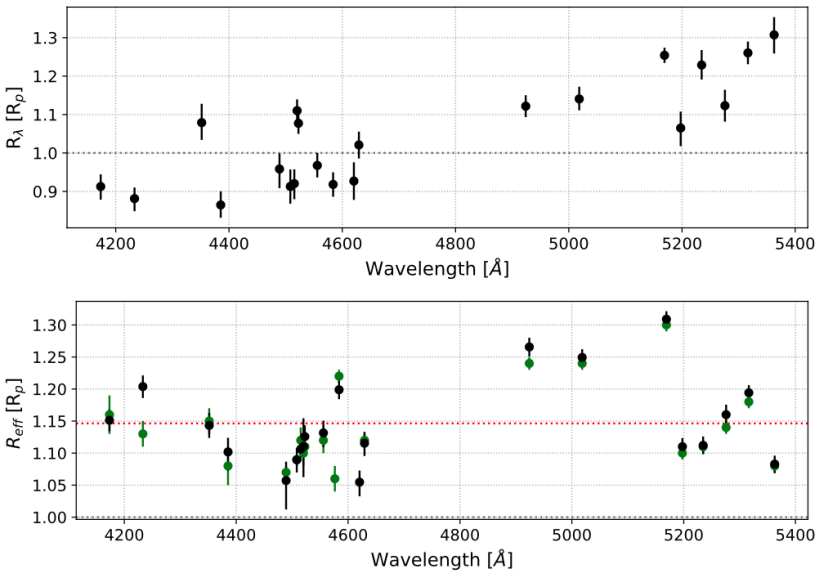

Figure 2.31: Top panel: Fitted Rλ for each of the lines. The dashed horizontal line indicates Rλ = $R_{\rm p}$. Bottom panel: Calculated R_{eff} values using the amplitude of the detected signal for each of the lines (black dots) and the values obtained by D'Arpa et al. (2024b) (green dots).

stem from the distinct data treatment methods and correction techniques employed, particularly in handling the **CLV** and **RME** effects. Both studies agree on the significant blue shifts observed in the sodium lines, indicative of strong atmospheric winds. However, while this study measured a shift of about -7 km s^{-1}, D'Arpa et al. (2024b) reported a slightly lower shift near -5 km s^{-1}. These variations highlight the sensitivity of velocity measurements to data reduction processes and underscore the need for consistent methodologies. The consistent detection of sodium with similar blue shifts in both studies reinforces the understanding of atmospheric circulation in KELT-9 b, characterized by high-speed day-to-night side winds. The slight discrepancies in absorption depths and shifts emphasize the influence of data quality, analysis techniques, and potential intrinsic variability in the atmospheric signals.

Overall, the sodium detections in KELT-9 b confirm the presence of complex and dynamic processes in its atmosphere. The comparison with D'Arpa et al. (2024b) highlights the importance of methodological consistency in interpreting high-resolution spectroscopic data and provides a clearer picture of sodium's role in the atmospheric dynamics of ultra-hot Jupiters.

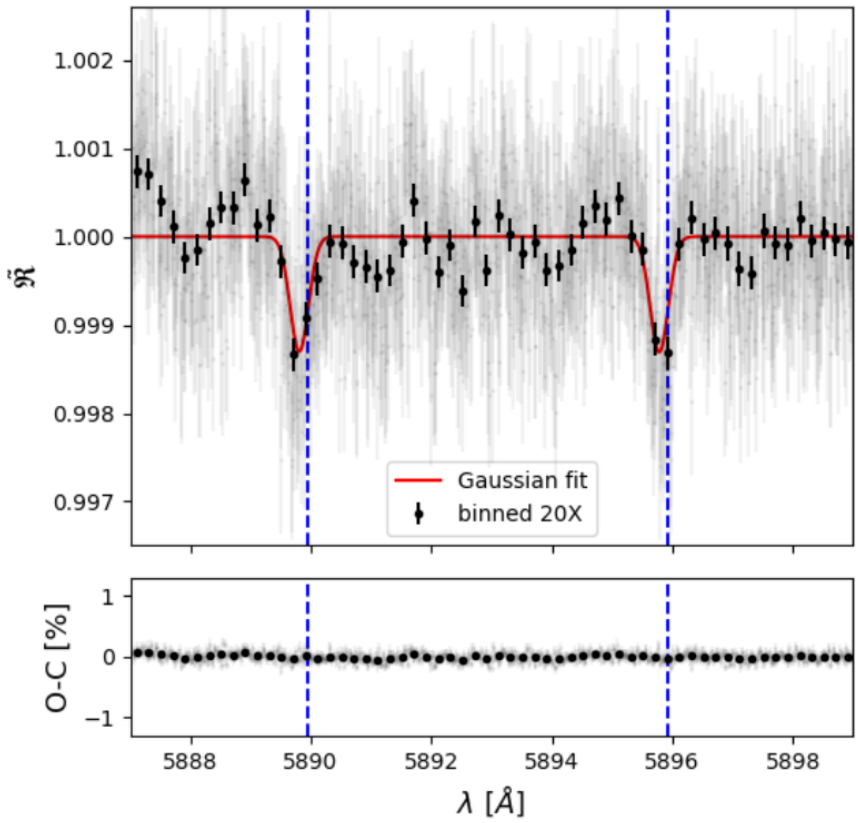

Figure 2.32: Final transmission spectrum of KELT-9 b centred around the Na I D (light gray), also binned by 20x in black circles. The red line is the **MCMC** Gaussian fit, while the dashed blue vertical lines indicate the rest frame transition wavelengths of the sodium doublet. From Sicilia et al. (2025).

Chapter 3

Validation of the method and application to other exoplanets

The framework I introduced in the previous chapter proved to be valid to extract and fit single lines transmission spectra. Particularly, despite it was developed to extract the Balmer series in the atmosphere of KELT-9 b, it was used in D'Arpa et al. (2024b) to extract and fit also metal lines. In single line analysis context, KELT-9 b represents a unique thanks to its extremely large temperature strongly influenced by the huge stellar irradiation of its A0 type host star. The stellar condition heavily influences the difficulty of extracting the transmission spectra in several ways: hotter stars, as the A and early F-type ones, are less affected by stellar activity due to their lack of an outer convective zone; I will discuss the impact of activity in the transmission spectra in Chapter 4 analysing G, K and M type stars. Another parameter having a major impact on the transmission spectrum of individual lines is the stellar rotation: fast rotating stars have more broadened lines with respect to non rotating stars. This impacts the transmission spectrum since this is computed by dividing the in-transit spectra by the master-out. With deeper lines, the relative change in the division causes a larger noise in the 2D tomography. Moreover, fast rotator stars cause a larger **Rossiter-McLaughlin Effect (RME)** that needs to be carefully removed as shown for KELT-9 b. In this chapter I will first introduce the results obtained within the collaboration with Valerio Fardella during his master thesis that I co-supervised, where we validated the framework on another target similar to KELT-9 b, KELT-20 b, and we tested it on other more complex targets. After proving the framework valid and showing the application to other targets, in Section 3.2 I will discuss several atomic detections in a target similar to KELT-9 b, TOI-1518 b. In Section 3.3 I will show a work concerning the application of the method, originally developed for **High Accuracy Radial velocity Planet Searcher for the Northern emisphere (HARPS-N)** data to WASP-94A b, an **Ultra Hot Jupiter (UHJ)** observed with **Echelle SPectrograph for Rocky Exoplanets and Stable Spectroscopic Observations (ESPRESSO)** spectrograph.

3.1 Testing the method: KELT-20 b, KELT-6 b, WASP-69 b, GJ-3470 b and WASP-107 b

During my PhD I had the opportunity to be co-supervisor of the Master Thesis of Valerio Fardella named "Analysis of the Balmer series in several exoplanets atmospheres". The aim of the work was to investigate exoplanetary atmospheres using high-resolution spectral data obtained from the **HARPS-N** spectrometer mounted on the Telescopio Nazionale Galileo, applying the method I developed for Kelt-9 b. In the work Valerio and myself tested the framework I developed for KELT-9 b and introduced in the previous Chapter to analyse the single lines of five planets: KELT-20 b, KELT-6 b, WASP-69 b, GJ-3470 b and WASP-107 b. In particular, we used KELT-20 b as a benchmark to validate the method, as it shows conditions similar to KELT-9 and it has been already analysed with other methods. Eventually we applied the method to a small sample of heterogenous target, KELT-6 b, WASP-69 b, GJ-3470 b and WASP-107 b. These planets are colder and smaller than KELT-9 b and KELT-20 b, and hence represents a valid opportunity to test the framework with target showing different conditions. In Table 3.1 we show the parameters of the planets and stars analysed in this section.

Table 3.1: Parameters of KELT-6, WASP-69, WASP-107, GJ-3470, and KELT-20 from Damasso et al. (2015), Bonomo et al. (2017), Anderson et al. (2017), Awiphan et al. (2016), and Lund et al. (2017) respectively.

	KELT-6/KELT-6 b	WASP-69/WASP-69 b	WASP-107/WASP-107 b	GJ-3470/GJ-3470 b	KELT-20/KELT-20 b
$M_\star$ [$M_\odot$]	1.126 ± 0.058	0.826 ± 0.029	0.69 ± 0.05	$0.539^{+0.047}_{-0.043}$	$1.76^{+0.14}_{-0.19}$
$R_\star$ [$R_\odot$]	$1.529^{+0.143}_{-0.137}$	0.813 ± 0.028	0.66 ± 0.02	0.547 ± 0.018	$1.565^{+0.057}_{-0.064}$
$T_{\rm eff}$ [K]	6272 ± 61	4700 ± 50	4430 ± 120	3600 ± 100	8720^{+250}_{-260}
Z [dex]	-0.27 ± 0.06 [Fe/H]	0.150 ± 0.080	0.020 ± 0.100 [Fe/H]	0.20 ± 0.10 [Fe/H]	$0.29^{+0.22}_{-0.36}$ [Fe/H]
$\log g$	4.12 ± 0.07	4.50 ± 0.15	4.5 ± 0.1	4.695 ± 0.046	$4.290^{+0.017}_{-0.020}$
γ [km/s]	1.1 ± 0.2	-9.62826 ± 0.00023	14.160 ± 0.002	26.51691 ± 0.00053	-23.3 ± 0.3
$v \sin i$ [km/s]	4.53 ± 0.26	2.20 ± 0.40	2.5 ± 0.8	$\lesssim 2$	117.4 ± 2.9
Spectral type	F8	K5	K6	M1.5	A2
P [days]	7.8455821 ± 0.0000070	3.8681382 ± 0.0000017	5.721490 ± 0.0000002	$3.3366496^{+0.0000039}_{-0.0000033}$	3.4741085 ± 0.0000019
M_p [M_J]	0.442 ± 0.019	0.250 ± 0.023	0.12 ± 0.01	0.0437 ± 0.0047	< 3.382
$R_{\rm p}$ [R_J]	1.18 ± 0.11	1.057 ± 0.047	0.94 ± 0.02	0.408 ± 0.016	$1.741^{+0.069}_{-0.074}$
ρ_p [g/cm^3]	$0.33^{+0.120}_{-0.120}$	$0.262^{+0.047}_{-0.039}$	0.19 ± 0.03	0.80 ± 0.13	0.80 ± 0.13
a [AU]	0.080 ± 0.001	$0.04527^{+0.00053}_{-0.00054}$	0.055 ± 0.001	0.0355 ± 0.0019	$0.0542^{+0.0014}_{-0.0021}$
$T_{\rm eq}$ [K]	1313^{+59}_{-38}	963 ± 18	770 ± 60	593.5 ± 96.5	2262 ± 73
i [deg]	$88.81^{+0.79}_{-0.91}$	86.71 ± 0.20	89.7 ± 0.2	$89.13^{+0.26}_{-0.34}$	$86.12^{+0.28}_{-0.27}$
λ [deg]	-36 ± 11	$0.4^{+2.0}_{-1.9}$	$118.1^{+37.8}_{-19.1}$	98^{+15}_{-12}	3.4 ± 2.1

3.1.1 Methods

We tested several steps of the framework that I developed and introduced in the previous chapter to assess the presence of hydrogen, sodium, and calcium in the atmospheres of the target investigated.

Table 3.2: Info about the observation nights for each target.

Target	Night	Date	# spectra	Average SNR
KELT-20	#1	2017-08-16	90	51
	#2	2018-07-12	116	78
	#3	2019-07-19	78	81
	#4	2019-08-26	30	13
	#5	2019-09-02	29	14
	#6	2022-07-41	30	10
KELT-6	#1	2015-04-11	31	47
WASP-69	#1	2016-06-04	17	36
	#2	2016-08-04	18	29
	#3	2019-07-24	25	32
	#4	2020-08-09	24	41
WASP-107	#1	2019-02-08	18	18
	#2	2019-05-04	20	20
GJ-3470	#1	2018-01-13	15	6
	#2	2018-01-23	17	8
	#3	2019-02-04	16	6
	#4	2019-12-28	18	13
	#5	2020-01-28	14	14
	#6	2022-12-24	15	18

Data Preparation and Normalization

We analysed the datasets obtained in almost ten years of the GAPS program with HARPS-N. A log of the transits observed can be seen in Table 3.2 The data normalization process was crucial for accurate spectral analysis. Each collected spectrum was divided by its continuum shape to bring their flux values to a common level. The shape of the spectrum was obtained by applying a Gaussian filter with a standard deviation large enough to smooth out all lines, typically set to $\sigma = 10,000$. This filtering allowed the extraction of a continuum that approximates the overall trend of the spectra without the influence of narrow spectral lines. The normalization method ensured that variations across different spectra were minimized, allowing for direct comparison of the observed absorption features.

A secondary normalization method was employed for specific spectral lines, such as Hα , when the initial approach produced an incorrect continuum slope. This alternative method involved selecting two equidistant intervals from the spectral line center, fitting linear functions within these intervals, and using the fitted lines to scale the spectra. This approach helped maintain the symmetry of the line shapes, critical for accurate absorption depth measurements.

Stellar Signal Removal and Master-Out Spectrum Creation

To isolate the planetary signal, a master-out spectrum was generated by averaging all out-of-transit spectra from each observation night. This master-out spectrum represents the star's contribution without the planet's interference. Each in-transit spectrum was then divided by the corresponding master-out spectrum, effectively removing the stellar component and revealing the planetary absorption features. The stellar spectra also underwent correction for systematic radial velocity shifts using the formula:

$$\lambda_{\text{star}} = \lambda_{\text{sun}} \sqrt{\frac{1 - \gamma/c}{1 + \gamma/c}} \tag{3.1}$$

where γ is the star's systemic radial velocity, allowing the spectra to be accurately analysed in the host star's reference frame.

Telluric Line Correction

Since the **HARPS-N** instrument is ground-based, the collected spectra were contaminated by telluric lines from Earth's atmosphere, particularly in regions between 5870–5940 Å and 6450–6600 Å. These lines were removed using the Molecfit software, which fits a model of the Earth's atmospheric absorption and corrects the observed spectra. The correction ensured that telluric absorption did not interfere with the planetary signals, particularly crucial for the accurate analysis of the Hα and sodium doublets.

Tomographic Mapping

The corrected spectra were arranged in a two-dimensional tomographic map with rows corresponding to individual spectra ordered by the orbital phase and columns representing radial velocity or wavelength values. The tomographic map provided a visual representation of how spectral lines vary during the planet's transit. The planetary absorption signal appeared as a dark trace within the map, indicating a reduction in flux where atmospheric absorption occurs.

Rossiter-McLaughlin Effect Correction

The Rossiter-McLaughlin (RML) effect, caused by the stellar rotation during the planetary transit, introduces apparent emission features that can obscure the true planetary absorption signals. The effect was corrected by calculating the obscured stellar flux for each in-transit spectrum using a limb-darkening model defined by:

$$I(\mu) = I_0[1 - c_1(1 - \mu) - c_2(1 - \mu)^2] \tag{3.2}$$

where μ is the distance from the star's edge, and c_1, c_2 are limb-darkening coefficients. By removing the calculated obscured flux from the master-out, the corrected tomographic maps better isolated the true planetary absorption features.

3.1.2 Results

KELT-20 b: validation of the method

The atmospheric analysis of KELT-20 b served as a benchmark to validate the methods employed in Chapter 2 due to its well-documented Balmer lines and sodium doublets observed in previous studies Fossati et al. (2023a); Casasayas-Barris et al. (2019) along with its properties similar to KELT-9 b's ones. The Hα absorption (shown in details in Fig. 3.1) feature was prominently detected with a depth of approximately 0.73%, significantly larger than the initially uncorrected depth of 0.69%. The corrected depth corresponds to an extended atmospheric height of about 25.97% of the planet's radius ($R_{pl+atm} = 1.2597 \pm 0.013 R_{pl}$).

Additionally, other lines in the Balmer series, including Hβ , Hγ , and Hδ , were identified, although with progressively smaller depths. The analysis indicated that the hydrogen atmosphere is both extended and hot, with line shapes suggesting the presence of high-energy processes such as photoionization and thermal escape. Comparisons with Fossati et al. (2023a) revealed similar line strengths, validating the transmission spectroscopy and normalization methods employed in this thesis. The detection of sodium (Na I) and calcium (Ca II) doublets also aligned well with previously reported values, confirming the method's robustness in isolating planetary atmospheric features. We show the results obtained in Fig. 3.2 and Fig. 3.3.

WASP-69 b: Detection of Na I D2

The atmosphere of WASP-69 b, a warm Jupiter with a K5-type host star, showed none of the Balmer lines. We observe an absorption signal in the in-transit spectrum of the D2 line of the sodium doublet corroborating the detection by Casasayas-Barris et al. (2017). This is evident in the transmission spectra (Fig. 3.4, fourth row). For the D1 line, there is no detection, while for the D2 line we obtained an absorption depth of (4.27 $\pm$ 1.16)%, which corresponds to a planet radius of (1.87 $\pm$ 0.03)Rpl. This result has a significance of 3.68σ (marginally detection) and is marginally comparable with the (5.8 $\pm$ 0.3)% by Casasayas-Barris et al. (2017).

KELT-6 b $H\gamma$ spurious detection

KELT-6 b, a warm sub-Jupiter, displayed no detection of $H\alpha$, $H\beta$, and $H\delta$ lines as any Gaussian fit gives meaningless results for their respective transmission spectra. In such cases where it is not possible to perform a Gaussian fit, it is not possible to iterate the process to obtain a more accurate correction of the RML effect since there is no value for the height of the atmosphere. We report the detection of $H\gamma$ with a depth of (3.14 $\pm$ 0.53)%. One possible explanation for the detection of $H\gamma$ without $H\alpha$ $H\beta$ is that the detected line is a stellar residual due to an inaccurate correction of the RML effect. The analysis of the Ca doublet for this target is difficult because of the low signal in the bluest part of **HARPS-N** spectrum. We did not detect any Na lines.

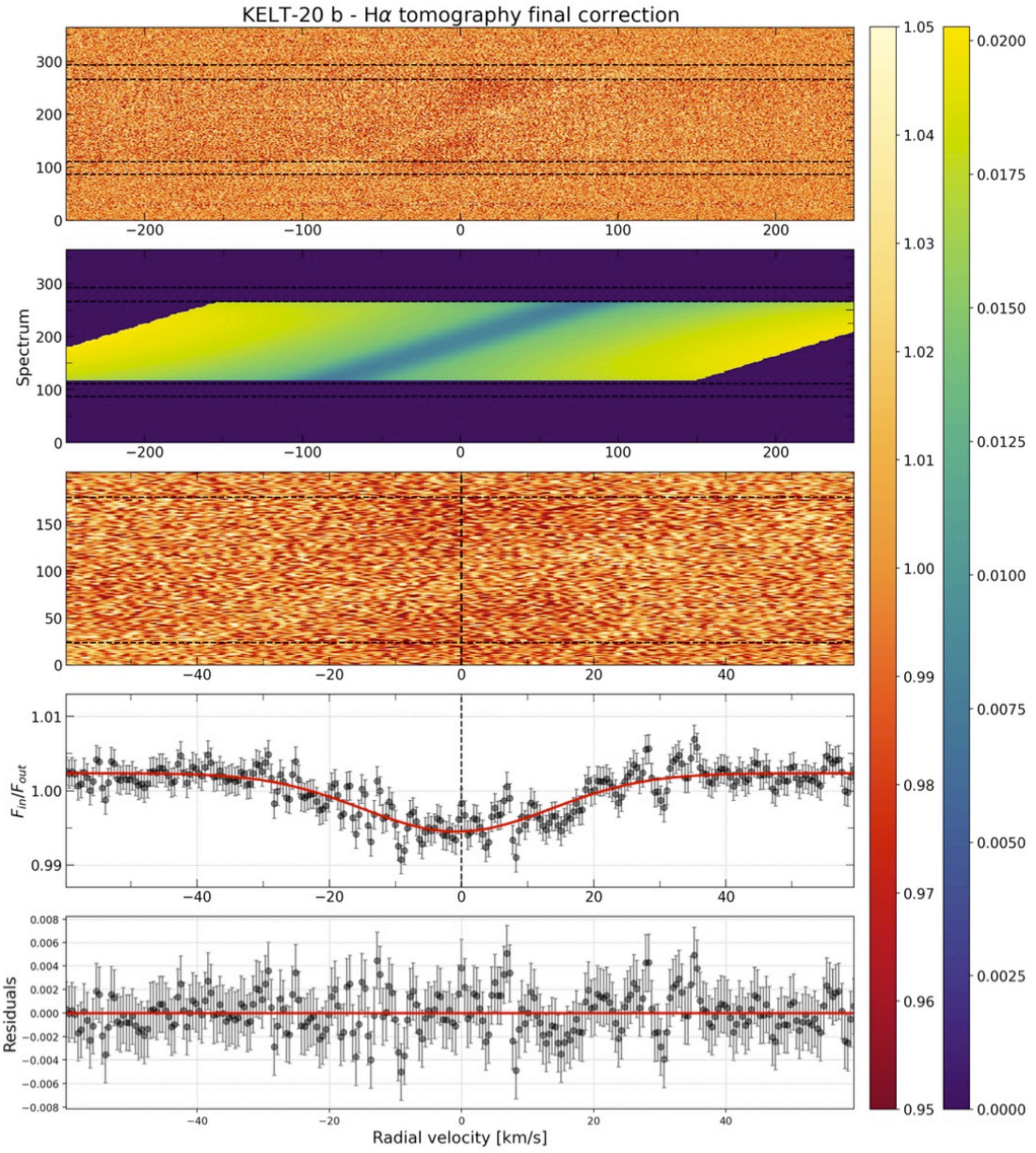

Figure 3.1: Hα results for KELT-20 b. First row: tomographies before the correction of the RML effect. The four black dashed horizontal lines indicate, starting from the bottom, the times t1, t2, t3 and t4 respectively. Second row: Correction terms for the RML effect of the last step of the iteration. They have been estimated starting from the ATLAS stellar models. Third row: tomographies after the correction of the RML effect. The black dashed horizontal lines have the same meaning of the ones in the first row. Fourth row: Transmission spectra of the Balmer series lines. The red curve are the Gaussian fits applied on them. Fifth panel: residuals of the Gaussian fits. Adapted from Valerio Fardella's master thesis.

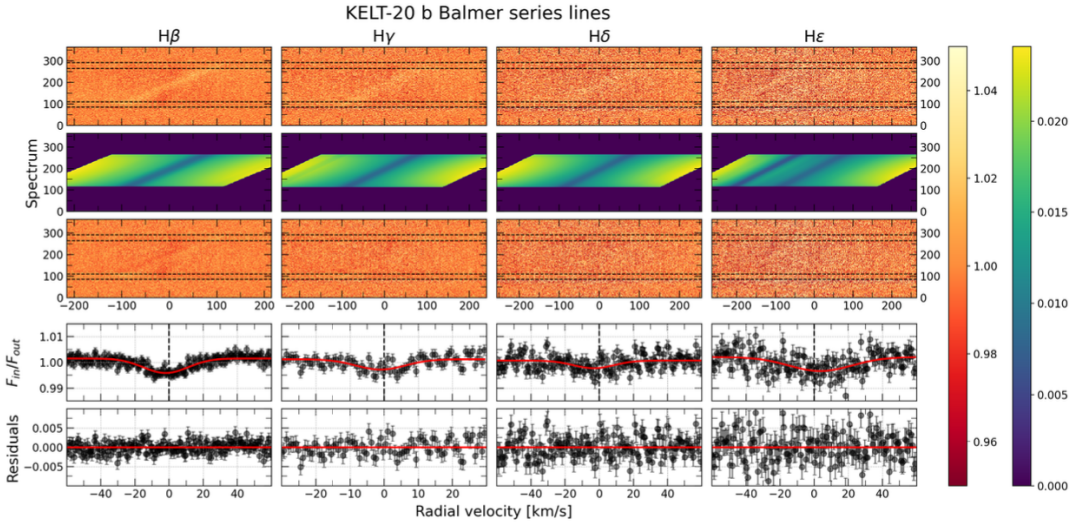

Figure 3.2: Same as Fig. 3.1 for the Hβ , Hγ , Hδ and Hϵ lines of KELT-20 b. Adapted from Valerio Fardella's master thesis.

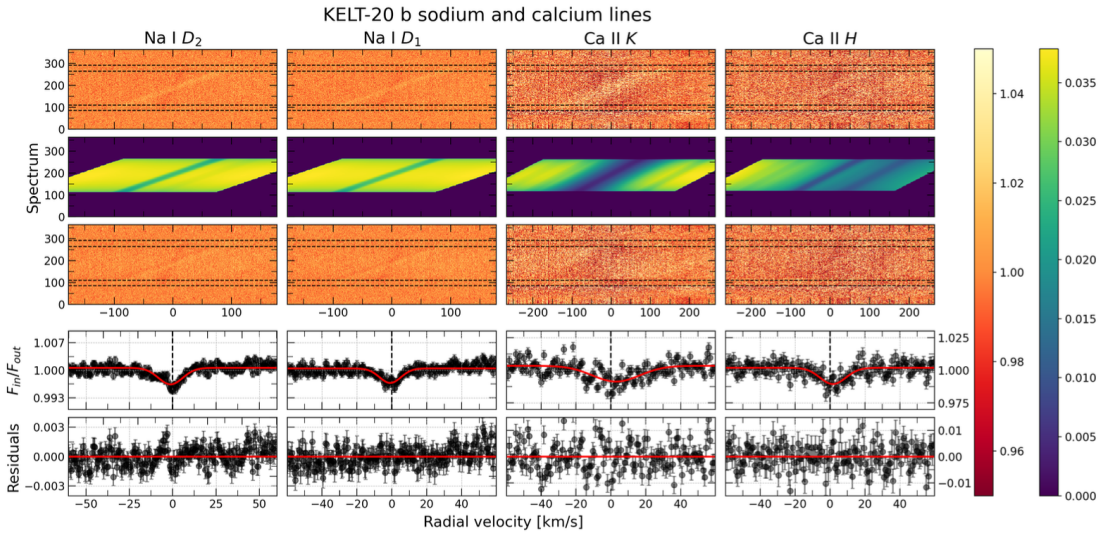

Figure 3.3: Same as Fig. 3.1 for the Na I and Ca II doublets of KELT-20 b. Adapted from Valerio Fardella's master thesis.

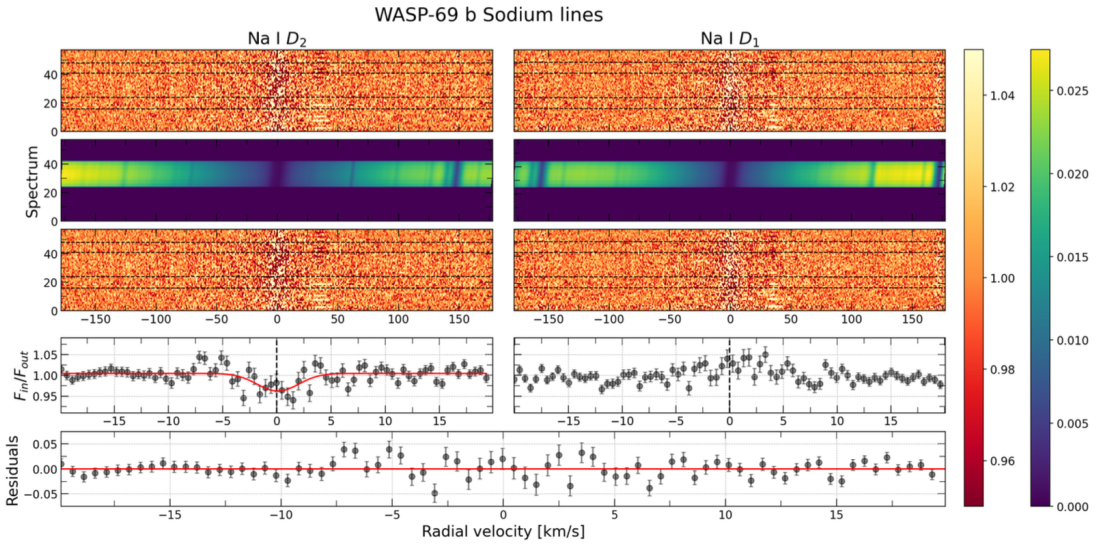

Figure 3.4: First row: tomographies before the correction of the RML effect of the D2 and D1. The four black dashed horizontal lines indicate, starting from the bottom, the times t1, t2, t3 and t4 respectively. Second row: Correction terms for the RML effect of the last step of the iteration. They have been estimated starting from the ATLAS stellar models. Third row: tomographies after the correction of the RML effect. The black dashed horizontal lines have the same meaning of the ones in the first row. Fourth row: Transmission spectrums of the Balmer series lines. The red curve in the left panel is the Gaussian fit for the D2. Fifth row: residuals of the Gaussian fit of the D2. Adapted from Valerio Fardella's master thesis.

GJ-3470 b and WASP-107 b non detections

Neither the Warm Jupiter WASP-107 nor the cooler GJ-3470 b show any detection in our analysis most probably due to the very noisy data. In particular, GJ-3470 b, is a cooler and less massive exoplanet compared to the other hot Jupiters analysed. Moreover, it orbits around a M dwarf type star, which is particularly challenging to analyse due to the large activity and noisy data.

3.1.3 Discussion and conclusions

The results of Fardella's master thesis align well with findings from other studies that utilize high-resolution spectroscopy for exoplanet atmospheric characterization. In particular, the pronounced Balmer series detections in KELT-20 b are consistent with studies that observe significant hydrogen-driven atmospheric escape. For example, Yan & Henning (2018) identified similar deep Hα absorption features in ultra-hot Jupiters, supporting the theory of photo-evaporation as a key atmospheric process in these planets.

The methods used to correct for the Rossiter-McLaughlin effect and telluric contamination introduced in the previous chapter proved highly effective, as validated by comparisons with Casasayas-Barris et al. (2019), where similar corrections allowed for precise measurements of atmospheric depths. The detailed correction for stellar activity and limb darkening further strengthened the robustness of the results, particularly in resolving fine spectral features that distinguish planetary signals from stellar noise.

The study confirms that hot Jupiters possess highly dynamic and extended hydrogen atmospheres that are prone to significant mass loss. The detection of extensive Balmer lines in the atmospheres of planets like KELT-20 b may indicate ongoing thermal escape, driven by high stellar irradiation levels supported by the large host star temperatures. These findings align with theories of photoionization-induced escape, where intense ultraviolet and X-ray fluxes from the host stars heat the upper atmospheres, causing them to expand and lose mass as discussed in Section 2.1.

Despite the non detection of Hα , Na and Ca in their atmospheres, the work done for WASP-69 b and GJ-3470 b have been used as starting point of the analysis I carried on in the visible part of the spectrum in Guilluy et al. (2024) discussed in Section 4.1.

3.2 Atmospheric characterisation of TOI-1518 b

In this section I will introduce the ongoing work that I am leading on the analysis of the **UHJ** TOI-1518 b with **HARPS-N** and GIANO-B data. The target was part of a proposal aimed to investigate the presence of Balmer lines in the atmospheres of planets orbiting A and early F-type stars, that was lately included in the BRIDGES programme (P.I. Borsa).

Table 3.3: Parameters from Cabot et al. (2021) used in all the analyses of TOI-1518 b.

Parameter	Value	Reference
Stellar parameters		
$M_\star$ ($M_\odot$)	1.79 ± 0.26	Cabot et al. (2021)
$R_\star$ ($R_\odot$)	1.95 ± 0.05	Cabot et al. (2021)
Effective temperature(K) . .	7300 ± 100	Cabot et al. (2021)
log g ($\log_{10}$(cm s^{-2}))	4.1 ± 0.2	Cabot et al. (2021)
Metallicity, [Fe/H](dex) . .	-0.10 ± 0.12	Cabot et al. (2021)
Planetary parameters		
Planetary mass, M_p (M_{jup})	< 2.3	Cabot et al. (2021)
Planetary radius, R_p (R_{jup})	1.875 ± 0.053	Cabot et al. (2021)
Orbital inclination, i (deg)	77.92 ± 0.24	Cabot et al. (2021)
Projected obliquity,λ (deg)	$240.34^{+0.93}_{-0.98}$	Cabot et al. (2021)

3.2.1 Introduction

Many UHJs, which have equilibrium temperatures exceeding 2000 K (Fortney et al. 2008) contain vaporized metals, both neutral and ionized, in their upper atmospheres (e.g., Casasayas-Barris et al. 2017; Hoeijmakers et al. 2018). These metals and the molecules containing them are recognized as strong sources of opacity in the optical and near-ultraviolet regions (Fortney et al. 2008). UHJs often exhibit thermal inversions (e.g., Haynes et al. 2015); however, the exact species responsible for the inversions are debated (Fortney et al. 2008; Lothringer et al. 2022). High-resolution spectroscopy has become a common method for detecting important species in **UHJ** atmospheres, and also serves as a mean of probing winds (Louden & Wheatley 2015; Casasayas-Barris et al. 2019) and extended atmospheres (Yan & Henning 2018). TOI-1518 b, a highly irradiated gas-giant planet possessing iron vapour in its atmosphere is among the first exoplanets discovered by **Transiting Exoplanet Survey Satellite (TESS)** with an high-resolution detection of an atmospheric species as shown by Cabot et al. (2021). This planet is orbiting a fast-rotating F0-type star of 7300K. Table 3.3 summarizes the physical properties of TOI-1518 and TOI-1518 b. The planet with an equilibrium temperature, Teq = 2498 K is ideal for a direct application of the single line analysis because of its conditions similar to KELT-9 b. The system parameters results in a scale height, H = 551 km and a transmission spectroscopy metric, **Transmission Spectroscopy Metric (TSM)** = 352. Usually, the best targets for transmission spectroscopy have a TSM larger than 90, underlying the potentiality of TOI-1518 b for transmission spectroscopy.

3.2.2 Observations and methods

We collected two transits of the planet during 5th and 7th of September 2023 with both **HARPS-N** and GIANO-B spectrographs at the **Telescopio Nazionale Galileo (TNG)**

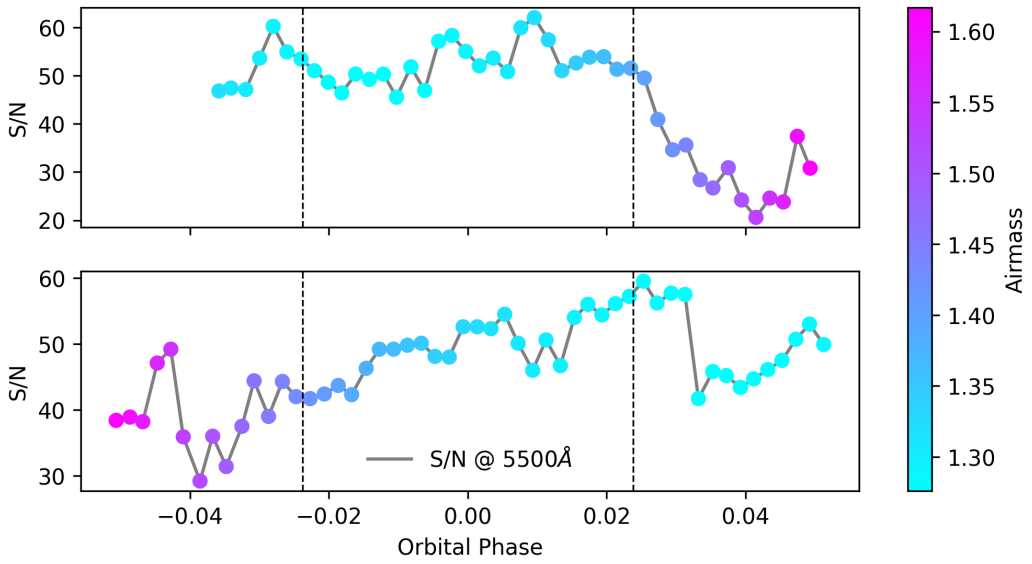

Figure 3.5: S/N as a function of the orbital phase for the two observed nights of TOI-1518 b (top and bottom panels refer to the 5th and 7th of September 2023, respectively). Dashed vertical lines represent the ingress and egress, while colormap shows the airmass.

in GIARPS configuration. The data have been obtained as part of the BRIDGES large programme within the Italian **Global Architecture of Planetary System (GAPS)** collaboration. We registered an average S/N ratio at 5500 Å of $\sim$ 50 for both nights as shown in Fig. 3.5 with no overall problems or anomaly conditions during the observing nights.

The **HARPS-N Data Reduction Software (DRS)** automatically computes the cross-correlation function between the collected raw 1D spectra and a stellar template obtaining the so called **CCF**, which represents an average line profile for all the stellar lines in the spectrum. We can apply to this **CCF** the same analysis employed for the individual lines and compute the master-out and, eventually, the 2D tomography in the stellar reference frame. This is shown in Fig. 3.6. From the plot we can clearly see the presence of both a dark region following the expected planetary trajectory and a brighter region that match the region of the stellar disk we expect the planet to cover during the transit. The first one represents the atmospheric absorption of the species in the atmosphere of our target, while the second one represents the **RME**. The results of this work are the subject of a paper in preparation within the Italian **GAPS** collaboration, led by myself with the contribution of Federico Biassoni, Francesco Borsa and Gloria Guilluy.

Single line analysis We analysed the single line of the targets with a straightforward application of the framework introduced in D'Arpa et al. (2024b) and discussed in the previous chapter analysing several lines belonging to H I, Na I, Ca II, Ti II, Fe I , Fe II,

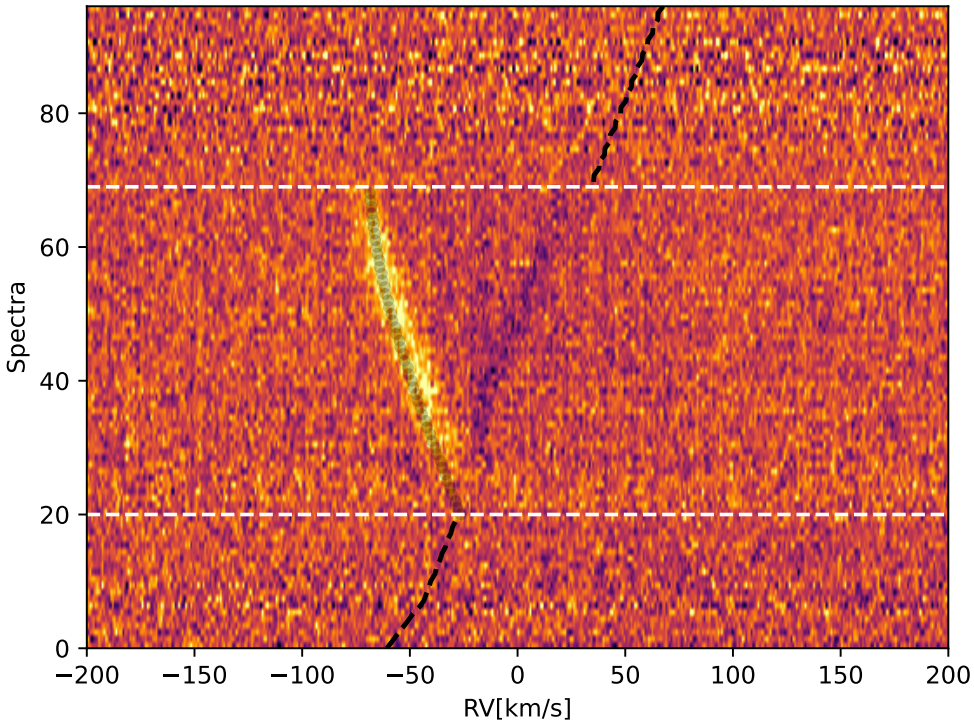

Figure 3.6: Residuals of the **Cross Correlation Function (CCF)** in the stellar reference frame for TOI-1518 b. The dark region following the expected planetary trajectory (dashed lines) represents the atmospheric absorption of the species in the atmosphere of our target. The brighter region that match the region of the stellar disk we expect the planet to cover during the transit (circles) represents the **RME**. The white dashed lines represent the ingress and egress of the transit.

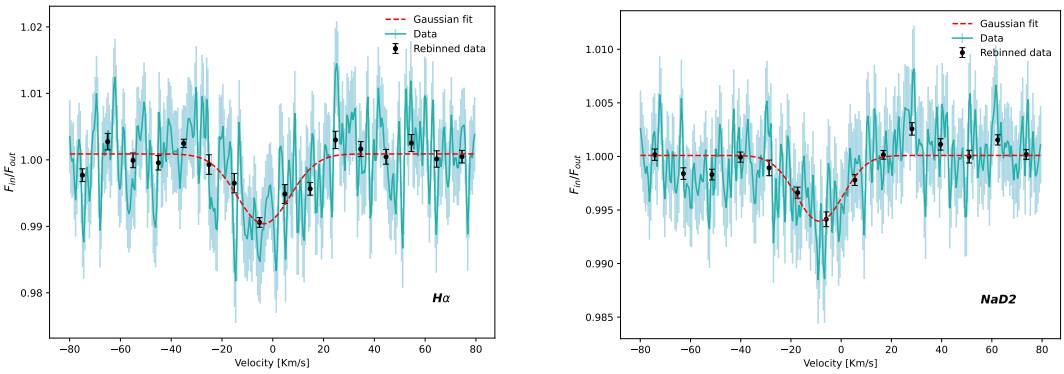

Figure 3.7: Detected lines in the atmosphere of TOI-1518 b.

Ba II, Mg I, Cr II and Sc II analogously to what done for KELT-9 b. Moreover, we also investigated the He I triplet that will be introduced in Chapter 4 with the same method discussed in Guilluy et al. (2024); D'Arpa et al. (2024a). Our analyses included the telluric removal with Molecfit and the modelling and removal of the **RME+Centre to Limb Variation (CLV)**.

Cross-correlation with templates Along with the single line analysis we also performed a cross-correlation with templates employing the method described in Biassoni et al. (2024a) and in Section 4.2.2. We employed 5 sets of the Kitzmann templates with temperature of 2500K, 3000K, 3500K, 4000K and 5000K and investigated all the available templates in the database [1] for each temperature.

3.2.3 Results

Single line analysis

We successfully detected the Hα line from the H I Balmer series without detecting any of the other lines in the series observable with **HARPS-N**. This result is not unexpected as the other Balmer series lines are weaker and have been detected only in few targets (HD189733 b, KELT-9 b, and KELT-20 b/MASCARA-2 b; e.g., Cauley et al. 2016; Cauley et al. 2019; Casasayas-Barris et al. 2019). We also detected one of the two lines in the Sodium doublet. We show the two detections in Fig. 3.7. Apart from the two lines shown in Fig. 3.7, we were not able to detect any other line. We were also not able to investigate the Ca II H & K lines due to the low S/N ratio in the bluest part of the **HARPS-N** spectrum. In the nIR we tried unsuccessfully to detect the He I triplet. Orell-Miquel et al. (2024) in their catalogue level analysis showed that the He I triplet has never been detected in planets around hot stars such as TOI-1518. This is mostly due to the lack of XUV stellar irradiation in the stars of hotter spectral types (A, F and G), making no previous ionization of He, needed to form the He I metastable triplet.

[1] https://cdsarc.cds.unistra.fr/viz-bin/cat/J/A+A/669/A113

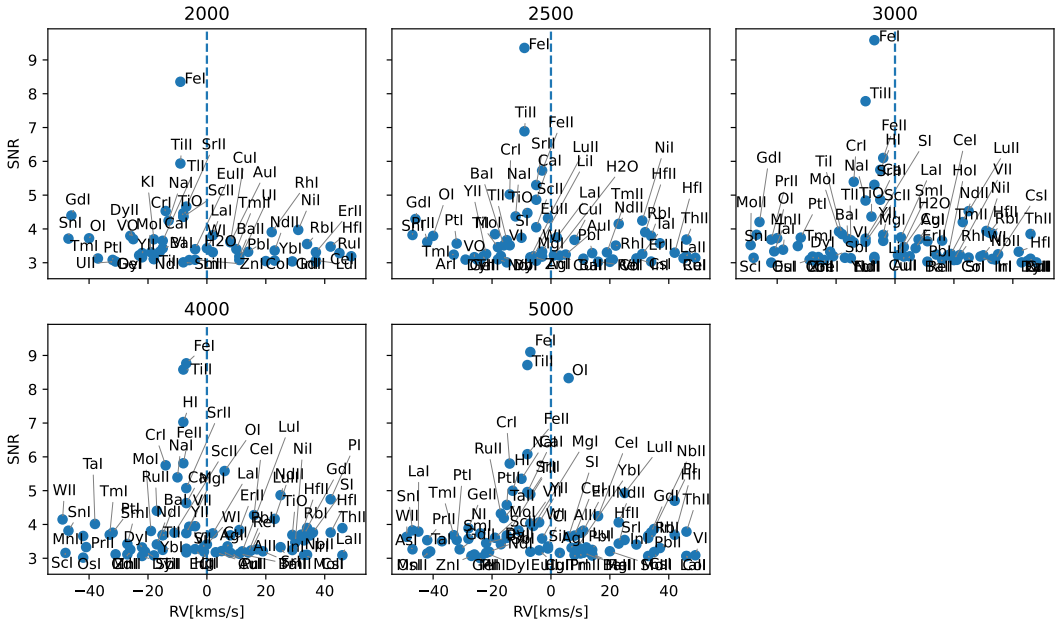

Figure 3.8: SNR vs **Radial Velocity (RV)** for the investigated species in TOI-1518 b with SNR larger than 3σ.

Cross-correlation with templates

The single line analysis is a powerful tool to investigate key feature of atomic species like the atmospheric depth and the rotational broadening. However, as discussed in the previous chapter, this method requires a large S/N ratio and it is not the best method to assess the presence of atomic species in the atmosphere. The primate is handled by the cross-correlation with templates, which manages to better detect the investigated species by combining multiple lines. We tested more than 40 atomic species, both neutral and ionised, with the different temperature templates. In Fig. 3.8 we show all the species and their signal to noise ratio, SNR, that help us understanding the significance of the detection. We selected only the species with SNR larger than 3 σ, and as we can see, there are several species with SNR larger than 4 σ which is often the threshold set for the detection. In Fig. 3.9 we selected for each temperature only the species with a SNR larger than 3.5 σ to account for species below the 4 σ threshold that can be considered tentatively detected. The number of species we investigated increases with the temperature templates used since it results in more ionised species showing lines in the visible range of **HARPS-N** spectrum. We also consider only the species with a velocity shift between -20 km s^{-1}and 20 km s^{-1}as we consider the detection of species with larger shifts due to spurious signals. We investigated individually all the species in Fig. 3.9 to evaluate if the signal was arising from the planetary atmosphere or from other effects such as aliases. From Fig. 3.10 to Fig. 3.14 we show the Kp (defined in Section 5.4) vs **RV** maps for all the detected and tentatively detected species.Considering all the templates, we detected Ca II, Cr II, Fe I, Fe II, Na I, Ti II, Sc II, Sr II and tentatively

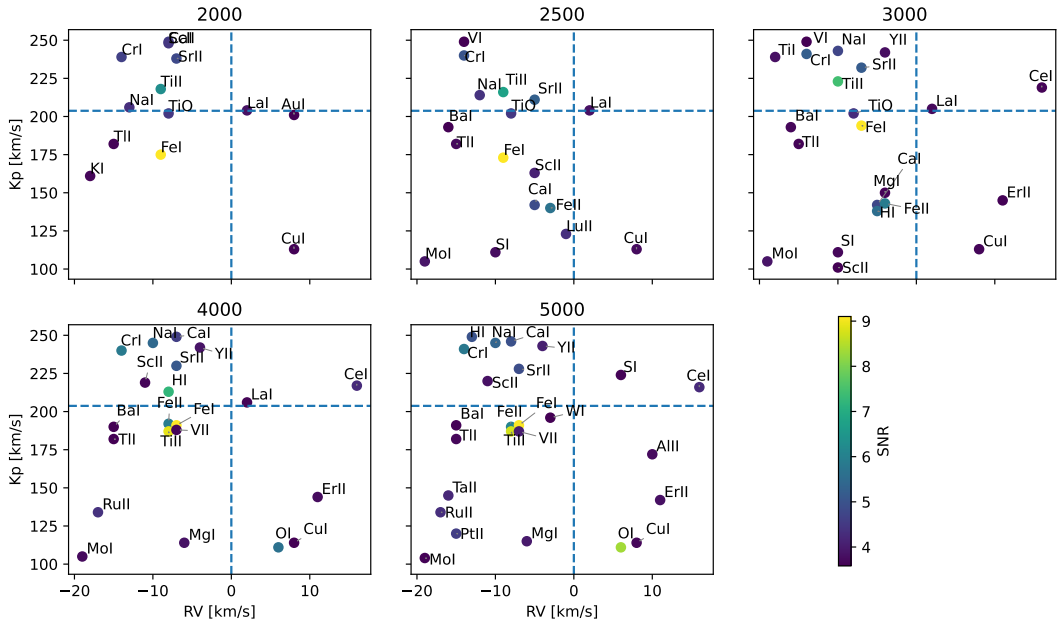

Figure 3.9: Kp vs **RV** for the investigated species for each temperature template in the atmosphere of TOI-1518 b. We selected only the species with a SNR larger than 3.5 σ and a velocity shift between -20 km s^{-1}and 20 km s^{-1}. The colormap represents the SNR, while the dashed lines represent the expected position of the signal in terms of RV and Kp.

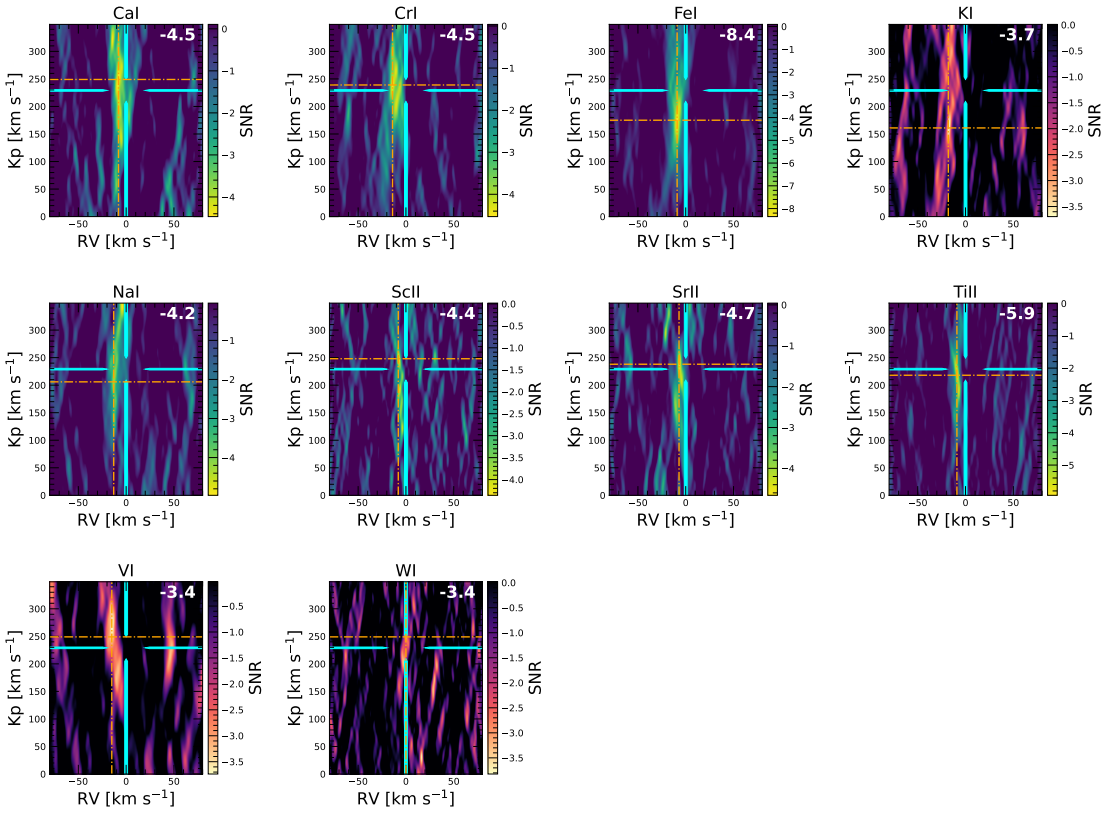

Figure 3.10: Kp vs **RV** maps for all the detected and tentatively detected species with the 2000K templates in TOI-1518 b. We used two different colormaps for the species with SNR larger than 4 σ and the ones without. In each panel the SNR is represented negatively. We also show with the cyan lines the expected position of the signal, **RV** = 0 km s^{-1}and Kp = 226 km s^{-1}.

detected Al II, Mg I, V I, V II, Y II, K I and W I.

Multiple lines analysis

We detected several species with the cross-correlation that we were not able to detect with the single line analysis. This is the reason why we use the cross-correlation with templates, to increase the signal considering all the individual lines together. However, this technique does not hold information neither on the depths of the lines and hence on their height in the atmosphere nor on the width of the lines and hence on the rotational broadening. To acknowledge these quantities we need single line analysis. Since for species such as Fe II and Ti II we can clearly see a detection in the cross-correlation but not the single lines we tried a different approach. We combined all the 2D tomographies we computed for the single lines individually computing the weighted average for both Fe II and Ti II. We used the same line-lists employed for KELT-9 b. In Fig. 3.15 we show the combined tomographies in the stellar reference frame and the transmission spectra. In the tomographies we can clearly see once again the bright region due to the

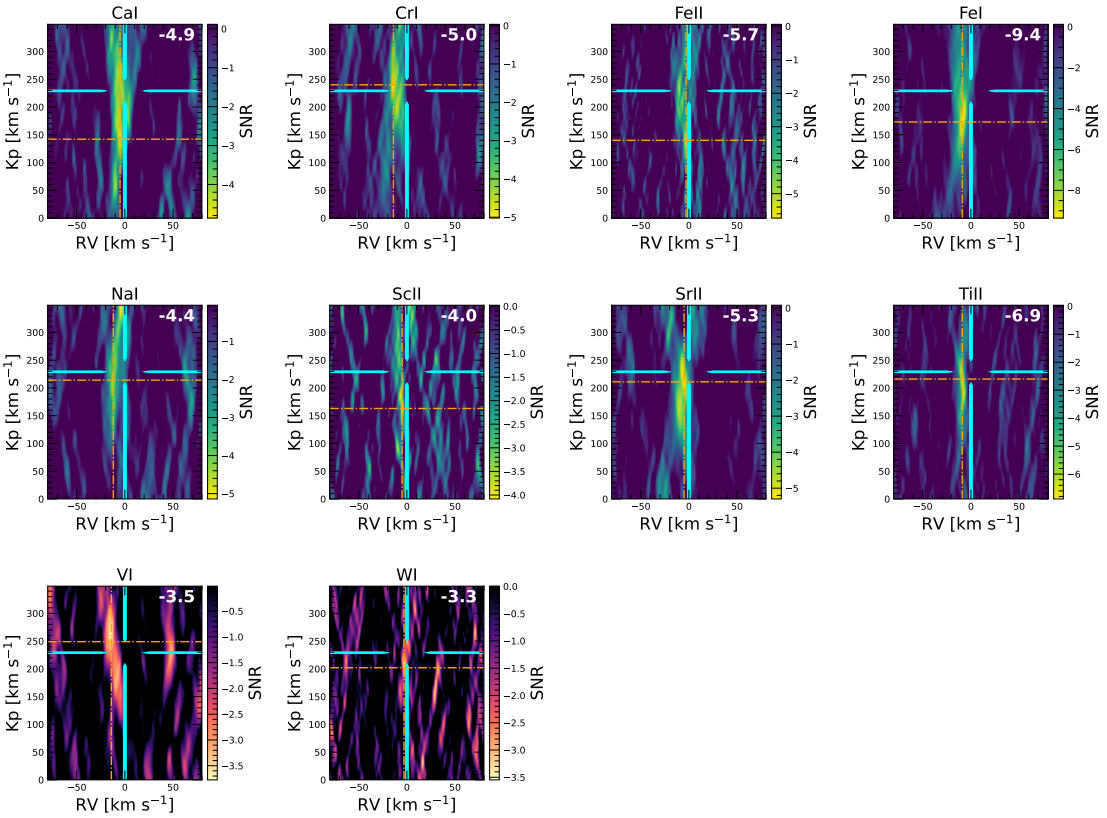

Figure 3.11: Same as Fig. 3.10 for the 2500K templates.

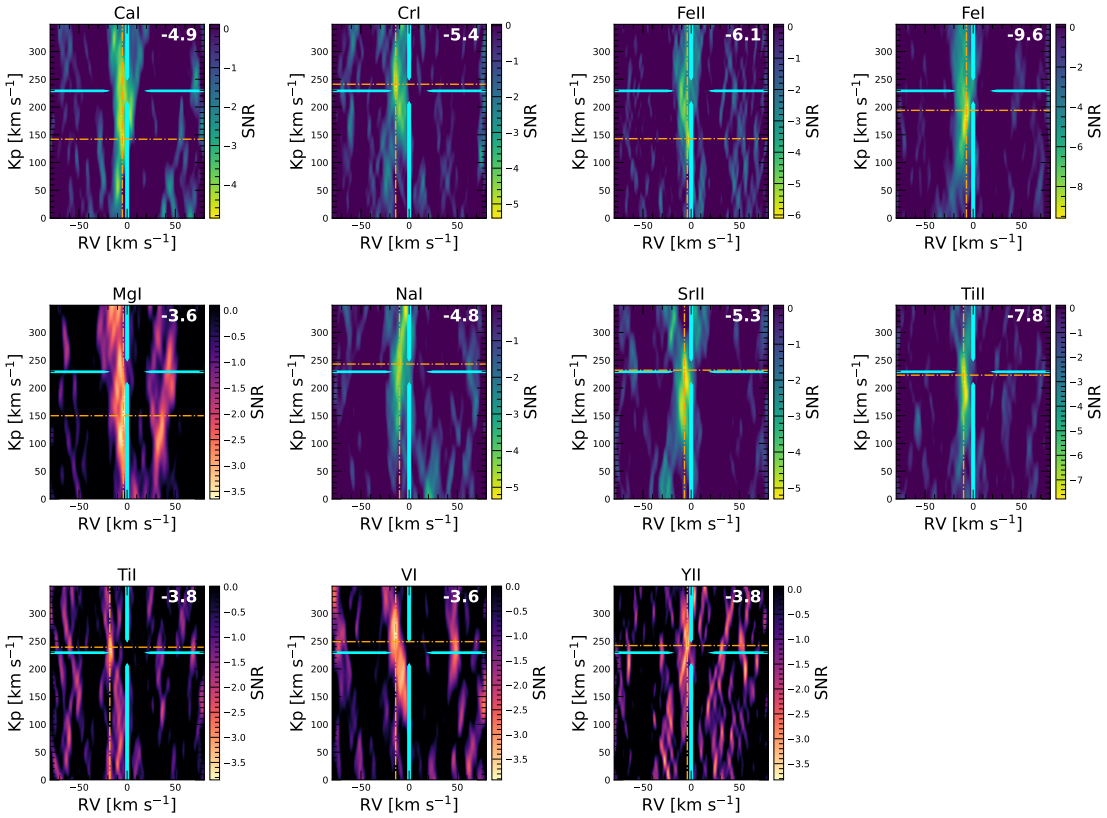

Figure 3.12: Same as Fig. 3.10 for the 3000K templates.

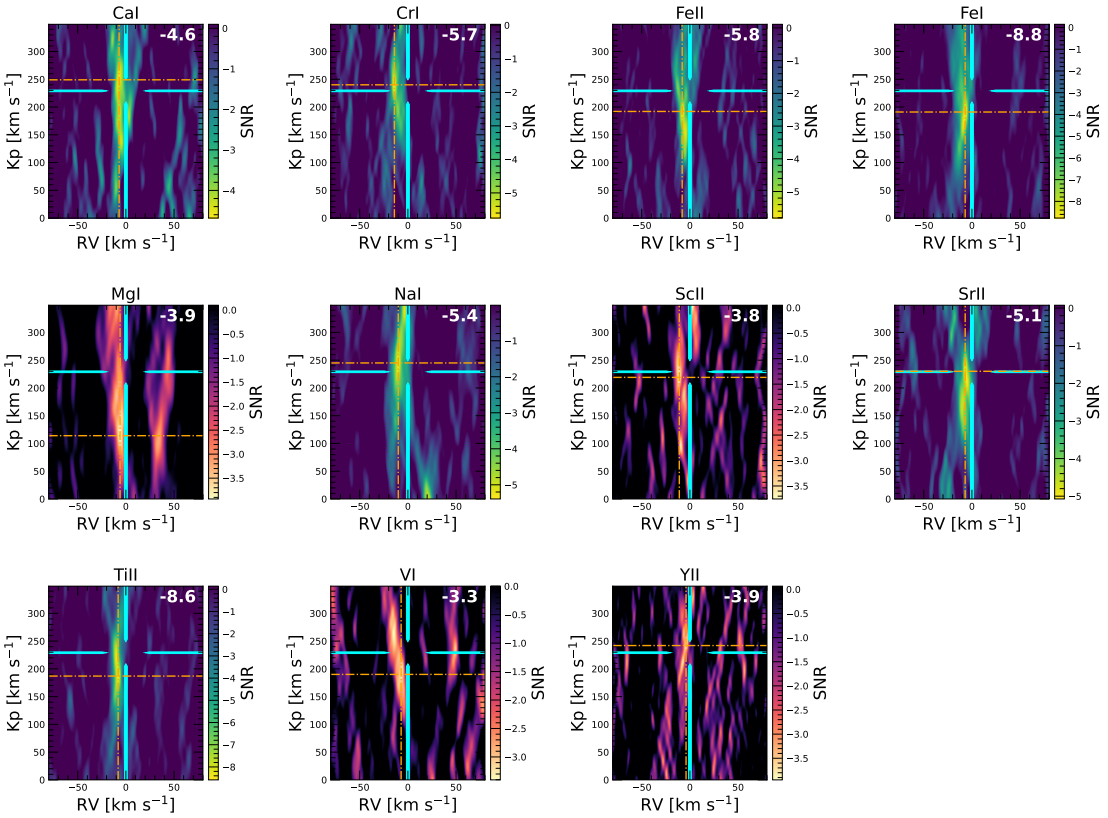

Figure 3.13: Same as Fig. 3.10 for the 4000K templates.

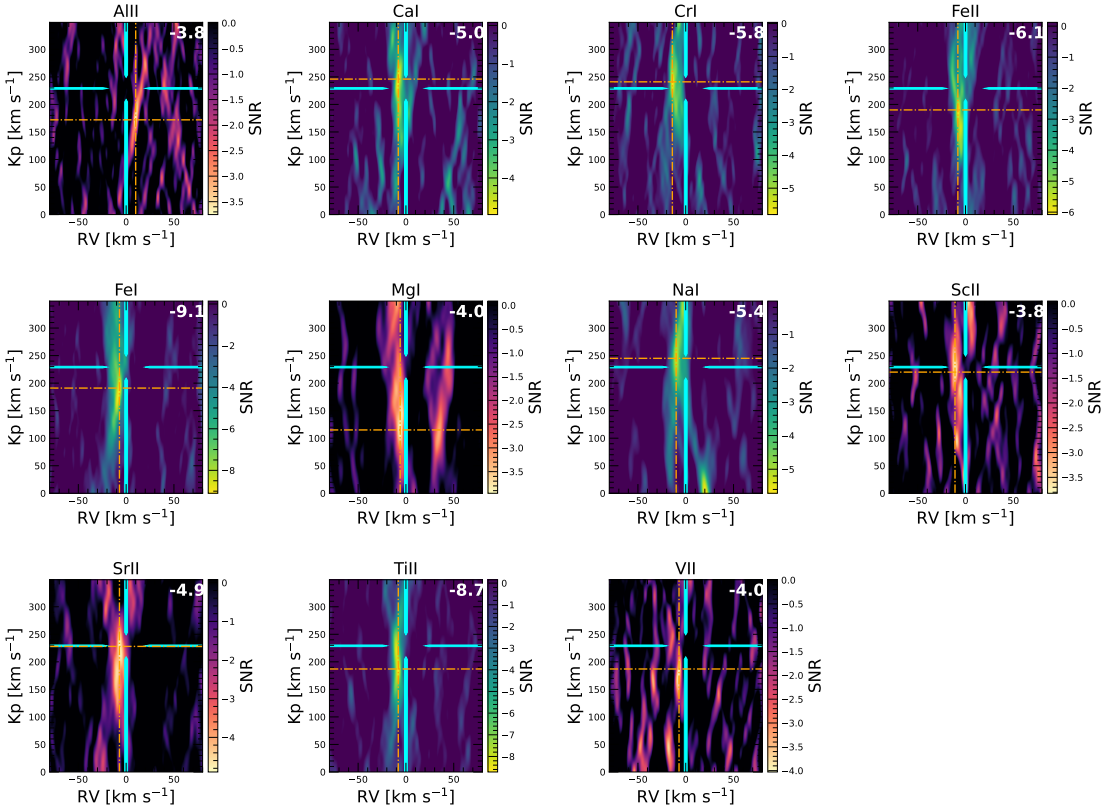

Figure 3.14: Same as Fig. 3.10 for the 5000K templates.

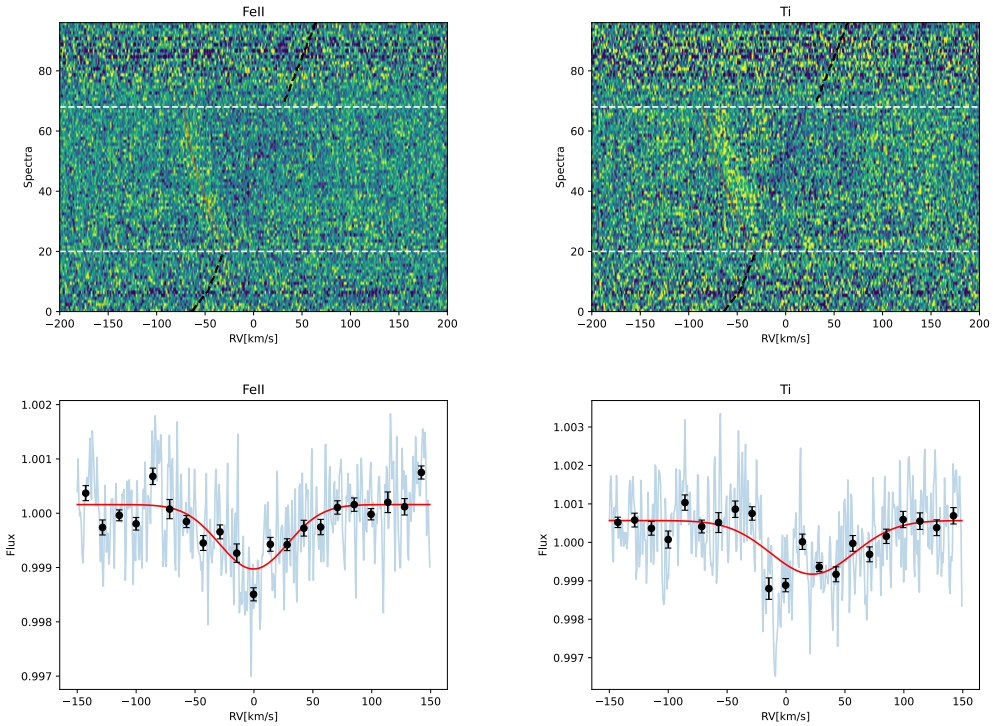

Figure 3.15: Result of the multiple lines analysis for the Fe II and Ti II in the atmosphere of TOI-1518 b. We show the tomographies in the stellar reference frame in the top panels, while in the bottom one we show the transmission spectrua with data re-binned and the Gaussian fit.

RME and the darker region representing the planetary signal. The absorption is clearly visible also in the transmission spectra, despite the Ti II one is quite noisy. I want to stress that this is a preliminary test to assess the impact of this method that we named multiple lines analysis. The test has been performed without the correction for the **RME** and **CLV** since in this case the combination of these effects may not play a significative role due to the geometry of the system that leads the planetary signal and the **RME** to not overlap as can be seen in Fig. 3.6. However, a final analysis would require the modelling and removal of **RME+CLV** as done for the single line analysis.

3.2.4 Discussion and conclusions

In this section we analysed the atmosphere of TOI-1518 b employing both the single line analysis, the cross-correlation with templates and the multiple line analysis. Our results returned the presence of the Hα line, the Na D2 line and the absence of the He I triplet. These results are expected in ultra hot jupiters orbiting hot stars. The single line detection did not return any other detection of the several atomic species investigated which includes Ca II, Ti II, Fe I , Fe II, Ba II, Mg I, Cr II and Sc II. On the other hand, most of these species have been detected employing five different set of templates varying from 2500K ton 5000K, including Ca II, Cr II, Fe I, Fe II, Na I, Ti II, Sc II, Sr

II. Moreover, we tentatively detected Al II, Mg I, V I, V II, Y II, K I and W I. We also started developing a method to combine the individual lines of the non detected species obtaining a preliminary detection of an average line for Fe II and Ti II. Once this method will be corroborated, we will be able to retrieve important information on these species, including their average height in the atmosphere and their average rotational profile.

3.3 Investigating the atmosphere of WASP-94A b with ESPRESSO

In this section I will discuss the preliminary results of the work I am leading on the analysis of the **Hot Jupiter (HJ)** WASP-94A b with **ESPRESSO** collected within the **Granted Time Observation (GTO)** collaboration.

3.3.1 Introduction

With the start of operation of **ESPRESSO** (Pepe et al. 2010, 2014), our capabilities for the studies regarding the atmospheric characterisation in the optical band have been enhanced. **ESPRESSO** achieved pioneering results by providing time-resolved measurements of transmission spectra (Ehrenreich et al. 2020; Borsa et al. 2021a), precise Rossiter-McLaughlin (**Rossiter-McLaughlin (RM)**) measurements (Santos et al. 2020), and high-precision characterizations of multi-planet systems (Damasso et al. 2020; Suárez Mascareño et al. 2020). Furthermore, the capability to detect relatively minor effects, such as the influence of stellar centre-to-limb variation (**CLV**) and the **RM** effect on transmission spectra, has been enhanced. These effects, which were previously masked by the signal-to-noise ratio (S/N) limitations, can now be accurately assessed due to the exceptionally high S/N and superior quality provided by the **ESPRESSO** data. The significance of the **RM** effect in atmospheric studies was previously discussed by Louden & Wheatley (2015), while the importance of **CLV** was highlighted in studies by Czesla et al. (2015) and Khalafinejad et al. (2017).

Among several targets observed with **ESPRESSO**, WASP-94A b is one of the planets showing the largest **TSM** with a value of 578 (Hord et al. 2024). This puffy ($\rho = 0.11$ g cm^{-3}) hot jupiter with a temperature of 1604 K orbits in less than four days around its F8-type host star (see Table 3.4 for the stellar and planetary parameters). HARPS data of the planet have been recently analysed by Ahrer et al. (2024) with the confirmation of the retrograde orbit as well as constrain the orbital misalignment (projected spin-orbit obliquity of λ = 123.0 $\pm$ 3.0 deg) and the tentative detection of Na absorption, independently of their treatment of the **RME**.

3.3.2 Methods

We collected two transits with **ESPRESSO** in 1UT mode in the August 2022 and we performed both the single line analysis and the cross-correlation with templates applying the same frameworks described in the other works in this thesis for **HARPS-N**

Table 3.4: Parameters adopted in the analysis of WASP-94A b.

Parameter	Value	Reference
Stellar parameters		
$M_\star$ ($M_\odot$)	1.450 ± 0.090	Bonomo et al. (2017)
$R_\star$ ($R_\odot$)	1.620 ± 0.050	Bonomo et al. (2017)
Effective temperature(K) . .	6153 ± 75	Bonomo et al. (2017)
log g ($\log_{10}$(cm s^{-2}))	4.27 ± 0.07	Stassun et al. (2017)
Metallicity, [Fe/H](dex) . .	0.26 ± 0.15	Bonomo et al. (2017)
Planetary parameters		
Planetary mass, M_p (M_{jup})	$0.456^{+0.036}_{-0.034}$	Bonomo et al. (2017)
Planetary radius, R_p (R_{jup})	$1.720^{+0.060}_{-0.050}$	Bonomo et al. (2017)
Orbital inclination, i (deg)	88.70 ± 0.70	Bonomo et al. (2017)
Projected obliquity,λ (deg)	123.0 ± 3.0	Ahrer et al. (2024)

spectrograph. The **ESPRESSO** data are similar to the **HARPS-N** ones because they share a similar data reduction procedures performed by the **DRS**. The telluric in the raw spectra are removed with Molecfit and the **RME+CLV** is modelled in the same way as **HARPS-N** data. In principle, ESPRESSO data have already the barycentric correction applied compared to HARPS-N data, however this difference is handled by Molecfit and hence does not require a different framework. The only ramining difference is the presence in the **ESPRESSO** data of the so called wiggles, modulation in the signal observed in most of the **ESPRESSO** studies and probably due to the tracking system of the **Very Large Telescope (VLT)**. Despite in our case the wiggles do not major affect the spectra, we removed them as in Borsa et al. (2021a) fitting a sinusoidal function to our data after the telluric removal and before proceeding with the rest of the analysis. We investigated the same species investigated for KELT-9 b and TOI-1518 b with the addition of Li and K that have stronger lines in the reddest part of **ESPRESSO** spectrum which is not covered by **HARPS-N**.

3.3.3 Results

Single line analysis

As mentioned at the beginning of the chapter, the single line analysis for stars with deep lines is challenging. In our case we can see from the 2D tomographies (e.g., Hα one in Fig. 3.16) that the region around the centre of the line is noisier than outside. We detected the Hα line but not the other Balmer lines. We detected both the lines in the sodium doublet, all three lines in the magnesium triplet as reported in Table 3.5 and in Fig. 3.16. We did not detect any other line investigated. We observe a strong blueshift in the observed lines suggesting the presence of winds similar to that discussed for KELT-9 b.

Table 3.5: Single line analysis results for WASP-94A b

Line	Depth [%]	R_p	FWHM [km s^{-1}]	v [km s^{-1}]
Hα	0.18 $\pm$ 0.04	1.07 $\pm$ 0.01	25.23 $\pm$ 5.71	-11.08 $\pm$ 2.52
Na D1	0.17 $\pm$ 0.02	1.07 $\pm$ 0.01	-29.89 $\pm$ 4.98	-15.39 $\pm$ 2.08
Na D2	0.14 $\pm$ 0.02	1.06 $\pm$ 0.01	50.05 $\pm$ 7.45	-28.08 $\pm$ 2.97
Mg I 5167.3216	0.18 $\pm$ 0.03	1.07 $\pm$ 0.01	46.19 $\pm$ 8.23	-9.91 $\pm$ 3.33
Mg I 5172.7	0.14 $\pm$ 0.03	1.06 $\pm$ 0.01	59.06 $\pm$ 11.86	-7.6 $\pm$ 4.52
Mg I 5183.62	0.19 $\pm$ 0.03	1.08 $\pm$ 0.01	27.27 $\pm$ 5.82	-15.97 $\pm$ 2.46

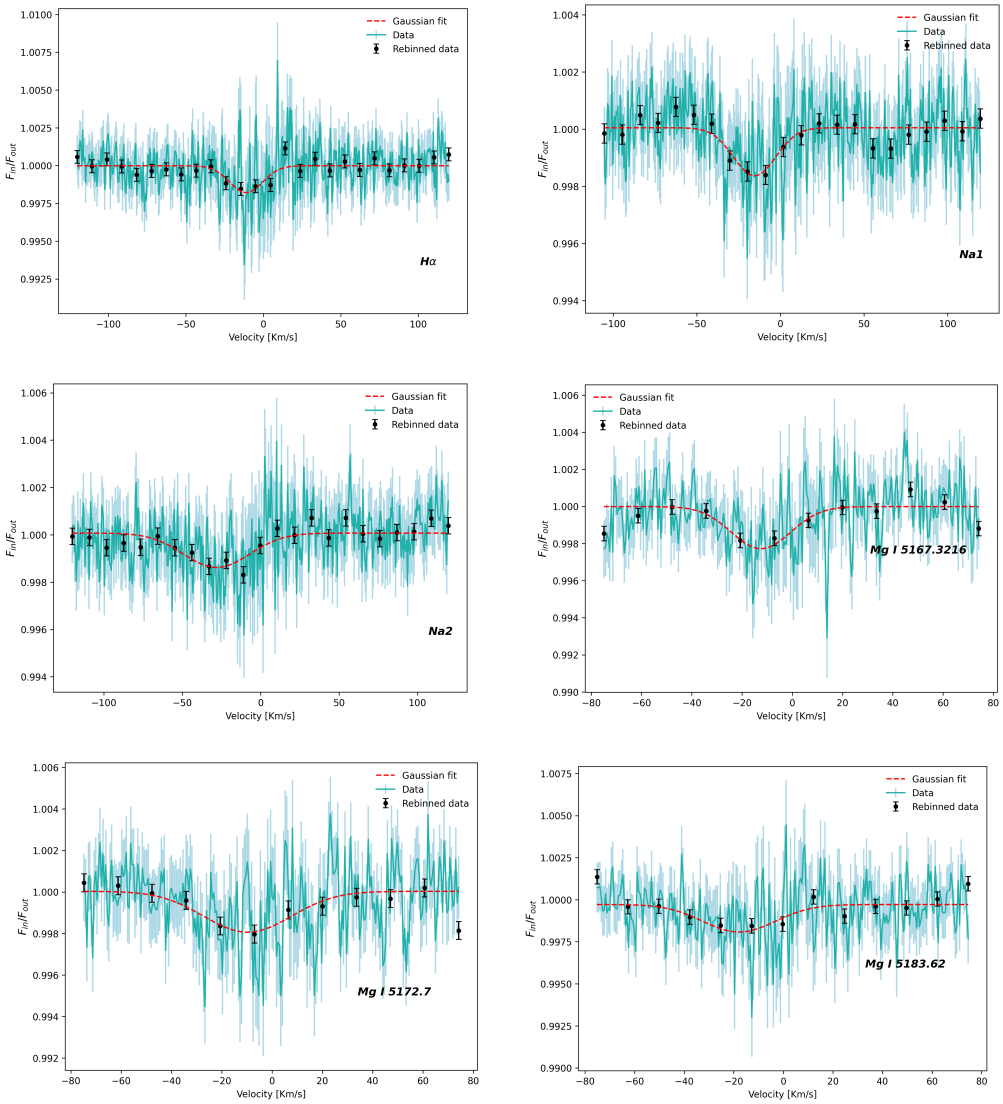

Figure 3.16: Result of the single lines analysis for the detected lines in the atmosphere of WASP-94A b. We show the transmission spectra with data re-binned and the Gaussian fit.

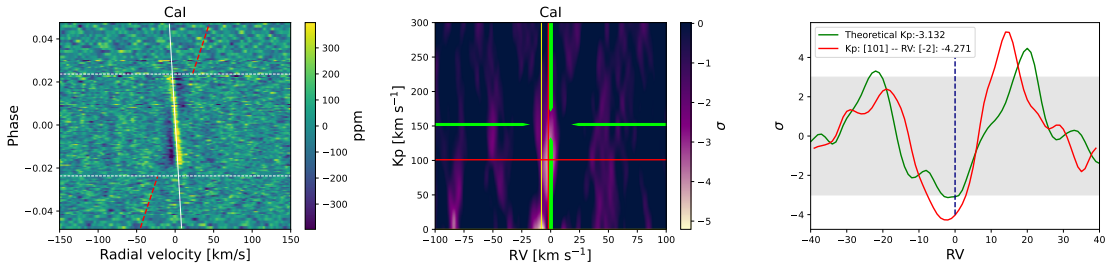

Figure 3.17: Example of the cross-correlation with templates result for the Ca II in the atmosphere of WASP-94A b. In the 2D tomography in the left panel, we can clearly see the overlap between the **RME** and the planetary signal. In the central panel we show the Kp vs **RV** map, while in the right panel the significance σ vs the **RV**.

Cross-correlation with templates

We performed the cross-correlation with templates employing 3 sets of templates with the temperatures spanning between 2000 K and 3000 K and we did not detect any atomic species including Na I and Mg I that we detected in single line. This may be due to the fact that in this system the **RME** trace is overlapping with the planetary signal as shown for the Ca II in Fig. 3.17. This means that either the planetary signal may be erased during the **RME** modelling and removal or that spurious signals arising from the correction may lead to a false detection as the one in the middle and right panel of Fig. 3.17.

3.3.4 Conclusions

Our preliminary results adds H I and Mg I to the already detected Na I in the atmosphere for WASP-94A b. However, the non detections with the cross-correlation with templates and the overlapping **RME** suggest a deeper investigation on the origin of our signal, including masking the region of the tomography affected by the **RME**.

Chapter 4

Star Planet Interaction: the role of Hα line and the He I triplet as indicators of the stellar activity and photo-evaporation

Stellar irradiation greatly affects the atmospheres of exoplanets orbiting close to their host stars, often leading to the expansion of the upper atmospheric layers and, in extreme cases, their evaporation (e.g., Bourrier & des Etangs 2018). This photo-evaporation process has shaped the demographics of close-in exoplanets, notably contributing to the formation of the Neptunian Desert—a region with a scant number of planets between Earth-sized and Jupiter-sized near their stars (Lecavelier Des Etangs 2007; Davis & Wheatley 2009; Szabó & Kiss 2011; Beaugé & Nesvorný 2013)—and the radius gap, which divides dense super-Earths from larger, more diffuse mini-Neptunes (Fulton et al. 2017; Fulton & Petigura 2018). Groundbreaking research on atmospheric escape began roughly twenty years ago (e.g., Vidal-Madjar et al. 2003, 2004), centering on the Ly-α transition of Hydrogen, the main component of hot gas giants' atmospheres. The atomic hydrogen produced from the thermal dissociation of H_2 absorbs stellar X-ray and extreme ultraviolet (EUV; collectively XUV) radiation within the thermosphere, significantly raising local temperatures and possibly leading to atmospheric expansion and escape (Penz et al. 2008). However, Ly-α observations are hindered by interstellar medium absorption (ISM) and geocoronal emission, complicating their interpretation. Seager & Sasselov (2000) and Oklopčić & Hirata (2018) proposed the He I 2^3S triplet at 1083.3 nm (known as He I) as a reliable diagnostic for examining atmospheric expansion and potential mass loss, as it is located in a near-infrared (nIR) spectrum region free from ISM and geocoronal interference. Following the landmark detection of an expanded atmosphere around the super-Neptune WASP-107 b (Spake et al. 2018), significant advancements have been made in this area, with nearly 40 planets now investigated for He I presence (Dos Santos 2023).

It has been observed that stellar activity can contaminate He I measurements leading to inaccurate estimations of He I absorption and mass-loss rate (e.g., Salz et al. 2018; Guilluy et al. 2020). Specifically, the plage-like active regions are darker than the rest of the stellar disc in the helium channel; a planet transiting over quiescent regions of the star would enhance the contribution of active regions in the observed flux, resulting in a stronger absorption at 1083.3 nm. Conversely, if the planet obscures an active region, the net effect would be a reduction in He I absorption. One approach to address these pseudo-signals is to simultaneously monitor stellar activity diagnostics in the optical (such as Hα , Ca I H&K, and Na I) that exhibit an opposite behaviour compared to He I (Guilluy et al. 2020).

In this Chapter I will introduce and discuss two works regarding the joint analysis of Hα and He I as indicators of stellar activity and ongoing photo-evaporation.

In Section 4.1 I will introduce and discuss the work led by Gloria Guilluy where I participated as the second author, leading the analysis and interpretation of the Hα line related results. In Section 4.2 I will introduce the work that I led on the atmospheric characterisation of photo-evaporating target TOI-5398 b.

4.1 A He I survey of close-in giant planets hosted by M-K dwarf stars with GIANO-B

The following work, led by Gloria Guilluy has been published in Guilluy, D'Arpa, et al. (2024). As second author, I entirely handled the analysis and interpretation of the results obtained from **High Accuracy Radial velocity Planet Searcher for the Northern emisphere (HARPS-N)** data. The tables and Figures in this section are from Guilluy, D'Arpa, et al. (2024).

4.1.1 Introduction

Being aware of the potential limitations arising from differences in instrumentation and data analysis techniques that may affect the identification of trends related to He I detection, we decided to undertake a uniform survey searching for He I in the atmospheres of all the exoplanets available within the atmospheric sample of the Global Architecture of Planetary Systems (**Global Architecture of Planetary System (GAPS)**) project (The **GAPS**-ATMO sample is described in Guilluy et al. 2022a), which encompasses of hot/warm Jupiter- and Neptune-like planets.
We divided the **GAPS** targets into two distinct sub-samples. The first sample comprises planets orbiting M-K dwarf planet hosts, which has been analysed in this work. The second dataset, consisting of planets around G-F-A main-sequence stars, will be the subject of a future study. We decided to focus this first paper on M-K dwarf stars as they are the best suited to host planets with an escaping He I atmosphere. Indeed, their high

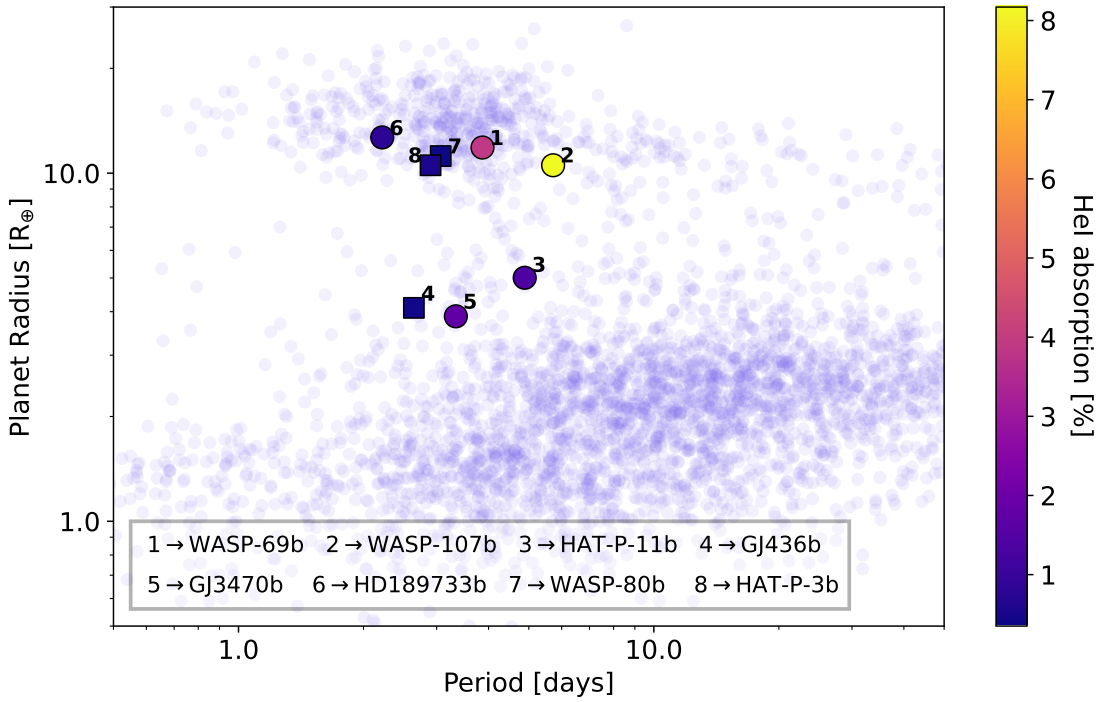

Figure 4.1: Known exoplanets as a function of their radius and period from the NASA Exoplanet Archive (Akeson et al. 2013). Targets analysed in this work and previous GIANO-B papers (Guilluy et al. 2020; Fossati et al. 2022; Guilluy et al. 2023) are highlighted. The marker colour reflects the He I absorption signal we found in this work. Circles and squares represent detections and non-detections, respectively. The non-detections are reported at 1σ.

XUV flux ionises the He I ground state which recombining populates the metastable 2^3S ground level (from which the 1083.3 nm absorption originates), and their moderately low mid-UV flux prevents the 2^3S ionisation (e.g., Oklopčić 2019; Biassoni et al. 2024b).

4.1.2 Case history and observations

The survey encompasses five targets, namely WASP-69 b, WASP-107 b, HAT-P-11 b, GJ 436 b, and GJ 3470 b. In this section, we provide a brief overview of the key characteristics of each system and summarise the existing He I studies presented in the literature. The stellar and planetary parameters we adopted in the analysis are reported in Table 4.6.

WASP-69 b is a warm Saturn orbiting a K5 star (Anderson et al. 2014). Due to its large expected atmospheric signal $2R_P H_{eq}/R_\star^2 \sim 283$ ppm (where H_{eq} is the atmospheric scale height, and R_P and $R_\star$ are the planetary and stellar radius respectively, Brown et al. 2001), WASP-69 b represents a prominent target for performing atmospheric stud-

Table 4.1: Observations log.

	Date^{+}	**N**$_{\rm obs}$	**Exp Time [s]**	**S/N**$_{\rm avg}$	$\sigma_{\rm T_c}$ **[min]**	**Telluric/stellar flag**
WASP-69 b	2019-07-24	60	200.0	53.42	0.62	x
	2020-08-09	54	200.0	54.39	0.72	
	2021-10-28	46	200.0	41.90	0.85	x
	2022-09-14	42	200.0	51.88	0.95	
WASP-107 b	2019-02-07	58	200.0	28.21	0.24	
	2019-05-04	60	200.0	24.55	0.26	x
HAT-P-11 b	2019-07-07	60	200.0	59.31	0.15	
	2020-06-18	60	200.0	65.22	0.16	
	2020-09-19	58	200.0	60.79	0.17	
GJ-436 b	2018-04-16	44	200.0	67.34	0.17	
	2020-02-19	38	200.0	87.39	0.20	
	2020-02-27	38	200.0	93.26	0.20	
	2022-03-03	30	200.0	78.45	0.24	
	2022-03-11	46	200.0	90.75	0.24	
	2022-12-24	42	200.0	81.61	0.25	
GJ-3470b	2018-01-13	38	200.0	20.16	0.27	x
	2019-02-04	52	200.0	21.41	0.32	x
	2019-12-28	64	200.0	31.23	0.36	
	2020-01-27	48	200.0	36.26	0.36	x
	2022-12-23	54	200.0	32.59	0.49	

From left to right: the observing night, the number of observed spectra, the exposure time, the average S/N across the selected spectral range (1082.49-1085.5 nm), the uncertainty on the mid-transit time for the observed transits calculated as $\sigma_{\rm T_c} = \sqrt{\sigma^2_{\rm T_0} + n^2 * \sigma^2_{\rm P}}$ (where T_0 and P are the mid-transit time and orbital period in the adopted ephemerids reported in Table 4.6 and n is the number of orbits between time $T_{\rm c}$ and T_0), and flag for significant telluric overlap/possible stellar activity issues. [$^{+}$]Beginning of the night.

ies. Tsiaras et al. (2018) and Estrela et al. (2021) found clues to the presence of water in the planet's atmosphere. Guilluy et al. (2022a) recently reported the presence of 5 molecules, and a possible hint of disequilibrium in its lower atmosphere. Sodium was also detected in its upper atmosphere (see e.g., Casasayas-Barris et al. 2017; Khalafinejad et al. 2021; Langeveld et al. 2022). Evidence of an extended helium atmosphere surrounding the planet has been reported by Nortmann et al. (2018) with **Calar Alto high-Resolution search for M dwarfs with Exoearths with Near-infrared and optical Échelle Spectrographs (CARMENES)**, by Vissapragada et al. (2020, 2022) with Palomar/WIRC, by Allart et al. (2023) with SPIRou, and by Tyler et al. (2024) with Keck/NIRSPEC.

WASP-107 b is a super Neptune orbiting a K6 star located at the upper radius border of the Neptunian desert (Anderson et al. 2017). Because of its large atmospheric scale height, it represents an excellent target for atmospheric studies. Kreidberg et al. (2018b) detected water using the **Wield Field Camera 3 (WFC3)** of **Hubble Space Telescope (HST)** finding evidence for a methane-depleted atmosphere and high-altitude condensates. Spake et al. (2018) also detected water using a wider wavelength coverage than Kreidberg et al. (2018b). Recently, photochemically produced sulphur dioxide (SO_2) was detected in its atmosphere (Dyrek et al. 2024). Detections of the extended helium atmosphere of WASP-107 b have been reported multiple times (e.g., Spake et al. 2018; Allart et al. 2018; Kirk et al. 2020; Spake et al. 2021).

HAT-P-11 b is a transiting warm Neptune-class exoplanet orbiting a K4V star, and located at the edge of the evaporation desert Bakos et al. (2010). Fraine et al. (2014), Tsiaras et al. (2018), and Chachan et al. (2019) detected the presence of water vapor in the atmosphere of HAT-P-11 b with low-resolution observations by using data from ***HST*** and *Spitzer*. Chachan et al. (2019) also suggested the presence of methane. More recently, at high-spectral resolution Basilicata et al. (2023) reported the detection of H_2O, NH_3, and a tentative one of CO_2 and CH_4. Ben-Jaffel et al. (2022) by studying the upper atmosphere found a phase-extended transit absorption of neutral hydrogen and singly ionised carbon, while several works (i.e. Allart et al. 2018, Mansfield et al. 2018, and Allart et al. 2023) reported the presence of metastable helium surrounding the planet.

GJ 436 b is a warm Neptune in the lower-mass edge of the Neptune desert orbiting a quiet M2.5V star Gillon et al. (2007). Its atmosphere has been extensively studied through various observations. According to low-resolution studies, there appears to be a scarcity of methane and a surplus of CO and CO_2 in the atmosphere, along with a slight deficiency of H_2O when compared to the predicted amounts based on equilibrium chemistry assuming solar metallicity (e.g., Stevenson et al. 2010; Knutson et al. 2014). Observations of the upper atmosphere of GJ 436 b n Ly-α line of neutral hydrogen revealed that the planet is surrounded by a giant coma of H I extending tens of planetary radii (e.g., Kulow et al. 2014; Ehrenreich et al. 2015; Lavie et al. 2017), while Nortmann et al. (2018) did not detect any evidence of a helium-extended atmosphere.

GJ 3470 b is a warm Neptune orbiting an M-dwarf and located very close to the Nep-

tunian desert Bonfils et al. (2012). Previous investigations of its atmosphere, based on observations from the ***HST***, have indicated the presence of a cloudy, hydrogen-rich atmosphere (Ehrenreich et al. 2014). Additionally, studies analysing visible range observations by Nascimbeni et al. (2013) and Chen et al. (2017) have detected a Rayleigh slope in the atmosphere. Benneke et al. (2019) obtained a robust detection of water absorption ($> 5\sigma$) by combining ***HST*** and *Spitzer* observations. They revealed a low-metallicity, hydrogen-dominated atmosphere similar to a gas giant, but strongly depleted in methane gas. In terms of upper atmospheric layers, Bourrier et al. (2018) have reported the existence of a giant hydrogen exosphere while Palle et al. (2020a) and Ninan et al. (2020) have identified evidence of He I absorption during transit. On the other hand, Allart et al. (2023) have reported a non-detection of He I in this planet's atmosphere.

The systems in our sample were observed using the GIARPS observing mode (Claudi et al. 2017) of the Telescopio Nazionale Galileo (**Telescopio Nazionale Galileo (TNG)**). In this configuration, the **TNG** is capable of simultaneously acquiring high-resolution (HR) spectra in the optical range (0.39-0.69 μm) and nIR range (0.95-2.45 μm) using the **HARPS-N** ($R \approx 115,000$) and GIANO-B ($R \approx 50,000$) spectrographs.

For the GIANO-B observations, we employed an ABAB nodding pattern, which allows for optimal subtraction of thermal background noise and telluric emission lines. Each target was scheduled for observations $\sim$1 h before, during, and $\sim$1 h after the planetary transit. Figure 4.2 displays the signal-to-noise ratio (S/N) averaged over the region of interest (1082.49-1085.5 nm) and the airmass as a function of the planet's orbital phase for each night and target considered. GIANO-B covers four spectral bands in the near-infrared (Y, J, H, K) divided into 50 orders. For our analysis, we focused on order #39 in the Y-band, where the He I triplet is located. One transit observation of WASP-69 b on UT 28 October 2021, was affected by thin clouds (cirri), prompting us to discard the AB pairs of observations with very low S/N compared to the others (lowest S/N in the pair less than 15, as shown in Fig. 2 of Guilluy et al. 2022a). Furthermore, we discarded the last transit of WASP-107 b, which took place on UT 09 April 2023, as the entire night was affected by seeing conditions of approximately 2 arcseconds. This resulted in a lower S/N compared to the data from the other observing nights (see Fig. 4.2), thereby preventing us from analysing this dataset. A detailed log of the GIANO-B observations is provided in Table 4.1.

The **HARPS-N** observations were carried out using the objAB observational setup, with fibre A on the target and fibre B on the sky. The light collected through the fibres is directed to a 4k $\times$ 4k charge-coupled device (CCD). The CCD is responsible for capturing the spectra from 69 different orders for each fibre, utilising the echelle spectrograph design. To process the **HARPS-N** data, the standard Data Reduction Software (**Data Reduction Software (DRS)**) was employed, specifically version 3.7 (Cosentino et al. 2012).

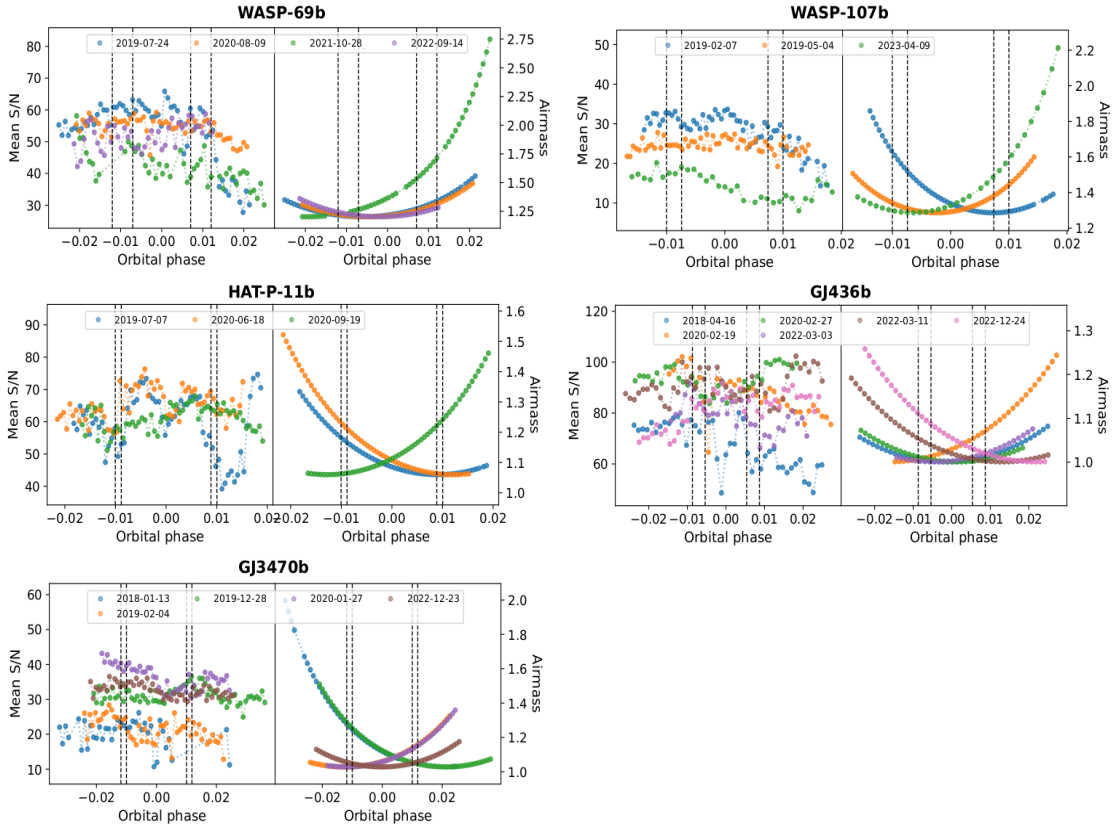

Figure 4.2: S/N in the region of interest (1082.49-1085.5 nm)(left panel) and airmass (right panel) measured during the GIANO-B observations for each investigated target. The vertical dashed lines mark the t_1, t_2, t_3, and t_4 contact points (from left to right). The dashed green line for WASP-107 b indicates the transit we had to discard for adverse seeing conditions.

4.1.3 Data analysis

In this section, we discuss the main steps of the analysis we performed on both GIANO-B (Sect. 4.1.3) and **HARPS-N** data (Sect. 4.1.3).

Analysis in the nIR

Currently, the most widely used technique for determining whether an exoplanet is surrounded by an extended or evaporating atmosphere is transmission spectroscopy. During a transit, the outgassed atoms produce additional absorption features superimposed on the stellar spectrum. Here, we outline the procedures we implemented to extract the planetary transmission spectra from the raw data obtained by GIANO-B.

Spectra extraction We applied several data processing steps to the GIANO-B raw data using the GOFIO pipeline (Rainer et al. 2018). These steps included dark subtraction, flat field correction, removal of bad pixels, spectra extraction (without considering

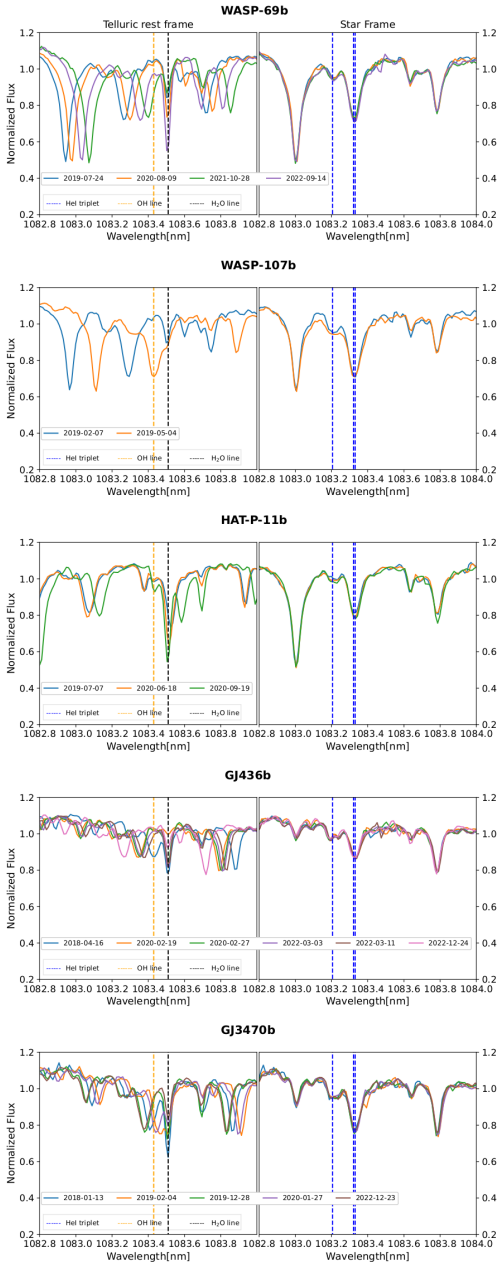

Figure 4.3: Left Panels: Averaged spectrum for each investigated night in the telluric rest frame, with overplotted vertical lines to show the position of the H_2O telluric transmission line at $\sim$1083.51 nm and the OH telluric emission line at $\sim$1083.43 nm in black and orange, respectively. Right Panels: Averaged spectrum for each investigated night after the telluric removal and the shift in the stellar rest frame. Vertical blue lines correspond to the He I triplet. The averaged spectra are plotted after being divided by their median value for visual purposes.

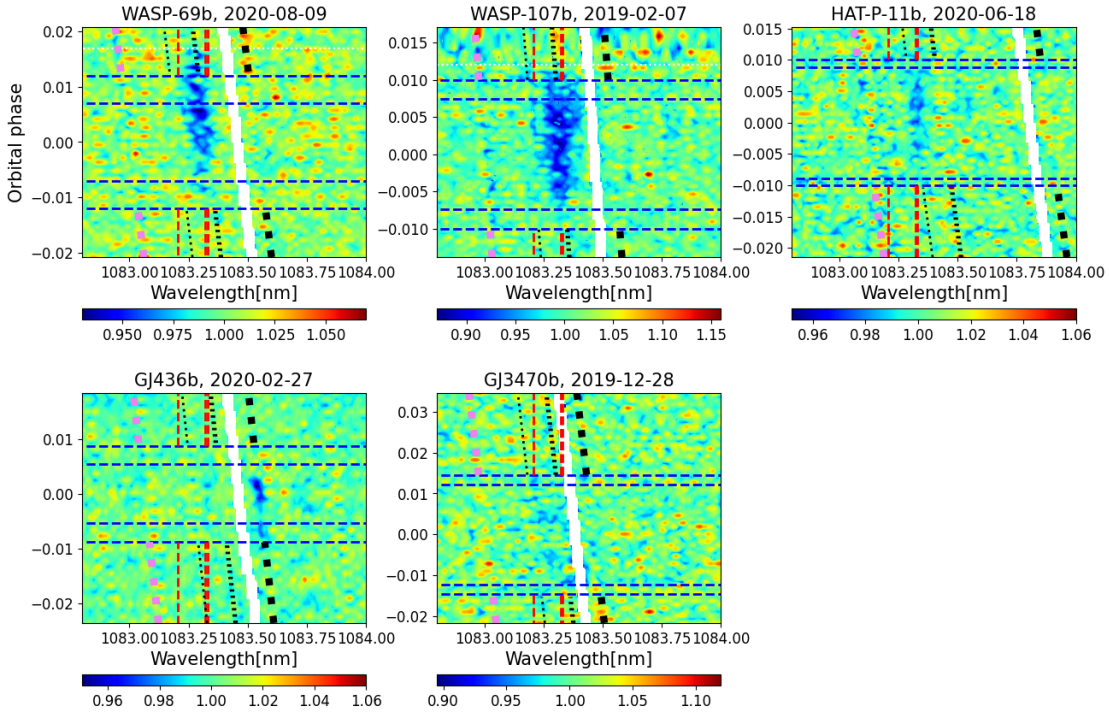

Figure 4.4: 2D transmission spectra maps. For each target, an example of transmission spectra shown in tomography in the planetary rest frame in the region of the He I triplet, as a function of wavelength and planetary orbital phase. The contact points t1, t2, t3, and t4 are marked with horizontal blue lines. The regions affected by OH contamination are masked. For some planets, some residuals are left at the position of the Si∼1083 nm line (highlighted in pink). This is due to the depth of the line (see e.g., Krishnamurthy et al. 2023; Zhang et al. 2023a). Black and red dotted lines mark the position of the He I lines in the stellar and planet rest frame, respectively. Lines with black squared mark the position of the strong H_2O telluric line at around 1083.51 nm. The corresponding 2D maps for all the investigated nights are shown in Fig 4.12.

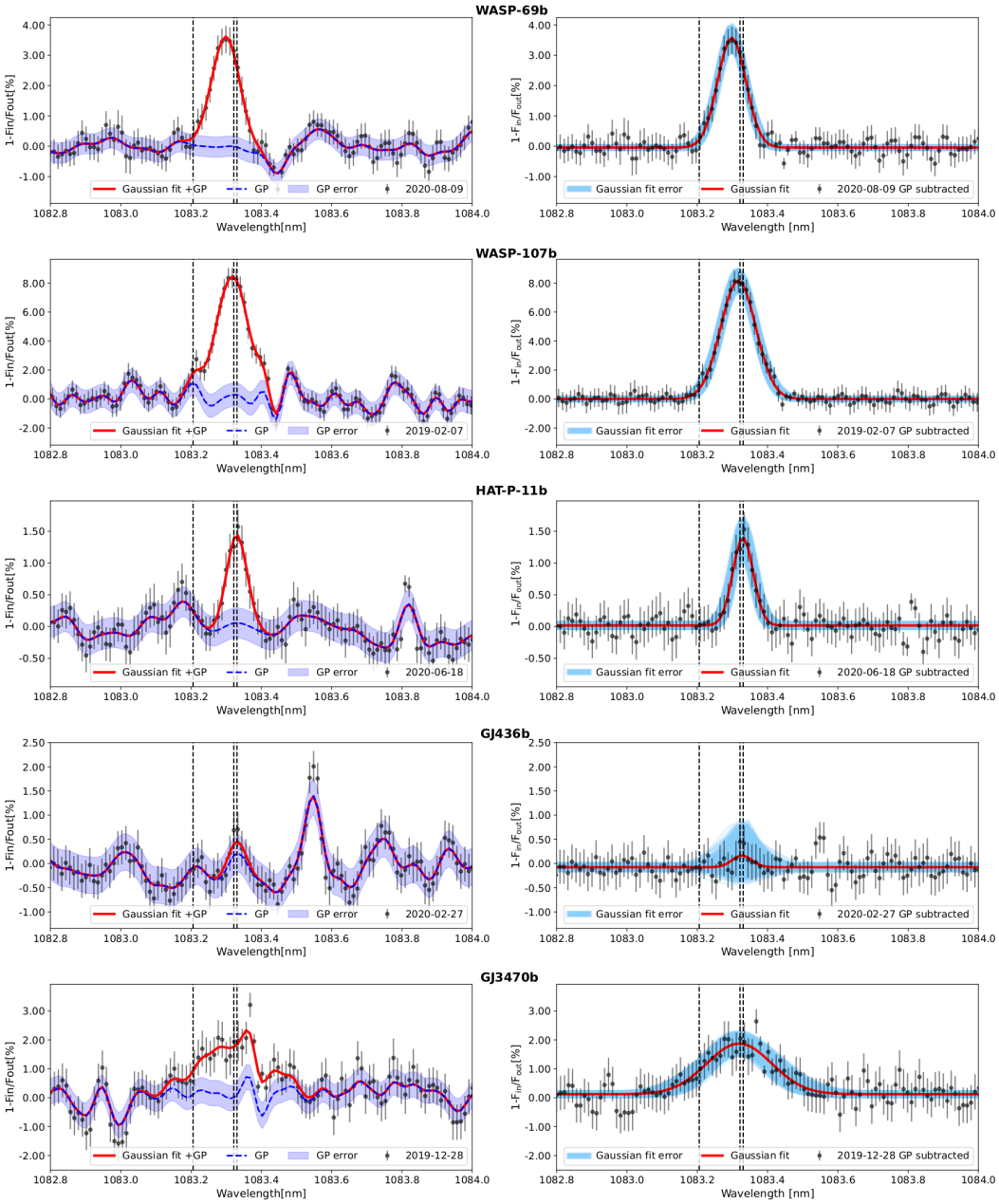

Figure 4.5: Example of **Gaussian Processes (GP)** correction. Left panel: transmission spectrum centred on the He I triplet (in the planet rest frame) with the **GP** regression model, along with the 1σ uncertainty intervals, (in blue) and the Gaussian+**GP** model (in red). Right Panel: Final spectrum after removing the **GP** model. Vertical black dotted lines indicate the position of the He I triplet. The spike in the right wing of the He I triplet in the GJ 3470 b transmission spectrum is a residual due to the OH emission line. The error intervals for the Gaussian fit were computed by displaying 1000 Gaussian fits within the 1σ uncertainties of the derived parameters, spanning the 16%-84% quantiles.

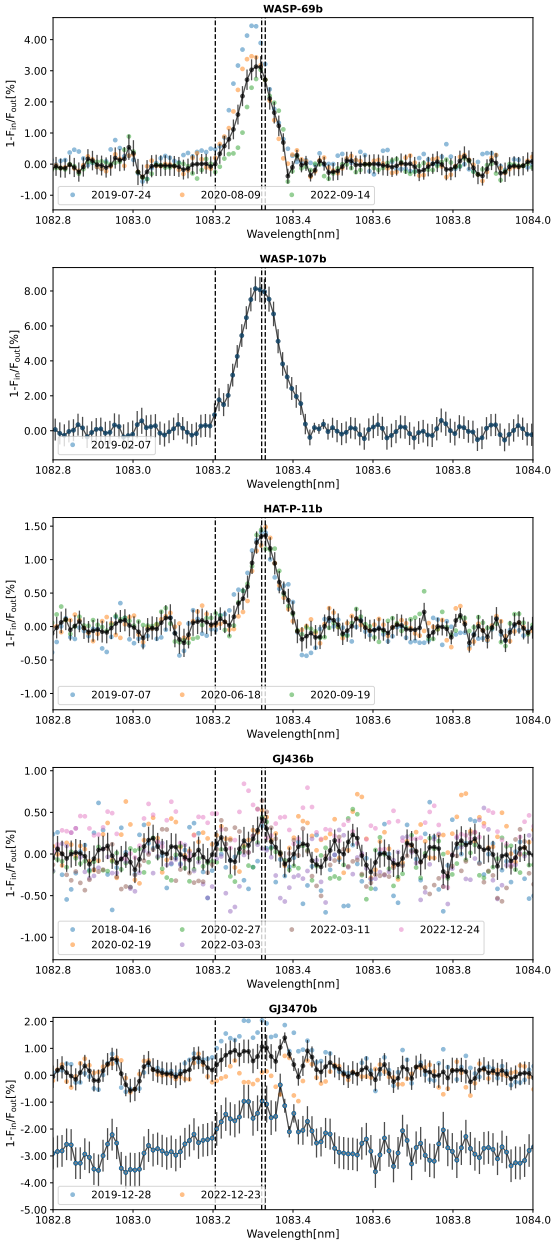

Figure 4.6: Transmission spectra centred on the He I triplet (in the planet rest frame) after removing the Gaussian process model. For each target, different colours refer to the different visits, while the black points show the weighted average over the observations. Vertical black dotted lines indicate the position of the He I triplet. For GJ 3470 b two different transmission spectra are reported, one by considering the two nights not affected by the OH contamination and one by considering only the night responsible for the He I signal. For WASP-69 b, the weighted averaged spectrum has been obtained by excluding the first night (i.e., UT 2019-07-24) as likely affected by stellar contamination.

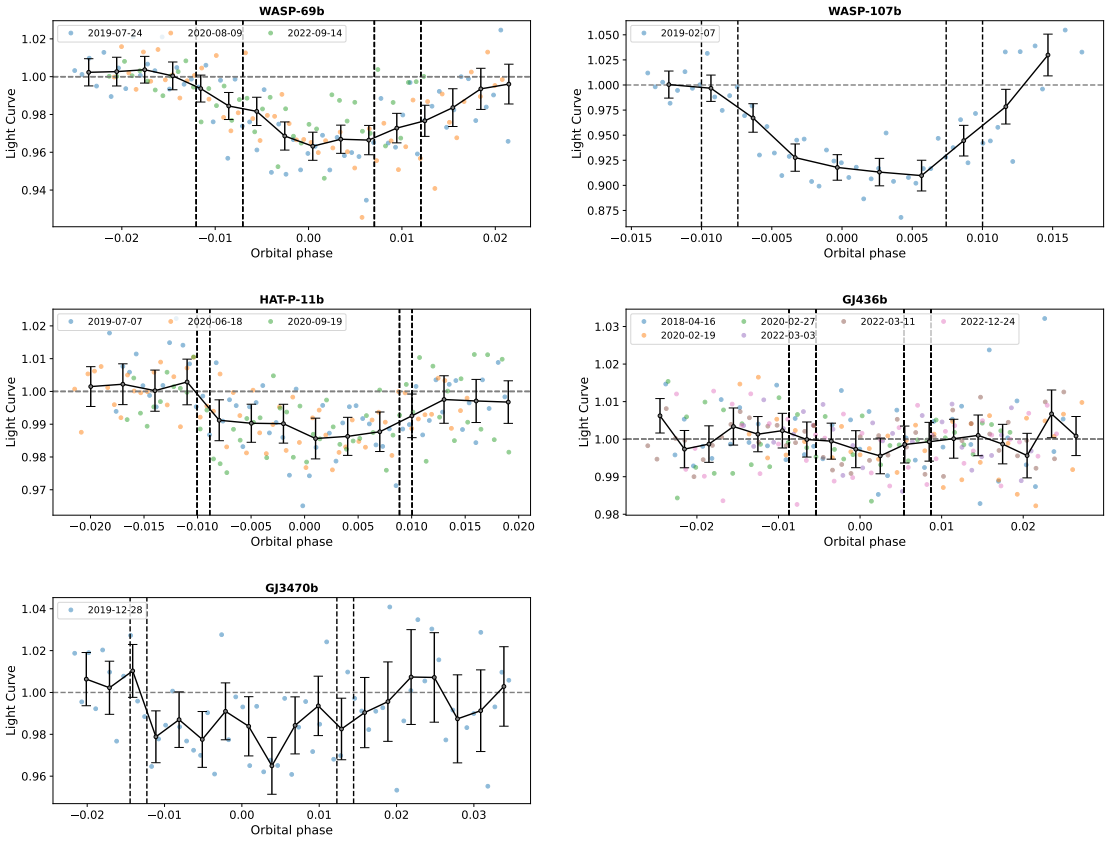

Figure 4.7: Transmission light curve of the He I in the planetary rest frame for the investigated targets. The vertical dashed lines mark the t_1, t_2, t_3, and t_4 contact points (from left to right). The grey horizontal dashed line is the continuum level.

the blaze function correction), and wavelength calibration using a U-Ne lamp spectrum as a template in the vacuum wavelength frame. We used the ms1d spectra, the multi-spectral 1D output, where the echelle orders are kept separated. To improve the initial wavelength solution, we employed the same approach described in similar previous works (e.g., Giacobbe et al. 2021; Guilluy et al. 2022a). We aligned all the spectra to the Earth's atmospheric rest frame, assuming it as the frame of the observer (neglecting any $\sim$10 m s^{-1} differences due to winds), by measuring any shifts relative to an average spectrum taken as a template for the night. Subsequently, we refined the wavelength solution by utilising an Earth's atmospheric transmission spectrum generated using the Sky Model Calculator[1].

For the remaining analysis, we focused exclusively on the order #39, which encompasses the He I triplet. The magnitude of these wavelength calibration refinements, for the considered nights and in the region around the He I triplet, is $\sim$0.7 km/s, approximately one-fourth of a pixel.

[1] https://www.eso.org/observing/etc/bin/gen/form?INS.MODE=swspectr+INS.NAME=SKYCALC

Telluric correction As our spectra were obtained from ground-based observations, it was necessary to account for the contribution of Earth's atmosphere. The telluric spectrum contains both emission and transmission lines. To correct for the transmission telluric lines, particularly the H_2O line at around 1083.51 nm (vacuum wavelength), we followed the approach proposed by Guilluy et al. (2023) and utilised the `Molecfit` **European Southern Observatory (ESO)** software (Smette et al. 2015; Kausch et al. 2015). An example of telluric removal is shown in the right panels of Fig. 4.3.
Within the spectral region of interest, there are two OH emission line doublets located close to the He I triplet. The first doublet is at approximately 1083.2103 nm, and 1083.2411 nm, while the second one is at 1083.4241 nm and 1083.4338 nm in vacuum wavelengths(Oliva et al. 2013). The GIANO-B resolving power is not able to distinguish between the two separate components of this second doublet, resulting in them being observed as a single, intense line in the spectra. The GIANO-B nodding acquisition mode automatically corrects for these emission lines, as described in Guilluy et al. 2020. However, due to variations in atmospheric seeing during the observing nights, the A-B subtraction may leave residual signals at the deepest OH doublet (i.e., around 1083.43 nm, as seen in the left panels of Fig. 4.3). To account for this, we visually inspected the GIANO-B raw spectra to identify the location of this OH line in our spectrograph and created a mask to exclude any possible residuals from our final transmission spectra (Guilluy et al. 2023).

Transmission spectra calculation To separate the stellar contribution from the potential planetary signal, we proceeded with the following steps:
(i) First, we shifted the spectra into the star rest frame using Eq. (1) from Guilluy et al. (2023) and the parameters listed in Table 4.6. As depicted in the right panels of Fig. 4.3, the He I triplet lines align in the stellar rest frame.
(ii) Next, we normalised each spectrum to the continuum by dividing it by its median value (neglecting the spectral region around the He I triplet), excluding spectra with significantly lower signal-to-noise ratios compared to the other exposures.
(iii) We created a master-out stellar spectrum, $S_{\rm out}(\lambda)$, by averaging the out-of-transit spectra (i.e., with an orbital phase smaller than t_1 or greater than t_4[2]). Individual transmission spectra, $T(\lambda, i)$, were derived by dividing each spectrum by $S_{\rm out}(\lambda)$.
(iv) Finally, we linearly interpolated the transmission spectra in the planet's rest frame using Eq. (2) from Guilluy et al. (2023). Fig. 4.4 displays examples of the transmission spectroscopy 2D maps in the planet's rest frame for each planet, while the 2D maps for all the investigated nights are presented in Fig. 4.12. For each investigated planet and each observed night, we then derived the fully in-transit transmission spectrum in the planet's rest frame $T_{\rm mean}$, which is computed by averaging the transmission spectra with an orbital phase between t_2 and t_3. We did not consider the influence of both centre-to-limb variations (**Centre to Limb Variation (CLV)**) and the Rossiter-McLaughlin Effect (**Rossiter-McLaughlin (RM)**) as previous studies have indicated a minimal impact on the He I (e.g., Allart et al. 2018, 2019; Nortmann et al. 2018).

[2]For those planets where there was a hint of a tail we discarded the corresponding spectra to compute the master stellar spectrum.

Table 4.2: Priors used in the **DE-MCMC** analysis.

Value	Priors
Peak $\text{Pos}_{\text{gauss}}$ [nm]	U[1083.29,1083.36]
σ_{jit}	U[0,+∞]
Ampl [%]	U[0,3]
λ [nm]	U[0.01,0.09]

To estimate the contrast c of the excess absorption at the position of the He I triplet, we fitted a Gaussian profile to each individual in-transit mean transmission spectrum with the **Differential Evolution Markov chain Monte Carlo (DE-MCMC)** (Ter Braak 2006) method, varying the peak position, the full-width half maximum (**Full Width at Half Maximum (FWHM)**), the peak value (c), and an offset for the continuum. Correlated noise in the transmission spectra (mainly caused by systematic effects such as fringing, variations in the instrumental profile, changes in the position of the star in the slit, etc) was modelled through the Gaussian process (**GP**) regression within the same DE-**The Markov Chain Monte Carlo (MCMC)** tools, using a covariance matrix described by a squared exponential kernel (see eq. 2 in Bonomo et al. 2023)[3]. We finally accounted for possibly uncorrelated noise with a jitter term σ_{jit}. We imposed several priors on the model parameters as well as on the **GP** hyper-parameters (see Table 4.2). For each target, Fig. 4.5 shows an example of correction with the **GP** regression model, the posterior distributions for the same nights are reported in Fig. 4.13. The best-fit parameters from the **DE-MCMC** Gaussian analysis, for each night are listed in Table 4.3. We determined the values and the 1σ uncertainties of the derived parameters from the medians and the 16%-84% quantiles of their posterior distributions. In cases of a He I non-detection, we reported 1σ upper limits on the excess absorption at the positions of the stellar He I lines (Guilluy et al. 2023).
For each investigated target, the transmission spectra from each night were then weight-averaged after subtracting the **GP** regression model to create the final transmission spectra (see Fig. 4.6). Table 4.4 reports for each planet the weight-averaged He I contrast c.

Light-Curves computation To monitor the variation of the He I signal during transit, we additionally performed spectrophotometry of the helium triplet within a passband of 0.075 nm centred at the peak of excess absorption in the planet rest frame (Allart et al. 2019). The computed transit light curves are presented in Fig. 4.7.

[3]We also ran the **DE-MCMC** analysis without the **GP**, and our findings remain compatible within 1-σ. However, the error bars on the model-free parameters (including the He I absorption) from the **GP** analysis are usually slightly larger, and thus more conservative, than those without the GPs, because they account for the correlated noise.

Table 4.3: Result night by night for the He I absorption

	Night	Peak position [nm]	Excess of absorption c [%]	**FWHM** [nm]	Significance [σ]
WASP-69 b	2019-07-24	1083.297 ± 0.003	4.3 ± 0.3	$0.0960^{+0.008}_{-0.006}$	14.2
	2020-08-09	$1083.2982^{+0.0049}_{-0.0044}$	3.6 ± 0.4	$0.0948^{+0.012}_{-0.010}$	9.0
	2022-09-14	$1083.3187^{+0.0069}_{-0.0073}$	$3.14^{+0.54}_{-0.55}$	$0.0764^{+0.015}_{-0.010}$	5.8
WASP-107 b	2019-02-07	1083.317 ± 0.005	$8.17^{+0.80}_{-0.76}$	$0.1176^{+0.015}_{-0.013}$	10.5
HAT-P-11 b	2019-07-07	$1083.3189^{+0.0092}_{-0.0098}$	1.4 ± 0.3	$0.1059^{+0.023}_{-0.018}$	4.9
	2020-06-18	$1083.3302^{+0.0064}_{-0.0066}$	1.4 ± 0.3	$0.0686^{+0.017}_{-0.012}$	4.5
	2020-09-19	1083.327 ± 0.009	1.4 ± 0.3	$0.0829^{+0.018}_{-0.015}$	4.3
GJ-436 b	2018-04-16		$<0.24(0.34)$		
	2020-02-19		$<0.34(0.44)$		
	2020-02-27		$<0.52(0.66)$		
	2022-03-03		$<0.38(0.52)$		
	2022-03-11		$<0.63(0.68)$		
	2022-12-24		$<0.39(0.45)$		
GJ-3470b	2019-12-28	$1083.319^{+0.021}_{-0.017}$	$1.75^{+0.39}_{-0.36}$	$0.2180^{+0.061}_{-0.053}$	4.7
	2022-12-23		$<0.10(0.22)$		

From left to right: the investigated night, the peak position, excess of absorption, and **FWHM** obtained from the **DE-MCMC** analysis, and the significance of the detection. The upper limits are reported at 1σ and at 2σ in brackets.

Analysis in the optical

To indicate the host star activity we derived the chromospheric emission from Ca II H and K lines of **HARPS-N** spectra ($\log \mathrm{R}'_{\mathrm{HK}}$). We used the definition of Noyes et al. (1984) and the implementation of Lovis et al. (2011) through the offline version of the **HARPS-N DRS** available through the Yabi workflow (Hunter et al. 2012) hosted at IA2 Data Center (`https://www.ia2.inaf.it/`). The only exceptions are GJ436 and GJ3470, for which the Noyes relations are not applicable as they have a colour index B-V>1.1, we thus utilised the equations provided in Suárez Mascareño et al. (2015). The derived $\log \mathrm{R}'_{\mathrm{HK}}$ are reported in Table 4.7.

We then derived transmission spectra in Hα similarly as described for the He I triplet and as already described in Chapter 2. We focused on raw data already processed by the **DRS** and we used `Molecfit` to remove telluric contamination. We obtained transmission spectra (2D maps for WASP-69 b and GJ-3470 b are in the upper panels of Fig. 4.8 and Fig. 4.9) by dividing the full in-transit spectra by the master out and we modelled **CLV** and **RM** similarly to Yan et al. (2017). However, instead of using models computed at different limb darkening angles μ, we used an analytical approach using Exotethys (Morello et al. 2020) to retrieve the limb darkening coefficients and then computing the stellar intensity profile $I(\mu)$ by adopting a quadratic limb darkening law. After shifting the transmission spectra into the planetary rest frame, we computed the weighted average of the full in-transit spectra (right bottom panel of Fig. 4.8 and Fig. 4.9), and we fitted a Gaussian to evaluate the absorption/emission depth, **FWHM**, and the velocity shift. Along with the Gaussian fit, to evaluate the zero absorption hy-

Table 4.4: Results combined.

Target	c [%]	Significance [σ]	Effective radius [R_p]	g_P [m s^{-2}]	H [km]	δ_{R_P}/H_{eq}
WASP-69 b	3.91±0.22	17.6	1.79±0.08	5.8±0.6	1060	56±8
WASP-69 b (without 2019-07-24)	3.46±0.32	10.7	1.71±0.08	5.8±0.6	1060	51±8
WASP-107 b (1 night)	$8.17^{+0.80}_{-0.76}$	10.5	2.19±0.11	3.37±0.31	1450	55±7
HAT-P-11 b	1.36±0.17	8.0	2.17±0.11	10.2±0.6	530	71±9
GJ 436 b	$<0.42(0.52)^{+}$		$<1.27(1.33)$	14.8±1.7	294	$< 24(29)$
GJ 3470 b (1 night)	$1.75^{+0.39}_{-0.36}$	4.7	2.05±0.25	8.2±1.6	470	55±19

From left to right: the investigated target, the contrast from the **DE-MCMC** analysis, the significance of the detection, the effective He I radius, the planet's gravity, the atmospheric scale height (computed by assuming a mean molecular weight of 1.3), and the ratio between the equivalent height of the He I atmosphere and the atmospheric scale height. [$^+$] $1\sigma(2\sigma)$ upper limits. For WASP-69 b, we also present results by excluding the first observing night (i.e., UT 2019-07-24), as it was likely affected by stellar contamination.

pothesis, we also performed a linear fit and we computed the **Bayesian Information Criterion (BIC)** to compare the two models (Kass & Raftery 1995). We considered the Gaussian model as preferable over the linear one only when accompanied by a lower **BIC** and a difference in **BIC** (ΔBIC) > 10. We did not use the **GP** correction in the optical as the **HARPS-N** spectra are much less affected by systematics, and so the use of GPs was not really necessary.

4.1.4 Results

In this work, we performed a He I high-resolution transmission spectroscopy survey of five gas giants namely WASP-69 b, WASP-107 b, HAT-P-11 b, GJ 436 b, and GJ 3470 b. In this section, we summarise our findings. The last column of Table 4.1, highlights the nights with significant telluric overlap and possible stellar activity issues.

Individual analyses

WASP-69 b We analysed four observing nights for WASP-69 b, namely 2019-07-24, 2020-08-09, 2021-10-28, and 2022-09-14. However, 2021-10-28 was affected by OH contamination, we thus decided to exclude data from this night when computing the final contrast value [4]. We measured a contrast of 3.91±0.22% (17.6σ), compatible with the value reported by Nortmann et al. (2018), Vissapragada et al. (2020), Vissapragada et al. (2022) and Tyler et al. (2024), while slightly higher than the one reported by Allart et al. (2023) with SPIRou (where they measured a maximum excess absorption of ∼3.1%). From the 2D map in Fig. 4.4 we can confirm the existence of a cometary tail following the planet (Nortmann et al. 2018; Tyler et al. 2024). Our He I signal appears to persist for approximately ∼50 minutes after egress. Nortmann et al. (2018) reported a 22 minutes of post-transit absorption, while Tyler et al. (2024) observed a longer duration of 1.28 hours after egress. The variations in tail lengths might be attributed to intrinsic

[4] If we also consider 2021-10-28 as an absorption signal of He I is still visible in the 2D map in Fig. 4.12, albeit affected by OH contamination, we measured a contrast of 3.88±0.21% (18.8σ)

atmospheric variability or to insufficient baseline coverage and lower S/N in our study and Nortmann et al. (2018) compared to Tyler et al. (2024). From Fig. 4.6, UT 2019-07-24 appears to show a more pronounced absorption compared to the other transit events, with a compatibility of $\sim$1.9σ with the contrast value of 3.46 $\pm$ 0.32% (10.7σ) obtained by averaging the other three nights. We thus analysed the Hα diagnostic in the visible to investigate whether this disparity in the He I absorption levels was attributable to stellar contamination.

HARPS-N observations were available only for UT 2019-07-24 and UT 2020-08-09. Our findings for the Hα are shown in Fig. 4.8, with the final transmission spectra in the bottom right panel. For UT 2020-08-09, we obtained a **BIC** of 268.6 for the Gaussian fit and 269.8 for the linear fit, resulting in a ΔBIC of 1.8. According to Kass & Raftery (1995), the linear fit is the model that better describes our data, hence excluding the presence of features in our transmission spectrum. This is also reinforced by the absence of features in the light curve shown in the bottom left panel of Fig. 4.8. On the other hand, we detected an emission signal during UT 2019-07-24 (1.45$\pm$0.19%, 7.6σ) with the Gaussian fit being the heavy favourite on the linear one (Gaussian **BIC**: 324.2, linear **BIC**: 352.2). Our detection is corroborated by the spectroscopic light curve, computed with a width of 20 km/s, which shows a clear emission feature during the first half of the transit (bottom left panel of Fig. 4.8). This finding was further corroborated by the `SLOPpy` routine (Sicilia et al. 2022), which also revealed an excess of absorption during UT 2019-07-24 in the Sodium doublet (Sicilia et al. 2025), in comparison to other nights.

This case appears similar to what was reported for HD189733 b in Guilluy et al. (2020) during the third night of observation, where an additional absorption in He I was observed in correspondence with an emission signal in Hα suggesting that the planet was transiting over quiescent regions of the stellar surface. Given the activity of WASP-69 (as indicated by the $\log \mathrm{R'_{HK}}$ measurements in Table 4.7) we would expect to have a nonuniform stellar disk, and thus a possible occultation during the transit of quiescent stellar features. However, this signal appears red-shifted in the stellar rest frame (17.4$\pm$3.0 km/s, see Fig. 4.10 in the appendix), while a pseudo signal caused by a plage-like region should be at rest in the star reference frame. An alternative explanation could be the presence of a flare. In this case, we would be observing the ejected material falling back to the star and hence moving away from us. This would account for the behaviour in He I and Hα , as well as the redshift in Hα in the stellar reference frame. The Hα line could be produced within a moving structure, for example, material falling toward the chromosphere or material moving away from us with the flare occurring near the edge of the star (thus explaining the redshift), while the He I absorption could be produced in a region outside the flare but irradiated by the XUV rays of the flare, which contribute to populating the atomic level from which the absorption that produces the line originates.

It is worth noting that Nortmann et al. (2018) also reported significantly different depths in the two **CARMENES** nights analysed in their study. This raises the question of whether a similar mechanism might be at play in their data.

In Fig. 4.4, the He I signal appears to be slightly tilted, indicating a different atmo-

spheric K_P compared to the one obtained from the radial velocity curves (see Table 4.6). We investigated a lag vector corresponding to possible atmospheric K_P in the range $0 \leq K_P \leq 250$ km s^{-1}, in steps of 1 km s^{-1}. We considered the two nights where the He I signal was less affected by the OH telluric emission line (i.e., UT 2019-07-24 and 2020-08-09). For each K_P value, we derived a 2D map (similar to those shown in Fig. 4.4) and a T_{mean} that we fitted with a Gaussian to determine the peak of He I absorption. We see that the He I absorption peak is maximised for an atmospheric K_P of approximately 80 km s^{-1} (lower than the one reported in the literature, see Table 4.6). We have to stress that given the width of the single line we are investigating, this result has to be taken just as a maximisation but without any statistical significance. 3D hydrodynamic simulations suggest that the He I signal in robust outflows may not precisely follow the expected K_P. Once the gas starts getting outside the planetary Roche lobe the velocity dynamics can differ (see e.g., Nail et al. 2024 and Gully-Santiago et al. 2024).

WASP-107 b We analysed two transits of WASP-107 b, i.e. 2019-02-07, and 2019-05-04. However, the second observing night was strongly affected by the OH emission line. If we consider only the first transit (i.e. UT 2019-02-07) we obtained an absorption of $8.17^{+0.80}_{-0.76}$% (10.5σ) compatible with 7.92±1.00% and 7.26±0.24% reported by Allart et al. (2019) and Kirk et al. (2020), respectively. Our 2D maps in Fig. 4.4 and the spectroscopic light curve in Fig. 4.7 could indicate the presence of a tail following the planet, in agreement with Fig.3 in Kirk et al. (2020) and Spake et al. (2021). Although our tail appears to be shorter than found in the latter study; this difference may be attributed to intrinsic atmospheric variability, as highlighted for WASP-69 b or to lower sensibility.

HAT-P-11 b We gathered three transit observations for HAT-P-11 b. We reported an extra absorption of 1.36±0.17% (8.0σ) in agreement with ∼1.2% and ∼1.3% reported by Allart et al. (2018) and Allart et al. (2023), respectively. According to Table 4.3, all the helium absorption measurements are compatible within 0.5σ.

GJ 436 b We collected six transits of GJ 436 b. We did not report any He I extra absorption for GJ 436 b, as our findings are consistent with zero absorption. Neither the single nights taken individually (see Fig. 4.4) nor the light curve (see Fig. 4.7) show evidence of helium absorption with a 1σ upper limits of 0.42 (0.52 at 2σ). The small He I feature in our final transmission spectrum (Fig. 4.6) could be due to correlated noise falling at the position of the stellar helium triplet not perfectly corrected with the **GP** regression model. Our result is in agreement with Nortmann et al. (2018), who did not find evidence of He I in the upper atmosphere of GJ 436 b (they reported a 90% confidence upper limits of 0.41% calculated from the standard deviation of the spectrum).

GJ 3470 b Here, we analysed five nights of observations, namely 2018-01-13, 2019-02-04, 2019-12-28, 2020-01-27, and 2022-12-24, that we will refer to as transit 1, tran-

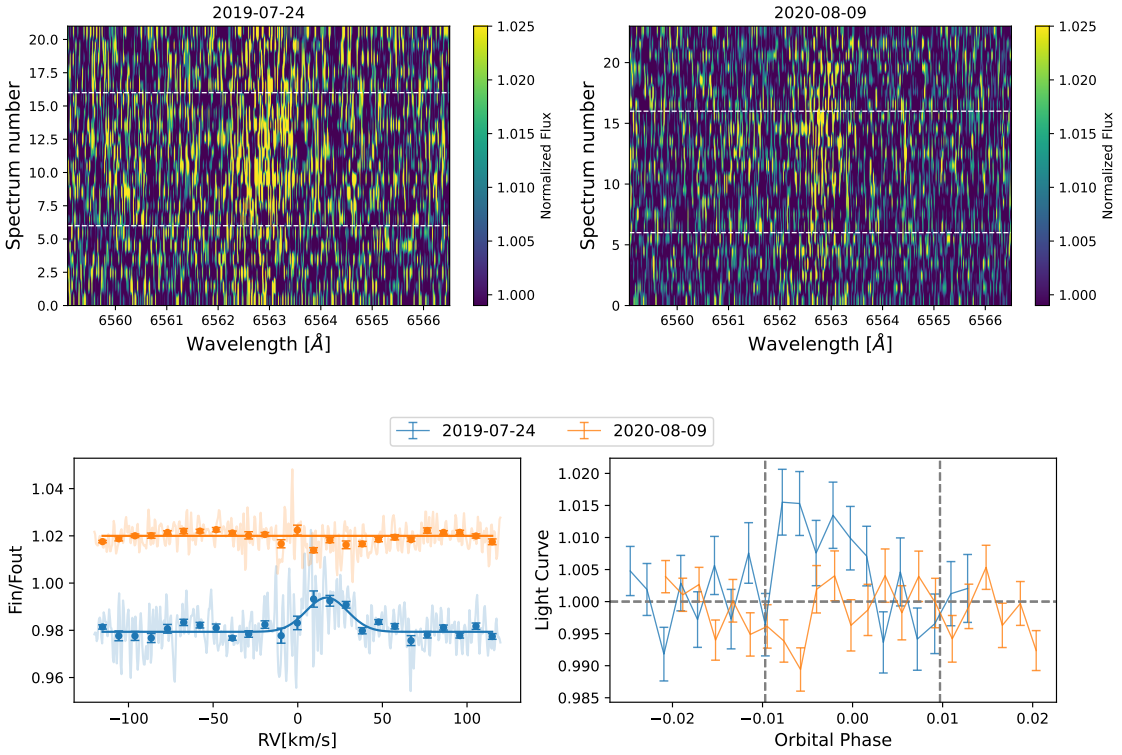

Figure 4.8: Hα transmission spectra and light curves for WASP-69 b. Top: 2D transmission spectroscopy maps in the stellar rest frame for UT 2019-07-24 (top-left) and UT 2020-08-09 (top-right). Red dotted lines mark the position of the Hα line in the planet rest frame. Bottom: spectroscopic light curves (bottom-left) and weighted average of the full in-transit spectra in the planet rest frame (bottom-right, the equivalent in the stellar rest frame is in the left panel of Fig. 4.10 in the appendix). Light colours indicate the not binned transmission spectra, while dots represent the transmission spectra binned 20$\times$(in **Radial Velocity (RV)**). We over-imposed the Gaussian profile derived from the best-fit parameters on the not-binned spectra.

sit 2, transit 3, transit 4, and transit 5 for simplicity. As the 2D maps in Fig. 4.12 show, three (i.e. transit 1, transit 2, and transit 4) were strongly contaminated by the OH telluric emission line, we thus decided to discard these nights. The 2D maps (Fig. 4.12) suggest that the majority of the signal originates from transit 3. If we account for only this transit, we obtained a tentative detection of the extra absorption of $1.75^{+0.39}_{-0.36}\%$ (4.7σ), in agreement with Ninan et al. (2020), $\sim$1.5% from their Figure 5, and Palle et al. (2020a), 1.5$\pm$0.3%. Allart et al. (2023) could not replicate the detection with SPIRou and only placed a 3σ upper limit on the presence of helium at 0.63%. Despite our detection being consistent at 3σ with no absorption, tomography reveals a hint of absorption at the helium triplet position.

It is worth noting that Palle et al. (2020a) observed variability across the analysed nights (see their Table 3) and attributed it to differences in the signal-to-noise ratio. However, in our investigation, we find comparable S/N between transit 3 and transit 5. The differences in the literature are not so surprising, considering our result.

Given the lack of homogeneity in the He I observation across the various investigated nights, we also analysed the Hα line in a similar way to WASP-69 b (Fig. 4.9). Out of the five nights under consideration, only three were usable in terms of S/N, namely transit 3, transit 4, and transit 5. We identified an absorption signal in Hα (3.48$\pm$0.26%, 13σ) at rest in the planet's reference frame during transit 3 (as depicted in panels a and e of Fig. 4.9). The **BIC** analysis confirms the absorption signal detected with a **BIC** value of 401.5 for the Gaussian and 462.5 for the linear fit. This particular night contributed to the majority of the He I signal. If this simultaneous absorption signal in both He I and Hα was due to stellar activity, it could be explained by the planet's passage over a quiescent region of the stellar disk, while the star presents filaments. These regions being darker than the rest of the star in both helium and Hα could have caused this pseudo-signal in absorption in both the stellar lines. On the other hand, it is also plausible that the Hα absorption feature may be attributed to an extended planetary hydrogen atmosphere. However, theoretical transmission profiles simulated using the ATES code (Caldiroli et al. 2022) and the new add-on module Transmission Probability Module (Biassoni et al. 2024b) are not able to reproduce an absorption depth/profile consistent with our observations. For this simulation, we assumed a Local Thermodynamic Equilibrium (**Local Thermal Equilibrium (LTE)**) profile, and adopted an X-ray luminosity of log(L_X)=27.58 measured by Spinelli et al. (2023) and two different X-ray-EUV relations derived by Johnstone et al. (2021) and Sanz-Forcada (2022), i.e., log(L_{EUV})=27.98 and log(L_{EUV})=28.40, respectively. Although the Hα population process may not be in the **LTE** regime (e.g., García Muñoz & Schneider 2019), our ATES analysis and the detection in only one of the three **HARPS-N** nights, make the hypothesis of a stellar origin for the feature detected in Hα the most plausible. Further analyses including more detailed radiative transfer models are needed to confirm this hypothesis.

Concerning transit 4 (shown in violet in Fig. 4.9), the one significantly impacted by the OH emission line in He I , the **HARPS-N** data were affected by both noise and systematics (as evident in both the light curve and the 2D maps in panels b and d of Fig. 4.9) and we had to remove two spectra for which the telluric correction with `Molecfit` did not work resulting in an overcorrection. In this case, the linear fit is favourite with

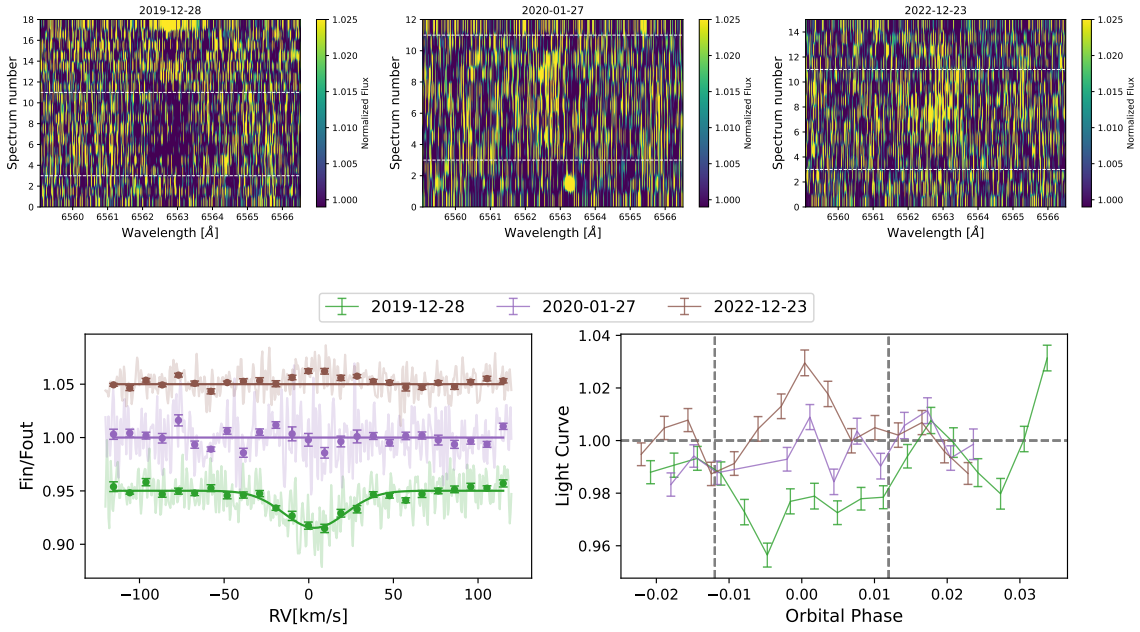

Figure 4.9: Hα transmission spectra and light curves for GJ-3470b. Top: 2D transmission spectroscopy maps in the stellar rest frame for UT 2019-12-28 (transit 3), UT 2020-01-27 (transit 4), and UT 2022-12-23 (transit 5) in left, middle, and right panels, respectively. Bottom: spectroscopic light curves (right panel) and weighted average of the full in-transit spectra in the planet rest frame (left panel, the equivalent in the stellar rest frame is in the left panel of Fig. 4.10).

respect to the Gaussian one (**BIC** 462.5 vs 447.4) consistently with the absence of features in the light curve. Hence, we do not detect any Hα signal in this night. Finally, during transit 5 (depicted in brown in Fig. 4.9), there appears to be an emission signal in Hα , as highlighted from both the 2D map (panel c) and the spectroscopy light curve (panel d). This signal seems more pronounced in the star's rest frame (right panel of Fig. 4.10 in the appendix) even if with a low significance$\sim 4\sigma$. Consequently, it may be attributed to stellar activity; for instance, the planet's transit over a dark region on the stellar disk, such as a filament, could potentially mimic a pseudo-signal in emission in both Hα and He I , thereby impacting our helium detection. However, considering the low significance of this detection, the small number of spectra (i.e., 15), and the moderate S/N ($\sim$ 38), we cannot dismiss the possibility that this result may be solely attributed to statistical noise. The latter hypothesis is supported by the **BIC** test which returns the same value for both the linear fit and the Gaussian one (**BIC**=398), hence hinting us to prefer the model with fewer parameters.

4.1.5 Statistical analyses

In this section, we looked for possible correlations between the He I absorption feature and the stellar/planetary parameters thought to be keys for the He I signal observabil-

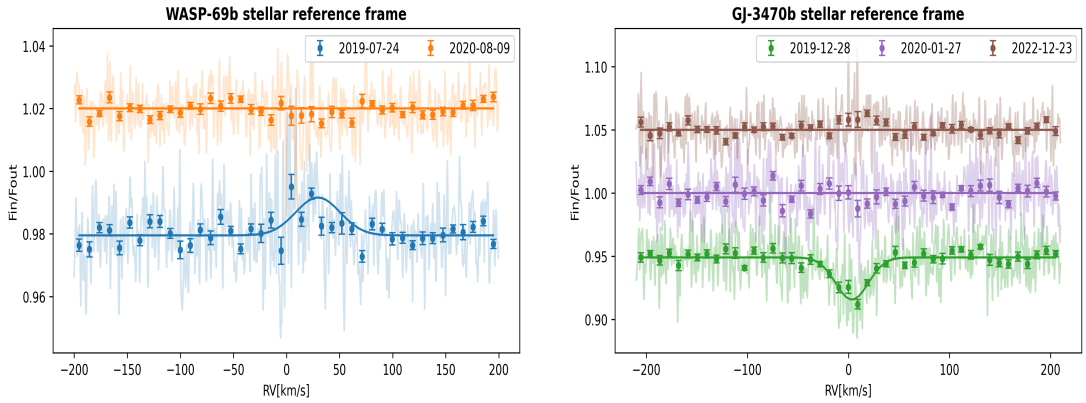

Figure 4.10: Weighted average of the full in-transit spectra in the star rest frame for WASP-69 b (left panel) and GJ3470b (right panel) centered on the Hα line. Light colors indicate the not binned transmission spectra, while dots show the transmission spectra binned 20$\times$(in **RV**). The overplotted fit is performed on the not-binned spectra and represents the model favorite by the **BIC** test.

ity. To achieve this goal, in addition to the findings presented in this work, we have also considered previous He I studies performed with GIANO-B around K-type stars, namely HD189733 b (Guilluy et al. 2020), WASP-80b (Fossati et al. 2022), and HAT-P-3 b (Guilluy et al. 2023).

For each planet in our sample, we derived the effective He I radius (e.g., Chen et al. 2018) that would produce the observed absorption contrast c (see Table 4.4). We then normalised it to the atmospheric $H_{\rm eq}$ to compute the quantity $\delta_{\rm R_P}/H_{\rm eq}$ (Nortmann et al. 2018), which represents the number of scale heights probed by the atmosphere in the spectral range under consideration. Here, $H_{\rm eq}$ is defined as $\frac{k_{\rm B}T{\rm eq}}{\mu g_{\rm P}}$ (see Table 4.4), where $k_{\rm B}$ is the Boltzmann constant, $T_{\rm eq}$ is the planetary equilibrium temperature (listed in Table 4.6), $g_{\rm P}$ is the planetary gravity calculated from the planetary mass and radius (see Table 4.4), and μ is the mean molecular weight. According to Fossati et al. (2022), we assumed a hydrogen-dominated atmosphere and hence μ=1.3 times the mass of a hydrogen atom (we opted for a hydrogen-dominated atmosphere rather than a hydrogen-and-helium atmosphere to mitigate uncertainties arising from the unknown helium abundance[5]). The derived $\delta_{\rm R_P}/H_{\rm eq}$ values for each investigated planet are presented in Table 4.4.

In Fig. 4.11, we examined how these derived constraints vary with respect to the EUV flux in the 200 to 504 Å range (which controls the He I metastable production, and therefore absorption, in the planetary atmosphere, Fossati et al. 2023b), effective temperature, planetary gravity, and $\log {\rm R'_{HK}}$. We used the EUV flux derived in Fossati et al. (2023b)

[5]The value of μ=1.3 is typically considered for hot Jupiters assuming solar abundances, but it also takes into account the presence of a mix of molecular hydrogen and electrons resulting from the ionisation of various elements, especially Na and K. Hydrogen and helium abundances are not the only factor to consider. We would like to emphasise that the adopted μ does not alter the final outcome, and does not influence the presence or absence of correlations.

from the scaling relations of Poppenhaeger (2022). We employed the same methodology to derive the EUV flux received by HAT-P-3 b, the only one missing in the sample analysed by Fossati et al. (2023b). As no X-ray measurements were present in the literature, we estimated it starting from our derived $\log R'_{HK}$ value (see Table 4.7) and the Mamajek & Hillenbrand (2008) relation, obtaining a value of Lx=$1.3^{+2.2}_{-0.8}$ 10^{27} erg/s. We then employed the Poppenhaeger (2022) relations to estimate the EUV flux. However, due to the large uncertainty on the derived X-ray luminosity, we were unable to constrain the coronal temperature (relation from Johnstone & Güdel 2015). As a result, considering a range of 1.25-2.1 MK for the coronal temperature, we obtained two different EUV flux values using the scaling relations of Poppenhaeger (2022): 36 erg s^{-1} cm^{-2} and 1095 erg s^{-1} cm^{-2}.

Trends related to the contrast c and atmospheric extension δ_{R_P}/H_{eq} are shown in the left and right panels of Fig. 4.11, respectively. To evaluate the strength of the possible correlations between the investigated parameters, we ran an **MCMC** varying the He I contrasts c according to a normal distribution with a standard deviation equal to the error we found on c. In the case of non-detection, we used a half-Gaussian distribution centred at zero with a standard deviation equal to the 1σ upper limit. We ran 10 000 iterations and at each **MCMC** step, we computed the Spearman rank-order correlation coefficient ρ to measure the strength of our relationships. The final mean values, the corresponding errors, and the p-values are reported in Table 4.5. The p-values were computed using a t-test under the null hypothesis that the correlation coefficients are significantly different from 0.

Table 4.5: Correlations between the investigated planetary and stellar parameters expected to influence the He I observability.

X, Y	ρ Spearman	Correlation Strength	p-value
F_{EUV},δ_{R_P}/H_{eq}	0.0118 $\pm$ 0.0029	null	0.98
F_{EUV},c	0.1677 $\pm$ 0.0029	low	0.69
T_{eff},δ_{R_P}/H_{eq}	-0.0278 $\pm$ 0.0028	null	0.95
T_{eff},c	-0.139 $\pm$ 0.0027	low	0.70
g_P,δ_{R_P}/H_{eq}	0.0658 $\pm$ 0.0028	null	0.88
g_P,c	-0.1898 $\pm$ 0.0026	low	0.65
$\log R'_{HK}$,δ_{R_P}/H_{eq}	-0.1292 $\pm$ 0.0028	low	0.76
$\log R'_{HK}$,c	0.1460 $\pm$ 0.0030	low	0.73

From left to right: the parameters investigated for the correlation, the Spearman value, the strength of correlation from Kuckartz et al. (2013), and the associated p-value.

Our findings do not show significant correlations between the investigated parameters (p-values > 0.05). The null hypothesis that any two parameters X, Y in Table 4.5 are uncorrelated is rejected with a confidence level not exceeding 90%, corresponding to a $< 2\sigma$ result. However, it is important to underline that we are still within the statistical limit of small numbers, so the results should be interpreted with caution. Furthermore, it is important to underscore that there might be variability among planets, attributable

in part to possible differences in helium abundance in the atmosphere. This variability could introduce additional noise, potentially hindering our ability to establish statistical correlations. Finally, $H_{\rm eq}$ might not be the correct physical length scale to consider in such an analysis. For instance, Zhang et al. (2023a) showed that the scale height does not correlate with the contrast measured for the deepest individual lines in a sample of exoplanets, attributing this effect to hydrodynamical effects arising in the upper part of the atmosphere. Even within the hydrostatic region of an atmosphere, in the presence of significant variations with altitude of temperature, gravity or even mean molecular weight, using a single scale height might be too simplistic.

These potential trends do not highlight any explanations that could justify the detection and non-detection of metastable He I in the upper atmospheres of the investigated planets[6]. The three planets with only upper limits on the He I detection, namely GJ 436 b, WASP-80b, and HAT-P-3 b do not seem to exhibit a clear correlation in the investigated parameter space. Fossati et al. (2023b) emphasised that the low-EUV stellar flux, influenced by the low [Fe/O] coronal abundance (Poppenhaeger 2022), could likely be the primary factor behind the He I non-detection. Rumenskikh et al. (2023) attributed the weak He I signature reported by Nortmann et al. (2018) (0.41%, 2σ) to the thinness of both the region populated by the absorbing He I ($<3{\rm R_P}$) and of the ${\rm R_P/R_\star}$ ratio and to the radiation pressure force which spreads He I atoms along the line of sight and around the planet. Yet, there is still no explanation for the non-detection in the atmosphere of HAT-P-3 b.

It is interesting to highlight that both HAT-P-3 b and GJ 436 b are on a polar orbit with a 3D true obliquity (ψ) of $75.7^{+8.5}_{-7.9}$ deg (Bourrier et al. 2023) and $103.2^{+12.8}_{-11.5}$ deg (Bourrier et al. 2022), respectively. On the other hand, WASP-80 b is well known to be on a relatively aligned orbit (Triaud et al. 2015). This may indicate that also the orbital obliquity does not influence the He I observability.

It is important to note that, in our study, in Fossati et al. (2022) and in Guilluy et al. (2020), we analysed multiple transit events for each planet, investigating the repeatability of the He I signal. However, this is not the case for HAT-P-3 b, as in Guilluy et al. (2023) only one night of observation was gathered and examined. Therefore, obtaining more data is essential to provide clarity on this non-detection.

4.1.6 Summary and conclusion

We employed the GIARPS mode of the **TNG**, focusing on GIANO-B observations to look for He I in the upper atmosphere of five planets hosted by the K and M dwarf stars of our sample, namely WASP-69 b, WASP-107 b, HAT-P-11 b, GJ 436 b, and GJ 3470 b. We measured a contrast c of the excess absorption of 3.91±0.22% (17.6σ), $8.17^{+0.80}_{-0.76}$% (10.5σ), and 1.36±0.17% (8.0σ) for WASP-69 b, WASP-107 b, and HAT-P-11 b, respectively, confirming the literature detections. Our analysis of WASP-69 b showed a night-to-night variability in the helium absorption levels, with the first transit exhibiting a higher absorption value compared to the others. We thus inspected the Hα line in

[6]The results remain consistent when we consider the contrast c (and the corresponding $\delta_{\rm R_P}/H_{\rm eq}$) obtained by excluding the night of UT 2019-07-24 for WASP-69 b, likely affected by stellar contamination.

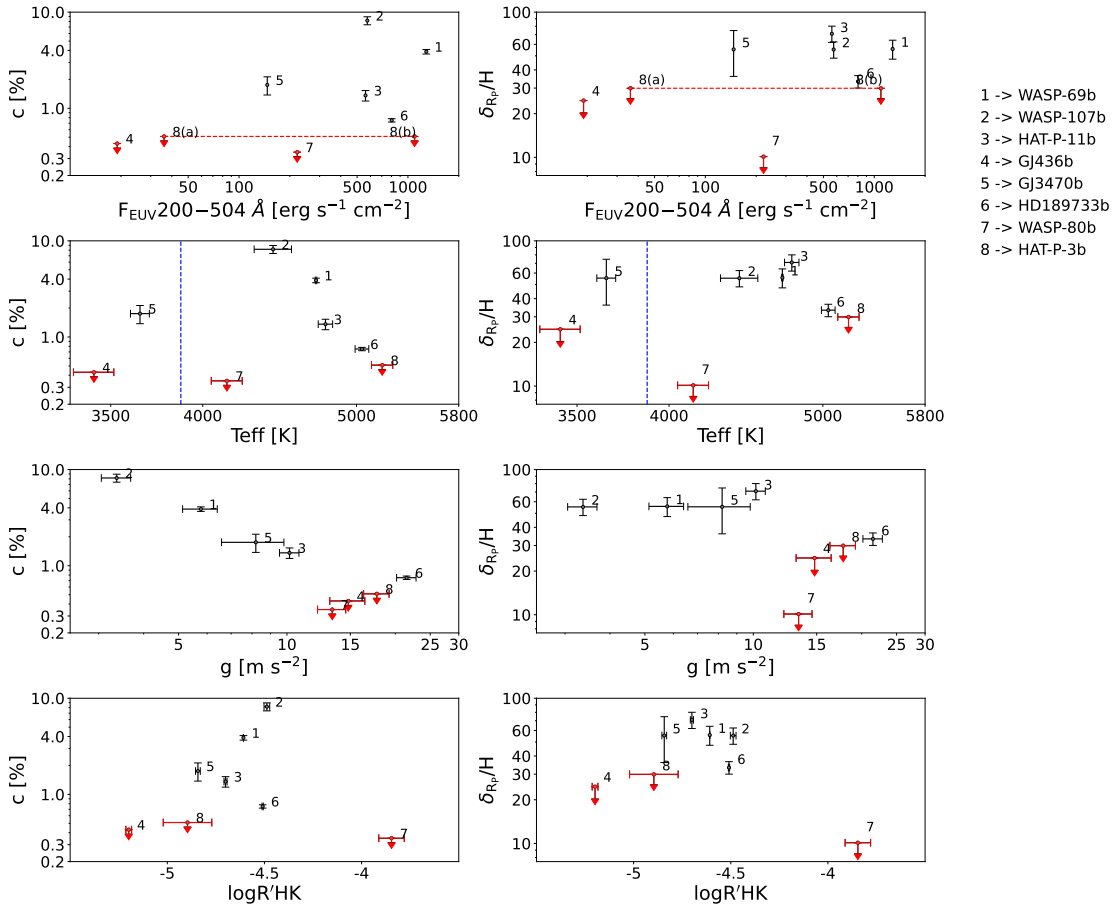

Figure 4.11: Correlation plots. Targets from this work, Guilluy et al. (2020), Fossati et al. (2022) and Guilluy et al. (2023). Contrast c (left panels) and $\delta_{\mathrm{R_P}}/H_{\mathrm{eq}}$ (right panels) as a function of the EUV flux in the 200 to 504 Å range, effective temperature and planetary gravity, and $\log \mathrm{R'_{HK}}$. Red markers indicate targets with only an upper limit on the He I detection (reported at 1σ). The vertical dashed blue lines in the effective temperature diagrams indicate the transition from M-type to K-type stars. The dashed horizontal line connects the two possible locations for HAT-P-3 b (for the two different coronal temperatures).

HARPS-N spectra, finding an opposite behaviour in Hα compared to that recorded in He I during UT 2019-07-29. We interpreted this as due to the effect of stellar activity, and we speculated on the possible origins of this effect.
We reported a detection of He I in the upper atmosphere of GJ 3470 b of $1.75^{+0.39}_{-0.36}\%$ (4.7σ). Our result is in agreement with previous studies by Ninan et al. (2020) and Palle et al. (2020a). However, if we consider only the two nights not affected by the OH emission line, the signal seems to appear from only one transit, supporting the literature discrepancy and indicating the presence of variability, whereby the extended atmosphere is more evident on certain nights than on others. Additional observations are mandatory to unveil the origin of the He I signal. An inspection of the Hα line reveals a hydrogen absorption signal during the same transit event. Our ATES simulations are not able to reproduce an absorption depth/profile consistent with our observations, thus making stellar activity the most plausible origin for this feature. Further analyses including more detailed radiative transfer models are needed to confirm this hypothesis.
In agreement with a previous work (Nortmann et al. 2018), we did not detect a He I excess of absorption for GJ 436 b (our finding is compatible with zero absorption).
We finally placed our results in the context of other He I analyses on planets orbiting K- and MV-type stars obtained with GIANO-B, namely HD189733 b (Guilluy et al. 2020), WASP-80b (Fossati et al. 2022), and HAT-P-3 b (Guilluy et al. 2023). We explored potential trends associated with stellar and planetary parameters believed to influence the He I detection, such as the EUV flux, the effective temperature, the planet's gravity, and the $\log \mathrm{R'_{HK}}$. Our analysis does not show any significant correlation and our investigation did not reveal any relationship between GIANO-B detections and non-detections in the atmospheres of planets around M-K dwarf stars and the parameters we explored. We emphasise that this could also be a consequence of the small sample size we are investigating. Moreover, both the stellar EUV flux and the helium abundance in the investigated atmospheres are highly uncertain, which may introduce potential noise when attempting to identify potential correlations. Additional observations are thus needed, together with the investigation of new parameters that could influence the He I observability.
Our work underscores the importance of a homogeneous He I survey encompassing both observation techniques and data analysis methods which are essential to understanding the key parameters governing the He I detectability. It also emphasises the necessity of simultaneous nIR and visible monitoring to investigate the potential presence of stellar activity pseudo-signals in He I measurements.

4.1.7 Additional Figures and Tables

Table 4.6: Adopted parameters

Parameter	Value	Reference
WASP-69		
Stellar Parameters		
Spectral type	K5	Anderson et al. (2014)
Stellar mass, $M_\star$ [$M_\odot$]	0.826±0.029	Anderson et al. (2014)

Table 4.6: continued

Parameter	Value	Reference
Stellar radius, $R_\star$ [$R_\odot$]	0.813±0.028	Anderson et al. (2014)
Effective temperature, $T_{\rm eff}$ [K]	4715±50	Anderson et al. (2014)
Metallicity, [Fe/H] [dex]	0.144±0.077	Anderson et al. (2014)
log $g_\star$ ($\log_{10}$[cm s^{-2}])	4.535±0.023	Anderson et al. (2014)
Systemic velocity, $v_{\rm sys}$ (km s^{-1})	-9.37±0.20	Gaia Collaboration et al. (2018)
Limb-darkening coefficients μ_1	0.26957980	EXOFAST
μ_2	0.26165142	EXOFAST
Magnitude (J-band)	8.032±0.023	Cutri et al. (2003)
WASP-69 b Parameters		
Orbital period, P [days]	3.86813888±9.1e-07	Kokori et al. (2023)
Transit epoch, T_0 [BJD_{TDB}]	2457269.01322±0.00027	Kokori et al. (2023)
Eccentricity, e	0 (fixed)	Anderson et al. (2014)
Argument of periastron, ω [deg]	90(fixed)	
Stellar reflex velocity, $K_\star$ [m s^{-1}]	38.1±2.4	Anderson et al. (2014)
Orbital major semi-axis, a [au]	0.04525±0.00053	Anderson et al. (2014)
Orbital inclination, i [deg]	86.71± 0.20	Anderson et al. (2014)
Planetary mass, $M_{\rm pl}$ [$M_{\rm jup}$]	0.260±0.017	Anderson et al. (2014)
Planetary radius, $R_{\rm pl}$ [$R_{\rm jup}$]	1.057±0.047	Anderson et al. (2014)
Impact parameter, b	0.686±0.023	Anderson et al. (2014)
Equilibrium temperature, $T_{\rm eq}$ [K]	963±18	Anderson et al. (2014)
Planet **RV** semi-amplitude, $K_{\rm p}$ [m s^{-1}]	127.1±1.5	This work
WASP-107		
Stellar Parameters		
Spectral type	K6	Anderson et al. (2017)
Stellar mass, $M_\star$ [$M_\odot$]	0.69±0.05	Anderson et al. (2017)
Stellar radius, $R_\star$ [$R_\odot$]	0.66±0.02	Anderson et al. (2017)
Effective temperature, $T_{\rm eff}$ [K]	4430±120	Anderson et al. (2014)
Metallicity, [Fe/H] [dex]	0.020±0.100	Anderson et al. (2014)
log $g_\star$ ($\log_{10}$[cm s^{-2}])	4.5±0.1	Anderson et al. (2014)
Systemic velocity, $v_{\rm sys}$ [km s^{-1}]	13.74±0.31	Gaia Collaboration et al. (2018)
Limb-darkening coefficients μ_1	0.29281680	EXOFAST
μ_2	0.24780640	EXOFAST
Magnitude (J-band)	9.378 ±0.021	Cutri et al. (2003)
WASP-107 b Parameters		
Orbital period, P [days]	5.72148926 ± 8.5e-07	Kokori et al. (2023)
Transit epoch, T_0 [BJD_{TDB}]	2457515.672118±7.5e-05	Kokori et al. (2023)
Eccentricity, e	0 (fixed)	Anderson et al. (2017)
Argument of periastron, ω [deg]	90 (adopted)	
Stellar reflex velocity, $K_\star$ (m s^{-1})	17±2	Anderson et al. (2017)
Orbital major semi-axis, a [au]	0.055 ±0.001	Anderson et al. (2017)
Orbital inclination, i [deg]	89.7±0.2	Anderson et al. (2017)
Planetary mass, $M_{\rm pl}$ [$M_{\rm jup}$]	0.12±0.01	Anderson et al. (2017)
Planetary radius, $R_{\rm pl}$ [$R_{\rm jup}$]	0.94±0.02	Anderson et al. (2017)
Impact parameter, b	0.09±0.07	Anderson et al. (2017)
Equilibrium temperature, $T_{\rm eq}$ [K]	770±60	Anderson et al. (2014)
Planet **RV** semi-amplitude, $K_{\rm p}$ [m s^{-1}]	105.2±2.5	This work
HAT-P-11		

Table 4.6: continued

Parameter	Value	Reference
Stellar Parameters		
Spectral type	K4 V	Bakos et al. (2010)
Stellar mass, $M_\star$ [$M_\odot$]	0.86 ± 0.06	Lundkvist et al. (2016)
Stellar radius, $R_\star$ [$R_\odot$]	0.76 ± 0.01	Lundkvist et al. (2016)
Effective temperature, $T_{\rm eff}$ [K]	4780 ± 50	Bakos et al. (2010)
Metallicity, [Fe/H] [dex]	0.31 ± 0.05	Bakos et al. (2010)
log $g_\star$ ($\log_{10}$[cm s^{-2}])	4.37±0.22	Stassun et al. (2017)
Systemic velocity, $v_{\rm sys}$ [km s^{-1}]	-63.24 ± 0.26	Gaia Collaboration et al. (2018)
Limb-darkening coefficients μ_1	0.26597299	EXOFAST
μ_2	0.26607108	EXOFAST
Magnitude (J-band)	7.608±0.029	Cutri et al. (2003)
HAT-P-11 b Parameters		
Orbital period, P [days]	4.88780201±1.7e-07	Kokori et al. (2023)
Transit epoch, T_0 [$BJD_{\rm TDB}$]	2455798.515261±2.3e-05	Kokori et al. (2023)
Eccentricity, e	$0.2577^{+0.0033}_{-0.0025}$	Basilicata et al. (2023)
Argument of periastron, ω [deg]	$19.0^{+2.9}_{-3.0}$	Basilicata et al. (2023)
Stellar reflex velocity, $K_\star$ [m s^{-1}]	11.21±0.36	Basilicata et al. (2023)
Orbital major semi-axis, a [au]	0.0532 ± 0.0010	Basilicata et al. (2023)
Orbital inclination, i [deg]	89.027 ± 0.068	Basilicata et al. (2023)
Planetary mass, $M_{\rm pl}$ [$M_{\rm jup}$]	0.0818 ± 0.0046	Basilicata et al. (2023)
Planetary radius, $R_{\rm pl}$ [$R_{\rm jup}$]	0.4466 ± 0.0059	Basilicata et al. (2023)
Impact parameter, b	$0.227^{+0.013}_{-0.015}$	Basilicata et al. (2023)
Equilibrium temperature $T_{\rm eq}$ [K]	847^{+46}_{-54}	Basilicata et al. (2023)
Planet **RV** semi-amplitude, $K_{\rm p}$ [m s^{-1}]	123.5±2.9	This work
GJ436		
Stellar Parameters		
Spectral type	M2.5V	Butler et al. (2004)
Stellar mass, $M_\star$ [$M_\odot$]	$0.556^{+0.071}_{-0.065}$	Lanotte et al. (2014)
Stellar radius, $R_\star$ [$R_\odot$]	0.455 ±0.018	Lanotte et al. (2014)
Effective temperature, $T_{\rm eff}$ [K]	3416 ±100	Lanotte et al. (2014)
Metallicity, [Fe/H] [dex]	0.02±0.20	Lanotte et al. (2014)
log $g_\star$ ($\log_{10}$[cm s^{-2}])	4.843±0.018	Lanotte et al. (2014)
Systemic velocity, $v_{\rm sys}$ [km s^{-1}]	9.59 ±0.0008	Fouqué et al. (2018)
Limb-darkening coefficients μ_1	0.026586002	EXOFAST
μ_2	0.37369888	EXOFAST
Magnitude (J-band)	6.900±0.024	Cutri et al. (2003)
GJ436 b Parameters		
Orbital period, P [days]	2.643897621 ± 9.6e-08	Kokori et al. (2023)
Transit epoch, T_0 ($BJD_{\rm TT}$)	2455290.751684 ± 5.2e-05	Kokori et al. (2023)
Eccentricity, e	$0.1616^{0.0041}_{-0.0032}$	Lanotte et al. (2014)
Argument of periastron, ω [deg]	$327.2^{+1.8}_{-2.2}$	Lanotte et al. (2014)
Stellar reflex velocity, $K_\star$ [m s^{-1}]	17.59 ±0.25	Lanotte et al. (2014)
Orbital major semi-axis, a [au]	$0.0308^{+0.0013}_{-0.0012}$	Lanotte et al. (2014)
Orbital inclination, i [deg]	$86.858^{+0.049}_{-0.052}$	Lanotte et al. (2014)
Planetary mass, $M_{\rm pl}$ [$M_{\rm jup}$]	$0.080^{+0.007}_{-0.006}$	Lanotte et al. (2014)
Planetary radius, $R_{\rm pl}$ [$R_{\rm jup}$]	0.366±0.014	Lanotte et al. (2014)
Impact parameter, b	$0.7972^{+0.0053}_{-0.0055}$	Lanotte et al. (2014)

Table 4.6: continued

Parameter	Value	Reference
Equilibrium temperature T_{eq} [K]	686±10	Turner et al. (2016)
Planet **RV** semi-amplitude, K_p [m s^{-1}]	$128.1^{+5.5}_{-5.0}$	This work
GJ3470		
Stellar Parameters		
Spectral type	M1.5	Kosiarek et al. (2019)
Stellar mass, $M_\star$ [$M_\odot$]	0.51±0.06	Kosiarek et al. (2019)
Stellar radius, $R_\star$ [$R_\odot$]	0.48±0.04	Kosiarek et al. (2019)
Effective temperature, T_{eff} [K]	3652±50	Kosiarek et al. (2019)
Metallicity, [Fe/H] [dex]	0.20±0.10	Kosiarek et al. (2019)
log $g_\star$ ($\log_{10}$[cm s^{-2}])	4.658±0.035	Kosiarek et al. (2019)
Systemic velocity, v_{sys} [km s^{-1}]	26.09±0.25	Gaia Collaboration et al. (2018)
Limb-darkening coefficients μ_1	0.086634767	EXOFAST
μ_2	0.34988822	EXOFAST
Magnitude (J-band)	8.794±0.026	Cutri et al. (2003)
GJ3470b Parameters		
Orbital period, P [days]	$3.33665266^{+0.0000003}_{-0.0000003}$	Stefànsson et al. (2022)
Transit epoch, T_0 [BJD_{TDB}]	$2456340.72559^{+0.00011}_{-0.0001}$	Stefànsson et al. (2022)
Eccentricity, e	$0.125^{+0.043}_{-0.042}$	Stefànsson et al. (2022)
Argument of periastron, ω [deg]	$-83.4^{+3.4}_{-1.7}$	Stefànsson et al. (2022)
Stellar reflex velocity, $K_\star$ [m s^{-1}]	$8.03^{+0.38}_{-0.37}$	Stefànsson et al. (2022)
Orbital major semi-axis, a [au]	$0.0288^{+0.0029}_{-0.0028}$	Kosiarek et al. (2019)
Orbital inclination, i [deg]	$88.88^{+0.62}_{-0.45}$	Biddle et al. (2014)
Planetary mass, M_{pl} [M_{jup}]	$0.03958^{+0.00412}_{-0.00403}$	Kosiarek et al. (2019)
Planetary radius, R_{pl} [R_{jup}]	0.346±0.029	Kosiarek et al. (2019)
Impact parameter, b	0.29±0.14	Biddle et al. (2014)
Equilibrium temperature T_{eq} [K]	604±98	Biddle et al. (2014)
Planet **RV** semi-amplitude, K_p [m s^{-1}]	114.7±0.5	This work

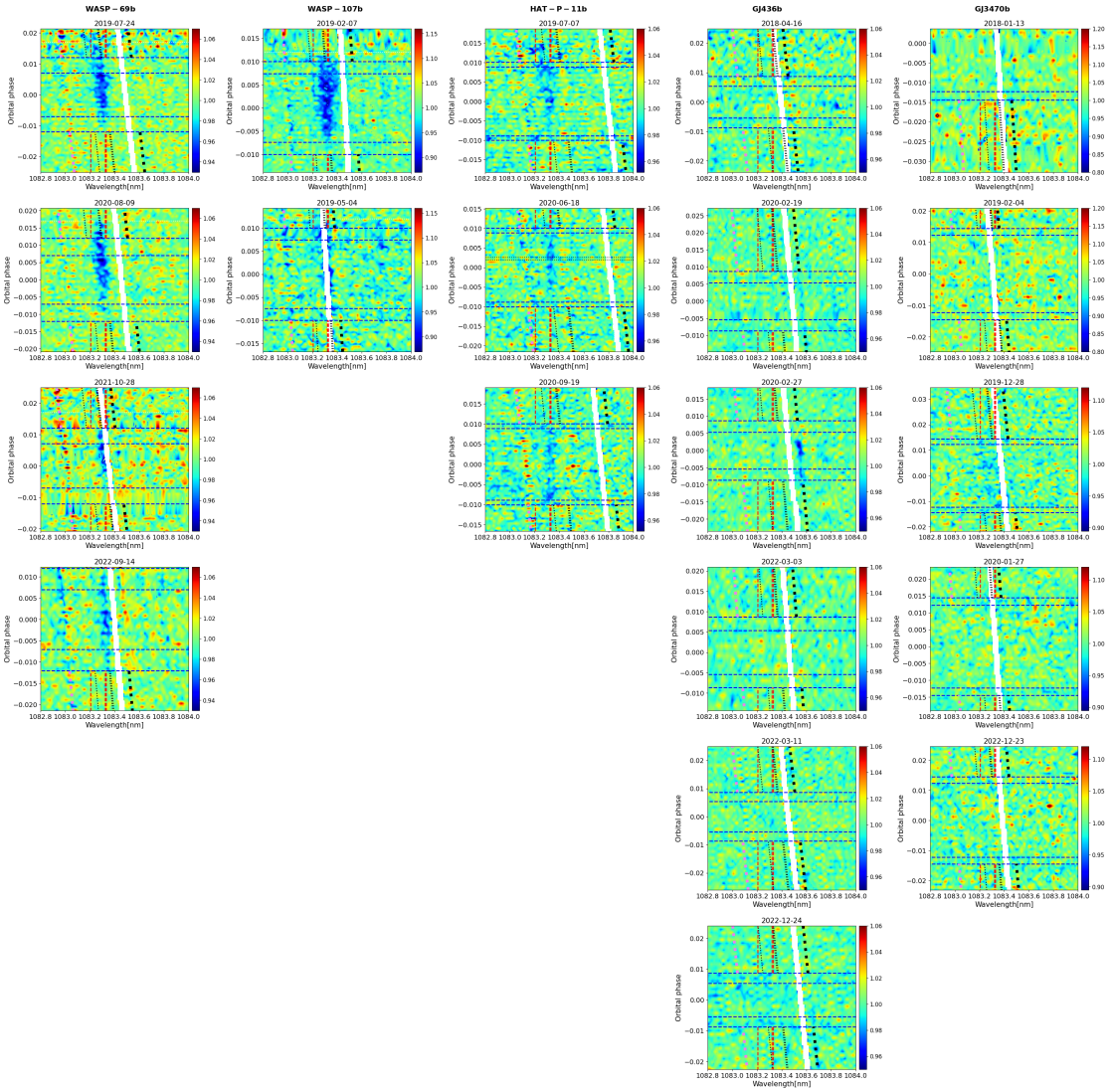

Figure 4.12: Same as Fig 4.4 but for all the investigated nights.

Figure 4.13: Corner-plots in the **DE-MCMC** analysis. The excess of absorption c [%], offset [%], peak position, and **FWHM** correspond to the parameters we used in the Gaussian fit, while the jitter term $\sigma_{\rm j}$, the semi-amplitude of the correlated noise h, the correlation length λ were used to parametrize the SE kernel within the **GP**.

Table 4.7: $\log R'_{HK}$ values.

	Night	$\log R'_{HK}$
WASP-69 b	2019-07-24	-4.561±0.008
	2020-08-09	-4.571±0.007
	2021-10-28	-4.608±0.006
	all	-4.567±0.011
WASP-107 b	2019-02-07	-4.431±0.017
	2019-05-04	-4.488±0.015
	all	-4.461±0.032
HAT-P-11 b	2019-07-07	-4.712±0.008
	2020-06-18	-4.675±0.005
	2020-09-19	-4.700±0.008
	all	-4.696±0.017
GJ3470b	2018-01-13	-4.814±0.092
	2019-02-04	-4.787±0.078
	2019-12-28	-4.795±0.019
	2020-01-27	-4.815±0.019
	2022-12-23	-4.842±0.013
	all	-4.809±0.054
GJ436 b	2018-04-16	-5.223±0.028
	2020-02-19	-5.183±0.010
	2020-02-27	-5.173±0.018
	2022-03-11	-5.182±0.015
	2022-12-24	-5.199±0.015
	all	-5.191±0.024

The $\log R'_{HK}$ measurements have been obtained from the Ca II H&K lines through the offline version of **HARPS-N** data reduction software (**DRS**) available through the Yabi web application (Hunter et al. 2012). For GJ436 and GJ3470, which have an index color B-V>1.1, we applied the Suárez Mascareño et al. (2015) formalism.

4.2 Photo-evaporating puzzle: exploring the enigmatic nature of TOI-5398 b atmospheric signal

High-resolution transmission spectroscopy has been predominantly applied to hot and massive exoplanets, such as Hot Jupiters (HJs), because of their high equilibrium temperatures due to the small distances from their host star (Guilluy et al. 2022a). The closeness and the subsequent high equilibrium temperature, $T_{\rm eq}$, favor the photo-evaporation processes, and enhance the scale height defined as

$$H = \frac{k_{\rm B} T_{\rm eq}}{\mu g_{\rm p}}, \tag{4.1}$$

where k_B is the Boltzmann's constant and μ is the mean molecular weight. In many cases, this leads to a large annulus that absorbs the starlight during the transit, resulting in a strong signal. However, the large HJs mass increases the surface gravity, $g_{\rm p}$, and hence diminishes the scale height. Therefore, the ideal targets for transmission spectroscopy are close and hot inflated planets with lower densities. The poorly-explored classes of Warm and Hot Saturn-like exoplanets combines these characteristics presenting an exciting opportunity to broaden our understanding of planetary atmospheres beyond the better-studied HJs.

The TOI-5398 system (see Table 4.8 for the parameters) serves as a fascinating target for atmospheric studies due to its compact planetary architecture consisting of two planets orbiting close to the host star (Mantovan et al. 2024a) with the outer one distant 0.0980 au from the star. The outer planet, TOI-5398 b, is a warm Saturn-like exoplanet with distinct features that make it an ideal candidate for transmission spectroscopy. It has an equilibrium temperature of 947 K resulting in a scale height H_b = 1106.1 km, (with μ = 1.3 assuming a hydrogen-dominated atmosphere, instead of a hydrogen-and-helium-dominated atmosphere as in Fossati et al. 2022) larger than the mean value of an **Hot Jupiter (HJ)** ($\sim$ 450 km) and the largest Transmission Spectroscopy Metric (**Transmission Spectroscopy Metric (TSM)**, Kempton et al. 2018) value (**TSM** = 288) among all known warm giant planets. Its position at the border of the Neptunian valley and savanna (Owen & Wu 2017; Armstrong et al. 2019) makes the target even more fascinating since its predicted evolution will lead it at the center of the savanna in the next hundreds of Myrs as shown in Fig. 4.14 and in Fig (E.1) from Mantovan et al. (2024b). The system evolution was strongly shaped by the closeness to the host star, a young age (650 Myr) G-type star responsible for the photo-evaporation of the planets as discussed by Mantovan et al. (2024b). Based on their findings, planet b underwent minimal mass loss and hence the present size and composition of this gas giant are probably primordial, while planet c, the inner sub-Neptune, on the other hand, was more profoundly influenced by photoevaporation as hinted by its modal density.

The stellar x-ray and extreme ultraviolet (XUV) flux plays a crucial role in influencing the atmospheric properties of young exoplanets. Understanding the interactions between the XUV flux and the atmospheres of distant worlds provides critical insights into the atmospheric escape processes, photochemistry, and overall atmospheric evolution.

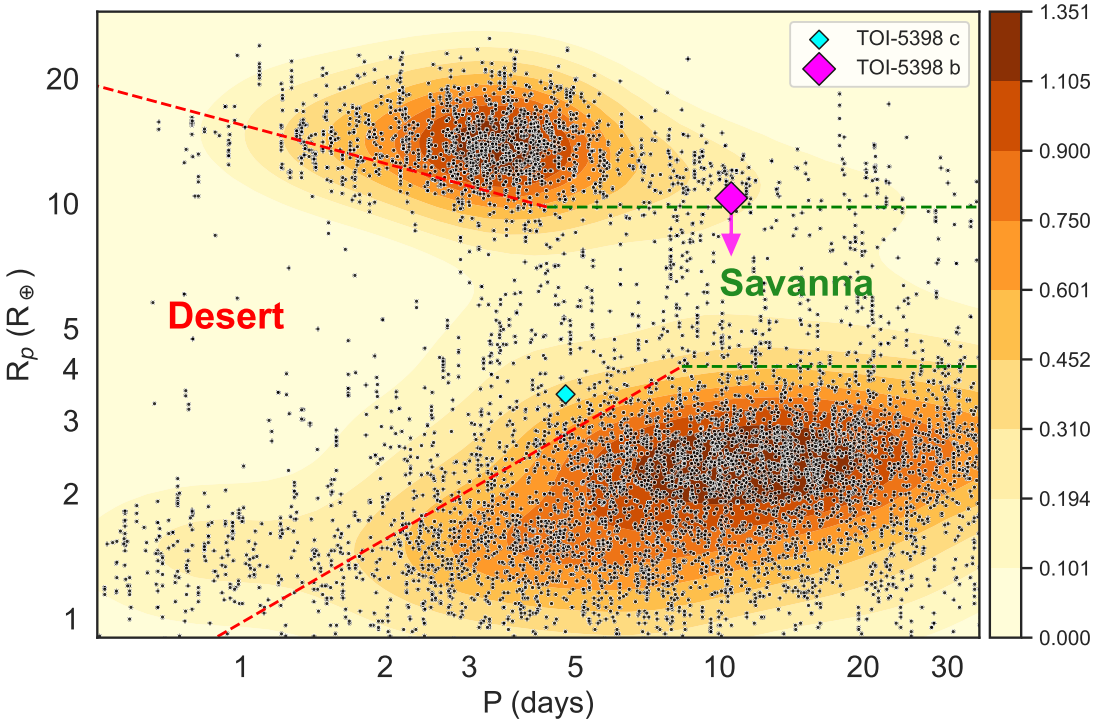

Figure 4.14: Known exoplanets as a function of their radius and period from the NASA Exoplanet Archive (Akeson et al. 2013) within the Neptunian desert and savanna. The color represents the density of planets. TOI-5398 b is highlighted with a purple diamond while the planet c is highlighted by a cyan one. The arrow indicates the expected position of the planet b within the Savanna at the end of its evolution according to Mantovan et al. (2024b). The marker size is proportional to the planetary mass.

The present study aims to explore the atmospheric composition of this intriguing exoplanet and contributes to the growing body of knowledge on diverse planetary systems. We aim to explore the composition of the upper layers of the atmospheres using different techniques involving both the visible and near-Infrared (nIR) part of our spectra, deepening our knowledge of the role of the XUV flux on the TOI-5398 system. For this purpose, we focus on lines arising from atomic species sensible to photo-evaporation such as He I and Hα , along with the search of other atomic species.

4.2.1 Observations

We observed the system TOI-5398 as part of the DDT proposal A46DDT4 (PI: G. Mantovan) on UT 25 March 2023 with the GIARPS observing mode (Claudi et al. 2017) of the Telescopio Nazionale Galileo (**TNG**). GIARPS allows for the simultaneous monitoring at High-Resolution in the visible band (0.39-0.69 μm) with **HARPS-N** ($R \approx 115,000$) and in the nIR (0.95-2.45μm) with GIANO-B ($R \approx 50,000$).
For the GIANO-B observations, we employed an ABAB nodding pattern (Claudi et al. 2017) to optimise thermal background noise subtraction. GIANO-B is an echelle spec-

Table 4.8: The stellar and planetary parameters adopted.

Parameters	*TOI-5398 b*	*TOI-5398 c*	Reference
Stellar Parameters			
Stellar mass, $M_\star$ ($M_\odot$)	1.146 ± 0.013		Mantovan et al. (2024a)
Stellar radius, $R_\star$ ($R_\odot$)	1.051 ± 0.013		Mantovan et al. (2024a)
Effective temperature, $T_{\rm eff}$ (K)	6000 ± 75		Mantovan et al. (2024a)
Metallicity, [Fe/H] (dex)	0.09 ± 0.06		Mantovan et al. (2024a)
log g ($\log_{10}$(cm s^{-2}))	4.44 ± 0.10		Mantovan et al. (2024a)
Systemic velocity, $v_{\rm sys}$ (km s^{-1})	9.95 ± 0.30		GaiaDR3
$v \sin i_*$ (km s^{-1})	7.5 ± 0.6		Mantovan et al. (2024a)
Planetary Parameters			
Orbital period, P (days)	$10.590547^{+0.000012}_{-0.000011}$	$4.77271^{+0.000016}_{-0.000014}$	Mantovan et al. (2024a)
Transit epoch, T_0 (BJD_{TDB})	$2459616.49232^{+0.00022}_{-0.00021}$		Mantovan et al. (2024a)
Eccentricity, e	≤ 0.13	≤ 0.14	Mantovan et al. (2024a)
Argument of periastron, $\omega_\star$ (deg)	$92.0^{+82.0}_{-45.0}$	172^{+79}_{-107}	Mantovan et al. (2024a)
Stellar reflex velocity, $K_\star$ (m s^{-1})	15.7 ± 1.5	$4.1^{+1.7}_{-1.6}$	Mantovan et al. (2024a)
Orbital semi-major axis, a (au)	0.0980 ± 0.0050	0.057 ± 0.003	Mantovan et al. (2024a)
Orbital inclination, i (deg)	$89.21^{+0.31}_{-0.21}$	≥ 88.4	Mantovan et al. (2024a)
Planetary mass, M_p (M_J)	0.185 ± 0.018	0.0345 ± 0.0125	Mantovan et al. (2024a)
Planetary radius, R_p (R_J)	0.9189 ± 0.0357	0.32 ± 0.02	Mantovan et al. (2024a)
Planetary density, ρ_p (g/cm^3)	0.29 ± 0.05	1.50 ± 0.68	Mantovan et al. (2024a)
Impact parameter, b	$0.272^{+0.069}_{-0.110}$	≤ 0.34	Mantovan et al. (2024a)
Projected obliquity, λ (deg)	$3.0^{+6.8}_{-4.2}$		Mantovan et al. (2024b)
Equilibrium temperature, T_{eq} (K)	947 ± 28	1242 ± 37	Mantovan et al. (2024a)
Planet radial-velocity semi-amplitude, K_p (km s^{-1})	101.58	132.14	This work

Table 4.9: Observations log.

N_{obs} (In/Out of transit)		Exp time [s]		S/N_{avg}	
HARPS-N	GIANO-B	**HARPS-N**	GIANO-B	**HARPS-N**	GIANO-B
47(24/23)	82(46/36)	600	300	43	33

From left to right: the number of observed spectra (N_{obs}), the exposure time, the average S/N (S/N_{avg}), across the selected spectral ranges (548.1-554.2 nm for **HARPS-N**, and 1082.49-1085.5 nm for GIANO-B, respectively).

trograph that covers four spectral bands in the near-infrared (Y, J, H, K) divided into 50 orders. For our analysis, we focused on order #39 in the J-band, where the He I triplet is located. The **HARPS-N** spectrum, on the other hand, is made by 69 orders along its wavelength range. We focused on orders #56 and #64 for the single-line analysis of the Na I doublet and Hα respectively, while we employed the whole spectrum for the cross-correlation with templates analysis. TOI-5398 b was scheduled for observations before, during, and after the planetary transit. Coincidentally, during the selected transit window, TOI-5398 c was also transiting (see Fig. 4.16). The impact of planet c transit on the analysis of planet b is further discussed in the next sections.

We observed the target with an exposure time of 600 s for **HARPS-N**, and 300 s for GIANO-B, collecting 47 and 82 spectra with an average Signal to Noise Ratio (S/N) of 43 and 33 for **HARPS-N** and GIANO-B, respectively. A summary log of the observations is provided in Table 4.9. The same dataset was used in Mantovan et al. (2024b) to analyse the geometry of the system and evaluate the impact of photo-evaporation on the two planets of the system.

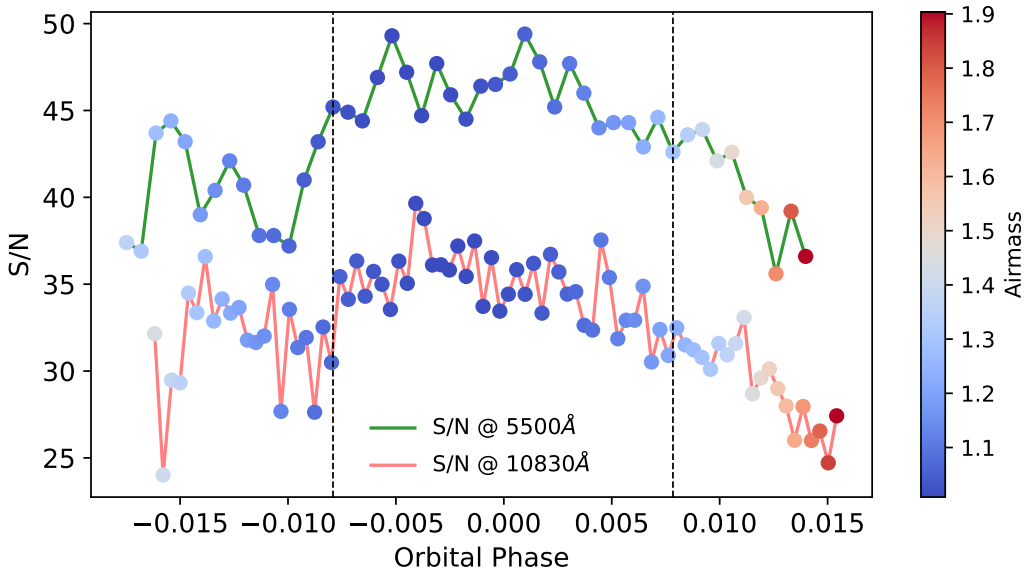

Figure 4.15: S/N as a function of the orbital phase for both the **HARPS-N** and GIANO-B datasets. The airmass is colour-coded. The dashed lines represent the ingress and egress of TOI-5398 b.

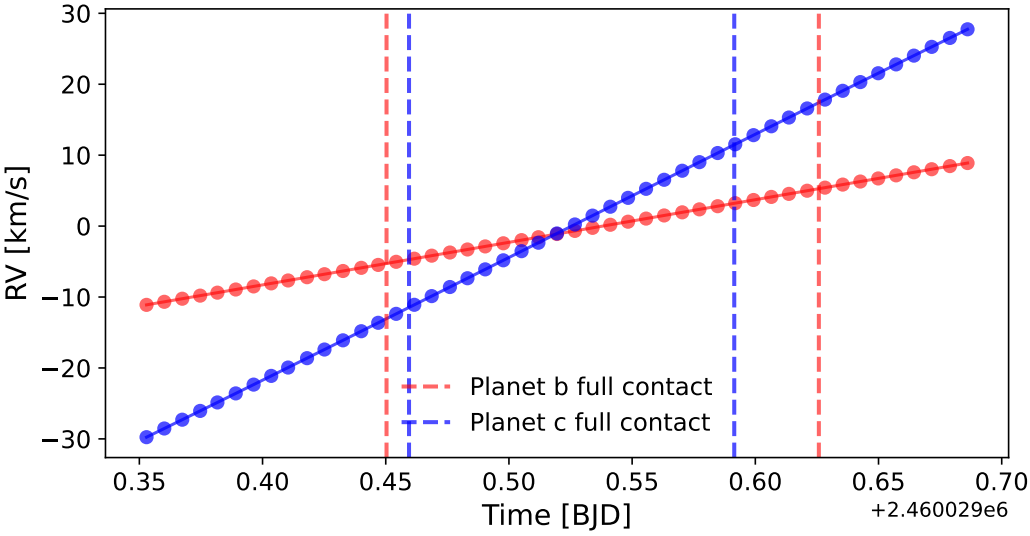

Figure 4.16: Radial velocity profile of the two planets observed as part of the DDT proposal A46DDT4 represented with red and blue dotted lines for planet b and c respectively. The transit of planet c is completely overlapping with planet b one.

4.2.2 Methods

Extraction of single-line transmission spectra

The GIARPS observing mode of the **TNG** is crucial for simultaneously observing both the visible and near-infrared (nIR) parts of the planetary spectrum. Recent studies by Guilluy et al. (2024) have demonstrated that combining data from **HARPS-N** and GIANO-B enables the retrieval of valuable information about the atmospheres of exoplanetary targets. In particular, the joint analysis of the He I triplet and Hα plays an important role in understanding if a detection may be affected by stellar activity (e.g., Guilluy et al. 2020, 2023). The two different datasets require different frameworks to extract the planetary signal around the studied lines. We discuss the different methodologies to extract the transmission spectra in the next subsections. Eventually, we apply an uniform analysis on the extracted spectra.

We do not include in our analyses any correction to take into account the presence of planet c. Despite planet c being closer, and hence hotter than planet b, the inner planet is almost five times denser than its outer companion, resulting in a smaller scale height ($\sim$ 880 km vs $\sim$ 1100 km). This is one of the reasons why we think that planet c do not play a major role in our analysis, as we deeply discuss in Section 4.2.4.

The main difference between the nIR and visible datsets concerns the modelling and removal of the Rossiter-McLaughlin Effect (**Rossiter-McLaughlin Effect (RME)**) and the Center-to-Limb Variation (**CLV**). In fact, we neglect the impact of the **RME** and **CLV** on the Helium triplet, as several studies have shown that these effects have little (or no) impact on the helium lines (e.g., Nortmann et al. 2018; Salz et al. 2018; Allart et al. 2019; Fossati et al. 2022; Allart et al. 2023; Guilluy et al. 2023) As stated before, we do not correct for planet c **RME+CLV** in the visible dataset as the **RME+CLV** impact depends on the size of the stellar disc obscured and planet c has a radius three times smaller than planet b. Therefore, the surface covered by planet c is almost 10 times smaller than the one obscured by planet b. This means that the intensity of **RME** effect should be 10 times smaller than planet b one. Moreover Mantovan et al. (2024b) discussed the same problem regarding their Rossiter analysis to retrieve the orbital obliquity and showed that the radial velocity **RME** of planet c is comparable with the stellar activity.

GIANO-B nIR region We adopted a procedure similar to the one described in Section 4.1.3, employing the `GOFIO` pipeline (Rainer et al. 2018) for extracting spectra from the raw GIANO-B images. This process involved dark subtraction, flat field correction, and removal of bad pixels. Additionally, we performed a preliminary wavelength calibration using a U-Ne lamp spectrum as a template in the vacuum wavelength frame. We focused on the ms1d spectra, with the echelle orders separated. To enhance the initial wavelength solution, we employed the same approach described in our previous sections (e.g., Giacobbe et al. 2021; Guilluy et al. 2022a, 2024, in Section 4.1). We aligned all the spectra to the Earth's atmospheric rest frame, assuming it as the frame of the observer (disregarding any $\sim$10 m s^{-1} differences due to winds), by measuring any shifts relative to an average spectrum taken as a template for the night. Subsequently, we re-

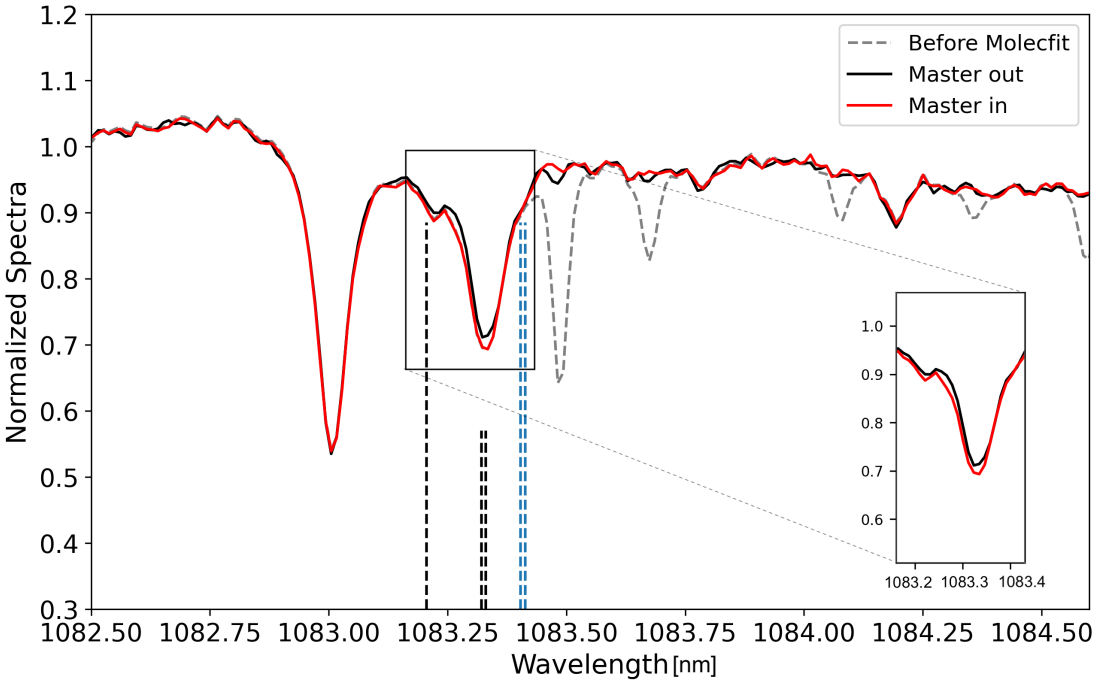

Figure 4.17: Master-out (black) and master-in (red) spectra in the star frame. The dashed grey line indicates the spectrum before the Molecfit correction, while vertical dashed black and blue lines denote the position of the stellar He I triplet and OH emission line, respectively. In-transit absorption is visible by eye, especially in the zoomed in panel.

fined the wavelength solution by utilizing an Earth's atmospheric transmission spectrum generated using the Sky Model Calculator[7]. For the remaining analysis, our focus was solely on order #39, which includes the He I triplet. The magnitude of the wavelength calibration refinements is $\sim$0.56 km s^{-1}, approximately one-fifth of a pixel.
To account for the Earth's atmosphere contamination, we utilised the **ESO** software `Molecfit` [8] (Smette et al. 2015; Kausch et al. 2015) to correct for the transmission telluric lines, with particular focus on the H_2O lines at approximately 1083.51 nm.

The GIANO-B nodding acquisition mode automatically corrects for OH emission lines. However, in our previous works (e.g., Guilluy et al. 2023, 2024), we observed that the A-B subtraction could leave residuals at the position of the deepest OH doublet (around 1083.43 nm) due to variations in atmospheric seeing during observations. To address this, we masked any potential residuals in the final transmission spectra as described in Guilluy et al. (2023).
To separate the stellar contribution from the potential planetary signal, we performed transmission spectroscopy on the GIANO-B spectra according to the following approach. To start, we moved the spectra to the star's rest frame and then we normalised the spectra to unity by median division excluding the spectral region around the He I triplet. Following that, we generated a master stellar spectrum, $S_{\rm out}(\lambda)$, by averaging the out-of-transit spectra (i.e., with an orbital phase smaller than t_1 or greater than t_4, the two ingress/egress contact points). We performed a visual comparison between the $S_{\rm out}(\lambda)$ and a Master-in spectrum, which was derived by averaging the in-transit between t_2 and t_3 (i.e., the full-transit contact points). An absorption feature is readily discernible in the stellar spectrum, precisely coinciding with the position of the He I triplet (Fig. 4.17). To better investigate this feature, we derived individual transmission spectra, $T(\lambda, {\rm i})$, by dividing each spectrum by $S_{\rm out}(\lambda)$. Finally, we linearly interpolated the transmission spectra in the planet's rest frame. The left panel of Fig. 4.18 displays the 2D transmission spectroscopy map, while the right panel shows the He I spectroscopic light curve computed within a passband of 0.075 nm centred at the peak of excess absorption in the planet rest frame (Allart et al. 2019). To quantify the contrast c of the extra absorption observed at the position of the He I triplet, we employed the Differential Evolution (DE) Markov chain Monte Carlo (**MCMC**) method (Ter Braak 2006). This involved fitting a Gaussian profile to the mean in-transit transmission spectrum, computed by averaging the 2D maps between the transit contact points t_2 and t_3. We fitted the peak position, the full-width at half maximum (**FWHM**), the contrast value (c), and an offset for the continuum. Correlated noise in the transmission spectrum was accounted for using Gaussian process (**GP**) regression within the same **DE-MCMC** framework, employing a covariance matrix described by a squared exponential kernel (Guilluy et al. 2024; Sicilia et al. 2024). Additionally, uncorrelated noise was taken into account through a jitter term $\sigma_{\rm j}$. The correction with the **GP** regression model is illustrated in Fig. 4.20, with detailed posterior distributions provided in Fig. 4.25. The best-fit parameters obtained from the **DE-MCMC** Gaussian analysis are summarised in Table 4.10. Parameter val-

[7] `https://www.eso.org/observing/etc/bin/gen/form?INS.MODE=swspectr+INS.NAME=SKYCALC`
[8] `http://www.eso.org/sci/software/pipelines/skytools/molecfit`

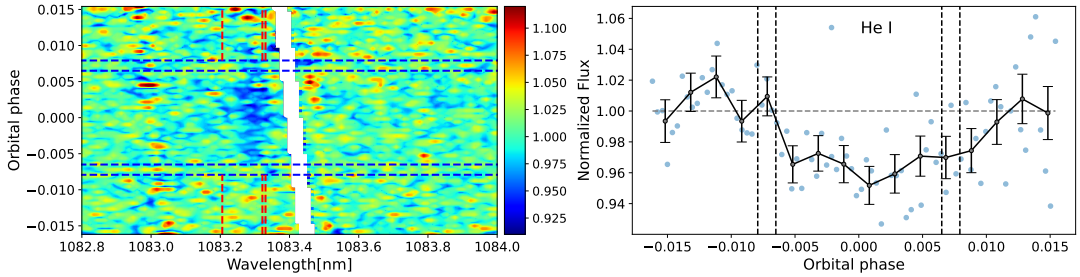

Figure 4.18: Left panel: 2D maps of transmission spectra in the planet rest frame in the region of the He I triplet, as a function of wavelength and planetary orbital phase for TOI-5398 b. The contact points t_1, t_2, t_3 and t_4 are marked with horizontal blue lines. The regions affected by OH contamination are masked. Some residuals are left at the position of the Si line ($\sim$1083 nm). This is due to the depth of the line, which can cause difficulties in spectral extraction (see, e.g., Krishnamurthy et al. 2023). Red dashed lines mark the position of the He I lines. Right panel: The light curve in the planet rest frame computed in a bandpass of 0.075 nm (equivalent to $\sim$ 20 km s^{-1}). Black points are computed with a phase bin of 0.002. Vertical black dashed lines indicate the position of the transit contact points t_1, t_2, t_3, t_4.

Table 4.10: Best-fit parameters for the single lines analysed.

Line	Peak position		Contrast c	R_{eff}	**FWHM**	Significance	δ_{R_P}/H_{eq}
	[nm]	[km s^{-1}]	[%]	[R_p]	[nm]	[σ]	
He I	$1083.2969^{+0.0052}_{-0.0042}$	$-8.09^{+1.44}_{-1.17}$	$3.57^{+0.51}_{-0.50}$	2.33 ± 0.02	$0.084^{+0.016}_{-0.012}$	6.9	79±9
Hα	$656.2834^{+0.0094}_{-0.0088}$	$1.94^{+4.42}_{-4.18}$	$1.39^{+0.28}_{-0.28}$	1.65 ± 0.11	$0.104^{+0.028}_{-0.022}$	5.0	39±7
Na D1	$589.5900^{+0.0011}_{-0.0011}$	$-0.98^{+0.54}_{-0.55}$	$3.79^{+0.50}_{-0.47}$	2.38 ± 0.13	$0.021^{+0.004}_{-0.003}$	7.9	82±12
Na D2	$588.9952^{+0.0017}_{-0.0017}$	$0.14^{+0.85}_{-0.82}$	$3.36^{+0.46}_{-0.44}$	2.28 ± 0.12	$0.028^{+0.004}_{-0.004}$	7.4	75±11

From left to right: the investigated spectral line, the peak position (both in air wavelength and velocity respect to the planetary reference frame), the excess of absorption c, the corresponding effective radius, the **FWHM**, the significance of the detection, and the ratio between the equivalent height of the atmosphere and the atmospheric scale height.

ues and their 1σ uncertainties were determined from the medians and the 16%-84% quantiles of their posterior distributions.
Table 4.10 reports also the effective He I radius (e.g., Chen et al. 2018) that would produce the observed absorption contrast c. We then normalised it to the atmospheric H_{eq} to compute the quantity δ_{R_P}/H_{eq} (Nortmann et al. 2018), which represents the number of scale heights probed by the atmosphere in the spectral range under consideration. Here, H_{eq} is computed by assuming a mean molecular weight of 1.3. (Fossati et al. 2022).

HARPS-N visible region We obtained the transmission spectra of the individual lines using a method similar to that outlined in Wyttenbach et al. (2015), thus comparing spectra during and outside of transit. The raw data have already been processed using version 3.7 of the **HARPS-N DRS**(Pepe et al. 2002). At this point, the 1D spectra we

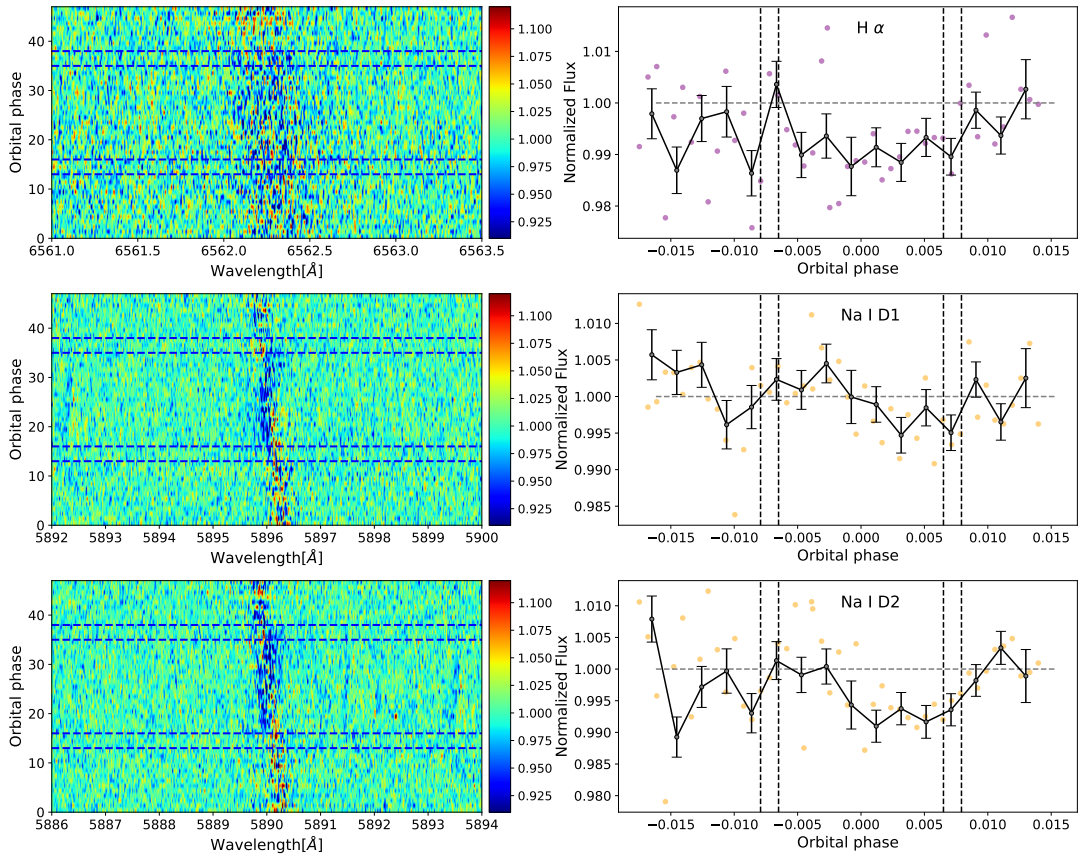

Figure 4.19: Same as Fig. 4.18 for the lines detected in the visible range.

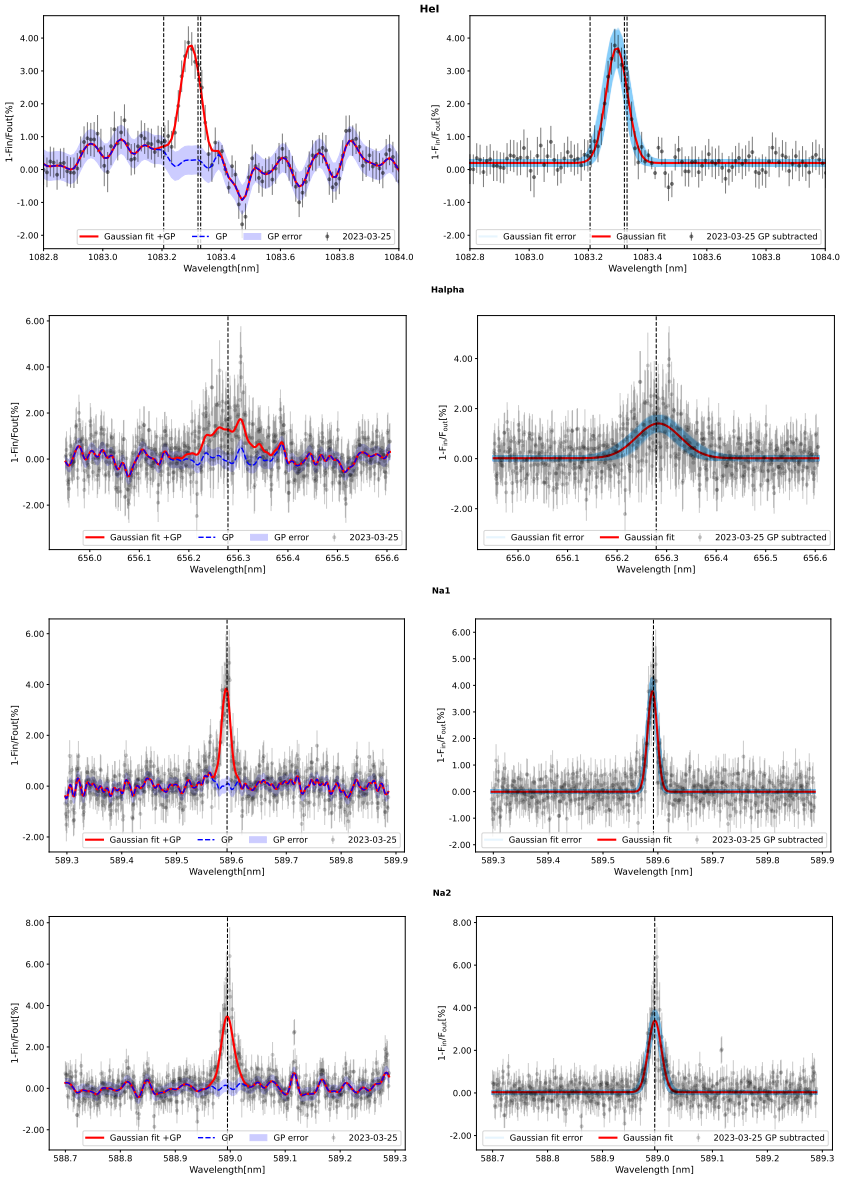

Figure 4.20: Transmission spectra of He I triplet, Hα and Na I doublet after the **GP** correction. For each investigated line, the **GP** correction is shown. Left panel: transmission spectrum centred on the line (in the planet rest frame) with overplotted the **GP** regression model, along with the 1σ uncertainty intervals (in blue), and the Gaussian+**GP** model (in red). Right Panel: Final transmission spectrum after removing the **GP** model. Vertical black dotted lines indicate the position of the investigated line. The error intervals for the Gaussian fit were computed by displaying 1000 Gaussian fits within the 1σ uncertainties of the derived parameters, spanning the 16%-84% quantiles.

employed include the stellar signal, the planetary signal, and telluric contamination, all presented in the solar system barycentric reference frame with the wavelength information provided in the air reference frame.
Correcting for telluric absorption is crucial, especially in the red region of the **HARPS-N** spectra, where the Earth's atmosphere shows significant H_2O and O_2 absorption features. Figure 4.24 illustrates an example of removing telluric lines near the Hα and Na I doublet regions. The software `Molecfit` provides telluric-corrected spectra in the solar barycentric reference frame. Consequently, we adjusted the spectra to the stellar reference frame by accounting for the star's systemic radial velocity, v_{sys}. The telluric-corrected spectra are then normalised to a common continuum level within a narrow wavelength range around each absorption line of interest. Before transitioning to the planetary reference frame, we must consider the combined effects of the Rossiter-McLaughlin Effect (**RME**) (Rossiter 1924; McLaughlin 1924) and Center-to-Limb Variations (**CLV**), which result from stellar rotation and limb darkening, respectively. We addressed the **RME+CLV** effects by employing a similar approach to that outlined by Yan et al. (2017), utilizing stellar models. Specifically, we used ATLAS9 stellar models (Kurucz 1992, 2005, 2014, 2017) to generate the disk-integrated stellar model based on the system parameters listed in Table 4.8. We computed spectra for both a non-rotating star and a rotating star. To determine the portion of the stellar disc obscured by the planet at each phase (referred to as the obscured region), we used `PyLightCurve` (Tsiaras et al. 2016) to calculate the planet's transit path. We then created a grid with a pixel size of 0.01 R_* $\times$ 0.01 R_* to approximate the stellar disc and calculated the stellar flux for the obscured region at each phase as already done in D'Arpa et al. (2024b) and described in Section 2.1.2. The intensity of each pixel was determined based on the limb darkening angle and the radial velocity shift relative to the stellar rotation axis. Using the ATLAS9 models, we computed the spectrum of the obscured region by summing the spectra of each pixel, each appropriately shifted by its own radial velocity. We derived the limb darkening coefficients for our stellar model using the `ExoTethys` (Morello et al. 2020) function `Sail` with a quadratic limb darkening law, consistent with ATLAS9. The integrated flux F_λ corresponds to the spectrum of the non-rotating model. Rotational broadening was obtained by summing the contributions of each pixel, each shifted by its own radial velocity. The observed master-out spectrum is broadened by stellar rotation, so we used the rotationally broadened model to normalize the continuum of the non-rotating model. Finally, we subtracted the modeled obscured region from the master-out spectra and divided all spectra by this result. Once the spectra in the stellar reference frame had been corrected, we shifted all the in-transit spectra to the planet reference frame by correcting for its radial velocity profile in a circular orbit scenario using the parameters listed in Table 4.8. The final transmission spectrum of each line is calculated as the error-weighted average of all the full in-transit spectra (t_2 - t_3) in the planet reference frame. We then performed a Gaussian fit returning the absorption depth, the **FWHM**, and the velocity shift with respect to the line wavelength corresponding to a zero radial velocity. At the beginning, we used the planetary radius to represent the size of the obscured region of the stellar disk. We then translated the line absorption depths, returned by the Gaussian fit, into planetary radii and we used

these values to repeat the **RME + CLV** removal with an increased size that accounts for both the planetary radius and the atmospheric extension. We repeat the loop, retrieving a new depth expressed in planetary radii, until the threshold convergence (0.001 R_p) is reached. Once we found the optimal value for the planet+atmosphere region of the stellar disk obscured, we used the same **DE-MCMC+GP** tool employed in the GIANO-B analysis to fit our final corrected transmission spectra. Fig. 4.20 shows the correction with the **GP** regression model, while the posterior distributions are provided in the Appendix in Fig. 4.25. The best-fit parameters obtained from the **DE-MCMC** Gaussian analysis are reported in Table 4.10. As for the He I contrast, we derived the corresponding effective radius for both Hα , and the Na I doublet. As noted in the previous work described in Section 4.1, the correlated noise is weaker in **HARPS-N** spectra compared to the GIANO-B ones. In this work we investigated and assessed the necessity of the **GP** regression model correction using the Bayesian information criterion (**BIC**, Kass & Raftery 1995). We considered the Gaussian+**GP** model as favourite compared to the simple Gaussian model (which also considered uncorrelated jitter) only if accompanied by a lower **BIC** and a difference in **BIC** (ΔBIC) > 10, along with a Bayesian Evidence $>$150. For all the three investigated lines (i.e., Hα , Na D1, and Na D2), the Gaussian+**GP** model emerged as the preferred choice. We provided the ΔBIC and the corresponding Bayesian evidence in Table 4.12. We computed the spectroscopic light curves similarly to the He I ones, considering a width of 20 km s^{-1}.

Cross correlation with templates

As introduced in Section 3.2, to optimize the detection of certain elements with hundreds of weak lines, the cross-correlation function (**Cross Correlation Function (CCF)**) is more suitable than transmission spectroscopy analysis (Brogi et al. 2012; Hoeijmakers et al. 2019; Borsa et al. 2021a), especially in the case of individual nights, since it allows to boost the S/N. We used the **CCF** method in the visible band searching for any exoplanetary signal. Before applying the **CCF** technique to our **HARPS-N** data, we employed the same telluric profile retrieved from the **HARPS-N** s1d spectra using `Molecfit`, and we used it to correct the **HARPS-N** e2ds orders from telluric lines for each exposure (Hoeijmakers et al. 2020). To improve the accuracy of the **CCF** analysis, we chose to omit the initial five orders and the last one from all exposures due to their low S/N. We constructed the mono-dimensional spectra from normalised telluric corrected e2ds orders. These 1D spectra were then cross-correlated with the templates at 2000K, 2500K and 3000K provided by Kitzmann et al. (2023) for each element, after convolving them with the **HARPS-N** resolution (R $\sim$ 115,000). Since these templates are derived using the Sun's radius as reference, before any **CCF** computation, we multiplied them by the ratio $(R_\odot/R_*)^2$ as stated in Kitzmann et al. (2023), using R_* from Table 4.8. The templates were shifted in radial velocities between [-200 $km\,s^{-1}$, +200 $km\,s^{-1}$] with a step of 1 $km\,s^{-1}$. The resulting **CCF** was then shifted in the stellar reference frame, interpolated in radial velocity between [-150 $km\,s^{-1}$, +150 $km\,s^{-1}$] maintaining the 1 $km\,s^{-1}$ step and divided by the mean of out-of-transit (master-out). To achieve a more precise normalisation and address any imperfections, we divided the **CCF** by the median values across the exposures. To remove any residual fluctuations we

performed a Fourier Transform discarding all the frequencies beyond the 100 $km\,s^{-1}$.

In this way, we investigated the presence of all the species given by Kitzmann et al. (2023) including both neutral and ionised elements, having at least one absorption line in the visible band covered by our order selection. The resulting CCFs for some elements exhibit the characteristic Doppler shadow. We removed it following the Rainer et al. (2021) approach: we shifted the data in the Doppler shadow reference frame and fitted each columns in a region where the Doppler shadow fell with a fifth-degree polynomial. However, the specific geometry of the TOI-5398 system is such that the Doppler shadow and the planetary trace overlap (see Casasayas-Barris et al. 2022; Sicilia et al. 2024, for a similar scenario). Therefore, in this scenario, the Doppler shadow signal may completely mask the potential planetary signal, and even if the Doppler shadow is modeled and removed, the potential planetary signal may also be eliminated. Figure 4.21 shows the **CCF** obtained with the Na I, Ca I, and Fe I templates at 2000K. The Doppler shadow for these elements was modeled out for Ca II and Fe I.

4.2.3 Results

Single Line and Cross correlation analyses

By the comparison of the out-of-transit spectra with the in-transit ones, we were able to discern clear He I, Hα , Na D1, and Na D2 absorption signals. Applying the framework described in Section 4.2.2, we estimated contrasts of the excess absorption of $3.57^{+0.51}_{-0.50}\%$ (6.9σ), $1.39^{+0.28}_{-0.28}\%$ (5.0σ), $3.79^{+0.50}_{-0.47}\%$ (7.9σ), and $3.36^{+0.46}_{-0.44}\%$ (7.4σ) for He I , Hα , Na D1, and Na D2, respectively. These values correspond to effective planetary radii of $\sim$2.33 $R_{\rm p}$, $\sim$1.65 $R_{\rm p}$, $\sim$3.81 $R_{\rm p}$, and $\sim$2.28 $R_{\rm p}$, the extensions of which are well below the planet's Roche Lobe radius ($\sim$5.8Rp), computed using Equation 2 from Eggleton 1983. This indicates that the planetary atmosphere is not escaping due to the gravitational pull of the star as discussed in the next Section. Assuming a scale height (H) of $\sim$ 1106 km, and considering 1σ uncertainties, we found that the He I atmosphere probes a number of scale heights varying between $\sim$ 70 and $\sim$ 88 H, while the Hα atmosphere varies between 32 and 46 H, Na D1 between 70 and 96 H and Na D2 between 64 and 86 H. We found the He I absorption signal to show a clear blueshift, $\sim$ 8km s^{-1}while the Optical species do not display either a significant blueshift or a redshift. He I and Hα have similar **FWHM**, larger than the Na I doublet ones. For the He I and Hα lines, our detections seem to be supported by the spectroscopic light-curves, which hint at the presence of an He I tail that we discuss later. The Na doublet light-curves do not show a clear transit signal, despite showing a decrease in flux on the second half of the transit. This is possibly related with the overlapping **RME** as discussed later. We also investigated the presence of other metal species in the atmosphere, analysing a wide forest of lines belonging to Mg I, Ca II, Fe I and Fe II, but unfortunately, we did not detect any significant line. The cross-correlation of the extracted spectrum with Kitzmann et al. (2023) templates did not return any detection of the investigated species. As already stated, this framework is particularly challenging in our case due to the overlap of the possible signals with the Doppler shadow. This affected also the extraction of single

lines in the visible spectrum of TOI-5398 b. An under-correction of **RME** may cause to miss the signal while an over-correction may lead to a false detection. We compared the results obtained applying the method described in Section 4.2.2 (already employed in Guilluy et al. 2024 and D'Arpa et al. 2024b) with the results obtained using SLOPpy (Sicilia et al. 2022) which employs a different method to model the **RME+CLV**, as described in 4.2.5.

Comparison with ATES predicted spectra

To support the interpretation of our He I observations, we conducted simulations of the atmospheres of the two planets and their respective He I absorptions using the 1D hydro-photoionisation self-consistent code ATES (Caldiroli et al. 2021) and the new transmission probability module (TPM, Biassoni et al. 2024b). The ATES code derives the 1D atmospheric radial profile such as temperature, pressure, density and velocity along with the mass loss rate $\dot{M}$.

For these simulations, we used the planetary parameters listed in Table 4.8 for planets b and c, while the stellar spectrum was calculated as follows. For the UV component, we adopted a stellar spectrum from the Phoenix library (Husser et al. 2013) to which we added the Lyman alpha emission following the prescriptions of Linsky et al. (2020) and as described in Locci et al. (2022). For the EUV and X-ray components, we produced a synthetic spectrum from a composite chromosphere-corona plasma emission measure distribution vs. temperature, EMD(T), constructed as follows: the coronal part (log T $>$ 5.5 K) was interpolated from the grid of EMDs provided by Wood et al. (2018) for a star with a surface X-ray flux Fx = 1.5×10^6 erg s^{-1} cm^{-2}(corresponding to Lx = 1×10^{29} erg s^{-1}), while the chromospheric section (log T from 4.0 to 5.5 K) was approximated as a power law following Sanz-Forcada et al. (2011), with the constraint that the F_{euv}/F_xratio follows the scaling law indicated by Johnstone et al. (2021). Then, the optically-thin XUV spectrum (1.24 - 1700 A) was computed adopting the plasma emissivities from the CHIANTI v7.13 atomic database as in Maggio et al. (2023).

We started our simulations for both planets assuming a constant He/H number abundance of $1/12$ alongside the overall atmosphere. This provided us a $\dot{M}$ of $10^{11.70}$ g s^{-1}and $10^{11.44}$ g s^{-1}for the planet b and c respectively, indicating that nowadays the innermost planet c is affected less than the planet b by the atmospheric escape effect. However, this doesn't exclude the possibility that in the past planet c may have experienced significantly greater atmospheric loss. We investigated the He I absorption profiles for both planets using the TPM module. For this analysis, we firstly simulated the atmospheric profiles changing the He/H number abundance, using the values of 0.01, 0.02, 0.04 and $1/12$. We then repeated the simulations varying the XUV flux to include the enhanced stellar activity of a young star. TOI-5398 is a G type star with an age comparable to the one of the Hyades cluster stars. According to Fig. 4 of Preibisch & Feigelson (2005), in such stars, the typical X ray luminosity is centred at Lx = 1×10^{29} erg s^{-1}, which is the value we adopted, with a variation from the pre–main sequence through the main sequence being almost a factor two. Therefore, we repeated the same simulations described above with varying the XUV luminosity of a factor two. We used

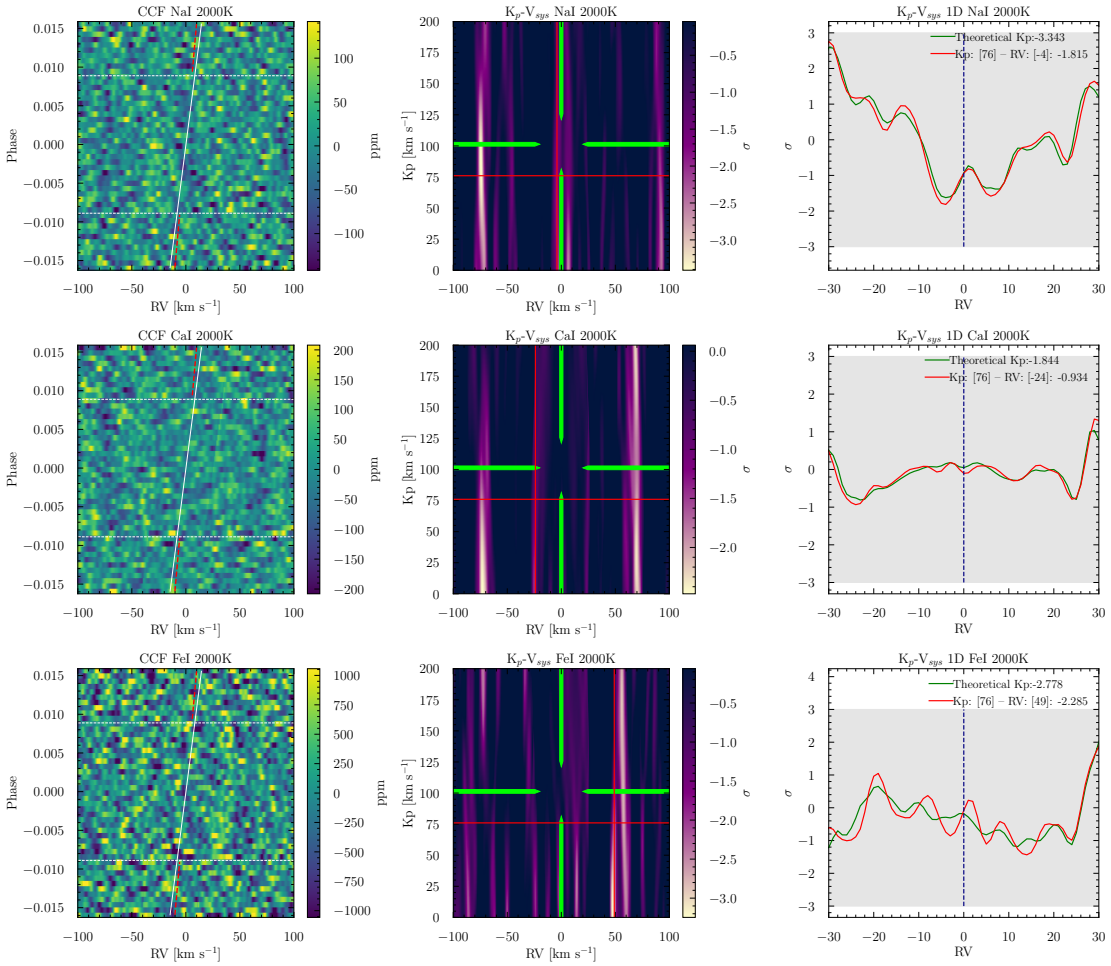

Figure 4.21: Cross correlation and K_p-V_{sys} maps of Na I, Ca I and Fe I obtained with the Kitzmann et al. (2023) templates at 2000K for TOI-5398 b. In the first column the **CCF** are depicted in terms of ppm. The dotted horizontal lines indicate the T1 and T4 contact points, while the red dashed line is the planetary trace. The Doppler shadow follows the white slanted line. Second columns are the K_p-V_{sys} maps. The planetary signal is expected to be limited between the green pointer in the middle of the figures, while the red lines point at the minimum value of the K_p-V_{sys} between K_p 75 km s^{-1}, 125 km s^{-1}and **RV** -50 km s^{-1}, +50 km s^{-1}. The last column is the K_p-V_{sys} 1D map evaluated at the K_p minimum value. The grey region is the 3σ edge, while the vertical navy dashed line refers to the **RV** 0 km s^{-1}.

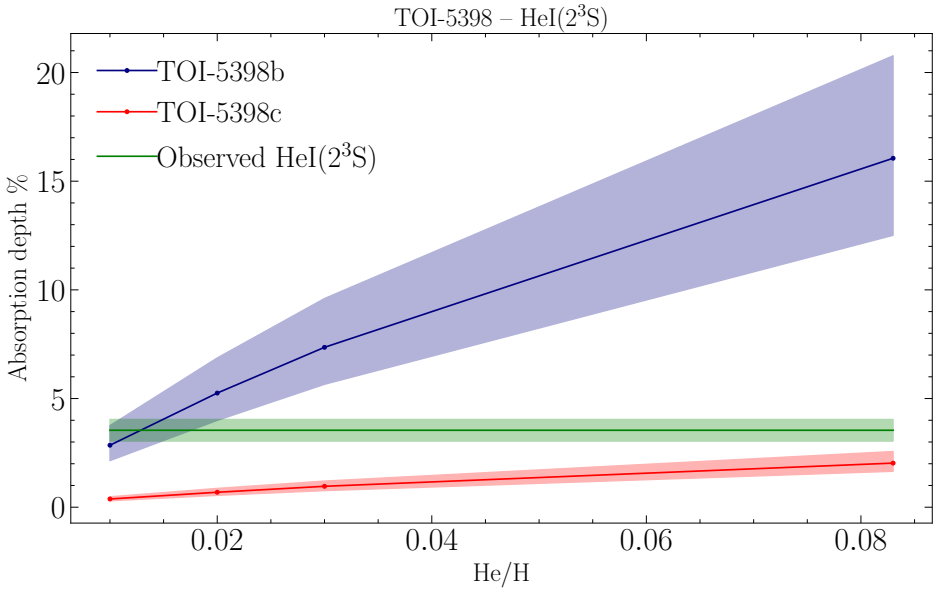

Figure 4.22: He I simulated absorption profiles for both planets changing the He/H number abundance. The green line corresponds to the He I observed signal with 1σ errorbars given in Table 4.10. The blue and red bands correspond to the simulations obtained for the two planets varying the X-ray luminosity of a factor 2.

the results as a function of the He/H number abundance to estimate the uncertainties of the values retrieved with the nominal luminosity. The resulting He I absorption profiles obtained with these different He/H number abundances for planet c are always below the observed signal, while for planet b, the simulations are consistent with the observed signal only with a He/H number abundance between 0.01 and 0.02 (see Fig. 4.22).

4.2.4 Discussion

Within the single-line analysis context, He I triplet in the nIR, and Hα and Na I doublet in the visible are among the pivotal lines studied in exoplanetary atmospheres, thanks to their strength and to their role as marker for features such as photo-evaporation and stellar activity. The Na I doublet has been detected in several hot exoplanets with temperatures ranging from WASP-69 b 963 K (e.g., Casasayas-Barris et al. 2017; Khalafinejad et al. 2021) until KELT-9 b 3921 K (e.g., Langeveld et al. 2022; D'Arpa et al. 2024b). Therefore, according to our detection, TOI-5398 b will be among the coldest (947 K) planets showing the Na I doublet to our knowledge. The He I and Hα distribution has recently been discussed by Orell-Miquel et al. (2024) who explored the high-resolution spectroscopy observations from **CARMENES** and GIARPS checking for He I and Hα signals in 20 exoplanetary atmospheres. From their work we can see that the joint detection of He I and Hα has been observed only in 2 targets: WASP-52 b (Chen et al. 2020; Kirk et al. 2022; Vissapragada et al. 2020) and HAT-P-32 b

(Czesla et al. 2022; Zhang et al. 2023b), with WASP-52 b being the only one with a detection of all the three species detected in this study.

The height distribution of the species in our atmosphere suggests that He I and Na I lay in an external atmospheric layer with respect to Hα . Hα forms through absorption from the n=2 level of neutral hydrogen, which is likely excited by the strong stellar Lyα line and/or by the photoionizing radiation of our young star followed by subsequent recombination and population of the n = 2 level as in solar-like stellar atmospheres (Cram & Mullan 1985). To justify the observed Hα absorption, it is necessary that hydrogen has a sufficient number of atoms in the excited level n=2. If we go too high in the planetary atmosphere, hydrogen finds itself in a less dense medium and has enough time to decay to the fundamental level n=1 before being able to absorb a photon in the Hα line. In the case of He I triplet, the situation is different because the lines form through absorption from a metastable level. Even if we are high in the atmosphere, the level decays over much longer timescales than those required for photon absorption in the lines. Moreover, in a less dense medium, the probability that the atom decays to the fundamental level due to collision is low, facilitating the process that produces the He I triplet.

Indeed, absorption of He I at 1083 nm is seen in certain cases even at a great distance from the planet along almost its entire orbit (see Zhang et al. 2023b, for example). The sodium retrieved height is more challenging to explain since the sodium atom has a low ionisation potential and therefore, far from the planet, it risks being ionised. However, the absorption of the two doublet lines starts from the fundamental level, so the atom does not need a dense surrounding medium to bring it to an excited level through thermal collisions to produce the line. Therefore, if it does not ionize too much, some absorption in the Na I doublet at a certain distance from the planet might be observable. In this case, we stress the mismatch between the results obtained with SLOPpy where the Na I doublet is found at 1.12 $R_{\rm p}$, much lower than our extension. Since the species is not detected via cross correlation with templates, the signal we detect may be due to a partially spurious signal arising from a residual of the **RME+CLV** contamination which overlaps with the planetary signal. This hypothesis could explain the fact that the Na doublet lines do not show a clear transit signal in the light-curve despite showing a flux decrease in the second half of the transit. Future observations and improvements in the **RME+CLV** modelling will be necessary to clarify this point.

The distribution of Hα and Na I resemble the same behaviour observed in WASP-52 b where Chen et al. (2020) find both sodium lines lying at an effective radius larger than Hα one. The extended atmosphere observed for our target may be explained taking into account the photo-evaporation induced by the host star. In fact, planets close to their host star experience a strong irradiation which causes the exoplanetary atmosphere to heat up and hence to expand. The larger thermal energy induces an increase in velocity making the particles belonging to the atmospheric species reach the Roche Lobe and escape from the planetary gravitational well. This is particularly relevant for younger stars which generally have a larger XUV flux such as TOI-5398. Mantovan et al. (2024b) evaluated photo-evaporation on the system during a period spanning from

3 Myr to 650 Myr. The two planets experienced a different evolutionary path, with planet b being less influenced by atmospheric escape, while, on the other hand, planet c experienced the loss of almost 60% of its mass, resulting in a less extended atmosphere nowadays. At this point of their evolutionary path, planet c should show a less extended atmosphere, while planet b remains dominated by an extended envelope despite experiencing a current larger mass loss. The simulations we performed with ATES retrieve a $\dot{M}$ of $10^{11.70}$ g s^{-1}and $10^{11.44}$ g s^{-1}for the planet b and c respectively, confirming that part of the outer layers of the atmosphere are currently undergoing atmospheric escape. This scenario is ideal for transmission spectroscopy due to the larger extension of the scattering annulus surrounding the planet.

From our results, we observe that TOI-5398 b shows an extended atmosphere which reaches $\sim 2.4\ R_{\rm p}$, still well under the Roche Lobe at $\sim 5.8\ R_{\rm p}$, computed using Equation 2 from Eggleton (1983). This does not question the photo-evaporation ongoing for the target, since we obtain the height from a geometrical point of view from the absorption depth of the lines detected. Since the latter is related to the point where the optical depth is one, the height does not represent an individual layer where the species lay, since it is distributed according to the density profile. Therefore, we are able to find particles overcoming the Roche Lobe despite observing an absorption that peaks well below.

The past and current status of the two planets along with the ATES models should help us addressing the possible contamination of planet c during the transit we observed. In Fig. 4.16 we showed that the two transits almost completely overlap and only three points of planet b are not affected by the planet c. While it is impossible to completely exclude the uncertain contribute of planet c, its role in the observed signal seems to be secondary as jointly supported by the two diagnostics: the planet c has a less extended atmosphere due to its past evaporation and the spectra retrieved by ATES (Fig. 4.22) confirm our suggestions since the He I arising from the planet c is not able to justify the absorption we observe even considering two times the nominal XUV flux. Particularly, in order to match the He I triplet retrieved absorption we should increase the XUV flux more than 10 times its value. On the other hand, planet b is expected to show hints of photo-evaporation and the ATES spectra manage to mimic the 3.57% absorption with a He/H number fraction ranging between 0.01 and 0.02 . While retrieving the He/H number fraction is not the main aim of our comparison with the **TSM** module, we are able not only to evaluate the contribution of the two planets but also to discern a range of He/H number fraction as a function of the XUV flux adopted, which, in a young star may vary. The use of models including the Hα line may be able to brake this degeneracy.

Observing the spectroscopic He I light-curve in Fig. 4.18, we note that the signal seems to continue beyond T_4. This may be an indication of the presence of an extended atmosphere or some sort of cometary tail trailing the planet. The tail may be a further proof of the planet b being photo-evaporating. As a further evidence, we have absorption of He I at -8 km s^{-1}, which could originate from the cometary tail driven by stellar winds. However, the tail does not seem to be present in the other species light-curve as in the He I one. This may arise from the lower amount of points in the visible band due to a larger exposure time.

Table 4.11: Best fit parameters with SLOPpy

Line	Peak position		Contrast c	R_{eff} [a]	**FWHM**	Significance
	[nm]	[km s^{-1}]	[%]	[R_p]	[nm]	[σ]
Hα	$656.2837^{+0.0055}_{-0.0053}$	$0.52^{+4.84}_{-4.21}$	$1.63^{+0.35}_{-0.36}$	0.92 ± 0.29	$0.042^{+0.014}_{-0.010}$	4.5
Na D1	$589.5901^{+0.0011}_{-0.0011}$	$-1.41^{+0.70}_{-0.72}$	$2.64^{+0.53}_{-0.51}$	1.12 ± 0.11	$0.007^{+0.002}_{-0.001}$	5.0
Na D2	$588.9953^{+0.0017}_{-0.0016}$	$0.47^{+1.47}_{-1.41}$	$2.21^{+0.48}_{-0.47}$	1.12 ± 0.11	$0.013^{+0.003}_{-0.002}$	4.6

[a] The R_{eff} is fitted in the analysis by SLOPpy and it is not retrieved from the contrast. Therefore we did not include the δ_{R_P}/H_{eq} as in Table 4.10.

4.2.5 Comparison with SLOPpy

We compared the results obtained in the visible range with the method described in this work with SLOPpy to evaluate the impact of different correction of the **RME+CLV**. The two methods differ by many factors but rely on the same idea of correcting for the part of the stellar disk obscured by the planet. Our method sets the extension of the atmosphere increasing iteratively the radius retrieved from the Gaussian fit until we reach the convergence of 0.001 R_p, as described in Section 4.2.2 and hence we retrieve the R_{eff} from the absorption depth. On the other hand, SLOPpy fits the size of the atmosphere by comparing the 2D map containing the modelled **RME+CLV** and the planetary signal employing an **MCMC** approach. We stress that the extension retrieved by SLOPpy is not the physical extension of the atmosphere but a corrective factor. Therefore, the major difference in the two frameworks is the extension adopted to perform the **RME + CLV** correction. We performed the comparison in the following way: we employed SLOPpy which returns the extracted transmission spectrum and fit it using an **MCMC** method to find the best Gaussian fit values and the best corrective radius factor to employ in the **RME+CLV** correction. Then, we applied the same **GP**+DEMCMC analysis described in Section 4.2.2 on the spectrum extracted with SLOPpy. The results are shown in Figure 4.23 and in Table 4.11. The **FWHM** and the velocity shift are within 1σ for both the Hα and Na I doublet, while, for the latter, the contrasts we retrieve are larger than SLOPpy's ones. A deep comparison between the two frameworks and their sensibilities is out of the scope of this work and hence we limit to say that, despite the difference in depth, in both cases we detect the presence of the two Na lines and the Hα in the atmosphere of planet b.

4.2.6 Conclusions

In this work we performed a nIR+optical High resolution transmission spectroscopy study of the Saturn-like planet TOI-5398 b, analysing one transit collected during the 25th of March 2023 with GIARPS observing mode at the **TNG**. The same dataset has been used before by Mantovan et al. (2024b) constraining the orbital parameters and evaluating the evolutionary path of the system.

We detected the presence of metastable He I with GIANO-B spectrograph and of Hα and Na I doublet with **HARPS-N** employing single-line analysis. According to the ExoAt-

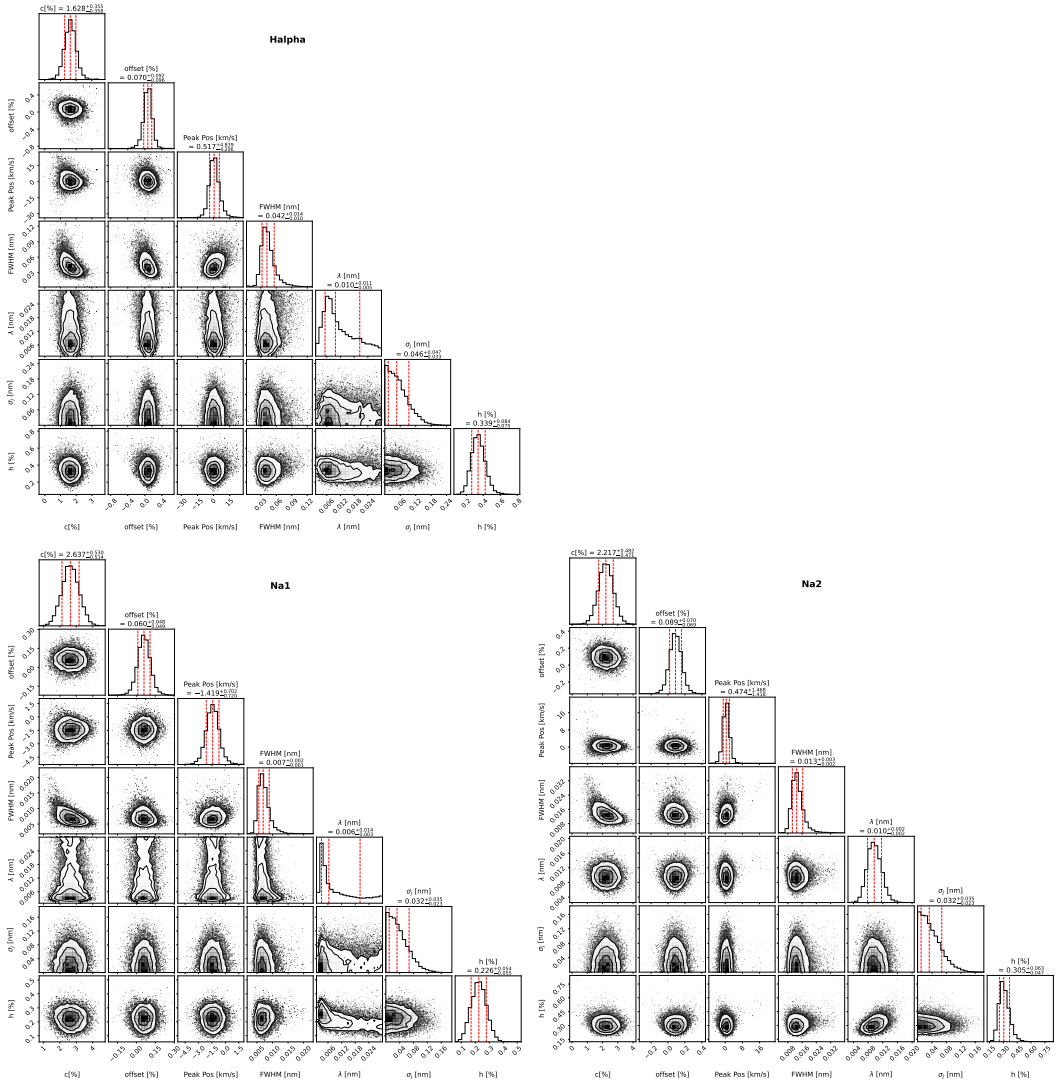

Figure 4.23: Same as Fig. 4.25 for SLOPpy.

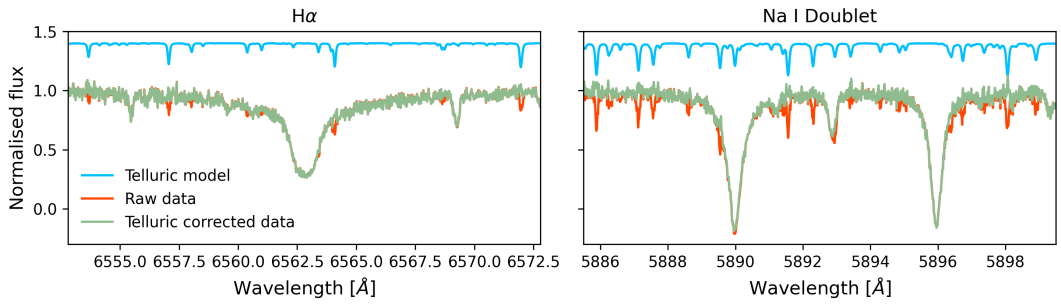

Figure 4.24: Example of telluric correction for the Hα and Na I doublet regions. After normalisation, the DRS processed data (in orange) was telluric corrected with `Molecfit` using the telluric model in blue, here shifted upwards for clarity.

mospheres database [9], this represents only one of the fewest simultaneous detection of He I, Hα and Na I doublet in the atmosphere of an exoplanet.

The cross-correlation with templates did not return any detection, probably due to the overlapping **RME**, the low temperature of the planet and the exiguous dataset. In fact, the difficulty of extracting the planetary signal in the atmosphere of smaller planets is enhanced by the fact that we observed only one transit. As discussed in Guilluy et al. (2024) the study of individual lines across different nights is crucial to identify possible contamination due to stellar activity and hence more transits will be necessary to further corroborate our detections.

Despite we attribute the signal detected to the planet b according to the evolutionary history of the system and to the ATES simulations, future individual observations of both planets will also be needed to definitely clarify the origin of the signals detected. Future observations with longer baselines would also help investigating the possible presence of a cometary tail along with 3D hydrodinamical simulations such as the ones performed in Matsakos et al. (2015) and Colombo et al. (2024).

4.2.7 Additional Figures and Tables

[9] https://research.iac.es/proyecto/exoatmospheres/index.php

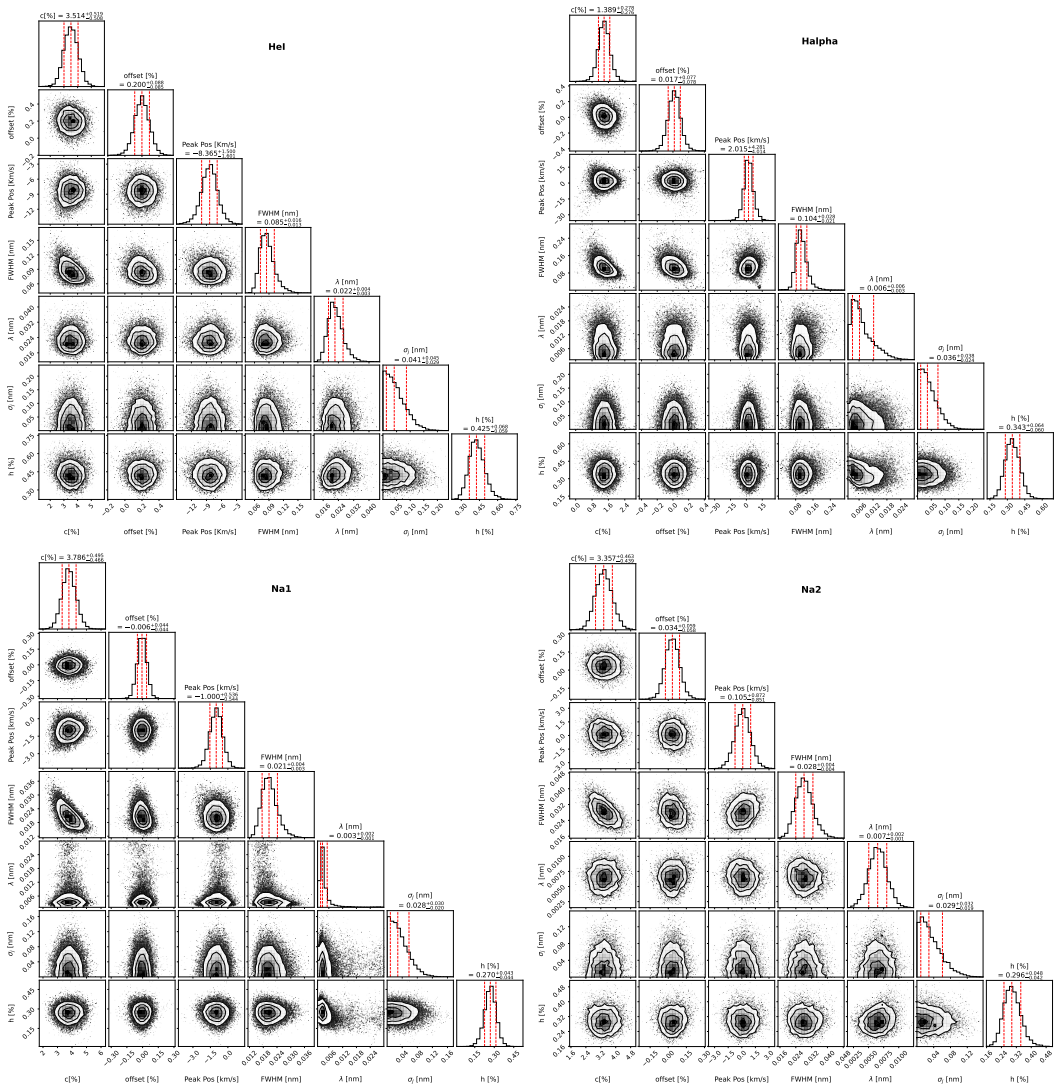

Figure 4.25: Posterior distribution of the investigated parameters in the **DE-MCMC** analysis for the four investigated lines. The excess of absorption c [%], offset [%], peak position, and **FWHM** correspond to the parameters we used in the Gaussian fit, while the jitter term σ_j, the semi-amplitude of the correlated noise h, the correlation length λ were used to parametrise the SE kernel within the **GP**.

Table 4.12: Gaussian+**GP** and Gaussian model comparison via **BIC** in **HARPS-N** spectra.

Line	ΔBIC	Evidence
Hα	13.3	783.8
Na D1	14.7	1518.6
Na D2	26.8	654277.3

From left to right: the investigated line, the ΔBIC, and the corresponding Bayesian evidence.

Chapter 5

Toward the Atmospheric Remote sensing Infrared Exoplanet Large Survey (Ariel) Space Mission: the systematics in Low-Resolution Spectroscopy

In the previous chapters I showed the peculiarities and challenges of extracting the transmission spectra from high resolution data. This includes the removal of telluric contamination and of stellar residuals such as **Rossiter-McLaughlin Effect (RME)** and **Centre to Limb Variation (CLV)**. While these effects can be hard to remove, high-resolution data are not affected by photo-spectroscopically calibration issues: since there is not a true continuum but only a pseudo-one due to the narrow wavelength bands, in the procedure to extract the transmission spectra, normalizations are widely used. The use of normalisations allow to limit the impact of many parameters used in the analysis such as the mass. On the other hand, low-resolution spectroscopy allows to measure the flux of the spectrum but is impacted by several parameters and by their uncertainties and accuracy. For example, Di Maio et al. (2023) showed the impact of mass uncertainties on the atmospheric retrievals at low-resolution. Moreover, as the systematics highly impact the analysis, the different pipelines used in literature may give rise to different results. I will discuss these effects in the next two sections. In Section 5.1 I will introduce an approach to select the parameters to obtain an homogenous analysis, while in Section 5.2 I will discuss the ongoing work on the comparison of different results obtained with different **Hubble Space Telescope (HST)** pipelines.

5.1 The problem of parameter determination

In the field of exoplanetary science, one of the fundamental challenges lies in addressing the diversity of parameters associated with a single planet. A given set of parameters, often derived from different observational techniques and studies, can vary significantly due to differences in methodologies, data quality, and underlying assumptions. Resources like the NASA Exoplanet Archive highlight this issue, as they collate and present a vast array of data for individual planets, sometimes with conflicting or incomplete entries.

Such variability in parameter estimates can pose significant challenges for scientific analysis. For instance, discrepancies in planetary mass, radius, or orbital characteristics can affect derived quantities like density, equilibrium temperature, and even habitability metrics. These inconsistencies can lead to systematic biases in population studies, hinder accurate modelling of planetary interiors or atmospheres, and complicate comparisons across planetary systems.

In addition to the NASA Exoplanet Archive, other resources, such as the Extrasolar Planets Encyclopaedia and specialized databases from large survey missions like **Transiting Exoplanet Survey Satellite (TESS)** or Kepler, also contribute to the wealth of information. However, these archives can sometimes report parameters based on distinct criteria or subsets of the available data, further emphasizing the need for careful cross-comparison and validation.

Ultimately, reconciling these differences is crucial for improving our understanding of planetary formation, evolution, and diversity. Efforts to integrate and homogenize data from multiple sources, standardize parameter reporting, and apply statistical methods for resolving discrepancies are essential steps toward this goal.

5.1.1 The Italian Ariel dry run

The Italian contingent of the **Atmospheric Remote sensing Infrared Exoplanet Large Survey (Ariel)** space mission has resolved to undertake an ambitious experiment aimed at assessing our capability to construct a comprehensive framework designed to replicate prospective results of the **Ariel** mission. This endeavour will commence with the analysis of a selected sample of stars and planets, specifically HD209458, WASP-69, HAT-P-14, HD189733, and WASP-80 with the goal of simulating the entire process, from the target selection to the analysis of the **Ariel** instruments.

The experiment involves several activities regarding the stars, the planets, their interaction and the atmospheres. The pipeline starts with the determination of the stellar and planetary properties. These steps are crucial to set the common conditions for the rest of the analyses that include: the investigation of the formation of the system, the astro-chemistry of the disk, the atmospheric evolution, the star-planet interaction, the planetary spectral synthesis and, eventually, the simulation and retrievals.

I focused on the working group devoted to the determination of the planetary parame-

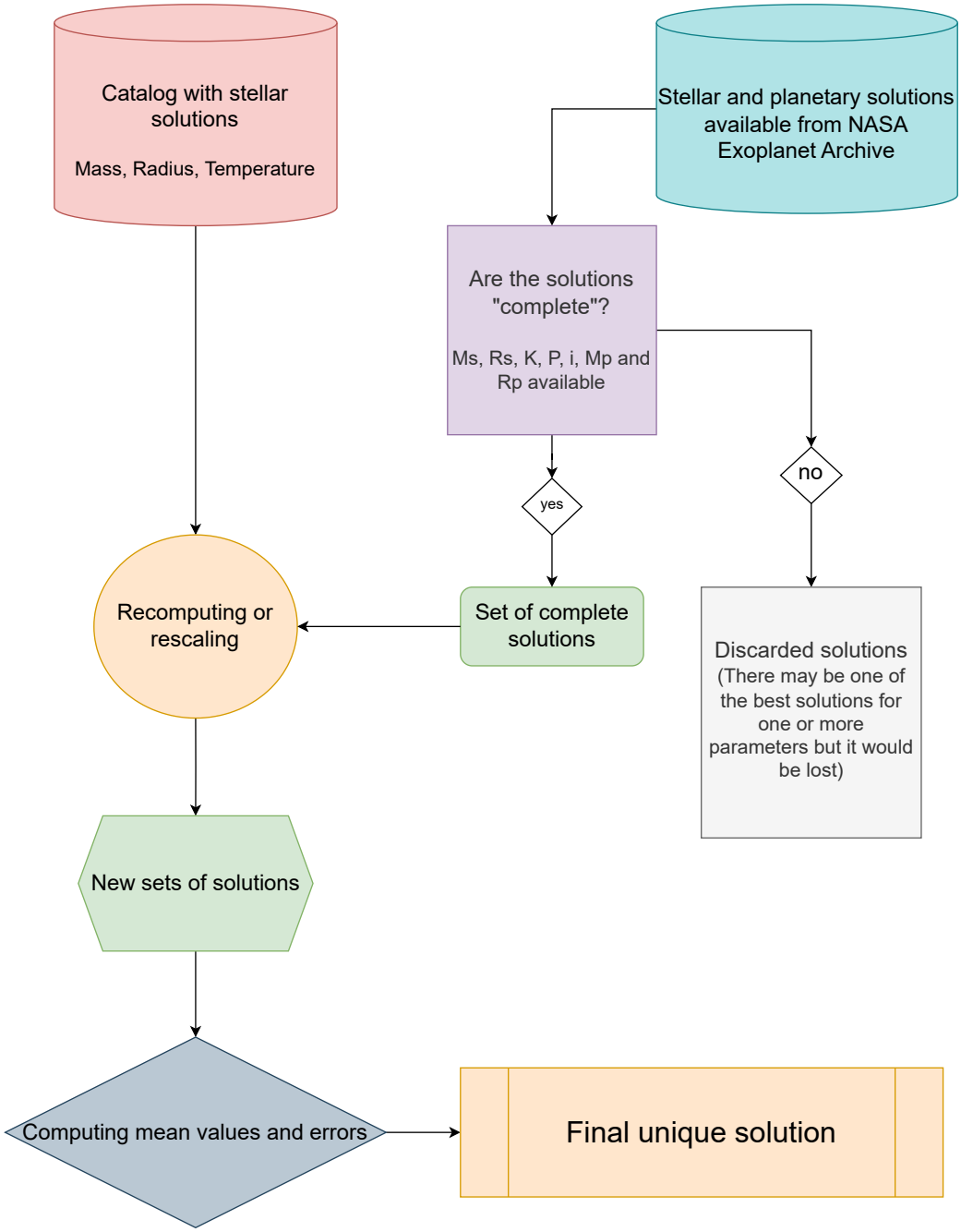

Figure 5.1: Diagram of the framework adopted within the Italian community for the dry run for the planetary parameters determination.

ters. In particular, the sample of targets selected showed the necessity of a criterion to homogenously select the planetary and orbital parameters for each planet since several solutions are available in literature. In order to homogenously select a set of parameters for our sample, I adopted the following strategy for each target:

- we start our framework considering a new set of stellar parameters. These have been computed in an homogenous way, from a specific working group within the collaboration, following the recipes described in Magrini et al. (2022). The new stellar parameters include the mass, Ms_{new}, the radius, Rs_{new}, and the effective temperature of the stars, T_{eff}. We show the results obtained for our sample in Table 5.1;
- we selected all the different set of stellar and planetary parameters in the Exoplanet Archive (called solutions);
- we filtered all the solutions retrieved from the Exoplanet Archive, selecting only the ones containing the stellar mass, Ms_{old}, the stellar radius, Rs_{old}, the radial velocity amplitude, K, the orbital period, P, the orbit inclination, i, the planetary mass, Mp_{old} and the planetary radius, Rp_{old};
- we obtain the planetary mass in two methods: we recompute a new value of M_p from Eq. 1.1 assuming a circular orbit (i.e., e = 0). We call this value Mp_{rec};
- the second way to obtain the mass is rescaling each old value according to the old and new values of the stellar mass, following the relation:

$$Mp_{res} = \frac{Mp_{old}}{Ms_{old}^{2/3}} \times Ms_{new}^{2/3} \tag{5.1}$$

- similarly to the mass, we rescale the planetary radius following:

$$Rp_{res} = \frac{Rp_{old}}{Rs_{old}} \times Rs_{new} \tag{5.2}$$

- we compute the mean values with the errors for the new masses (both rescaled and recomputed) and radii as shown in Fig. 5.2.

A diagram of the framework adopted, with all the different steps, can be seen in Fig. 5.1.

Starting from the new parameters computed, we recomputed the equilibrium temperature of the planet and the scale height of its atmosphere.

In Table 5.1 are shown the new values for the 5 stars sample, while in Table 5.2 the recomputed parameters. The masses and the radii we obtained with our framework are compared to the literature ones in Fig. 5.2, where it is possible to see how in some cases the masses and radii we get are not comparable with most of the literature solutions.

It is interesting to note that, the parameters retrieved by our framework may not be in agreement with the previous values in literature as this strongly depends on the new

Table 5.1: New stellar parameters obtained within the collaboration according to Magrini et al. (2022)

Star	Ms_{new} ($M_\odot$)	Rs_{new} ($R_\odot$)	$T_{\rm eff}$ (K)
HD209458	0.96246 ± 0.078	1.34883 ± 0.06	5665 ± 118
WASP-69	0.81748 ± 0.06	0.8984 ± 0.035	4693 ± 150
HAT-P-14	1.58269 ± 0.055	1.55942 ± 0.042	7187 ± 82
HD189733	0.76 ± 0.04	0.853 ± 0.023	5003 ± 92
WASP-80	0.66 ± 0.06	0.53 ± 0.01	3955 ± 100

Table 5.2: Results of our framework

Planet	Mp_{rec} (M_J)	Mp_{res} (M_J)	Rp_{res} (R_J)	a (AU)	$T_{\rm eq}$ (K)
HD209458 b	0.62 ± 0.03	0.62 ± 0.04	1.588 ± 0.077	0.045 ± 0.001	1500 ± 50
WASP-69 b	0.256 ± 0.022	0.255 ± 0.025	1.166 ± 0.074	0.045 ± 0.001	1010.3 ± 39.8
HAT-P-14 b	2.49 ± 0.08	2.47 ± 0.15	1.22 ± 0.11	0.0632 ± 0.0007	1719.7 ± 31.9
HD189733 b	1.096 ± 0.051	1.094 ± 0.063	1.30 ± 0.06	0.0303 ± 0.0005	1278.34 ± 31.2
WASP-80 b	0.597 ± 0.041	0.598 ± 0.055	0.89 ± 0.04	0.036 ± 0.001	732 ± 31

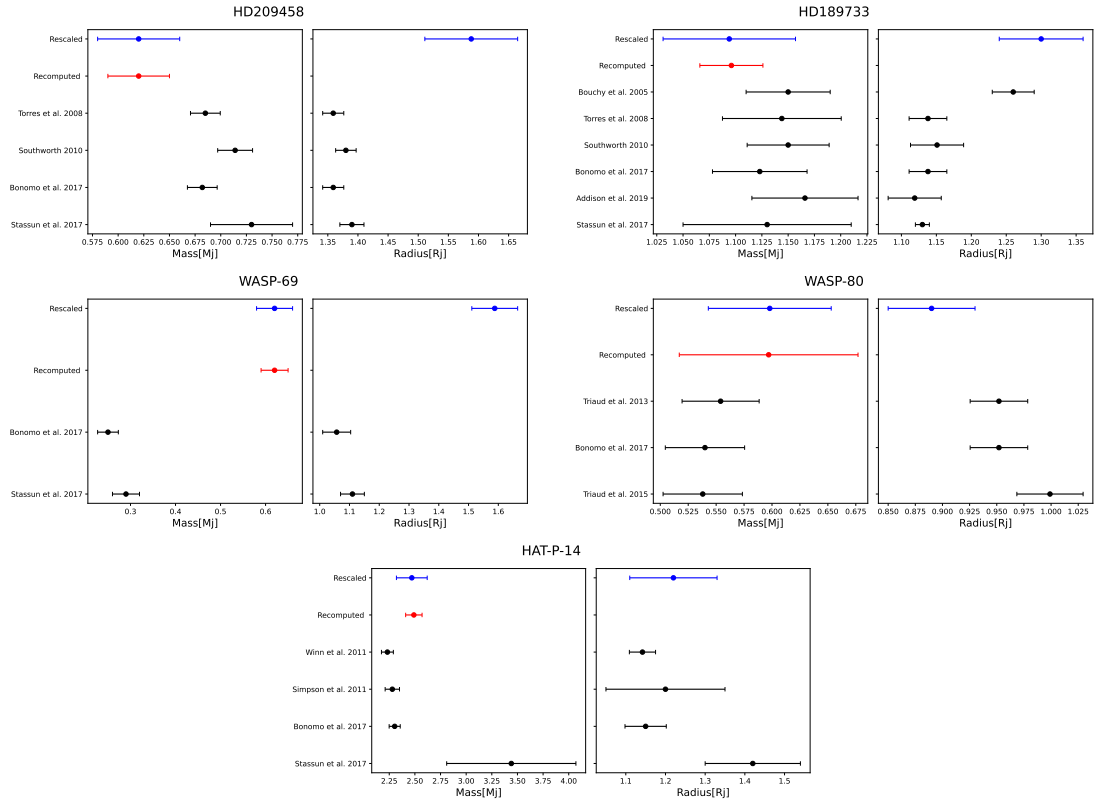

Figure 5.2: Masses and radii computed with our framework for each target. In blue the mean rescaled values for both the mass and the radius, while in red the recomputed mass value. We also show the literature values including only the filtered work as explained in the test.

stellar values obtained. Despite our way may be not relying on a direct measurement of the planetary parameters but only on the stellar ones, it allow us to use all the solutions already available in literature and combine them starting only from directly measured quantities such as the stellar radius, Rs_{old}, the radial velocity amplitude, K, the orbital period, P, the orbit inclination, i, the planetary mass, Mp_{old} and the planetary radius, Rp_{old}. Our future objective is to expand our framework to encompass the entire **Ariel** reference sample, thereby facilitating the derivation of a new catalogue of refined parameters that are essential for the ambitious objectives of the **Ariel** survey.

5.2 Comparison of HST pipelines

In the following Sections I will introduce the ongoing work I am leading with Lorenzo Mugnai from the University of Cardiff on the comparison of the **HST** pipelines to extract transmission spectra.

5.2.1 Introduction

Transit spectroscopy has emerged as a cornerstone technique for characterizing the atmospheres of exoplanets, providing insights into their chemical composition, thermal structure, and potential habitability (e.g., Charbonneau et al. 2002; Tinetti et al. 2007; Tsiaras et al. 2016; Swain et al. 2021; Mugnai et al. 2021). Over the past two decades, **HST** and the Spitzer Space Telescope have facilitated high-quality observations for dozens of exoplanets, significantly advancing our understanding of planetary atmospheres exploiting low-resolution transmission spectroscopy (e.g., Sing et al. 2016; Tsiaras et al. 2018; Edwards et al. 2023; Estrela et al. 2021). However, extracting reliable spectra from raw data involves complex data reduction processes that depend on specialized pipelines, each employing distinct approaches to address instrumental and astrophysical systematics. These methodological differences can introduce substantial biases, impacting the scientific conclusions drawn.

This has been highlighted recently by Mugnai et al. (2024) in a study where they investigated systematic biases introduced by different pipelines to extract transmission spectra from **HST Wield Field Camera 3 (WFC3)** G141 filter on catalogue-level comparisons. This approach moves beyond single-planet analyses, leveraging extensive datasets to statistically assess discrepancies between results generated by three pipelines commonly used: Iraclis (Tsiaras et al. 2016), EXCALIBUR (Roudier et al. 2021), and CASCADE (Carone et al. 2021). The strategy Mugnai et al. (2024) adopted included normalizing all data to a uniform spectral resolution to facilitate cross-comparison, assessing statistical properties such as variations in mean values, uncertainty estimates, and spectral shape, and conducting uniform retrievals on the spectra to evaluate differences in derived planetary properties, including atmospheric composition, temperature, and cloud pressure.

Mugnai et al. (2024) work and results constitute the starting point of ours, moving from their catalogue scale comparison to the individual target one, deepening the discrepan-

cies found in the only target in their catalogue to be analysed successfully with all the datasets considered. WASP-121 b (Delrez et al. 2016) was analysed across with all the pipelines investigated, serving as a benchmark for pipeline performance. Notable differences in molecular abundances and temperature estimates were observed, underlining the need for pipeline standardization. Among the exoplanets observed, WASP-121 b stands out as one of the most intensively studied hot Jupiters. Located approximately 850 light-years from Earth, this exoplanet exhibits an equilibrium temperature of about 2300 K, making it an ideal target for detailed spectroscopic analysis due to its enhanced height scale leading to a larger scattering area for the transmission spectroscopy and hence to a larger S/N ratio. Observations of WASP-121 b have revealed a complex atmospheric profile, including potential thermal inversions in its upper atmosphere and spectral signatures of molecules such as H_2O and TiO (e.g., Tsiaras et al. 2018; Changeat et al. 2024; Ouyang et al. 2023, for only low-resolution results). These features make WASP-121 b a compelling case for assessing the consistency and accuracy of various pipelines in data reduction and interpretation.

In this work we plan to evaluate the impact of different pipelines in the extraction of transmission spectra from **HST WFC3** G141 filter on an individual visit of WASP-121 b. **HST WFC3** performed three visits (ID: 14468 and ID: 15134 by Thomas Mikal-Evans) of WASP-121 b with the last two collected being part of a phase-curves. We decided to select the first visit (i.e., the one with only the primary transit of the planet) as most of the pipelines used in this comparison have been developed to extract transmission spectra during transit and not during whole phase-curves. Focusing on one visit only is important in the case of WASP-121 b as Changeat et al. (2024) stressed the variability of the signal detected with the **WFC3** for this target, with the two visits collected as part of phase-curves being mostly affected by clouds and hence giving rise to flat spectra which may be harder to compare.

In Section 5.2.2, we describe the pipelines used in this work and we illustrate the different methodologies employed to extract the different white and spectroscopic light-curves. In Section 5.2.3, we report the results we obtained and their impact on atmospheric retrievals in Section 5.2.4, while in Section 5.3 we discuss our results and we give a short summary highlighting the main conclusions.

5.2.2 Methods

In their work Mugnai et al. (2024) deepened the comparison between the transmission spectra of WASP-121 b extracted from **HST WFC3** data in several studies:

- Tsiaras et al. (2018) employing Iraclis;
- Edwards et al. (2023) employing an updated version of Iraclis;
- Evans et al. (2016) employing a personal pipeline;
- Roudier et al. (2021) employing EXCALIBUR.

In addition they added their analysis employing CASCADE. It is extremely important to

stress that all the analyses listed have been performed using the same stellar, planetary and orbital parameters from Delrez et al. (2016), removing one of the possible causes of inhomogeneities. Their results, displayed in Fig. 5.3, show that the comparison between the studied employing Iraclis is biased by the different data's availability with Tsiaras et al. (2018) utilising a single transit observation from proposal ID: 14468 by Thomas Mikal-Evans, while Edwards et al. (2023) incorporated two more transit observations belonging to the phase-curves from proposal ID: 15134 (Mikal-Evans). The EXCALIBUR spectrum is similar in shape with Edwards et al. (2023) but with a clear offset. The same happens for the spectrum obtained by Tsiaras et al. (2018) with the one by CASCADe, while Tsiaras et al. (2018) and Evans et al. (2016) have very similar spectra. The discrepancies by the extracted spectra are clear in the different results obtained with the retrievals using **Tau Retrieval for Exoplanets (TauREx)** (Al-Refaie et al. 2021).

The main reason for the different shapes is due to the visits analysed. Tsiaras et al. (2018), Evans et al. (2016) and CASCADe analysed only the first visit while Edwards et al. (2023) and EXCALIBUR analysed all the three visits. As pointed by Changeat et al. (2024), the second and third visits collected (ID: 15134) are mostly affected by clouds and hence flatten the spectra obtained employing all the three visits. On the other hand, the observed offsets analysing the same datasets can be due to the different pipelines employed.

To address this difference, our strategy relies on performing the comparison of the different pipelines analysing only the first visit (ID: 15134) as has been analysed by all the pipelines investigated in Mugnai et al. (2024). Unfortunately, this rules out EXCALIBUR as only the results obtained using simultaneously all the visits are currently available. Additionally we analysed the first visit data employing the publicly available PACMAN pipeline (Zieba & Kreidberg 2022) and we repeated the analysis by Tsiaras et al. (2018) and Edwards et al. (2023) using Iraclis.

In the next sections we are going to introduce a short summary of the different pipelines used in this work to analyse **HST WFC3** G141 data of WASP-121 (see Fig. 5.4 for a comparison of the data reduction steps).

Description of the pipelines

Several pipelines has been developed to extract the transmission spectra of exoplanets collected with **HST WFC3**

Iraclis (Tsiaras et al. 2016) The Iraclis pipeline performs several processes, starting fram the .raw files, such as zero-read subtraction, reference pixel correction, non-linearity correction, dark current subtraction, gain conversion, sky-background subtraction, calibration, flat-field correction, and the correction of bad pixels and cosmic rays. Subsequently, the pipeline extracts the flux from spatially scanned spectroscopic images to create the final transit light curves for each wavelength band. These light curves are fitted using known literature values (e.g., Delrez et al. 2016, in our specific case), with the only free parameters being the planet-to-star radius ratio and the transit mid-time,

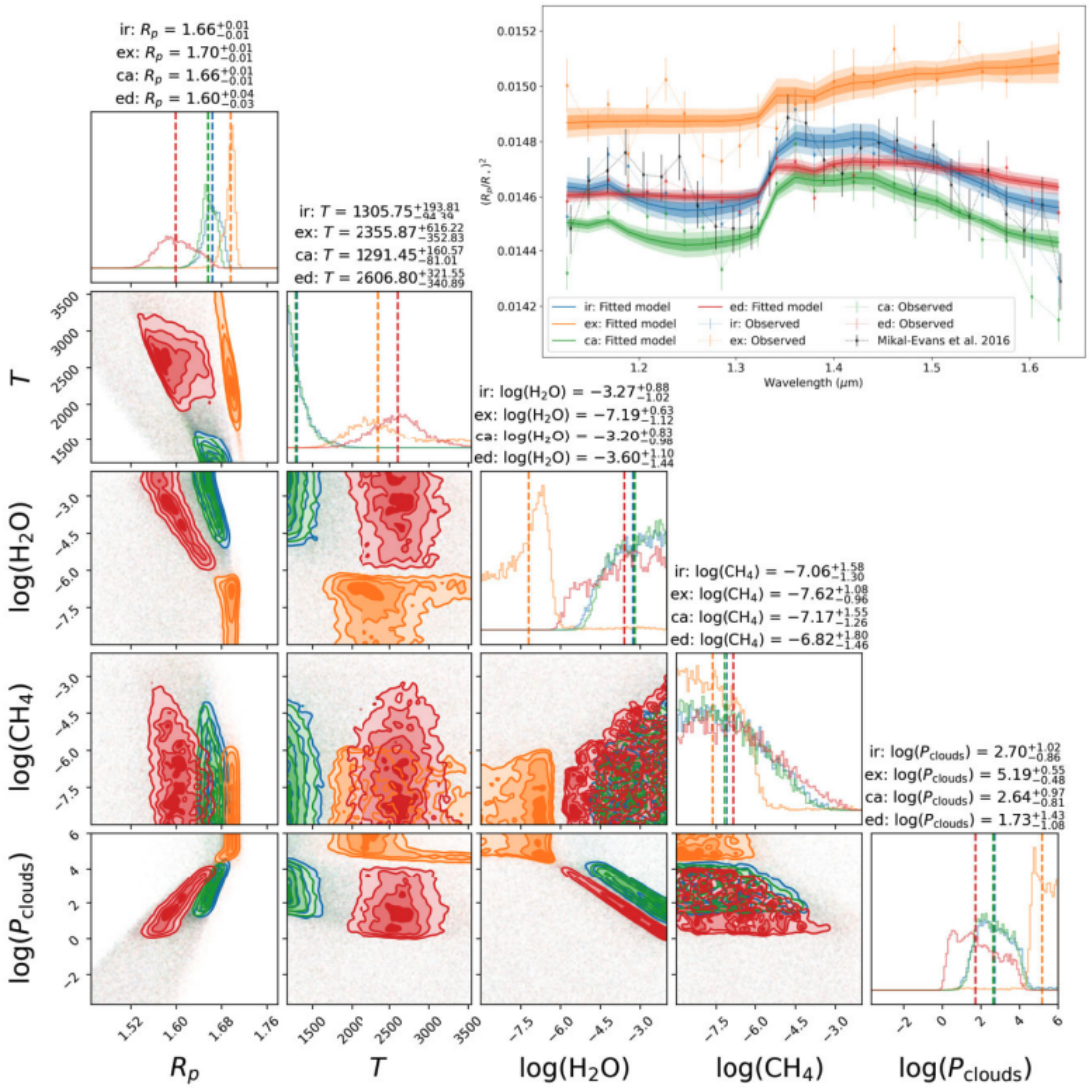

Figure 5.3: The corner plot delineates the retrieval results for all WASP-121 b spectra. The colour coding remains consistent with the rest of the paper: blue represents the Tsiaras et al. (2018) data, red signifies Edwards et al. (2023), orange denotes Excalibur, and green symbolizes Cascade. Atop each panel column, the fitted values for each data set are displayed: 'ir' corresponds to the Iraclis data set from Tsiaras et al. (2018), 'ex' to Excalibur, 'ca' to Cascade, and 'ed' to Edwards et al. (2023). The top right panel illustrates the fitted transmission spectra derived from the parameters retrieved for each data set, represented as solid lines. The corresponding filled areas indicate the 1σ and 2σ uncertainties. The observed data points, along with their uncertainties, are depicted using the same colour scheme. The observed data points are connected with coloured dotted lines, to help the reader. The black data points in the top right panel are from Evans et al. (2016) for comparison. Adapted from Mugnai et al. (2024).

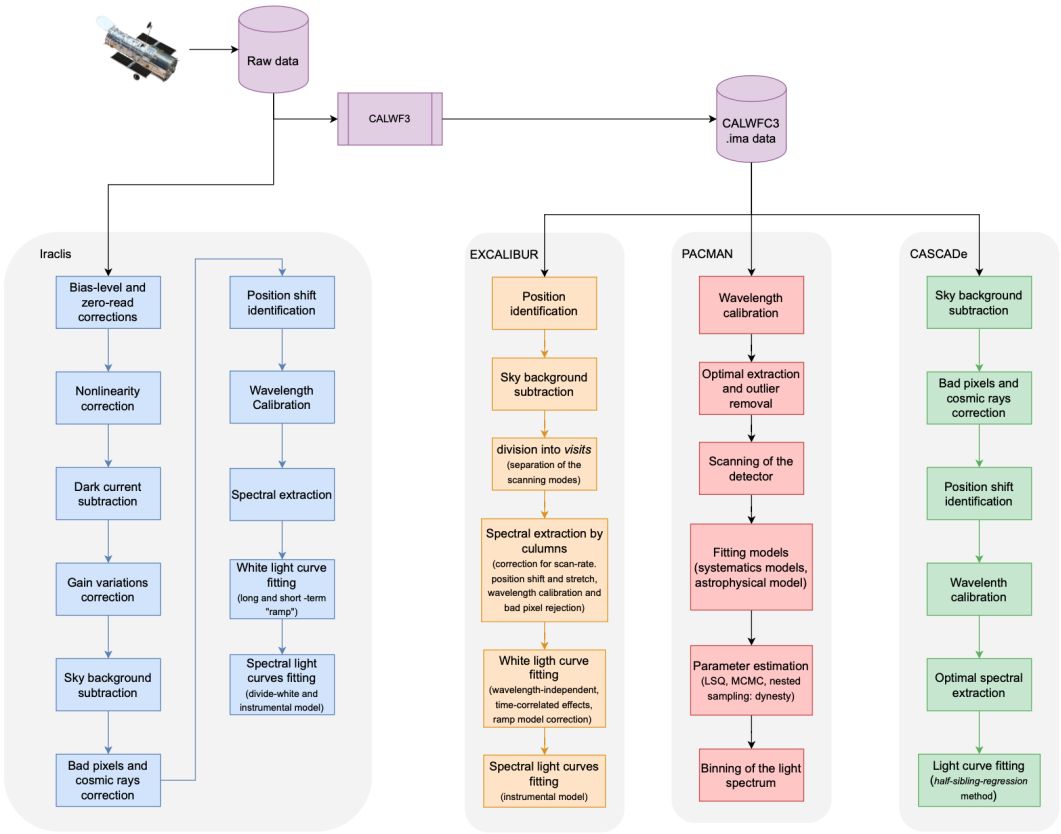

Figure 5.4: Comparison of data reduction steps across pipelines. The data reduction steps for the Iraclis pipeline are delineated following Tsiaras et al. (2016), for EXCALIBUR as per Roudier et al. (2021), and for CASCADE within the appendices of Carone et al. (2021). Adapted from Mugnai et al. (2024) with the inclusion of PACMAN from Zieba & Kreidberg (2022).

Table 5.3: Parameters from Delrez et al. (2016) used in all the analyses of WASP-121 b.

Parameter	Value	Reference
Stellar parameters		
$M_\star$ ($M_\odot$)	$1.353^{+0.080}_{-0.079}$	Delrez et al. (2016)
Stellar radius, $R_\star$ ($R_\odot$)	1.458 ± 0.030	Delrez et al. (2016)
Effective temperature(K) . .	6460 ± 140	Delrez et al. (2016)
log g ($\log_{10}$(cm s^{-2}))	$4.242^{+0.011}_{-0.012}$	Delrez et al. (2016)
Metallicity, [Fe/H](dex) . .	0.13 ± 0.09	Delrez et al. (2016)
Planetary parameters		
Planetary mass, M_p (M_{jup})	$1.183^{+0.064}_{-0.0062}$	Delrez et al. (2016)
Planetary radius, R_p (R_{jup})	1.865 ± 0.044	Delrez et al. (2016)
Orbital inclination, i (deg)	87.6 ± 0.6	Delrez et al. (2016)
Major semi-axis, a (au) . . .	$0.02544^{+0.00049}_{-0.00050}$	Delrez et al. (2016)

alongside the coefficients for **HST** systematics. The limb-darkening coefficients are derived from the quadratic formula by Claret (2000) based on the stellar parameters with the models taken from Exotethys package (Morello et al. 2020). Finally, the spectral light curves are fitted using the divide-white technique presented by Kreidberg et al. (2014), with a normalization factor added for accounting for the slope.

CASCADe (Carone et al. 2021) CASCADe pipeline starts reading the 'ima' intermediate data products generated by the CALWFC3 data reduction pipeline. Then, using the target acquisition image, the initial position of the target on the detector is determined, and based on that the wavelength solution and spectral trace is calculated. After that, the background is subtracted, the data are filtered using directional filters to determine and flag bad-pixel creating a cleaned and smoothed dataset. After determining the relative movement (including rotation and scaling changes) of the telescope, the pipeline corrects the wavelength for each time step. Finally the 1D spectra are extracted both in an optimal way (using an extraction profile based on the cleaned and smoothed data) as well as using an extraction aperture.

PACMAN (Zieba & Kreidberg 2022) Similarly to CASCADe, PACMAN starts its path from the 'ima' intermediate data products. The pipelines creates a reference spectrum based on the throughput of the respective grism (G102 or G141) and a stellar model with the possibility to use a stellar spectrum from MAST or a black body spectrum. This template is used for the wavelength calibration of the **WFC3** spectra. The position of the star is determined in the direct images which are commonly taken at the start of **HST** orbits to create an initial guess for the wavelength solution using the known dispersion of the grism. Using the reference spectrum as a template, the shift and scaling in wavelength-space that minimizes the difference between the template and the first spec-

trum in the visit are determined. The trace of the planet retrieved is used to optimally extract the 1D spectra. Several methods can the be employed to fit the extracted white and spectroscopic light curves, including models that account both for astrophysical and systematic effects as described in Kreidberg et al. (2014).

Strategy

To evaluate the impact of the pipelines in the extracted spectra, we straightforwardly employed PACMAN and Iraclis pipelines and we used the Iraclis analyses by Edwards et al. (2023) and Tsiaras et al. (2018), and the CASCADe analysis performed in Mugnai et al. (2024). Moreover we employed Evans et al. (2016) results as benchmark since they have been conducted with an independent pipeline. These literature works have been conducted with the same parameters from Delrez et al. (2016) and hence we ran both Iraclis and PACMAN with the same parameters. For Iraclis we tried to use the closest configuration as the ones used in the previous papers.

5.2.3 Lightcurves comparison

We computed for each pipeline the white and spectroscopic lightcurves. Both show a similar shape but a clear offset between the curves obtained by different pipelines. We will discuss and deepen the comparison in the next sections.

White Lightcurve

All the pipelines return the white lightcurve as output except for CASCADe that does not use the Kreidberg et al. (2014) divide-white correction.

In Fig. 5.5, we show, in the top panel, the different white lightcurves with their fitted models produced by each pipeline, while in the bottom panel are shown the residuals. Starting from the latter, it can be seen that the lightcurves produced from Iraclis and their models are coherent among them and show similar trend in the residuals. PACMAN data and models are slightly above the Iraclis ones but the residuals are the same amplitude of the other ones, despite showing different trends, probably due to the different treatment of the systematics.

Transmission spectra

The spectroscopic lightcurves, or transmission spectra, reflect the results of the white lightcurves. As can be seen in the top panel of Fig. 5.6 the PACMAN lightcurve shows a positive offset respect to the Iraclis ones which are similar among them. The CASCADe spectrum has a trend opposite to PACMAN showing a clear negative offset respect to Iraclis spectra. The Iraclis spectra show a common behaviour with the one obtained by Evans et al. (2016) and a comparison among them is discussed in the next sections. In the bottom panel of Fig. 5.6 we can see the transmission spectra divided by their median value. All the spectra show a similar shape with some features clearly visible.

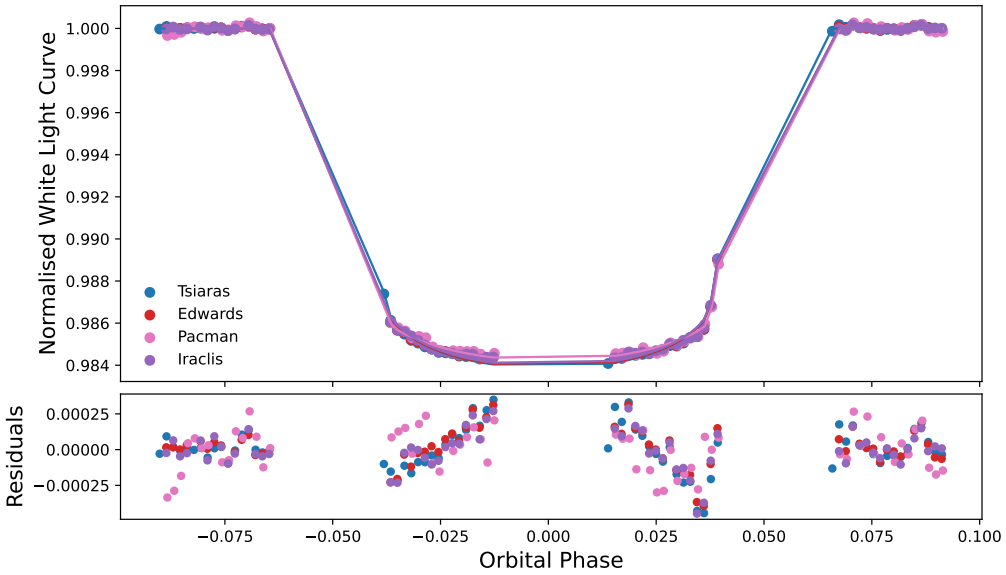

Figure 5.5: Comparison of the white light curves extracted employing different pipelines. Top panel: data and fitted model. Bottom panel: residuals.

To quantitatively evaluate the differences between the spectra we adopted the metrics introduced in Mugnai et al. (2024):

$$\mathrm{MK1}_{A,B} = \frac{(S_{pA}(\lambda) - \hat{S}_{pA}) - (S_{pB}(\lambda) - \hat{S}_{pB})}{\max[\sigma_A(\lambda), \sigma_B(\lambda)]}, \tag{5.3}$$

and

$$\mathrm{MK2}_{A,B} = \frac{S_{pA}(\lambda) - S_{pB}(\lambda)}{\max[\sigma_A(\lambda), \sigma_B(\lambda)]}, \tag{5.4}$$

where $S_p(\lambda)$ denotes the values of the spectral bin, while $\sigma_B(\lambda)$ denotes the standard deviation within that bin. A and B are placeholders for the two pipelines being compared. We used Evans et al. (2016) spectrum as benchmark to compare the other extracted with the different pipelines. In Fig. 5.6 top right panel we used the MK1 metric to evaluate the discrepancies without removing the median value, $\hat{S}$, as done in the bottom right panel where we used the MK2 metric. In both cases we report the comparison as histograms with normal distributions fitted to them and the fit parameters reported in the legends. We can see from the use of MK1 that the offsets from PACMAN and CASCADe are clearly visible from their values of σ while Iraclis based results are once again comparable among them.

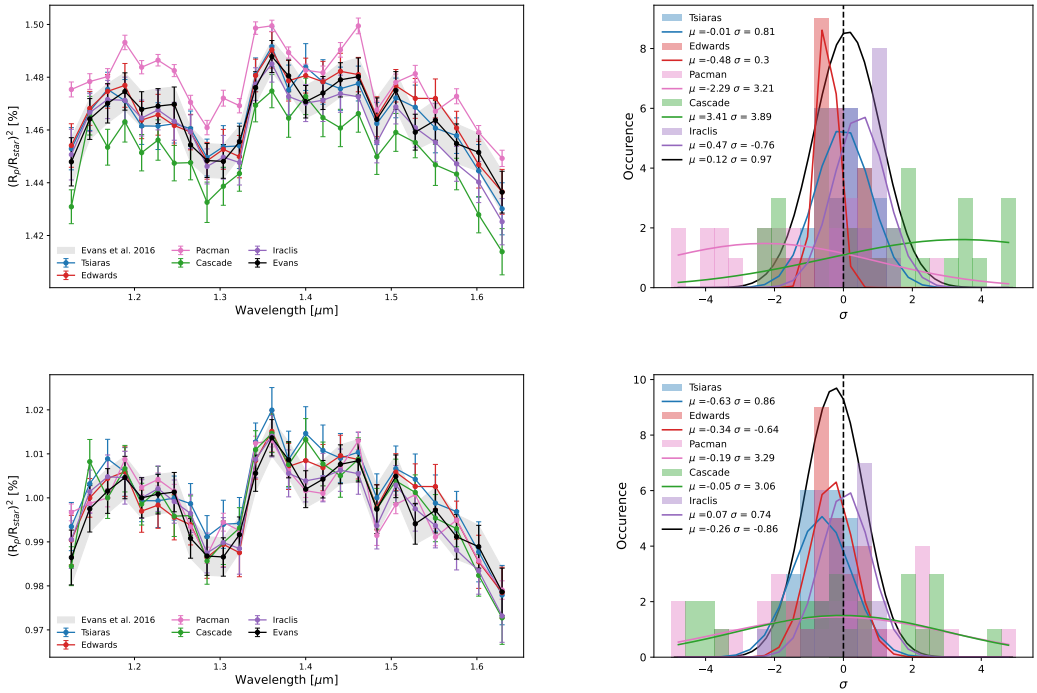

Figure 5.6: Comparison of the transmission spectra extracted employing all the different pipelines discussed in the text. In the top left panel we show the extracted spectra, while in the left bottom panel we show the extracted spectra divided by its own median value. In the right panels we show the histograms computed employing MK1 and MK2 metrics as described in the text, and the fit with normal distributions.

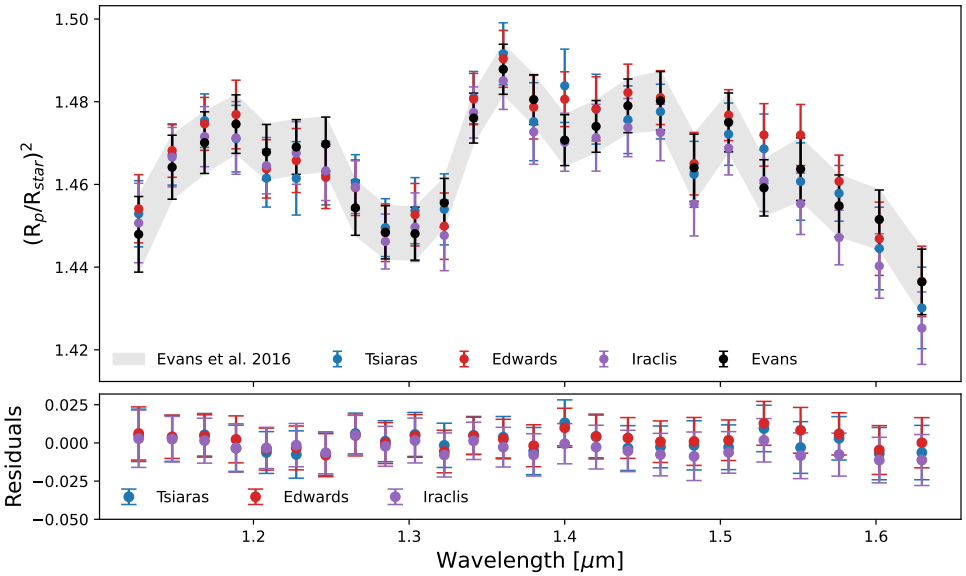

Figure 5.7: Comparison of the transmission spectra extracted employing the Iraclis pipelines. Top panel: transmission spectra extracted with the Iraclis pipeline by Tsiaras et al. (2018), Edwards et al. (2023) and in this work. We use Evans et al. (2016) as benchmark comparison. Bottom panel: Residuals among the three Iraclis spectra and Evans et al. (2016).

Evolution of Iraclis pipeline

As discussed in the previous sections, the Iraclis pipeline results obtained by Tsiaras et al. (2018), Edwards et al. (2023) and computed by us, are similar among them as can be seen from the lightcurves and the metrics. We ran a deeper comparison between the spectra obtained with Iraclis employing Evans et al. (2016) as benchmark, computing the residuals between Iraclis results and Evans et al. (2016) ones. As shown in Fig. 5.7, the results obtained by Tsiaras et al. (2018), Edwards et al. (2023) and our analysis, are comparable among them for each spectral bin.
Therefore, we can consider Iraclis pipelines self-consistent with itself across several years of development.

5.2.4 Impact on atmospheric retrievals with TauREx

The atmosphere of WASP-121 has proven to be one of the most studied in the past years: several studied reported the detection of H_2O, CO, VO, TiO (Tsiaras et al. 2018; Changeat & Edwards 2021).

We employed **TauREx** (Al-Refaie et al. 2021) to evaluate the impact of the discrepancies noted in the previous sections to the atmospheric retrievals. At the moment we only used the same recipe described in Mugnai et al. (2024), with free chemistry and fitting

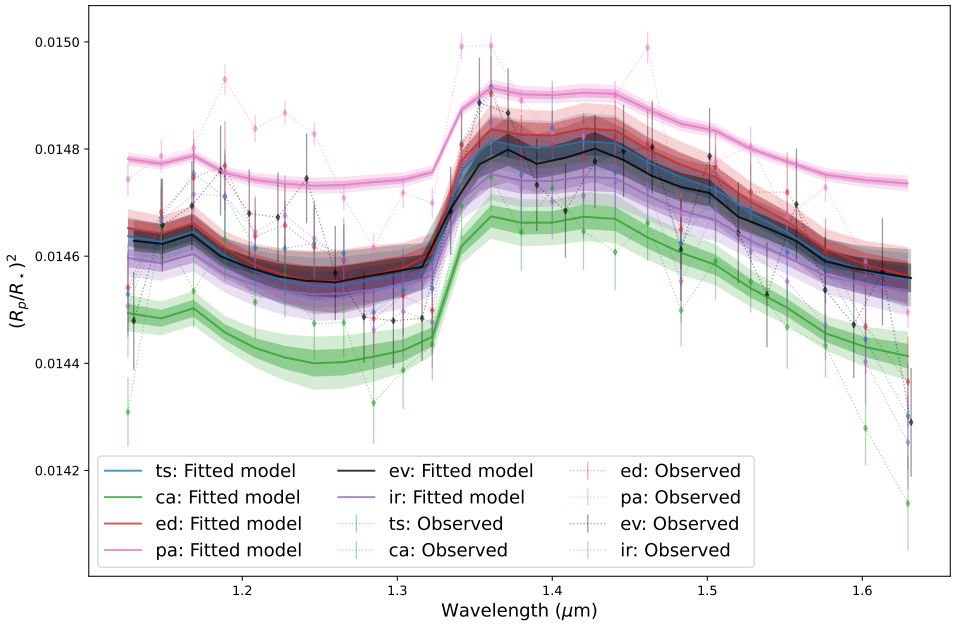

Figure 5.8: Spectra and their best fitting models retrieved with **TauREx** employing the free chemistry and the same strategy of Mugnai et al. (2024). We use 'ts' for Tsiaras et al. (2018), 'ca' for CASCADe, 'ed' for Edwards et al. (2023), 'pa' for PACMAN, 'ev' for Evans et al. (2016) and 'ir' for our Iraclis run.

only for H_2O, CH_4,

$$R_\mathrm{p}$$

, T_{eq} and clouds pressure.

We show the results in Fig. 5.8, Fig. 5.9 and in Table 5.4. We note that the H_2O and CH_4 abundances, and the clouds pressure are all comparable among them. The radius retrieved with PACMAN reflects its offset in the transmission spectrum with a larger radius obtained respect to the other. The parameter that seems mostly affected by the different pipelines is the temperature showing a correlation with the radius.

Table 5.4: Parameters values retrieved from the cornerplots.

Pipeline	R_p [$R_\oplus$]	T [K]	$\log(H_2O)$	$\log(CH_4)$	$\log(P_\mathrm{clouds})$
Tsiaras et al. (2018)	$1.66^{+0.01}_{-0.01}$	$1287.11^{+215.22}_{-99.59}$	$3.29^{+0.85}_{-0.99}$	$7.10^{+1.53}_{-1.27}$	$2.75^{+0.97}_{-0.87}$
CASCADe	$1.66^{+0.01}_{-0.01}$	$1279.10^{+169.82}_{-91.44}$	$3.16^{+0.74}_{-0.94}$	$7.20^{+1.55}_{-1.19}$	$2.78^{+0.87}_{-0.78}$
Edwards et al. (2023)	$1.66^{+0.01}_{-0.01}$	$1311.27^{+201.35}_{-115.88}$	$3.21^{+0.79}_{-0.97}$	$7.06^{+1.54}_{-1.29}$	$2.82^{+0.96}_{-0.82}$
PACMAN	$1.68^{+0.01}_{-0.01}$	$1201.76^{+77.93}_{-36.88}$	$3.53^{+0.84}_{-0.79}$	$7.55^{+1.26}_{-0.98}$	$2.64^{+0.79}_{-0.83}$
Evans et al. (2016)	$1.66^{+0.02}_{-0.02}$	$1362.12^{+279.35}_{-157.34}$	$3.33^{+0.90}_{-1.02}$	$6.95^{+1.58}_{-1.41}$	$2.59^{+1.00}_{-0.94}$
Iraclis	$1.66^{+0.01}_{-0.01}$	$1277.62^{+186.41}_{-93.88}$	$3.34^{+0.91}_{-0.99}$	$7.03^{+1.53}_{-1.33}$	$2.54^{+1.04}_{-0.87}$

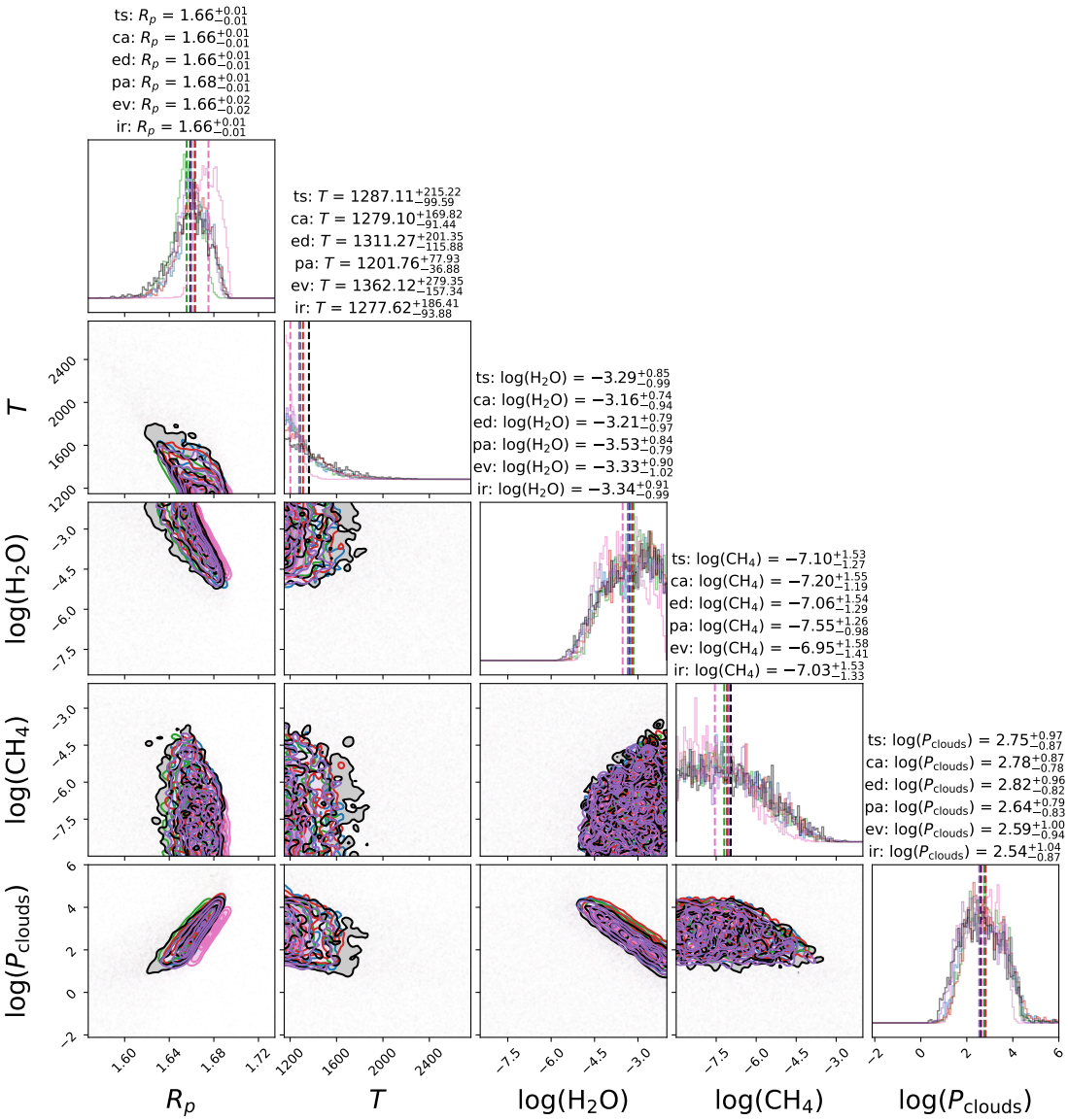

Figure 5.9: Corner plot of the retrievals with **TauREx** employing the free chemistry and the same strategy of Mugnai et al. (2024) for all the pipelines investigated and for the benchmark Evans et al. (2016). We use 'ts' for Tsiaras et al. (2018), 'ca' for CASCADe, 'ed' for Edwards et al. (2023), 'pa' for PACMAN, 'ev' for Evans et al. (2016) and 'ir' for our Iraclis run.

This initial test proved the need of running more complex retrievals including other molecules and to investigate the impact on the equilibrium chemistry.

5.3 Conclusions

As the era of the **James Webb Space Telescope (JWST)** and the **Ariel** space mission approaches, the challenges posed by the possibility of pipeline-dependent biases operating on an entire observational catalogue must be taken seriously and understood. The advent of these next-generation telescopes promises unprecedented data quality, allowing researchers to delve into more intricate questions about exoplanets. However, the very richness of this data also amplifies the potential pitfalls of pipeline discrepancies. While this study highlights issues observed with **HST-WFC3** data, the implications extend far beyond. In the **JWST** and **Ariel** era, where the focus will be on planetary population studies and comparative planetology, ensuring consistency and reliability across pipelines is paramount. Addressing these discrepancies is not just about refining our current understanding of exoplanets but is crucial for harnessing the full potential of upcoming observational capabilities. Only by resolving the challenge posed by pipeline-dependent results can we truly capitalize on the advanced data, asking deeper questions and drawing more precise conclusions about the Universe's myriad exoplanets.

Our preliminary results on **Ultra Hot Jupiter (UHJ)** WASP-121 b seems to hint that discrepancies in the extracted transmission spectra do not have a large impact on the retrievals. While this holds true for free chemistry with few molecules, we still need to:

- investigate more complex scenario including more molecules and equilibrium chemistry;
- try to address the origin of the differences evaluating the different steps in the analysis;
- Explore the effects on other types of planets and with data of varying SNR.

Chapter 6

Summary and conclusions

In this thesis, I have introduced and discussed several works focused on the investigation of exoplanetary atmospheres trough transmission spectroscopy, paying special attention to the methodology and other phenomena that could influence the atmospheric detections. This chapter summarises the main results and conclusions of this work.

The exoplanetary atmospheres analysed to date display remarkable variation in their chemical makeup, temperature-pressure dynamics, and cloud and haze distribution. Future observations, utilizing both terrestrial and space-based instruments, will further illuminate this complexity, offering promising advancements in the study of exoplanetary atmospheres. The **James Webb Space Telescope (JWST)** has recently begun making significant contributions in this domain, and by the early next decade, **Atmospheric Remote sensing Infrared Exoplanet Large Survey (Ariel)** is expected to facilitate atmospheric analysis of approximately 1000 exoplanets, including those as large as Jupiters and Neptunes down to super-Earth sizes. Furthermore, large ground-based observatories like the ELT will pave the way for new research opportunities, including the potential to detect biosignatures in the atmospheres of rocky exoplanets located within the habitable zone.

6.1 Chapters resume

Within this context, in this work I focused on the atmospheric characterization of extrasolar planets through transmission spectroscopy observations, working primary with High-Resolution Spectroscopy. I introduced the new framework to extract single line transmission spectra of the exoplanetary atmospheres I developed for high resolution observations. This method has been applied to several chapters in the thesis.

More precisely:

- In Chapter 2 I introduced the method I developed for the extraction and analysis of transmission spectra from high resolution spectroscopy data collected with **High Accuracy Radial velocity Planet Searcher for the Northern emisphere**

(HARPS-N) spectrograph. This method has been originally developed for the **Ultra Hot Jupiter (UHJ)** KELT-9 b, the hottest exoplanet known, orbiting around an A0 type star, making it the perfect target for transmission spectroscopy. The framework was first shown in D'Arpa et al. (2024b), where I analysed six transit observations of the ultra-hot Jupiter KELT-9 b taken with the **HARPS-N** spectrograph mounted at the **Telescopio Nazionale Galileo (TNG)**. Using the single line analysis method, I examined a range of metal lines across various atomic species, from the lightest elements like hydrogen to the heavier ones like iron. By using data from six nights of observations, the atmospheric signal strength was significant, allowing me to identify 70 distinct lines from seven species: Na I, Ca I, Ca II, Fe I, Fe II, Mg I, Ti II, Sc II, and Cr II. This is the highest number of lines detected using this technique compared to any previous studies. This method enabled us to validate prior detections and make new discoveries, including the identification of Hϵ and Hζ , which had previously been considered tentative. Notably, Hζ showed greater depth than anticipated, potentially affected by normalization issues due to low signal-to-noise in the blue range covered by **HARPS-N**. The first-time detection of Cr II and Sc II single lines in an exoplanet's atmosphere was achieved, in addition to many new lines from already known species. However, He, Li, Be, K, Sr, Y, Ni, Ba, and Mn single lines were not observed. In this study, single line analysis proved to be an effective method for validating and supporting findings from cross-correlation techniques while offering crucial insights into line width and depth. This, in turn, provided information about atmospheric turbulence and stratification, as well as the atmospheric chemical and physical structure. By comparing our absorption lines with **Non Local Thermal Equilibrium (NLTE)** models, we confirmed detected features and identified regions where line blending might occur. The extensive number of detected lines helped to confirm the presence of winds and enhanced our understanding of the atmospheric stratification of KELT-9 b.

In the same chapter I discussed the use of **NLTE** models to constrain the abundances of atomic species such as Mg, Fe and O in the atmosphere of KELT-9 b. Our preliminary results from **Fossati, D'Arpa and Borsa, in prep.** return a sub-solar abundance of Mg, a solar/super-solar abundance of Fe and a solar/sub-solar abundance of O. In future this will be the basis for the future constraining of C/O ratio to evaluate the formation history of the target.

I also introduced several other works carried on within the **Global Architecture of Planetary System (GAPS)** collaboration for the study of KELT-9 b, including Stangret et al. (2024) and Sicilia et al. (2025). In these two works, KELT-9 b has been analysed in single line employing different frameworks. The results proved my method and the other ones to be consistent among them with the detection of Fe and Na in the two works, respectively.

- In Chapter 3 I introduced the application of the method to several other targets, considering both targets similar to KELT-9 b and targets with different conditions. We validated the framework on another target similar to KELT-9 b, KELT-20 b,

and we tested it on other more complex targets, KELT-6 b, WASP-69 b, GJ-3470 b and WASP-107 b. The results for KELT-20 b align well with findings from other studies that utilize high-resolution spectroscopy for exoplanet atmospheric characterization like Casasayas-Barris et al. (2017), corroborating the method developed for KELT-9 b. For the other targets we found the detection of Na in WASP-69 b and the possible detection of Hγ in KELT-6 b, with WASP-107 b and GJ-3470 b not showing any single line feature. Despite the non detection of Hα , Na and Ca in their atmospheres, the work done for WASP-107 b and GJ-3470 b, have been used as starting point of the analysis I carried on in the visible part of the spectrum in Guilluy et al. (2024) discussed in Section 4.1.

After the validation of the method, I introduced its application to two other targets: TOI-1518 b and WASP-94A b. In the ongoing work that I am leading on the analysis of the **UHJ** TOI-1518 b with **HARPS-N** and GIANO-B data, we focused on both the single line analysis, detecting Hα and Na D2 lines, and the cross-correlation with templates, detecting Ca II, Ti II, Fe I , Fe II, Ba II, Mg I, Cr II and Sc II, and tentatively detecting Al II, Mg I, V I, V II, Y II, K I and W I with several sets of templates. We also started developing a method to combine the individual lines of the non detected species obtaining a preliminary detection of an average line for Fe II and Ti II. Once this method will be corroborated, we will be able to retrieve important information on these species, including their average height in the atmosphere and their average rotational profile.

I then extended the method, originally developed for analysing **HARPS-N** data to the data of two transits of WASP-94A b collected with **Echelle SPectrograph for Rocky Exoplanets and Stable Spectroscopic Observations (ESPRESSO)**. The two instruments share similar pipelines to reduce the data and hence adapting the framework did not present particular challenges. Our preliminary results in single line adds H I, Mg I to the already detected Na I in the atmosphere for WASP-94A b. However, the non detections with the cross-correlation with templates and the overlapping **Rossiter-McLaughlin Effect (RME)** suggest a deeper investigation on the origin of our signal, including masking the region of the tomography affected by the **RME**.

- In Chapter 4 I showed the application of single line analysis to extract and use the Hα line as a diagnostic for two mechanisms regarding the star-planet interaction: the stellar activity and the photo-evaporation.

  We investigated the role of the Hα as a stellar activity indicator in Guilluy, D'Arpa, et al. (2024), where I led the analysis of the visible data. In this work, we employed the GIARPS mode of the **TNG**, focusing on GIANO-B observations to look for He I in the upper atmosphere of five planets hosted by the K and M dwarf stars, WASP-69 b, WASP-107 b, HAT-P-11 b, GJ 436 b, and GJ 3470 b. We measured a contrast c of the excess absorption of $3.91\pm0.22\%$ (17.6σ), $8.17^{+0.80}_{-0.76}\%$ (10.5σ), and $1.36\pm0.17\%$ (8.0σ) for WASP-69 b, WASP-107 b, and HAT-P-11 b, respectively, confirming the literature detections. Our study of WASP-69 b

revealed nightly variations in helium absorption levels, with the initial transit showing a greater absorption than subsequent ones. We examined the Hα line in **HARPS-N** spectra and found it behaved inversely compared to He I data on UT 2019-07-29. This difference was attributed to stellar activity, prompting us to consider its possible causes.
For GJ 3470 b, we observed He I in its outer atmosphere at a level of $1.75^{+0.39}_{-0.36}\%$ (4.7σ), though this varied slightly depending on the selected nights for analysis. Analysing the Hα line indicated hydrogen absorption during the same transit event. Our ATES simulations could not match the observed absorption depth and profile, suggesting stellar activity as the most likely source of this feature. Additional research with advanced radiative transfer models is necessary to support this theory.
Consistent with earlier findings (Nortmann et al. 2018), we found no excess He I absorption in GJ 436 b (our results indicate no significant absorption).

We examined the involvement of Hα and He I triplet as markers for photo-evaporation, as outlined in D'Arpa et al. (2024a). This study presented a nIR+optical high-resolution transmission spectroscopy analysis on planet TOI-5398 b, which shares similarities with Saturn. The data, originating from an observation on March 25, 2023, with the GIARPS mode at the **TNG**, was also previously utilized by Mantovan et al. (2024b) to define orbital parameters and appraise the system's evolutionary trajectory. Using the GIANO-B spectrograph, we identified the He I triplet, while Hα and the Na I doublet were detected using **HARPS-N** through single-line analysis. Per the ExoAtmospheres database[1], this scenario is one of the sparse instances of concurrent detections of He I, Hα , and Na I doublet in an exoplanet's atmosphere. Cross-correlation with templates did not yield detections, likely inhibited by overlapping **RME**, the planet's low temperature, and limited data. The extraction challenge is compounded by observing only one transit, making it tricky to detect atmospheric signals in smaller planets. Following the analysis in Guilluy et al. (2024), examining individual lines over different nights is essential to rule out potential contamination from stellar activity, necessitating further transits to substantiate our findings. Although we associate the detected signal with planet b, based on the system's evolutionary model and ATES simulations, future observations of both planets are crucial to definitively ascertain the signal sources. Extended baseline observations would be beneficial in investigating a possible cometary tail alongside 3D hydrodynamical simulations, as undertaken in Matsakos et al. (2015) and Colombo et al. (2024).

- Finally, in Chapter 5, I moved from high- to low-resolution spectroscopy, focusing on the role of parameter selection and on the impact of the pipelines adopted to analyse **Hubble Space Telescope (HST) Wield Field Camera 3 (WFC3)** data.

  I first introduced the work I'm carrying within the Italian **Ariel** collaboration to develop a framework to adopt an homogenous set of stellar and planetary atmo-

[1] https://research.iac.es/proyecto/exoatmospheres/index.php

spheres. Right now, the framework has been tested on a restricted sample of five targets belonging to the Italian Dry Run, HD209458, WASP-69, HAT-P-14, HD189733, and WASP-80 but in future we aim to extend it to other targets, to build an homogenous database.

Then I introduced the ongoing work that I am leading along with Lorenzo Mugnai, on the comparison of the pipelines to extract **HST WFC3** transmission spectra. We employed several available pipelines to analyse the data of the **UHJ** WASP-121 b evaluating both the discrepancies on the white light curves and on the transmission spectra. We also evaluated the impact of the differences in the spectroscopic light curves on the atmospheric retrievals. Our preliminary results seem to hint that discrepancies in the extracted transmission spectra do not have a large impact on the retrievals. While this holds true for free chemistry with few molecules, we still need to investigate more complex scenario including more molecules and equilibrium chemistry and trying to address the origin of the differences evaluating the different steps in the analysis. Once the framework will be corroborated, we will apply it to other targets and scenarios.

6.2 Impact of the thesis and future developments

Overall in this thesis I introduce my works with transmission spectroscopy, employing both high- and low-resolution data.

6.2.1 High-Resolution Spectroscopy

For the High-Resolution Spectroscopy side, I mainly focused on the development and application of a framework to extract and analyse transmission spectra around narrow regions of the spectrum, the so called single line analysis.
The framework I developed proved to be reliable, especially in D'Arpa et al. (2024b) where the results obtained with KELT-9 b are generally on agreement with the previous obtained in literature. The detection of 70 lines is a record in one single work, with the first ever detection of Hϵ and Hζ along with Cr II and Sc II single lines and a detailed analysis of the stratification and rotational properties of the atmosphere. Moreover the study proved to be powerful when comparison with models is needed as shown for the **NLTE** ones. Simultaneously, in D'Arpa et al. (2024a) and Guilluy, D'Arpa, et al. (2024), I extended the original application of the method to the specific case of the study of the Hα and He I lines as a probe for stellar activity and photo-evaporation. This joint use of the two lines proved to be a valid framework to discriminate the spurious signal due to stellar activity from the signal arising from the exoplanetary atmosphere.

Most of the work introduced regarding high-resolution spectroscopy have been carried on within the Italian **GAPS** collaboration, where I have been recently appointed as co-responsible of the Working Group on the analysis of the visible species with HARPS-N. Within this context, my aim is to conclude the ongoing works as author and co-author. In particular, I have already introduced: the work on TOI-1518 b with the detection of

several species via single line analysis and cross-correlation and with the development of the promising multiple line analysis; and the constraining of C/O ratio employing the single line analysis that would establish a first time ever of constraining the C/O ratio without employing models and would allow to reconstruct the formation history of the hottest planet known. KELT-9 b and KELT-20 b represent also a unique opportunity for the study of the Paschen series lines in the nIR with GIANO-B thanks to their large temperature, allowing us to extend the framework originally developed for the Balmer series to their nIR counterparts.

In this thesis I analysed high-resolution data of 11 planets including some of the most studied in the field such as KELT-9 b and WASP-69 b. While linking all the results among them may be non trivial, it is still possible to draw some conclusions regarding the species detected, the way they have been detected and the planetary and stellar properties of the systems investigated. In Fig. 6.1 I show the targets investigated highlighting their atmospheric scale height as a function of the planetary equilibrium temperature and of the stellar temperature considering the detections of Hα , He I and metal lines. It is clear the opposite behaviour of Hα (and metals) and He I with the first one being detected only in hotter planets orbiting around hotter stars, while the latter being detected only on colder planets around colder stars. The only exception is TOI-5398 b which is the only target with the joint detection of Hα , He I and metal lines. The nature of the detection of Hα and He I is strongly connected to the stellar irradiation, especially the XUV flux, as deeply discussed in the previous chapters and needs to be further investigated in the next years. However, as already discussed, the peculiarity of TOI-5398 b arises from its age of $\sim$ 650 Myr showing that the age of the systems plays a key role in the detection of certain species. It is important to stress that, while the analyses in this thesis have been carried employing homogenous methods, Fig. 6.1 do not take into account key factors such as the stellar activity, the observative conditions, the instrumental limitations and other possible factors affecting the results, and hence it represents only a limited comparison.

However, the variegate sample of planets with a large amount of data collected by the **GAPS** collaboration would represent in the near future an occasion to test the framework I developed for the single line analysis on a catalogue level to address the points raised from the analyses introduced in this thesis. Particularly, a deep study to understand why we are able or not to detect a certain species in the atmosphere of a planet as a function of the stellar and planetary parameters. This would help us identifying the future steps to take to better understand the physics of transmission spectroscopy applied to the exoplanetary atmospheres.

However, before proceeding with the ambitious project of a survey level study, a refinement of the code and a better synergy with the cross-correlation technique and, hopefully, the multiple line analysis-hopefully is required. Along with this as already discussed for WASP-94A b, my framework can also be extended to other high-resolution data to study targets visible from the Southern Hemisphere such as the ones that will be observed by the upcoming PLATO mission, exploiting **European Southern Observatory (ESO)** instruments such as HARPS and ESPRESSO.

Figure 6.1: Hα , He I and metal lines detection and non detection in the atmospheres of the planets analysed in this thesis with High-Resolution data as a function of the stellar and planetary temperatures. The size of the circles is proportional to the scale height of each target.

6.2.2 Low-Resolution Spectroscopy

For the Low-Resolution side, I introduced a new framework to create an homogenous set of planetary and stellar parameters for five targets blowing to the Italian **Ariel** dry run. While, at the moment limited to a specific initiative, the ongoing work on the selection of an homogenous set of planetary and stellar parameters arise from the increasing numbers of solutions for each target that may be find in literature with the NASA Exoplanet Archive and the Exoplanet.eu[2] websites representing only part of the several catalogues available online. With the catalogue level analyses, as discussed for the High-Resolution side, becoming an hot topic in the recent and future years, the problem of an homogenous statistically created catalogue has to be faced now. Once the framework will be further developed, I will apply it to homogenous stellar analysis already presented in literature or in preparation to help creating a robust database to be used in the future works, especially related to the **Ariel** mission when we will have to deal with almost 1000 exoplanetary atmospheres to analyse.

The work in preparation on the comparison of several **HST WFC3** pipelines lays within the same context of the parameters selection, underlying the necessity of further homogeneity in the analysis. The preliminary results for one visit of the **UHJ** WASP-121 b represents only the first step of an ambitious project of comparison on a catalogue level, once the method developed for WASP-121 b will be finally published. Important results from this work will help us focusing on the key steps of the data extraction and reduction to improve before the **Ariel** mission will be launched.

6.2.3 On the synergy between High- and Low-Resolution Spectroscopy

While in this thesis the High- and Low-Resolution spectroscopy have been considered as two separate techniques, within the **Ariel** Italian Dry Run we are working on the possibility to combine GIANO-B high resolution data with **HST** low-resolution ones. Four out of five targets selected have been observed and analysed with GIANO-B and **HST** although with different analyses and parameters used. In our project we aim to re-analyse the available data employing the homogenous set of parameters the we retrieved with the framework I developed. For the **HST** data we will follow the same approach described for WASP-121 b employing different pipelines. Once all the high- and low-resolution spectra will have been extracted, we will use both **Tau Retrieval for Exoplanets (TauREx)** and GUIBRUSH (Giacobbe et al. in preparation) to perform a joint retrievals analysis. If the joint use of the High- and Low-Resolution data will prove powerful, it will possible to start planning future on-ground based observative campaigns simultaneous to the **Ariel** mission.

Despite the general interest in the exoplanetary field is related to the discovery and characterisation of Earth-like planets, with the clear goal to find life in other worlds, nowadays investigation of exoplanetary atmospheres is mainly limited to hot and large planets. While this is mainly due to the instrumental limitation of our time, the new

[2] https://exoplanet.eu/home/

generation of instruments will shift the interest to smaller and colder Earth-like planets in just few years. Therefore, it is necessary for us to address the several challenges arising from relatively easy targets, such as **UHJ** orbiting around low-active stars, to develop strong and corroborated frameworks to be ready for the exciting times that are waiting for us.

References

Ahrer, E., Seidel, J. V., Doyle, L., et al. 2024, MNRAS, 530, 2749

Akeson, R. L., Chen, X., Ciardi, D., et al. 2013, PASP, 125, 989

Al-Refaie, A. F., Changeat, Q., Waldmann, I. P., & Tinetti, G. 2021, ApJ, 917, 37

Allart, R., Bourrier, V., Lovis, C., et al. 2019, A&A, 623, A58

Allart, R., Bourrier, V., Lovis, C., et al. 2018, Science, 362, 1384

Allart, R., Lemée-Joliecoeur, P. B., Jaziri, A. Y., et al. 2023, A&A, 677, A164

Alonso-Floriano, F. J., Snellen, I. A. G., Czesla, S., et al. 2019, A&A, 629, A110

Anderson, D. R., Collier Cameron, A., Delrez, L., et al. 2014, MNRAS, 445, 1114

Anderson, D. R., Collier Cameron, A., Delrez, L., et al. 2017, A&A, 604, A110

Armstrong, D. J., Meru, F., Bayliss, D., Kennedy, G. M., & Veras, D. 2019, ApJ, 880, L1

Astudillo-Defru, N. & Rojo, P. 2013, A&A, 557, A56

Awiphan, S., Kerins, E., Pichadee, S., et al. 2016, MNRAS, 463, 2574

Baglin, A., Auvergne, M., Barge, P., et al. 2007, in American Institute of Physics Conference Series, Vol. 895, Fifty Years of Romanian Astrophysics, ed. C. Dumitrache, N. A. Popescu, M. D. Suran, & V. Mioc (AIP), 201–209

Bakos, G. Á., Torres, G., Pál, A., et al. 2010, ApJ, 710, 1724

Baruteau, C., Crida, A., Paardekooper, S. J., et al. 2014, in Protostars and Planets VI, ed. H. Beuther, R. S. Klessen, C. P. Dullemond, & T. Henning, 667–689

Basilicata, M., Giacobbe, P., Bonomo, A. S., Scandariato, G., & et al. 2023, Submitted

Batalha, N. M. 2014, Proceedings of the National Academy of Science, 111, 12647

Beaugé, C. & Nesvorný, D. 2013, ApJ, 763, 12

Ben-Jaffel, L., Ballester, G. E., Muñoz, A. G., et al. 2022, Nature Astronomy, 6, 141

Benneke, B., Knutson, H. A., Lothringer, J., et al. 2019, Nature Astronomy, 3, 813

Biassoni, F., Borsa, F., Haardt, F., & Rainer, M. 2024a, A&A, 691, A283

Biassoni, F., Caldiroli, A., Gallo, E., et al. 2024b, A&A, 682, A115

Biddle, L. I., Pearson, K. A., Crossfield, I. J. M., et al. 2014, MNRAS, 443, 1810

Birkby, J. L. 2018, in Handbook of Exoplanets, ed. H. J. Deeg & J. A. Belmonte, 16

Bonfils, X., Gillon, M., Udry, S., et al. 2012, A&A, 546, A27

Bonomo, A. S., Desidera, S., Benatti, S., et al. 2017, A&A, 602, A107

Bonomo, A. S., Dumusque, X., Massa, A., et al. 2023, A&A, 677, A33

Borsa, F., Allart, R., Casasayas-Barris, N., et al. 2021a, A&A, 645, A24

Borsa, F., Fossati, L., Koskinen, T., Young, M. E., & Shulyak, D. 2021b, Nature Astronomy, 6, 226

Borsa, F., Rainer, M., Bonomo, A. S., et al. 2019, A&A, 631, A34

Borsato, N. W., Hoeijmakers, H. J., Prinoth, B., et al. 2023, A&A, 673, A158

Bourrier, V., Attia, O., Mallonn, M., et al. 2023, A&A, 669, A63

Bourrier, V., Cegla, H. M., Lovis, C., & Wyttenbach, A. 2017, A&A, 599, A33

Bourrier, V. & des Etangs, A. L. 2018, in Handbook of Exoplanets, ed. H. J. Deeg & J. A. Belmonte, 148

Bourrier, V., Ehrenreich, D., Allan, A., et al. 2018, A&A, 619, A1

Bourrier, V., Zapatero Osorio, M. R., Allart, R., et al. 2022, A&A, 663, A160

Bozza, V., Shvartzvald, Y., Udalski, A., et al. 2016, ApJ, 820, 79

Brogi, M., de Kok, R. J., Albrecht, S., et al. 2016, ApJ, 817, 106

Brogi, M., Snellen, I. A., De Kok, R. J., et al. 2012, Nature, 486, 502

Brown, T. M., Charbonneau, D., Gilliland, R. L., Noyes, R. W., & Burrows, A. 2001, ApJ, 552, 699

Bryson, S., Coughlin, J., Batalha, N. M., et al. 2020, AJ, 159, 279

Butler, R. P. & Marcy, G. W. 1996, ApJ, 464, L153

Butler, R. P., Vogt, S. S., Marcy, G. W., et al. 2004, ApJ, 617, 580

Cabot, S. H. C., Bello-Arufe, A., Mendonça, J. M., et al. 2021, AJ, 162, 218

Caldiroli, A., Haardt, F., Gallo, E., et al. 2022, A&A, 663, A122

Caldiroli, A. et al. 2021, A&A, 655, A30

Carone, L., Mollière, P., Zhou, Y., et al. 2021, A&A, 646, A168

Casasayas-Barris, N., Borsa, F., Palle, E., et al. 2022, A&A, 664, A121

Casasayas-Barris, N., Palle, E., Nowak, G., et al. 2017, A&A, 608, A135

Casasayas-Barris, N., Pallé, E., Yan, F., et al. 2018, A&A, 616, A151

Casasayas-Barris, N., Pallé, E., Yan, F., et al. 2019, A&A, 628, A9

Cauley, P. W. & Ahlers, J. P. 2022, AJ, 163, 122

Cauley, P. W., Kuckein, C., Redfield, S., et al. 2018, AJ, 156, 189

Cauley, P. W., Redfield, S., Jensen, A. G., & Barman, T. 2016, AJ, 152, 20

Cauley, P. W., Shkolnik, E. L., Ilyin, I., et al. 2019, The Astronomical Journal, 157, 69

Cegla, H. M., Lovis, C., Bourrier, V., et al. 2016, A&A, 588, A127

Chachan, Y., Knutson, H. A., Gao, P., & et al. 2019, The Astronomical Journal, 158, 244

Changeat, Q. & Edwards, B. 2021, The Astrophysical Journal Letters, 907, L22

Changeat, Q., Skinner, J. W., Cho, J. Y. K., et al. 2024, ApJS, 270, 34

Charbonneau, D., Brown, T. M., Burrows, A., & Laughlin, G. 2007, in Protostars and Planets V, ed. B. Reipurth, D. Jewitt, & K. Keil, 701

Charbonneau, D., Brown, T. M., Latham, D. W., & Mayor, M. 2000, ApJ, 529, L45

Charbonneau, D., Brown, T. M., Noyes, R. W., & Gilliland, R. L. 2002, ApJ, 568, 377

Chen, G., Casasayas-Barris, N., Pallé, E., et al. 2020, A&A, 635, A171

Chen, G., Guenther, E. W., Pallé, E., et al. 2017, A&A, 600, A138

Chen, G., Pallé, E., Welbanks, L., et al. 2018, A&A, 616, A145

Claret, A. 2000, A&A, 363, 1081

Claudi, R., Benatti, S., Carleo, I., et al. 2017, European Physical Journal Plus, 132, 364

Collier Cameron, A., Bruce, V. A., Miller, G. R. M., Triaud, A. H. M. J., & Queloz, D. 2010, MNRAS, 403, 151

Colombo, S., Pillitteri, I., Petralia, A., Orlando, S., & Micela, G. 2024, A&A, 683, A226

Cosentino, R., Lovis, C., Pepe, F., et al. 2012, Society of Photo-Optical Instrumentation Engineers (SPIE) Conference Series, Vol. 8446, Harps-N: the new planet hunter at TNG, 84461V

Covino, E., Esposito, M., Barbieri, M., et al. 2013, A&A, 554, A28

Cram, L. E. & Mullan, D. J. 1985, ApJ, 294, 626

Cutri, R. M., Skrutskie, M. F., van Dyk, S., et al. 2003, VizieR Online Data Catalog, II/246

Czesla, S., Klocová, T., Khalafinejad, S., & et al. 2015, Astronomy & Astrophysics, 582, A51

Czesla, S., Lampón, M., Sanz-Forcada, J., et al. 2022, A&A, 657, A6

Damasso, M., Bonomo, A. S., Astudillo-Defru, N., et al. 2018, A&A, 615, A69

Damasso, M., Esposito, M., Nascimbeni, V., et al. 2015, A&A, 581, L6

Damasso, M., Rodrigues, J., Castro-González, A., & et al. 2020, Astronomy & Astrophysics, 641, A96

Damiano, M., Micela, G., & Tinetti, G. 2019, ApJ, 878, 153

D'Arpa, M. C., Guilluy, G., Mantovan, G., et al. 2024a, A&A, 692, A77

D'Arpa, M. C., Saba, A., Borsa, F., et al. 2024b, A&A, 690, A237

Davis, T. A. & Wheatley, P. J. 2009, MNRAS, 396, 1012

Delrez, L., Santerne, A., Almenara, J. M., et al. 2016, MNRAS, 458, 4025

Deming, D., Wilkins, A., McCullough, P., et al. 2013, ApJ, 774, 95

Di Maio, C., Changeat, Q., Benatti, S., & Micela, G. 2023, A&A, 669, A150

Dos Santos, L. A. 2023, in Winds of Stars and Exoplanets, ed. A. A. Vidotto, L. Fossati, & J. S. Vink, Vol. 370, 56–71

Dyrek, A., Min, M., Decin, L., et al. 2024, Nature, 625, 51

Edwards, B., Changeat, Q., Tsiaras, A., et al. 2023, ApJS, 269, 31

Edwards, B. & Tinetti, G. 2022, AJ, 164, 15

Eggleton, P. P. 1983, ApJ, 268, 368

Ehrenreich, D., Bonfils, X., Lovis, C., et al. 2014, A&A, 570, A89

Ehrenreich, D., Bourrier, V., Wheatley, P. J., & et al. 2015, Nature, 522, 459

Ehrenreich, D., Prinoth, B., Hoeijmakers, H. J., & et al. 2020, Astronomy & Astrophysics, 640, A89

Estrela, R., Swain, M. R., Roudier, G. M., et al. 2021, AJ, 162, 91

Evans, T. M., Sing, D. K., Wakeford, H. R., et al. 2016, ApJ, 822, L4

Ferland, G. J., Chatzikos, M., Guzmán, F., et al. 2017, Rev. Mexicana Astron. Astrofis., 53, 385

Fischer, D. A. & Valenti, J. 2005, ApJ, 622, 1102

Fortney, J. J., Marley, M. S., Saumon, D., & Lodders, K. 2008, ApJ, 683, 1104

Fossati, Young, M. E., Shulyak, D., et al. 2021, A&A, 653, A52

Fossati, L., Biassoni, F., Cappello, G. M., et al. 2023a, A&A, 676, A99

Fossati, L., Guilluy, G., Shaikhislamov, I. F., et al. 2022, A&A, 658, A136

Fossati, L., Pillitteri, I., Shaikhislamov, I. F., et al. 2023b, A&A, 673, A37

Fossati, L., Shulyak, D., Sreejith, A. G., et al. 2020, A&A, 643, A131

Fouqué, P., Moutou, C., Malo, L., et al. 2018, MNRAS, 475, 1960

Fraine, J. D., Deming, D., Benneke, B., & et al. 2014, Nature, 513, 526

Fressin, F., Torres, G., Charbonneau, D., et al. 2013, ApJ, 766, 81

Fulton, B. J. & Petigura, E. A. 2018, AJ, 156, 264

Fulton, B. J., Petigura, E. A., Howard, A. W., et al. 2017, AJ, 154, 109

Gaia Collaboration, Brown, A. G. A., Vallenari, A., et al. 2018, A&A, 616, A1

García Muñoz, A. & Schneider, P. C. 2019, ApJ, 884, L43

Gaudi, B. S., Stassun, K. G., Collins, K. A., et al. 2017, Nature, 546, 514

Giacobbe, P., Brogi, M., Gandhi, S., et al. 2021, Nature, 592, 205

Gillon, M., Pont, F., Demory, B. O., et al. 2007, A&A, 472, L13

Gould, A. & Loeb, A. 1992, ApJ, 396, 104

Guilluy, G., Andretta, V., Borsa, F., et al. 2020, A&A, 639, A49

Guilluy, G., Bourrier, V., Jaziri, Y., et al. 2023, A&A, 676, A130

Guilluy, G., D'Arpa, M. C., Bonomo, A. S., et al. 2024, A&A, 686, A83

Guilluy, G., Giacobbe, P., Carleo, I., et al. 2022a, A&A, 665, A104

Guilluy, G., Giacobbe, P., Carleo, I., et al. 2022b, A&A, 665, A104

Gully-Santiago, M., Morley, C. V., Luna, J., et al. 2024, AJ, 167, 142

Haynes, K., Mandell, A. M., Madhusudhan, N., Deming, D., & Knutson, H. 2015, ApJ, 806, 146

Helling, C., Iro, N., Corrales, L., et al. 2019, A&A, 631, A79

Henry, G. W., Marcy, G. W., Butler, R. P., & Vogt, S. S. 2000, ApJ, 529, L41

Hoeijmakers, H. J., Ehrenreich, D., Heng, K., et al. 2018, Nature, 560, 453

Hoeijmakers, H. J., Ehrenreich, D., Kitzmann, D., et al. 2019, Astronomy & Astrophysics, 627, A165

Hoeijmakers, H. J., Seidel, J. V., Pino, L., et al. 2020, A&A, 641, A123

Hord, B. J., Kempton, E. M. R., Evans-Soma, T. M., et al. 2024, AJ, 167, 233

Howard, A. W., Marcy, G. W., Johnson, J. A., et al. 2010, Science, 330, 653

Hunter, A., Macgregor, A. B., Szabo, T. O., Wellington, C. A., & Bellgard, M. I. 2012, Source Code for Biology and Medicine

Husser, T. O., Wende-von Berg, S., Dreizler, S., et al. 2013, A&A, 553, A6

Irwin, P. G. J., Teanby, N. A., de Kok, R., et al. 2008, J. Quant. Spectr. Rad. Transf., 109, 1136

Ivshina, E. S. & Winn, J. N. 2022, ApJS, 259, 62

Jara-Maldonado, M., Alarcon-Aquino, V., Rosas-Romero, R., & et al. 2020, Springer, 573

Johnson, J. A., Aller, K. M., Howard, A. W., & Crepp, J. R. 2010, PASP, 122, 905

Johnstone, C. P., Bartel, M., & Güdel, M. 2021, A&A, 649, A96

Johnstone, C. P. & Güdel, M. 2015, A&A, 578, A129

Kass, R. E. & Raftery, A. E. 1995, Journal of the American Statistical Association, 90, 773

Kausch, W., Noll, S., Smette, A., et al. 2015, A&A, 576, A78

Kempton, E. M. R., Bean, J. L., Louie, D. R., et al. 2018, PASP, 130, 114401

Khalafinejad, S., Lillo-Box, J., Curto, G. L., & et al. 2017, Astronomy & Astrophysics, 645, A96

Khalafinejad, S., Molaverdikhani, K., Blecic, J., et al. 2021, A&A, 656, A142

Khalafinejad, S., von Essen, C., Hoeijmakers, H. J., et al. 2017, A&A, 598, A131

Kirk, J., Alam, M. K., López-Morales, M., & Zeng, L. 2020, AJ, 159, 115

Kirk, J., Dos Santos, L. A., López-Morales, M., et al. 2022, AJ, 164, 24

Kitzmann, D., Hoeijmakers, H. J., Grimm, S. L., et al. 2023, A&A, 669, A113

Knutson, H. A., Fulton, B. J., Montet, B. T., et al. 2014, ApJ, 785, 126

Koch, D., Borucki, W., Basri, G., et al. 2007, in IAU Symposium, Vol. 240, Binary Stars as Critical Tools & Tests in Contemporary Astrophysics, ed. W. I. Hartkopf, P. Harmanec, & E. F. Guinan, 236–243

Kokori, A., Tsiaras, A., Edwards, B., et al. 2023, ApJS, 265, 4

Komacek, T. D. & Showman, A. P. 2016, ApJ, 821, 16

Kosiarek, M. R., Crossfield, I. J. M., Hardegree-Ullman, K. K., et al. 2019, AJ, 157, 97

Kreidberg, L., Bean, J. L., Désert, J.-M., et al. 2014, Nature, 505, 69

Kreidberg, L., Line, M. R., Parmentier, V., et al. 2018a, AJ, 156, 17

Kreidberg, L., Line, M. R., Thorngren, D., Morley, C. V., & Stevenson, K. B. 2018b, ApJ, 858, L6

Krishnamurthy, V., Hirano, T., Gaidos, E., et al. 2023, MNRAS, 521, 1210

Kuckartz, U., R:adiker, S., Ebert, T., & Julia, S. 2013, 2nd ed. Wiesbaden: Springer Fachmedien

Kulow, J. R., France, K., Linsky, J., & Loyd, R. O. P. 2014, ApJ, 786, 132

Kurucz, R. L. 1992, in Symposium-International Astronomical Union, Vol. 149, Cambridge University Press, 225–232

Kurucz, R. L. 2005, Memorie della Societa Astronomica Italiana Supplementi, 8, 73

Kurucz, R. L. 2014, in Determination of Atmospheric Parameters of B, 39–51

Kurucz, R. L. 2017, ATLAS9: Model atmosphere program with opacity distribution functions, Astrophysics Source Code Library, record ascl:1710.017

Langeveld, A. B., Madhusudhan, N., & Cabot, S. H. C. 2022, MNRAS, 514, 5192

Lanotte, A. A., Gillon, M., Demory, B. O., et al. 2014, A&A, 572, A73

Lavie, B., Ehrenreich, D., Bourrier, V., et al. 2017, A&A, 605, L7

Lecavelier Des Etangs, A. 2007, A&A, 461, 1185

Lecavelier Des Etangs, A., Vidal-Madjar, A., Désert, J. M., & Sing, D. 2008, A&A, 485, 865

Line, M. R., Stevenson, K. B., Bean, J. L., et al. 2016, The Astronomical Journal, 152, 203

Line, M. R., Wolf, A. S., Zhang, X., et al. 2013, ApJ, 775, 137

Linsky, J. L., Wood, B. E., Youngblood, A., et al. 2020, ApJ, 902, 3

Locci, D., Petralia, A., Micela, G., et al. 2022, PSJ, 3, 1

Lopez, E. & Fortney, J. J. 2013, in American Astronomical Society Meeting Abstracts, Vol. 221, American Astronomical Society Meeting Abstracts #221, 333.04

Lothringer, J. D. & Barman, T. 2019, ApJ, 876, 69

Lothringer, J. D., Sing, D. K., Rustamkulov, Z., et al. 2022, Nature

Louden, T. & Wheatley, P. J. 2015, ApJ, 814, L24

Lovis, C., Ségransan, D., Mayor, M., et al. 2011, A&A, 528, A112

Lund, M. B., Rodriguez, J. E., Zhou, G., et al. 2017, AJ, 154, 194

Lundkvist, M. S., Kjeldsen, H., Albrecht, S., et al. 2016, Nature Communications, 7, 11201

Madhusudhan, N., Agúndez, M., Moses, J. I., & Hu, Y. 2016, Space Sci. Rev., 205, 285

Madhusudhan, N., Amin, M. A., & Kennedy, G. M. 2014, ApJ, 794, L12

Madhusudhan, N. & Seager, S. 2009, ApJ, 707, 24

Maggio, A., Pillitteri, I., Argiroffi, C., et al. 2023, ApJ, 951, 18

Magrini, L., Danielski, C., Bossini, D., et al. 2022, A&A, 663, A161

Mamajek, E. E. & Hillenbrand, L. A. 2008, ApJ, 687, 1264

Mansfield, M., Bean, J. L., Oklopčić, A., et al. 2018, ApJ, 868, L34

Mantovan, G., Malavolta, L., Desidera, S., et al. 2024a, A&A, 682, A129

Mantovan, G., Malavolta, L., Locci, D., et al. 2024b, A&A, 684, L17

Mao, S. & Paczynski, B. 1991, ApJ, 374, L37

Marcy, G. W. & Butler, R. P. 1996, ApJ, 464, L147

Matsakos, T., Uribe, A., & Königl, A. 2015, A&A, 578, A6

Mayor, M. & Queloz, D. 1995, Nature, 378, 355

McLaughlin, D. 1924, The Astrophysical Journal, 60

Morello, G., Claret, A., Martin-Lagarde, M., et al. 2020, AJ, 159, 75

Mugnai, L. V., Swain, M. R., & Estrela, R. 2021, Monthly Notices of the Royal Astronomical Society, 531, 35

Mugnai, L. V., Swain, M. R., Estrela, R., & Roudier, G. M. 2024, MNRAS, 531, 35

Murgas, F., Chen, G., Nortmann, L., Palle, E., & Nowak, G. 2020, A&A, 641, A158

Nail, F., Oklopčić, A., & MacLeod, M. 2024, A&A, 684, A20

Nascimbeni, V., Piotto, G., Pagano, I., et al. 2013, A&A, 559, A32

Ninan, J. P., Stefansson, G., Mahadevan, S., et al. 2020, ApJ, 894, 97

Nortmann, L., Pallé, E., Salz, M., et al. 2018, Science, 362, 1388

Noyes, R. W., Weiss, N. O., & Vaughan, A. H. 1984, ApJ, 287, 769

Oklopčić, A. & Hirata, C. M. 2018, ApJ, 855, L11

Oklopčić, A. 2019, ApJ, 881, 133

Oliva, E., Origlia, L., Baffa, C., et al. 2006, in Society of Photo-Optical Instrumentation Engineers (SPIE) Conference Series, Vol. 6269, Society of Photo-Optical Instrumentation Engineers (SPIE) Conference Series, ed. I. S. McLean & M. Iye, 626919

Oliva, E., Origlia, L., Maiolino, R., et al. 2013, A&A, 555, A78

Orell-Miquel, J., Murgas, F., Pallé, E., et al. 2024, A&A, 689, A179

Oshagh, M., Santos, N. C., Ehrenreich, D., et al. 2014, A&A, 568, A99

Ouyang, Q., Wang, W., Zhai, M., et al. 2023, Research in Astronomy and Astrophysics, 23, 065010

Owen, J. E. 2019, Annual Review of Earth and Planetary Sciences, 47, 67

Owen, J. E. & Wu, Y. 2017, ApJ, 847, 29

Palle, E., Nortmann, L., Casasayas-Barris, N., et al. 2020a, A&A, 638, A61

Palle, E., Oshagh, M., Casasayas-Barris, N., et al. 2020b, A&A, 643, A25

Penz, T., Micela, G., & Lammer, H. 2008, A&A, 477, 309

Pepe, F., Mayor, M., Benz, W., et al. 2000, in From Extrasolar Planets to Cosmology: The VLT Opening Symposium, ed. J. Bergeron & A. Renzini, 572

Pepe, F., Mayor, M., Galland, F., et al. 2002, A&A, 388, 632

Pepe, F., Molaro, P., Cristiani, S., et al. 2014, Astronomische Nachrichten, 335, 8

Pepe, F. A., Cristiani, S., Rebolo Lopez, R., et al. 2010, in Society of Photo-Optical Instrumentation Engineers (SPIE) Conference Series, Vol. 7735, Ground-based and Airborne Instrumentation for Astronomy III, ed. I. S. McLean, S. K. Ramsay, & H. Takami, 77350F

Perryman, M., Hartman, J., Bakos, G. Á., & Lindegren, L. 2014, ApJ, 797, 14

Petigura, E. A., Marcy, G. W., Winn, J. N., et al. 2018, AJ, 155, 89

Pino, L., Désert, J.-M., Brogi, M., et al. 2020, The Astrophysical Journal Letters, 894, L27

Piskunov, N. E., Kupka, F., Ryabchikova, T. A., Weiss, W. W., & Jeffery, C. S. 1995, A&AS, 112, 525

Pollacco, D. L., Skillen, I., Collier Cameron, A., et al. 2006, PASP, 118, 1407

Poppenhaeger, K. 2022, MNRAS, 512, 1751

Preibisch, T. & Feigelson, E. D. 2005, ApJS, 160, 390

Quirrenbach, A., Amado, P. J., Caballero, J. A., et al. 2014, in Society of Photo-Optical Instrumentation Engineers (SPIE) Conference Series, Vol. 9147, Ground-based and Airborne Instrumentation for Astronomy V, ed. S. K. Ramsay, I. S. McLean, & H. Takami, 91471F

Rainer, M., Borsa, F., Pino, L., et al. 2021, A&A, 649, A29

Rainer, M., Harutyunyan, A., Carleo, I., et al. 2018, in Society of Photo-Optical Instrumentation Engineers (SPIE) Conference Series, Vol. 10702, Ground-based and Airborne Instrumentation for Astronomy VII, 1070266

Rasio, F. A. & Ford, E. B. 1996, Science, 274, 954

Redfield, S., Endl, M., Cochran, W. D., & Koesterke, L. 2008, ApJ, 673, L87

Ricker, G. R., Winn, J. N., Vanderspek, R., et al. 2015, Journal of Astronomical Telescopes, Instruments, and Systems, 1, 014003

Ridden-Harper, A., de Mooij, E., Jayawardhana, R., et al. 2023, The Astronomical Journal, 165, 211

Rossiter, R. 1924, The Astrophysical Journal, 60

Roudier, G. M., Swain, M. R., Gudipati, M. S., et al. 2021, AJ, 162, 37

Rumenskikh, M. S., Khodachenko, M. L., Shaikhislamov, I. F., et al. 2023, MNRAS, 526, 4120

Salz, M., Czesla, S., Schneider, P. C., et al. 2018, A&A, 620, A97

Sánchez-López, A., Lin, L., Snellen, I. A. G., et al. 2022, A&A, 666, L1

Santos, N. C., Cristiani, S., Pepe, F. A., & et al. 2020, Astronomy & Astrophysics, 639, A77

Sanz-Forcada, J. 2022, Astronomische Nachrichten, 343, e20008

Sanz-Forcada, J., López-Puertas, M., Nortmann, L., & Lampón, M. 2022, in The 21st Cambridge Workshop on Cool Stars, Stellar Systems, and the Sun, Cambridge Workshop on Cool Stars, Stellar Systems, and the Sun, 138

Sanz-Forcada, J., Micela, G., Ribas, I., et al. 2011, A&A, 532, A6

Seager, S. 2013, Science, 340, 577

Seager, S. & Sasselov, D. D. 2000, ApJ, 537, 916

Showman, A. P., Tan, X., & Parmentier, V. 2020, Space Sci. Rev., 216, 139

Sicilia, D., Malavolta, L., Pino, L., et al. 2022, A&A, 667, A19

Sicilia, D., Malavolta, L., Scandariato, G., et al. 2025, A&A, 693, A316

Sicilia, D., Scandariato, G., Guilluy, G., et al. 2024, A&A, 687, A143

Sing, D. K., Fortney, J. J., Nikolov, N., et al. 2016, Nature, 529, 59

Siverd, R. J., Pepper, J., Stanek, K., et al. 2009, in IAU Symposium, Vol. 253, Transiting Planets, ed. F. Pont, D. Sasselov, & M. J. Holman, 350–353

Smette, A., Sana, H., Noll, S., et al. 2015, A&A, 576, A77

Snellen, I. A. G., de Mooij, E. J. W., & Burrows, A. 2010, A&A, 513, A76

Spake, J. J., Oklopčić, A., & Hillenbrand, L. A. 2021, AJ, 162, 284

Spake, J. J., Sing, D. K., Evans, T. M., et al. 2018, Nature, 557, 68

Spinelli, R., Gallo, E., Haardt, F., et al. 2023, AJ, 165, 200

Stangret, M., Fossati, L., D'Arpa, M. C., et al. 2024, A&A, 692, A76

Stassun, K. G., Collins, K. A., & Gaudi, B. S. 2017, AJ, 153, 136

Stefànsson, G., Mahadevan, S., Petrovich, C., et al. 2022, ApJ, 931, L15

Stevens, D. J. & Gaudi, B. S. 2013, PASP, 125, 933

Stevenson, K. B., Harrington, J., Nymeyer, S., & et al. 2010, Nature, 464, 1161

Suárez Mascareño, A., Rebolo, R., González Hernández, J. I., & Esposito, M. 2015, MNRAS, 452, 2745

Suárez Mascareño, A., Faria, J. P., Figueira, P., et al. 2020, Astronomy & Astrophysics, 640, A69

Swain, M. R., Estrela, R., Roudier, G. M., & Sotin, C. 2021, The Astronomical Journal, 161, 284

Szabó, G. M. & Kiss, L. L. 2011, ApJ, 727, L44

Ter Braak, C. J. F. 2006, Statistics and Computing, 16, 239

Tinetti, G., Drossart, P., Eccleston, P., et al. 2016, in Society of Photo-Optical Instrumentation Engineers (SPIE) Conference Series, Vol. 9904, Space Telescopes and Instrumentation 2016: Optical, Infrared, and Millimeter Wave, ed. H. A. MacEwen, G. G. Fazio, M. Lystrup, N. Batalha, N. Siegler, & E. C. Tong, 99041X

Tinetti, G., Tennyson, J., Griffith, C. A., & Waldmann, I. 2012, Philosophical Transactions of the Royal Society of London Series A, 370, 2749

Tinetti, G., Vidal-Madjar, A., Liang, M.-C., et al. 2007, Nature, 448, 169

Traub, W. A. & Oppenheimer, B. R. 2010, in Exoplanets, ed. S. Seager, 111–156

Triaud, A. H. M. J., Gillon, M., Ehrenreich, D., et al. 2015, MNRAS, 450, 2279

Triaud, A. H. M. J., Martin, D. V., Ségransan, D., et al. 2017, A&A, 608, A129

Tsiaras, A., Waldmann, I. P., Rocchetto, M., et al. 2016, ApJ, 832, 202

Tsiaras, A., Waldmann, I. P., Tinetti, G., Tennyson, J., & Yurchenko, S. N. 2019, Nature Astronomy, 3, 1086

Tsiaras, A., Waldmann, I. P., Zingales, T., et al. 2018, AJ, 155, 156

Turner, J. D., de Mooij, E. J., Jayawardhana, R., et al. 2020, The Astrophysical Journal Letters, 888, L13

Turner, J. D., de Mooij, E. J. W., Jayawardhana, R., et al. 2020, ApJ, 888, L13

Turner, J. D., Pearson, K. A., Biddle, L. I., et al. 2016, MNRAS, 459, 789

Tyler, D., Petigura, E. A., Oklopčić, A., & David, T. J. 2024, ApJ, 960, 123

Vidal-Madjar, A., Arnold, L., Ehrenreich, D., et al. 2010, A&A, 523, A57

Vidal-Madjar, A., Désert, J. M., Lecavelier des Etangs, A., et al. 2004, ApJ, 604, L69

Vidal-Madjar, A., Lecavelier des Etangs, A., Désert, J. M., et al. 2003, Nature, 422, 143

Vissapragada, S., Knutson, H. A., Greklek-McKeon, M., et al. 2022, AJ, 164, 234

Vissapragada, S., Knutson, H. A., Jovanovic, N., et al. 2020, AJ, 159, 278

von Essen, C., Mallonn, M., Welbanks, L., et al. 2019, A&A, 622, A71

Waldmann, I. P., Tinetti, G., Rocchetto, M., et al. 2015, ApJ, 802, 107

Wolszczan, A. & Frail, D. A. 1992, Nature, 355, 145

Wood, B. E., Laming, J. M., Warren, H. P., & Poppenhaeger, K. 2018, ApJ, 862, 66

Wyttenbach, A., Ehrenreich, D., Lovis, C., Udry, S., & Pepe, F. 2015, Astronomy & Astrophysics, 577, A62

Wyttenbach, A., Mollière, P., Ehrenreich, D., et al. 2020, Astronomy & Astrophysics, 638, A87

Yan, F., Casasayas-Barris, N., Molaverdikhani, K., et al. 2019, Astronomy & Astrophysics, 632, A69

Yan, F. & Henning, T. 2018, Nature Astronomy, 2, 714

Yan, F., Pallé, E., Fosbury, R. A., Petr-Gotzens, M. G., & Henning, T. 2017, Astronomy & Astrophysics, 603, A73

Zeng, L., Jacobsen, S. B., Sasselov, D. D., et al. 2019, Proceedings of the National Academy of Science, 116, 9723

Zhang, M., Dai, F., Bean, J. L., Knutson, H. A., & Rescigno, F. 2023a, ApJ, 953, L25

Zhang, Z., Morley, C. V., Gully-Santiago, M., et al. 2023b, Science Advances, 9, eadf8736

Zieba, S. & Kreidberg, L. 2022, The Journal of Open Source Software, 7, 4838